

UNIVERSITE
CATHOLIQUE
DE LOUVAIN

Louvain-La-Neuve

FACULTE DES SCIENCES APPLIQUEES

Modeling of damage mechanisms in AlMgSi alloys

Understanding the role of homogenization on the extrudability

Dissertation présentée par
Denis Lassance
pour l'obtention du grade
de Docteur en Sciences Appliquées

Composition du Jury:

Pr. Thomas PARDOEN (co-Promoteur)	Université Catholique de Louvain
Pr. Francis DELANNAY (co-Promoteur)	Université Catholique de Louvain
Pr. Patrick BERTRAND (Président du jury)	Université Catholique de Louvain
Pr. Yves BRECHET	INP Grenoble
Pr. Bruno DE MEESTER DE BETZENBROECK	Université Catholique de Louvain
Pr. Sybrand VAN DER ZWAAG	Technische Universiteit Delft
Dr. Claude VAN DORPE	Sapa RC Profile

Mars 2006

©Presses universitaires de l'UCL & Denis LASSANCE
Place de l'université, 1
B-1348 Louvain-La-Neuve (Belgique)

Toute reproduction d'un extrait quelconque de ce livre,
hors des limites restrictives prévues par la loi,
par quelque procédé que ce soit, et notamment par photocopie ou scanner,
est strictement interdite pour tous pays.

Imprimé en Belgique

ISBN: 2-87463-017-9

Université Catholique de Louvain
Faculté des Sciences Appliquées
Place Sainte Barbe, 2, B-1348 Louvain-La-Neuve, Belgium

...”employ another metal instead of iron.” ”Copper?” said Morgan. ”No! That would be too heavy. I have better than that to offer.” ”What then?” asked the major. ”Aluminium!” ”Aluminium?” cried his three colleagues in chorus. ”Unquestionably, my friends. This valuable metal possesses the whiteness of silver, the indestructibility of gold, the tenacity of iron, the fusibility of copper, the lightness of glass. It is easily wrought, is very widely distributed, forming the base of most of the rocks, is three times lighter than iron, and seems to have been created for the express purpose of furnishing us with the material for our projectile.” (speaking about the aluminium capsule being shot into space)

Jule Verne
From the earth to the moon
Chapter 7

Abstract

With the growth in importance of the aluminium industry, has come increased demand to invest into the quality improvement of the different aluminium based hot extruded products. One of the main mechanisms, which can influence deformation at high temperature within the 6xxx aluminium, is linked to the presence of the AlFeSi intermetallic phases. These phases severely restrict hot workability when present as hard and brittle plate-like precipitates β -AlFeSi. Damage initiation occurs in these alloys by decohesion or fracture of these intermetallic inclusions.

The negative effect of the β -AlFeSi particles can be mitigated by performing a long homogenization heat treatment at a sufficiently high temperature, by which this phase transforms into the more rounded meta-stable cubic α -AlFeMnSi phase.

The understanding and modeling of the deformation and fracture behavior of aluminium alloys at room and at hot working temperature is very important for optimizing manufacturing processes such as extrusion. The ductility of 6xxx aluminium alloys can be directly related to chemical composition and to the microstructural evolution occurring during the heat treatment procedures preceding extrusion if proper physics based deformation and fracture models are used. In this thesis, room temperature and hot tensile tests are adopted to address the problem experimentally. The damage evolution mechanisms is defined at various temperatures and a micromechanics based model of the Gurson type considering several populations of cavities nucleated by different second phase particles groups is developed on the basis of the experimental observations. This model allows relating quantitatively microstructure and ductility at various temperatures strain rates and stress triaxialities. Finite element simulations based on an enhanced micromechanics-based model are used to validate the model. Finally, the effect of some key factors that determine the extrudability of aluminium is also discussed and a correlation between the ductility calculations in uniaxial tension and the maximum extrusion speed is developed for one defined profile.

Remerciements

Il existe de nombreux jeux, mais ils ont tous je crois un point commun : il faut maîtriser certaines connaissances et techniques pour y jouer. Ainsi, parle-t-on d'initiateur, de maître ou encore de mentor. Thomas Pardoën et Francis Delannay ont su jouer ce rôle admirablement avec moi et je leur en suis extrêmement reconnaissant. Ils ont su transmettre leur passion pour ce jeu - sérieux - qu'est la recherche.

Je veux aussi ici les remercier pour avoir toujours su m'aider, me soutenir, m'orienter, me conseiller et surtout pour avoir su me laisser une grande liberté et beaucoup d'autonomie tout en gardant un oeil bienveillant sur moi. Ils m'ont laissé libre de choisir les directions vers lesquelles mes travaux se sont orientés et la manière de les aborder ; ils ont toujours su me témoigner une grande confiance. Grâce à eux, ces années de thèse ont été un grand enrichissement pour moi. Travailler avec eux a été stimulant et le jeu en a toujours valu la chandelle. Je voudrais aussi les remercier pour leur gentillesse et pour l'intérêt qu'ils ont porté à mes travaux depuis quatre ans.

Je voudrais également remercier Laurence Ryelandt d'avoir accepté de me suivre de près durant cette thèse. Elle a joué son rôle parfaitement, et ses remarques et corrections m'ont été précieuses. Aussi, je remercie Claude Van Dorpe, Johanne Etienne, Marc Ryckeboer et toutes les autres personnes de Sapa qui m'ont fait profiter de leur expérience, de leur connaissance et de leur temps.

Yves Brechet, Bruno de Meester de Betzenbroeck, Sybrand van der Zwaag et Claude Van Dorpe m'ont fait l'honneur de participer à ce jury. Je veux les remercier pour cela.

J'ai eu la chance de faire ma thèse dans de bonnes conditions grâce à l'unité d'Ingénierie des Matériaux et des Procédés. Je voudrais ainsi remercier Marc, Pascal, Laurence, Sophie, Albert, Emile et le restant de l'équipe.

Enfin, comment parler de l'unité IMAP sans avoir une pensée pour les thésards

avec qui j'ai partagé (ou non) un bureau durant ces années: Yannick, Frédérique, Florence, Arnaud, Astrid, Damien, Gauthier, Cédric, Aude, Marc, Victor,... Merci pour tous les bons moments passés, les soupers, les conférences, Mealor! Je tiens à les remercier pour l'ambiance plus que sympathique.

Je voudrais aussi remercier mes parents et ma soeur pour m'avoir fourni depuis très longtemps déjà un cadre familial propice à un épanouissement personnel et scolaire. Mes parents sont responsables de mon existence, et donc en quelque sorte de celle de cette thèse. Je n'ai jamais eu l'occasion de les remercier "formellement" pour tout ce qu'ils ont fait pour moi, pour leurs encouragements et leur amour. Je les remercie donc pour tout cela. J'ai aussi une pensée pour toute ma famille, la maman de Jean-Yves et tous mes amis qui n'ont jamais cessé de prendre des nouvelles de mes travaux et pour tout ceux qui, à leur manière, ont clairé ces années.

Enfin, tous ceux qui me connaissent un tant soit peu sauront bien que les mots qui suivent sont dérisoires par rapport à ce que je pense de celui qui m'accompagne depuis toutes ces années. Jean-Yves, je voudrais te remercier ici pour toutes ces heures, celles passées à m'écouter, celles passées à me relire, celles passées à me supporter, celle passées à mes côtés... Merci pour tout.

Contents

General introduction	1
1 Theoretical background	7
1.1 Background on extrusion	9
1.2 Background on the metallurgy of AlMgSi alloys	11
1.3 Background on homogenization treatment	14
1.3.1 Intermetallic phases in the ENAA 6xxx series	15
1.3.2 Morphological changes	16
1.3.3 Influence of the alloy content	18
1.3.4 Improvement of extrudability	18
1.4 Surface quality considerations	19
1.4.1 Surface cracking	20
1.4.2 Pick-up and die-lines	20
1.5 Micro-mechanisms of ductile fracture	21
1.6 Micromechanics-based constitutive model for ductile fracture	23
1.6.1 Local approach to fracture	23
1.6.1.a Void nucleation	24
1.6.1.b Growth of isolated void	25
1.6.1.c Micromechanical model by Gurson for porous solids	26
1.6.1.d Influence of the void shape	28
1.6.1.e Void coalescence conditions	28
1.6.2 Unified extended model for void growth and coalescence	30
2 The starting point	33
2.1 Introduction on industrial extrusion	36
2.2 Material and Industrial testing	37
2.2.1 Material	37
2.2.2 Homogenization tests	38
2.2.3 Extrusion tests	38

2.3	Results of the extrusion tests	39
2.3.1	Surface defect A	41
2.3.2	Surface defect B	43
2.3.3	Evolution of the extrusion temperature	43
2.4	Microstructure investigation around the surface defects	45
2.4.1	TEM investigation at the defects locations	45
2.4.2	DSC investigation at the defects locations	46
2.4.2.a	The DSC methodology	48
2.4.2.b	DSC measurements	49
2.5	First conclusions	49
3	Microstructure evolution during homogenization	53
3.1	Introduction	55
3.2	Materials and Experimental techniques	57
3.2.1	Material	57
3.2.2	Experimental techniques for microstructure analysis	58
3.2.2.a	Scanning Electron Microscopy (SEM)	58
3.2.2.b	Quantification of the relative α -AlFeMnSi and β -AlFeSi fraction by SEM and EDS	58
3.2.2.c	Measurements of the intermetallics shape by Image analysis (IA)	60
3.3	Results	60
3.3.1	SEM investigations of the microstructure evolution	60
3.3.2	Quantification of the microstructure evolution	62
3.4	Conclusions	67
4	Growth and coalescence of penny-shaped voids	71
4.1	Introduction	74
4.2	Void cell calculations with initially penny-shaped voids	78
4.2.1	Numerical procedures	78
4.2.2	Results of the unit cell calculations without particle	79
4.2.3	Results of the unit cell calculations with particle	85
4.3	The constitutive model	89
4.3.1	The model	90
4.3.1.a	Before void nucleation	90
4.3.1.b	Void nucleation condition	91
4.3.1.c	Void growth model	92
4.3.1.d	Void coalescence condition	93
4.3.2	Assessment of the model	94
4.3.2.a	Assessment of the void coalescence condition	94
4.3.2.b	Assessment of the void growth model	94
4.4	Parametric study and discussion	95
4.4.1	No nucleation stage - low to large stress triaxiality	96
4.4.2	No nucleation stage - very low stress triaxiality	99

4.4.3	Delayed void nucleation	103
4.4.4	Simple model for the ductility of metals with penny shape voids	106
4.5	Conclusions	109
5	Micromechanics of low and high temperature fracture in 6xxx Al alloys	113
5.1	Introduction	116
5.2	Materials, Experimental methods and Mechanical data reduc- tion scheme	118
5.2.1	Materials	118
5.2.2	Characterization of the damage nucleation and evolution	119
5.2.3	Tensile tests	121
5.2.4	Inverse procedure to determine uniaxial flow properties	122
5.3	Experimental results	125
5.3.1	Mechanical tensile tests	125
5.3.1.a	Nominal stress-strain relationships	125
5.3.1.b	Yield stress evolution	129
5.3.1.c	Uniform elongation - Hardening behavior . . .	129
5.3.1.d	Inverse identification of the materials flow curves	133
5.3.1.e	True average fracture strain ϵ_f	133
5.3.2	Fracture mechanisms	140
5.3.2.a	In situ tensile tests at room temperature . . .	140
5.3.2.b	Interrupted tensile tests at high temperature .	143
5.3.2.c	Fracture surface	144
5.4	Micromechanical modeling	146
5.4.1	Physical model	146
5.4.2	Micromechanics-based full constitutive model	149
5.4.2.a	Introduction	149
5.4.2.b	Before void nucleation	151
5.4.2.c	Void nucleation condition	151
5.4.2.d	Void growth model	152
5.4.2.e	Onset of void coalescence	156
5.4.2.f	Void coalescence	158
5.4.3	Numerical method and problem formulation	158
5.4.4	Results of the modeling	160
5.4.4.a	Parameters identification	160
5.4.4.b	Deformation at room temperature	162
5.4.4.c	Deformation at high temperature	163
5.5	Discussion and conclusions	166

6	Parametric study and optimization of extrusion conditions	171
6.1	Introduction	173
6.2	Influence of the homogenization temperature and holding time	174
6.3	Influence of the Mg and Si content	176
6.4	Influence of the Mn content	177
6.5	Influence of Fe content	178
6.6	Influence of the thermal treatment on Mg ₂ Si dissolution . . .	179
6.6.1	Mg ₂ Si phase dissolution/growth	180
6.6.1.a	The dissolution/growth model	180
6.6.1.b	Results	183
7	Conclusions	189
	Bibliography	199
A	Effect of the anisotropy distribution parameter λ_0	207
B	Important geometrical relationships	213
C	Expressions for the parameters of the void growth model	217
D	Klocker formulation for void aspect parameter k	223
E	Flow curves identification	227

List of Figures

1	Temperature path of the aluminium heating process during the production of extrusion profiles. Homogenization and extrusion are displayed schematically.	2
2	The β -to- α transformation in AlMgSi aluminium alloys: (a) β particles in the as-cast state and (b) α particles after homogenization at 580°C for 3h30.	4
1.1	The Direct Extrusion process.	10
1.2	Evolution of the load during extrusion.	11
1.3	Pseudo binary phase Al/Mg ₂ Si diagram.	13
1.4	The β network in as-cast AlMgSi alloys.	17
1.5	The β -to- α transformation in AlMgSi aluminium alloys (a) β particles in the as-cast state (b) α particles after homogenization at 580°C for 3h30.	17
1.6	Physical sequence of damage mechanisms in aluminium alloys.	22
1.7	Dimples on the fracture surface of an ENAA 6060 tensile specimen with second phase particles at the bottom responsible for damage nucleation.	23
1.8	Unit cell geometry representing volume element that the model aims at describing.	30
2.1	The industrial 1800T press used during the extrusion tests.	39
2.2	Shape of the extruded profile.	40
2.3	Surface defects appearing during the extrusion tests: (a) <i>defect A</i> appears on the outside edges of the profiles (b) <i>defect B</i> appears at an inside protuberance of the profiles.	41
2.4	Evolution of the defect A intensity with ram speed for different homogenization treatments: (a) the upper profile and (b) the lower profile.	42

2.5	Evolution of the defect B intensity with ram speed for different homogenization treatments: (a) the upper profile and (b) the lower profile.	44
2.6	Evolution of the extrusion temperature with ram speed for the different homogenization conditions.	45
2.7	TEM micrographs of samples close to the surface defects A locations: (a-b) AlFeSi cracked particles and (c-e) pure silicon inclusions.	47
2.8	TEM micrographs of samples close to the surface defects B locations: evidence of Mg ₂ Si precipitations.	48
2.9	Sketch of the power-compensated null balance principle of a DSC.	48
2.10	(a) DSC scans of the samples taken at the surface defect A place with heating rates from 5 to 80°C/min, (b) zoom in the temperature range of interest.	50
2.11	Extrapolation of the eutectic melting onset temperature to infinite slow heating rate.	51
3.1	Graphical representation of ENAA6060 and ENAA6005A chemistry limits.	56
3.2	Various SEM micrographs showing β intermetallic β -AlFeSi particles in as-cast AlMgSi alloys.	61
3.3	Microstructure of the ENAA 6060 alloy after homogenization at 585°C: (a) 120 minutes, (b) 180 minutes, (c) 240 minutes, (d) 300 minutes.	62
3.4	Microstructure of the ENAA 6060 alloy after homogenization at 600°C: (a) 30 minutes, (b) 60 minutes, (c) 90 minutes, (d) 120 minutes.	63
3.5	Assembly of EDX measurements on (a) as-cast sample and (b) homogenized sample 3h30 at 585°C.	64
3.6	S-ratio distribution of iron bearing intermetallic in ENAA 6060 for (a) an as-cast sample and a fully homogenized sample, (b) for samples homogenized 150 minutes, 240 minutes and 300 minutes at 585°C.	65
3.7	Absolute error of $f_{\alpha \text{ apparent}}$ made by incorrect allocation of α -AlFeMnSi or β -AlFeSi particles, as a function of the critical S_{ratio} , called S_{crit}	66
3.8	Evolution of the α -AlFeMnSi particles ratio during homogenization (a) at 585°C and (b) at 600°C for the three studied alloy.	68
3.9	Evolution of the intermetallic particles mean aspect ratio during homogenization (a) at 585°C and (b) at 600°C for the three studied alloy.	69

4.1	Sequence of damage mechanisms starting with particle fracture, followed by a stable void growth stage from an initially very flat geometry, void coalescence, and crack propagation; the sequence is related to the overall stress strain curve associated to a representative volume of material.	75
4.2	Model material consisting of a periodic packing of unit cells involving one particle. The unit cell is approximated by a cylindrical cell to simplify the numerical analysis.	76
4.3	Fine initial meshes used to model unit cell (a) without and (b) with the presence of a particle.	79
4.4	Results of the FE unit cell calculations for various initial void aspect ratio W_0 ranging between 0.001 and 1, under a constant stress triaxiality $T = 1$, with $n = 0.1$ and $E/\sigma_0 = 500$, for (a,b,c) $f_p = 1\%$ and (d,e,f) for $f_p = 10\%$; (a,d) overall axial stress versus axial strain curves; (b,e) evolution of the porosity as a function of the axial strain; (c,f) evolution of the void aspect ratio as a function of the axial strain. The onset of coalescence is indicated by a bullet.	83
4.5	Variation of the ductility ϵ_f as a function of the void aspect ratio W_0 for $n = 0.1$; (a) for different particle volume fraction $f_p = 0.1, 1$ and 10% with a stress triaxiality $T = 1$, (b) for different stress triaxiality $T = 2/3, 1$ and 1.5 with $f_p = 1\%$. The results obtained from the FE unit cell simulations are compared to the predictions of the void coalescence condition using the evolution of the state variables calculated either by the FE unit cell method or by the constitutive model.	84
4.6	Results of the FE cell calculations for uniaxial tension conditions, i.e. $T = 1/3$, very flat initial voids $W_0 = 0.01$, and various particle volume fractions f_p ; (a) axial stress versus axial strain curves; (b) evolution of the porosity; (c) evolution of the void aspect ratio.	87
4.7	Results of the FE unit cell calculations with and without the presence of particles surrounding a flat initial void ($W_0 = 0.01$) for two different stress triaxialities ($1/3$ and 1) and three different particle volume fractions $f_p = 0.1, 1$ and 10% , with $n = 0.1$ and $E/\sigma_0 = 500$; (a) axial stress - axial strain curves; (b) evolution of the porosity as a function of the axial strain; (c) evolution of the void aspect ratio as a function of the axial strain.	89

4.8	Variation of the overall axial stress as a function of the overall axial strain predicted by FE unit cell calculations for flat voids ($W_0 = 0.01$) surrounded by particles with different stiffness ($E_p/E = 1, 2, 4, 10$). The volume fraction of particles is $f_p = 1\%$. The particles are spherical, i.e. $W_p = 1$. The plastic properties of the matrix are described by $n = 0.1$ and $E/\sigma_0 = 500$	90
4.9	Variation of the ductility as a function of the stress triaxiality for penny-shaped voids of aspect ratio $W_0 = 0.01$ and for three volume fractions of particles $f_p = 0.1\%$, 1% and 10% , considering (a) different strain hardening exponents $n = 0.01, 0.1, 0.2, 0.3$ with $E/\sigma_0 = 500$ and $\lambda_0 = 1$; (b) different ratios $E/\sigma_0 = 100, 500, 2500$ with $n = 0.1$ and $\sigma_0 = 1$; (c) three different anisotropy distribution parameters $\lambda_0 = , 1, \text{ and } 2$, with $E/\sigma_0 = 500$ and $n = 0.1$	98
4.10	Variation of the ductility as a function of the anisotropy distribution parameters λ_0 for penny-shaped voids of aspect ratio $W_0 = 0.01$, for three relative void spacings $\chi_0 = 0.114, 0.247, \text{ or } 0.531$, two strain hardening exponents $n = 0.1$ and 0.3 , and a stress triaxiality T equal to 1	99
4.11	Variation of the saturation porosity attained under uniaxial tension condition, normalized by the particle volume fraction, as a function of the particle volume fraction for initially flat voids ($W_0 = 0.01$) and two different strain hardening exponents $n = 0.1$ and 0.3 . The threshold particle volume fraction f_p^* under which no coalescence takes place is also indicated on the figure	100
4.12	Variation of the transition stress triaxiality as a function of the particle volume fraction for initially flat voids ($W_0 = 0.01$) and $n = 0.1$. The transition stress triaxiality is the stress triaxiality under which, for a given volume fraction of particles, no void coalescence takes place (the porosity either saturates with straining or decreases). This figure can also be interpreted as giving the variation of the threshold particle volume fraction as a function of the stress triaxiality	101
4.13	Variation of the ductility as a function of the particle volume fraction for different initial void aspect ratios $W_0 = 0.01, 0.05, 0.2, 0.5$, strain hardening exponent $n = 0.1$ or 0.3 and a stress triaxiality equal to $1/3$. The necking condition predicted by the Considere criterion is indicated on the figure to show the range of particle volume fraction for which fracture can be expected before the occurrence of necking under uniaxial tension conditions	102

4.14	Variation of the ductility and nucleation strain vs. triaxiality for a material involving 1% of spherical particles of stiffness $E_p/E = 10$ giving rise to penny-shaped voids ($W_0 = 0.01$) when a nucleation stress σ_c is attained; (a) for various nucleation stresses $\sigma_c/\sigma_0 = 0, 4, 5, 6$ and $n = 0.1$; (b) for two nucleation stresses $\sigma_c/\sigma_0 = 0, 5$ and two strain hardening exponents $n = 0.1$ and 0.2	104
4.15	Variation of the normalized void growth strain (i.e. the strain increment from void nucleation to void coalescence) normalized by the nucleation strain as a function of the stress triaxiality for various void nucleation stress σ_c/σ_0 and for two different initial void aspect ratios $W_0 = 0.01$ (penny shape void) and 1 (spherical void). This plot can be seen as a failure map that determines whether the fracture is controlled more by the void nucleation stage or by the void growth stage.	105
4.16	Variation of the void aspect ratio of initially penny-shaped voids as a function of the overall strain for three different stress triaxialities: comparison between the simple evolution law (19) (which is independent of the stress triaxiality) and the FE predictions.	107
4.17	Variation of the ductility as a function of the stress triaxiality for three particle volume fractions in the case of initially penny-shaped voids : comparison between the simple model (23) and the FE predictions.	109
5.1	Evolution of the transformation of the β -AlFeSi particles into α -AlFeSi particles during homogenization at 585°C; (a) volume fraction of α -AlFeSi particles; (b) mean aspect ratio.	120
5.2	Geometry of the test specimens, dimensions in mm: smooth and notched round bars.	122
5.3	Illustration of the iterative inverse identification procedure applied to the alloy ENAA 6060 at 20°C; (a) comparison between the experimental and simulated load-displacement curves (for three different iterations) and (b) the corresponding true stress-true strain curves.	124
5.4	3D representation of the finite element meshes used to simulate the tensile tests on the smooth and notched round bars; (a) smooth specimen (b) notched specimen with a notch radius equal to 5mm (c) notched specimen with a notch radius equal to 2mm.	125

5.5	Nominal stress- strain curves for the alloy ENAA 6060 homogenized at 585°C for 2h30 and deformed at different temperatures ranging 20°C to 590°C, at a strain rate of 0.2 s ⁻¹ (a) all curves; (b) only the curves corresponding to temperatures larger than 550°C.	126
5.6	Nominal stress- strain curves for the alloy ENAA 6005A homogenized at 585°C for 2h30 and deformed at different temperatures ranging 20°C to 590°C, at a strain rate of 0.2 s ⁻¹ (a) all curves; (b) only the the curves corresponding to temperatures larger than 550°C.	127
5.7	Nominal stress-nominal strain curves for athe alloy ENAA 6060 homogenized at 585°C with different holding times (2h30, 3h30 and 4h30) and deformed at 550°C, under a strain rate of 0.2 s ⁻¹	128
5.8	Nominal stress-nominal strain curves for the alloy ENAA 6005A homogenized at 585°C with different holding times (2h30, 3h30 and 4h30) and deformed at 550°C, under a strain rate of 0.2 s ⁻¹	129
5.9	Nominal stress-nominal strain curves obtained at three different strain rates: 0.02, 0.2 and 2 s ⁻¹ for the alloys (a) ENAA 6060 homogenized at 585°C for 4h30 and (b) ENAA 6005A homogenized at 585°C for 3h30. Both alloys are deformed at 550°C.	130
5.10	Variation of the yield stress as a function of the deformation temperature for aluminium alloys (a) ENAA 6060 and (b) ENAA 6005A. Both alloys were homogenized at 585°C for three different holding times and deformed at a strain rate of 0.2 s ⁻¹	131
5.11	Variation of the (true) uniform strain as a function of test temperature for alloys (a) ENAA 6060 and (b) ENAA 6005A. Both alloys were homogenized at 585°C with different holding times (2h30, 3h30 and 4h30) and deformed at a strain rate of 0.2 s ⁻¹	132
5.12	True stress-true plastic strain flow curves at 20°C obtained after inverse indentification for the alloys (a) ENAA 6060 and (b) ENAA 6005A. Both alloys were homogenized at 585°C for different holding times.	134
5.13	True stress-true plastic strain flow curves for different strain rates equal to 0.02, 0.2 and 2 s ⁻¹ at (a,c) 450°C and (b,d) 550°C for the alloys (a,b) ENAA 6060 and (c,d) ENAA 6005A. Both alloys were homogenized at 585°C.	136

5.14	Variation of the strain hardening exponent n and strain rate sensitivity exponent m identified with the iterative inverse procedure as a function of the test temperature for the alloys ENAA 6060 and ENAA 6005A, both homogenized at 585°C for 24h.	137
5.15	Variation of the average true fracture strain ϵ_f as a function of the test temperature for the alloys (a) ENAA 6060 and (b) ENAA 6005A homogenized at 585°C for different holding times (2h30, 3h30 and 4h30).	138
5.16	Variation of the true fracture strain ϵ_f for different strain rates as a function of the deformation temperature for the alloy ENAA 6005A homogenized at 585°C for 3h30 (28% α -AlFeSi).	139
5.17	Variation of the fracture strain ϵ_f for various notch radius as a function of the test temperature for the alloys (a) ENAA 6060 and (b) ENAA 6005A homogenized at 585°C for 4h30 and deformed.	141
5.18	SEM micrographs taken during in situ uniaxial testing of the alloy ENAA 6060 at low strains. Two damage nucleation mechanisms are observed (a) particle/matrix decohesion and (b) particle fracture.	142
5.19	Dependence of the fracture mode on the orientation of the long axis of the intermetallic particles with respect to the loading direction.	143
5.20	SEM micrographs taken during in-situ tensile test performed at room temperature on the alloy ENAA 6060 and showing the opening of the voids for (a) voids nucleated by interface decohesion, (b) voids nucleated by particle fragmentation.	144
5.21	SEM micrographs taken during in-situ tensile test performed at room temperature on the alloy ENAA 6060 and showing the end of the opening of the void at the end of the damage process, the interactions between the large voids initially nucleated by particle decohesion and the interactions between the large voids and the smaller voids nucleated by particle fragmentation.	145
5.22	SEM micrographs showing some features of the process of (a) void nucleation and growth and (b) void growth and coalescence, the alloy ENAA 6060, deformed at 550°C (samples machined and polished from prestrained unloaded specimens). Only particle/matrix interface decohesion is observed.	146
5.23	Fractographies showing the presence of the intermetallic particles within the dimples.	147

5.24	Fracture surfaces of ENAA6060 specimens deformed at 570°C and 580°C revealing the change of fracture mode resulting from the melting of at least some of the intermetallic particles.	148
5.25	Fracture surface observed at 590°C for the alloy ENAA 6060.	148
5.26	Damage initiation mechanisms in aluminium alloys ENAA 6xxx at room temperature and at high temperature.	149
5.27	Model material for first population of primary particles.	150
5.28	Evolution of the local triaxiality (a) and local strain rate (b) as a function of the local plastic strain during FE calculations of the uniaxial tensile tests in the more loaded central element.	159
5.29	Evolution of the calculated ductility (fracture strain) as a function of the α -AlFeMnSi content for aluminium alloys ENAA 6060 (a) and ENAA 6005A (b) deformed at 20°C with different tensile specimen geometries: uniaxial tension with necking, notch 1 with radius of 5 mm and notch 2 with radius of 2 mm.	163
5.30	Comparison between models with one population and with several populations for aluminium alloys ENAA 6060 deformed at 20°C with uniaxial tensile specimen geometries.	164
5.31	Evolution of the ductility (fracture strain) as a function of the deformation temperature for the alloys (a) ENAA 6060 and (b) ENAA 6005A; for different homogenization conditions.	165
5.32	Evolution of the ductility (fracture strain) as a function of α -AlFeMnSi content for aluminium alloys ENAA 6060 (a) and ENAA 6005A (b) deformed at 550°C with different strain rates: 0.02, 0.2 and 2 s ⁻¹	166
6.1	Experimental and predicted evolution of the α -AlFeMnSi content (a), fracture strain (considering a maximum deformation temperature of 580°C) (b) and relative ram speed (c) with homogenization time for the aluminium alloy ENAA 6060 homogenized at 585°C.	176
6.2	Predicted evolution of the relative ram speed with homogenization time for the aluminium alloy ENAA 6060 homogenized at 585°C and at 600°C.	177
6.3	Evolution of the α -AlFeMnSi content with homogenization time for the aluminium alloys ENAA 6060 and ENAA 6005A homogenized at 585°C and at 600°C.	178
6.4	Evolution of the relative ram speed with homogenization time for the aluminium alloys ENAA 6060 and ENAA 6005A homogenized at 585°C and at 600°C.	179
6.5	Predicted evolution of the α -AlFeMnSi content with homogenization time for the aluminium alloys ENAA 6005A containing 0.04 and 0.1 wt.% Mn homogenized at 585°C.	180

6.6	Predicted evolution of the relative ram speed with homogenization time for the aluminium alloys ENAA 6005A containing 0.04 and 0.1 wt.% Mn homogenized at 585°C. . . .	181
6.7	Evolution of the relative ram speed with Fe wt.% content for the aluminium alloys ENAA 6060 and ENAA 6005A homogenized at 585°C for 3h30.	182
6.8	Predicted evolution of the Mg ₂ Si particles radius (in μ m) for different initial radii during homogenization at (a) 585°C and (b) 600°C.	185
6.9	Predicted evolution of the Mg ₂ Si particles radius (in μ m) for different initial radii during reheating to the extrusion temperature for different α/β -AlFeSi initial contents: 20/80 (a) and 80/20 (b).	186
7.1	Perspective leading to the development of a full intelligent manufacturing tool.	196
A.1	Effect of the anisotropy distribution parameter λ_0 on the variation as a function of the overall axial strain of (a) the overall axial stress; (b) the porosity; (c) the relative void spacing; (d) the void aspect ratio; for a constant relative void spacing $\chi_0 = 0.114$, penny-shaped voids ($W_0 = 0.01$), $T = 1$, and $n = 0.1$	211
E.1	True stress true plastic strain flow curves for different strain rates equal to 0.02, 0.2 and 2 s ⁻¹ at (a,d) 570°C, (b,e) 580°C and (c,f) 550°C for the alloys (a,b) AA 6060 and (c,d) AA 6005A. Both alloys were homogenized at 585°C.	232

List of Tables

1.1	Some eutectic melting temperatures in AlMgSi alloys. . . .	19
2.1	Chemical composition (wt.%) of the aluminium alloy ENAA 6060 used during the industrial tests.	38
2.2	Different homogenization parameters used for extrusion tests.	38
2.3	Some eutectic melting temperatures in AlMgSi alloys. . . .	45
3.1	Chemical composition of the alloy (wt%) homogenized in laboratory.	57
4.1	Summary of the equations of the simple model for the ductility	109
5.1	Chemical composition (wt.%) of the aluminium alloys studied.	119
5.2	Values of the strain hardening exponent n and strain rate sensitivity exponent m identified with the iterative inverse procedure as a function of the test temperature for the alloys ENAA 6060 and ENAA 6005A, both homogenized at 585°C for 24h.	137

List of symbols

Symbol	Description
A_0	initial macroscopic tensile specimen section area
A_f	final macroscopic tensile specimen section area
α	analytical function of the hardening exponent n
α_2	analytical function of the state variables W and f
χ	relative void spacing
χ_0	initial relative void spacing
χ_c	critical relative void spacing for final failure
C	analytical function of the state variables W and f
$C_{Mg,Si}$	Mg or Si particle interface concentration
$\Delta\epsilon_{nucleation}$	nucleation deformation interval
Δf_α	error on α -AlFeSi particles assignment
δ	Kronecker tensor
E	matrix Young's modulus
E_p	particle Young's modulus
ϵ	strain
ϵ_n	nominal strain
ϵ_f	fracture strain
ϵ_u	uniform elongation
ϵ_{nucl}	nucleation strain
ϵ_{growth}	growth strain
$\dot{\epsilon}$	strain rate
$\dot{\epsilon}_0$	reference strain rate
$\bar{\epsilon}^p$	plastic strain
$\dot{\bar{\epsilon}}^p$	plastic strain rate
e_e^p	equivalent plastic rate

Symbol	Description
$\dot{\epsilon}_{ij}^p$	ij components of the overall plastic strain rate tensor
$\dot{\epsilon}_{kk}^p$	kk components of the overall plastic strain rate tensor
$\dot{\epsilon}_{\theta\theta}^S$	local circumferential strain rate at $z=0$
$\dot{\epsilon}_{ZZ}^S$	local strain rate at $Z=0$
e_z	unit vector parallel to the main cavity axis
η	analytical function of the state variables W and f
f	void volume fraction
f_0	initial void volume fraction
\dot{f}_{nucl}	nucleation void volume fraction increasing rate
\dot{f}_{growth}	growth void volume fraction increasing rate
f_c	critical void volume fraction for coalescence
f_F	ultimate void volume fraction at fracture
$f^{A \text{ or } B}$	primary void volume fraction
f_2	secondary void volume fraction
f_α	relative intermetallic α -AlFeSi fraction
f_p	particles volume fraction
f_p^*	threshold particle volum fraction for coalescence
f_s	saturation porosity
g	analytical functions of the state variables W and f
γ	geometric factor depending on the arrangement of voids
J	tensor associated to the void axis and defined by $(1 - 2\alpha_2)e_z \otimes e_z + \alpha_2 e_x \otimes e_x + \alpha_2 e_y \otimes e_y$
k	parameter of Beremin criterion for void nucleation
κ	analytical functions of the state variables W and f
L_{ijkl}	elastic moduli
L_z	unit cell radius in z direction
$L_x = L_y$	unit cell radius in x (or y) direction
λ	relative void spacing
λ_0	initial relative void spacing
m	strain rate sensitivity exponent
n	strain hardening exponent
n_α	number of α -AlFeSi particles
n_β	number of β -AlFeSi particles
ν	Poisson ratio
ν_p	particle Poisson ratio

Symbol	Description
P	projector tensor defined by $e_z \otimes e_z$
P_e	ellipse perimeter
ϕ_{growth}	growth-mode yield surface
$\phi_{coalescence}$	coalescence-mode yield surface
q	parameter that has been calibrated has a function of f_0 , W_0 , and n (see [72])
R	void radius
R_0	initial void radius
R_z	void radius in z direction
$R_x = R_y$	void radius in x (or y) direction
R_{pz}	particle radius in z direction
R_{px}	particle radius in x direction
σ_{princ}^{max}	maximum principal stress
σ_c^{bulk}	critical particle stress for fracture
σ_c^{interf}	critical matrix/particle interface stress for fracture
σ_e	equivalent stress
σ_0	initial yield stress
σ_n	nominal stress
σ_y	flow stress
σ_h	hydrostatic Cauchy stress
σ_{nucl}	nucleation stress
$\dot{\sigma}_{ij}$	stress rate tensor
s or σ'	deviatoric part of the Cauchy stress tensor
σ_h^g	generalized hydrostatic stress defined by $\sigma : J$
T	stress triaxiality
\dot{U}_z	displacement rate in z direction
\dot{U}_x	displacement rate in x direction
V_{max}	maximum relative extrusion speed
v	particle interface growing velocity
W	void aspect ratio
W_0	initial void aspect ratio
W_p	particle aspect ratio
$W_{\beta-AlFeSi}$	β -AlFeSi particle mean void aspect ratio
$W_{\alpha-AlFeSi}$	α -AlFeSi particle mean void aspect ratio

Symbol	Description
X	tensor associated to the void axis and defined by $2/3e_z \otimes e_z - 1/3e_x \otimes e_x - 1/3e_y \otimes e_y$
$\ \!\ $	von Mises norm

Aluminium is the third most abundant element in the earth's crust. We may not always be aware of it, but aluminium is present in every aspect of our daily life - our mobility, nutrition, accommodation and leisure. Today, aluminium is the world's second most used metal and the aluminium industry is an important stakeholder in society. So it should not be a surprise that, since 1900 when worldwide production was a mere 1000 tonnes per annum, by the end of the twentieth century annual use of aluminium had reached 10 millions tonnes in Western Europe alone.

The main properties which make aluminium and its alloys valuable materials are their strength, lightweight, recyclability, corrosion resistance, durability, ductility, formability and conductivity. Due to their unique combinations of properties, the variety of applications of aluminium alloys continues to increase. It is essential in our daily lives. We cannot fly, go by high speed train, high performance car or fast ferry without it. We cannot get heat and light into our homes and offices without it. We depend on it to preserve our food, our medicine and to provide electronic components for our computer. Physically, chemically and mechanically, aluminium is a metal like steel, brass, copper, zinc, lead or titanium. It can be melted, cast, formed, and machined much like these metals and it conducts electric current.

General introduction

To the problem of extrudability ...

With the growth in importance of the aluminium industry, has come increased demand to invest into the quality improvement of the different aluminium based products and particularly extruded products. These last ones constitute more than 50% of the market for aluminium products in Europe of which the *building industry* consumes the majority. Aluminium extrusions are used in commercial and domestic buildings for windows and door frame systems, prefabricated houses/building structures, roofing and exterior cladding, curtain walling, shop fronts, etc. Furthermore, extrusions are also used in *mass transport* for airframes, road and rail vehicles and in marine applications. The term **extrusion** is usually applied to both the process, and the product obtained, when a hot billet of aluminium is pushed through a shaped die. Sometimes, extrusion presses are designed to push the die into the billet. The versatility of the process in terms of both alloys available and shapes possible makes it one of the most valued assets helping the aluminium producer to supply users with solutions to their design requirements. All aluminium alloys can be extruded but some are less suitable than others, requiring higher pressure, allowing only low extrusion speed and/or having less than acceptable surface finish and section complexity. The term **extrudability** is used to embrace all of these issues.

The biggest share of this extrusion market is taken by the ENAA 6xxx, AlMgSi series. This group of alloys has an attractive combination of properties, relevant for both use and production. In general, they can be extruded with ease and their overall extrudability is good. Those containing the lower limits of magnesium and silicon (e.g. ENAA 6060 and ENAA 6063) extrude at high speed, but the production needs ask for higher and higher production rates with the best surface finish. Indeed, this demand and the continued development of structural aluminium alloys (as well as their use in very critical components) make *the prediction of the surface finish and of the fracture resistance to remain very important.*

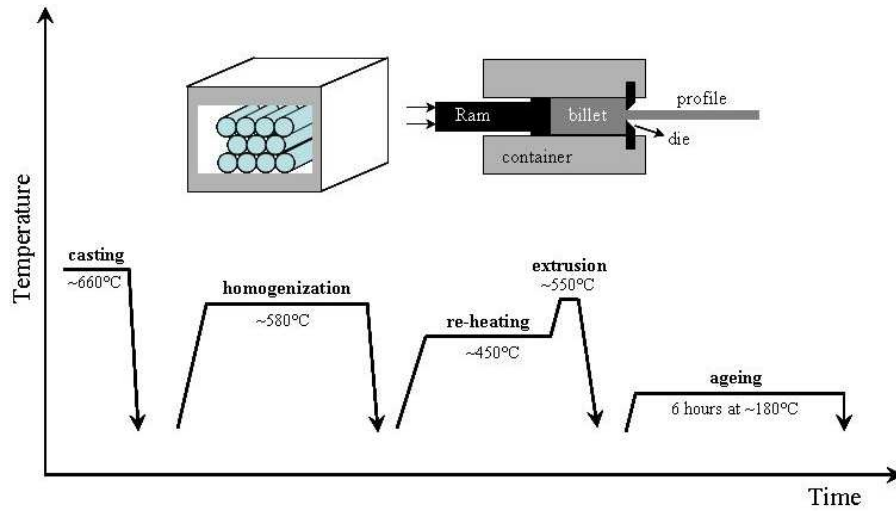


Figure 1 – Temperature path of the aluminium heating process during the production of extrusion profiles. Homogenization and extrusion are displayed schematically.

Surface appearance in the mill-finish condition or after is one of the most important characteristics of high quality ENAA 6xxx extrusion. Surface cracking, pick-up and tearing, all detract the appearance of the extruded profile. Those who have spent time near the press will know that the die can play a significant role, sometimes an overriding one, in determining the quality of the surface. Nevertheless many surface problems remain hot fracture problems and have microstructural origins. All these defects present the largest problem for the extruder.

Figure 1 shows the different process steps that are carried out for the production of aluminium extrusion profiles, such as frames and pipes. The scheme shows that, after casting, the material is homogenized. During this homogenization process the aluminium billets are annealed in a furnace for a few hours at temperatures between 530°C and 600°C . Subsequently the billets are cooled down, transported to the extrusion press, re-heated and extruded in a press. During this process, the billets are pressed through a die with a shaped opening. In an optional final step, the profiles are artificially age-hardened. Among all these steps, the **homogenization** of the AlMgSi alloys is a very important one, since it gives significant changes in the microstructure of the alloy, leading to an improved capacity of undergoing extensive plastic deformation without cracking and melting, i.e. to an improved extrudability of the material and improved properties of the final extruded product. The main reasons for homogenizing

AlMgSi alloys are the following:

1. to obtain a uniform distribution of alloying elements in solid solution,
2. to dissolve low melting point Mg_2Si and Si particles which cause tearing during extrusion,
3. to transform $\beta\text{-AlFeSi}$ phase particles to $\alpha\text{-AlFeMnSi}$ phase, which gives better extrusion properties.

There are two main mechanisms which can influence deformation at high temperature within the ENAA 6xxx aluminium family. The first one concerns the soluble Mg_2Si phase. Deformation properties depend largely on the ability of this phase to get into solution during extrusion in order to soften the material and to avoid eutectic melting reactions during hot forming. The second mechanism is linked to the presence of the AlFeSi intermetallic phases. These phases severely restrict hot workability when present as hard and brittle plate-like precipitates $\beta\text{-AlFeSi}$. Damage initiation occurs in these alloys by decohesion or fracture of these intermetallic inclusions as referred by Agarwal, Bae and Kobayashi [2, 8, 9, 89]. These problems can be partially resolved by applying an adequate homogenization heat treatment, before forming. During this step, the low melting point particles (Mg_2Si , Si) get into solution while the majority of the brittle plate-like $\beta\text{-AlFeSi}$ intermetallic particles transform to multiple rounded $\alpha\text{-AlFeMnSi}$ intermetallic inclusions. The change in morphology is represented in Figure 2. Figure 2(a) shows that the β particles in the as-cast state appear as needles in a two dimensional micrograph. Figure 2 (b) shows that after homogenization these β plates are transformed into a string of separated rounded α particles. The β -to- α transformation considerably improves the extrusion process of the aluminium since the transformed α particles improve the ductility of the material and consequently the surface quality of the extruded product. Often, the as-cast microstructure is not extrudable at all and many cracks appear during extrusion.

Since the Mg_2Si and the Si particles dissolve rather fast, it is the β -to- α transformation kinetics which determines the minimum homogenization time to get the material in a suitable state for extrusion. A better understanding of the homogenization conditions on the β -to- α transformation and on the surface defects appearance is important, since it gives a better insight into the extrusion defects origins. *It is one of the objectives of this research to characterize the effects of the heat treatments on the microstructure evolution, to establish a direct relationship between the process parameters and the behavior of the alloys during extrusion.*

At a macroscopic scale, the mechanical properties of materials result from a homogenization of phenomena operating at multi-length lower scales. In order to allow a quantitative understanding of how the microstructural features exert coupling effects which govern the mechanical properties, it is necessary to

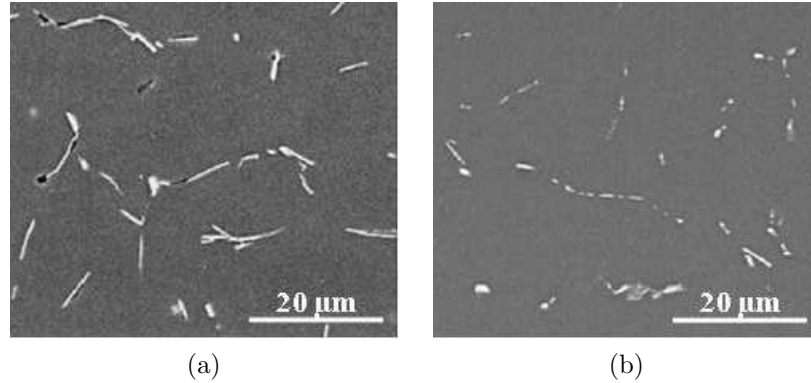


Figure 2 – The β -to- α transformation in AlMgSi aluminium alloys: (a) β particles in the as-cast state and (b) α particles after homogenization at 580°C for 3h30.

elucidate the physics acting at the lower scales thanks to **micromechanical models**. This type of modeling aims to simulate the plasticity and fracture of materials at microstructural inhomogeneities. The microstructural inhomogeneities are mainly associated with the presence of voids and second phases such as particles, which, being commonly present in many materials, play a very important role in triggering the fracture process and then in determining the mechanical response.

Aluminium alloys of the ENAA 6xxx family typically contain such inhomogeneities as second-phase particles of different sizes, i.e., coarse ellipse-shaped AlFeSi inclusions (from 1 to 20 μm), rounded AlFeMnSi particles (smaller than 5 μm) and fine disc- or needle-shaped Mg_2Si precipitates (smaller than 1 μm). All types of second-phase particles make significant positive and negative contributions to the mechanical properties of the aluminium alloys. The brittle Fe-bearing inclusions cleave or separate from the matrix during extrusion processes or under service loading to act as crack initiators or as a preferential crack propagation path. They are detrimental to ductility and fracture toughness of materials. Mg_2Si precipitates are the major contributors to the strength of alloys and are associated with the slip and deformation capability, but can also be very detrimental if present in the material during processing as large undissolved precipitates can melt at the working temperatures. The most effective approach to display explicitly the independent influences and to analyze the coupled influences from every population of second-phase particles is to construct an entire model, in which quantitative relationships are revealed between ductility and the volume fractions, sizes and shapes of the different second-phase particles. This work will consider the coupled influences of several types of second-phase particles (β -AlFeSi and α -AlFeMnSi) on ductility.

The **outline** of the thesis and the methodology of the research are now presented.

Chapter 1 is devoted to a short presentation of the current background on extrusion of aluminium alloys ENAA 6xxx, on the metallurgy of these alloys family and on micromechanical modeling of fracture of metallic alloys.

The starting point of this research is then presented in **Chapter 2**, which firstly relates macroscopically the appearance of extrusion surface defects for ENAA 6xxx aluminium alloys to the homogenization process parameters through full-scale industrial extrusion tests. This first step of the research relates to the manufacture of shaped aluminium profiles. It aims at understanding and at controlling some metallurgical mechanisms concerned within various stages of the process. The optimization of the temperatures and holding times during the homogenization, as well as the cooling rate after homogenization allows, *in fine*, to extrude healthy profiles at higher rates. By now, the extrudability problems are solved in majority by "tests and errors" thanks to the experience and the intuition of technicians and experienced engineers. *The objective of this research is to study the relationship between the parameters of heat treatment, the microstructure of the materials and the cracking defects during extrusion, in order to develop a robust strategy of optimisation of the homogenization and extrusion conditions.* This objective goes hand in hand with the acquisition by the company Sapa RC Profile in Ghlin, Belgium, of a new continuous homogenization furnace for which it is advisable to control the parameters of the thermal cycle applied to each type of material. Furthermore, the microstructural origin of the extrusion surface defects is elucidated by scanning electron microscopy (SEM), transmission electron microscope (TEM) and differential scanning calorimetry (DSC).

In **Chapter 3**, investigations are made to study the influence of the homogenization parameters on the microstructure. This experimental chapter focuses on the effect of the homogenization temperature and time on the β -to- α transformation. We study common extrusion alloys in commercial practice, such as ENAA 6060 and ENAA 6005A alloys. Most of experiments are performed by energy dispersive x-ray analysis (EDS) coupled with SEM to characterize the change in nature of the intermetallic particles. The accompanying intermetallic morphology change is measured by image analysis (IA).

New efforts are currently made to introduce more physics into the micromechanical models. As the cleavage of the elongated β -AlFeSi intermetallic particles during straining induces the formation of very flat voids (penny-shaped voids), we study the damage mechanisms associated with such voids. The goal of **Chapter 4** is to contribute to that effort by addressing in details the specific problem of the growth and coalescence on initially penny-shaped voids resulting

from the fracture of particles. State-of-the-art models rely on a simple approach which consists in assimilating the initially flat void to an equivalent spherical void, leading to the definition of an effective initial porosity, e.g. [45]. This approach neglects the particular initial shape of the void which affects both the void growth rates and, later, the fulfillment of the coalescence condition. In this chapter, the response of elastoplastic solids containing initially penny-shaped voids, resulting either from particle fracture, from partial decohesion or from total decohesion of flat particles, is studied in the case of spheroidal void geometry and axisymmetric loading conditions. This chapter allows to determine correct assumptions to be used to describe this void population in a micro-mechanical void growth model accounting for several void populations as presented in the following chapter.

The mechanical behavior of the ENAA 6xxx aluminium alloys is investigated in **Chapter 5** from a campaign of uniaxial tension tests on smooth and notched cylindrical rods at various deformation temperatures and strain rates with different second phase particles contents. In this chapter, a physical model is presented to describe the effect of alloys microstructure on damage mechanisms and Finite Elements simulations are carried out based on this micromechanics-based void growth model that is potentially applicable to relate microstructure and ductility in a wider range of alloys. The model used is a Gurson type constitutive model considering several populations of cavities in order to account for the fact that experimental data have shown that a second population of cavities is likely to appear before coalescence and thus tends to decrease the strain at the onset of coalescence. This contribution allows us to determine different limiting parameters and fracture microstructural origins and helps in correctly modeling the mechanical behavior of ENAA 6xxx aluminium alloys.

The final Chapter, **Chapter 6**, presents to a short parametric study. We find indeed interesting from an industrial point of view, to summarize the effects of some extrusion process parameters on ductility of ENAA 6xxx alloys. It is why we present in this last section general trends about the relationships between process parameters (e.g. homogenization conditions, ram speed), microstructure (e.g. initial particles fraction and shape), flow properties (e.g. yield stress, strain hardening coefficient) on the ductility.

Finally, this study ends with some conclusions.



Theoretical background

Chapter 1

Theoretical background

This section gives a short presentation of the current background on extrusion and homogenization of aluminium alloys, on the metallurgy of the AlMgSi alloys family, and their surface problems, and on micromechanical modeling of fracture of metallic alloys.

1.1 Background on extrusion

Although extrusion is a modern process, it precedes the development of aluminium which was commercially available only following the invention in 1886, by Hall and Heroult, of the electrolytic process to extract the metal from bauxite. Among the industrial methods by which aluminium billets can be transformed to increasingly complex shapes, extrusion has no rival and has firmly established itself as a major industrial process. This one converts a cast billet of solid metal into a continuous length of generally uniform cross-section by forcing it through a die which is shaped to produce the required form of product. Generally it is a hot working operation, the metal being heated to give it a suitable flow stress (i.e. degree of softness and ductility), but it can also in some instances be carried out in the cold. In the modern process, cast billets of cylindrical shape, loaded into a composite cylinder (container), are extruded through the die under the pressure exerted by a ram actuated hydraulically.

Figure 2.1 illustrates the essential principle of the direct extrusion process. The die is located at one end of the container and the metal to be extruded is pushed towards it, hence moving relative to the container. The process is

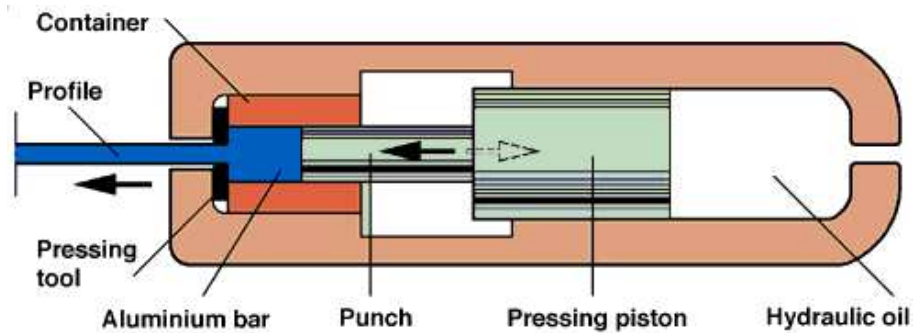


Figure 1.1 – The Direct Extrusion process.

typically conducted at relatively high temperature because the lower flow stress of the material permits larger section reductions to be achieved, lowering the power requirements and processing times. Almost all metals tend to shear at the container interface, adding to the force required to extrude the metal and depositing a layer at that interface. As the extrusion proceeds, impurities on the billet surface and the peripheral segregation are sheared off and collect in the discard (end of the billet where the impurities are discharged and which is not extruded in consequence), which should therefore be large enough to ensure that impurities do not appear in the product. Aluminium alloys are generally extruded using a dummy block (end of the press punch in contact with the aluminium billet) with a very close fit in the container. Consequently, the surface is rarely drawn into the profile because the material sticks to the container wall and impurities on the surface are held there, eventually entering the billet discard. Generally, there is only a small temperature difference between the billet and the container, and the difference in velocity between the center of the billet and the periphery is low for the aluminium alloys. The only lubricant used is usually a token of graphite-based grease on the face of the dummy block of the ram. This is because the surface is a very important feature of the product and is formed from the interior of the billet by the shear occurring in the conical zone adjacent to the die known as the *dead metal zone*.

Figure 1.2 shows that the load in direct extrusion initially increases very rapidly as the billet upsets to fill the container. There is a further increase in pressure until extrusion begins. The cone-shaped deformation zone develops in front of the die aperture and the maximum strain rate develops in this zone. After the peak pressure has been reached, the extrusion pressure falls as the billet length decreases. In indirect extrusion, the process is characterised by the absence of friction between the billet surface and the container. The load required is therefore always decreased compared with the direct mode.

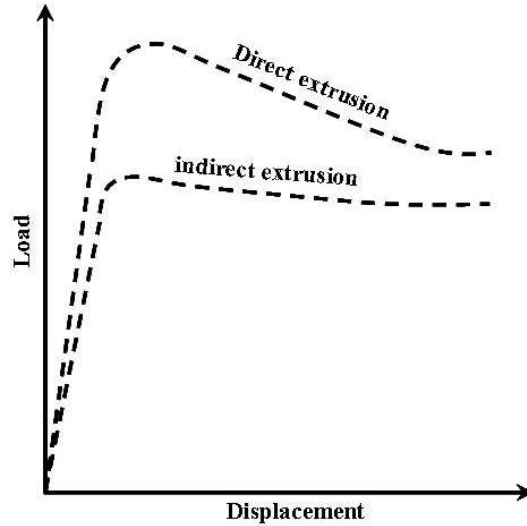


Figure 1.2 – Evolution of the load during extrusion.

It is recognised that the structure of the material also requires careful control and hence the entire process must be considered. Microstructural features of importance for property control of aluminium alloys include the coherency and distribution of strengthening precipitates, degree of recrystallization, grain size and shape, crystallographic texture, nature and distribution of the intermetallic particles including the dispersoids and constituents phases (resulting from the iron impurities and the excess of silicon). Beginning with the as-cast ingot which exhibits a heterogeneous morphology, processing includes a **homogenization treatment**, to reduce segregation, to remove low melting point phases, and transform the intermetallic hard phase in order to improve hot workability. This thermal treatment also serves to precipitate dispersoid-forming elements such as chromium, manganese and zirconium, so that they may perform their role of grain control during processing. Before extrusion, the billets are re-heated to the extrusion temperature (typically around 450°C) to get the material in its softest conditions. A final ageing treatment step after extrusion can also be applied to harden the final products.

1.2 Background on the metallurgy of AlMgSi alloys

Aluminium alloys of the AlMgSi family are the most commonly used for extrusion purposes. Their extrudability depends to a large extent on chemical

composition, casting practices and mainly on the homogenization treatment conditions. During extrusion, the material preferably needs to be in its softest conditions. Therefore, a fast cooling is needed after homogenization in order to avoid any Mg_2Si re-precipitation. The re-heating step to the extrusion temperature must also be correctly controlled for the same reasons.

A second occurring phenomenon is the insoluble phase which is formed by aluminium, iron and silicon. The hard, plate-like β -AlFeSi phase severely restricts hot workability. This phase is to a large extent responsible for the occurrence of local "surface cracking" phenomena, leading to a poor surface finish. During the homogenization process, the transformation of the brittle β -AlFeSi phase to the more rounded α -AlFeMnSi phase takes place and is one solution for the problems of surface. The process parameters, in particular the homogenization temperature, time and cooling rate, the billet temperature and the ram speed determine the surface quality. One of the objective of this study is to clearly elucidate the relation between these parameters and the surface defects. A better knowledge of the fundamental mechanisms responsible for hot cracking and tearing off during extrusion is necessary in order to allow optimization of the process parameters. This section aims at summarizing the actual "state-of-the-art" in the ENAA 6xxx aluminium alloys metallurgy and on surface defect mechanisms.

The AlMgSi system, designating the Mg_2Si alloys, are today the most widely used in the extrusion market. This ENAA 6xxx series alloys have the following qualities:

1. Good corrosion resistance
2. Good surface finish
3. Good formability
4. Medium strength

These advantages make them suitable for architectural sections and structural applications. **Magnesium** and **silicon** are the main adding elements and combine to form the stoichiometric compound, magnesium silicide Mg_2Si , which makes the ENAA 6xxx series alloys heat treatable and capable of achieving medium strength after artificial ageing following extrusion (T6 conditions). The proportion of magnesium to silicon required is 1.73:1 (in weight). In a balanced alloy, aluminium and magnesium silicide can be treated as a quasi-binary system, thereby simplifying the phase diagram representation as shown in Figure 1.3.

An increase in the Mg_2Si content results in improved tensile properties of the final products, but is accompanied by a loss of extrudability. However, when overall productivity is considered, increased Mg_2Si content can improve productivity by decreasing the storage time required between extrusion and artificial ageing (it is known but not clearly understood that a long storage time before

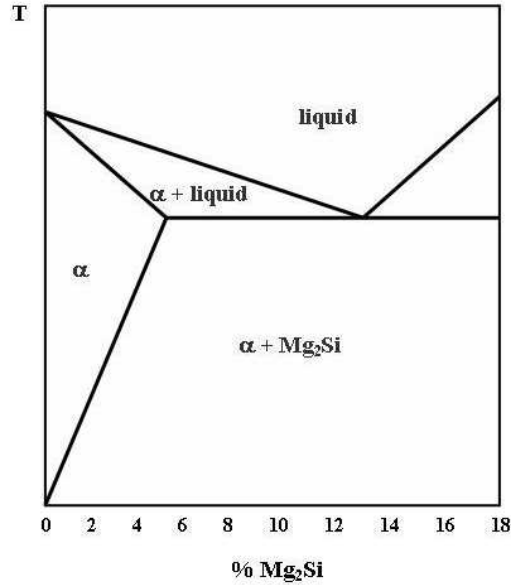


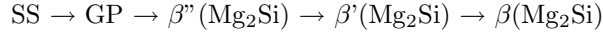
Figure 1.3 – Pseudo binary phase Al/Mg₂Si diagram.

ageing allows the formation of small Guinier-Preston zones which will facilitate a quick precipitation of the hardening β' -Mg₂Si phase). To obtain full age-hardened properties, without the need of a separate solution heat treatment, the Mg₂Si must dissolve into solution during the homogenization step and during extrusion as the deforming material passes through the deformation zone. To ensure that all these precipitates are dissolved after extrusion, they must be fine and uniformly dispersed, as large precipitates require extended soak times for complete dissolution. This can be obtained by good casting practices, homogenization, rapid post-homogenization cooling, rapid reheating to the extrusion temperature and controlled cooling after extrusion. Rapid precipitation of the Mg₂Si phase occurs in the temperature range from 310°C to 420°C and will result in coarse precipitates unless this temperature window is traversed rapidly on cooling and reheating. The mechanism for strengthening has been studied at great length. It was found that:

1. Appreciable strengthening occurs at room temperature over an extended period of time.
2. Zones are formed - short ageing times at around 200°C produce fine needle shaped zones approximately 6 nm in diameter and 20-100 nm in length.
3. Further ageing causes 3-dimensional growth to rod shaped particles with

a structure corresponding to a highly ordered Mg_2Si .

4. At higher temperatures, this transition phase, designated β' , undergoes diffusionless transformation to the equilibrium Mg_2Si .
5. The normal precipitation sequence may be designated:



Silicon combines with **iron** in preference to magnesium to form AlFeSi phases. An excess of silicon over that required for the formation of Mg_2Si phases and of the iron phases, increases strength but decreases the extrudability. Silicon has been showed to decrease the ram speed. The loss of ductility is considered to be due to **silicon** or Mg_2Si precipitates in the grain boundaries. Loss of toughness can be controlled however with minor additions of **manganese** and/or **chromium**. An excess of **magnesium** in the 6xxx series alloys is much more detrimental than an excess of **silicon** to the extrudability, and contributes little to strength. **Iron** is present in this series as a controlled impurity. An increase in the iron content can therefore decrease the strength of the alloy by removing the excess of silicon. This is often a cause of low mechanical properties. However, a secondary effect of the iron phase is to refine the Mg_2Si precipitates thus producing an increase of the maximum strength after age-hardening (T6 strength). The $\beta\text{-Al}_5\text{FeSi}$ phase, which is present in as-cast billets, has an adverse effect on the hot working characteristics. To permit higher extrusion speeds, without the appearance of surface tears, a homogenization treatment must be applied to refine and transform this phase into the preferred $\alpha\text{-Al}_{12}(\text{FeMn})_3\text{Si}$ phase. Iron is also reported to cause a reduction in corrosion resistance and to improve toughness.

The three minor additions of **manganese**, **chromium** and **zirconium** are added to improve toughness by forming stable, incoherent dispersoids during homogenization. These additions increase the quench sensitivity by providing nucleation sites for the age-hardening precipitates. Increasing the **manganese** and **chromium** content beyond that required for adequate toughness further decreases extrudability. Recrystallisation is inhibited with the addition of these elements by forming intermetallic particles which are capable of pinning grain boundaries. Small additions of **manganese** reduce also surface defects by promoting a fine dispersion of Mg_2Si and accelerating the $\beta\text{-Al}_5\text{FeSi}$ to $\alpha\text{-Al}_{12}(\text{FeMn})_3\text{Si}$ phases transformation during homogenization.

1.3 Background on homogenization treatment

As-cast aluminium alloys tend to have very non-uniform microstructure. Wrought alloys for extrusion are given an ingot heat treatment to modify this cast structure. This is referred to as homogenization. Industrial homogenization for

aluminium is a two- or three-step process, with heating, holding at high temperature and often subsequent cooling. When the heating starts at room temperature, the solid solution is strongly supersaturated. The first reactions are nucleation and precipitation. Many of the freshly formed precipitates redissolve at higher temperature, and are thus of little interest. The freshly formed particles that survive homogenization are Fe-, Mn-, and Zr-bearing particles and dispersoids. The holding temperature is usually chosen as high as possible, with a reasonable safety limit relative to the equilibrium solidus temperature of the alloy. The major reactions involving particles during the holding period are coarsening of dispersoid and transformation of the Fe-bearing particles from one phase to another.

1.3.1 Intermetallic phases in the ENAA 6xxx series

The ENAA 6xxx series alloys are also called AlMgSi, since their main alloying elements are Mg and Si, which allow age-hardening by coherent or semi-coherent Mg-Si precipitates. However, besides Mg and Si also other elements such as Fe and Mn can be present. Since Fe has a very low solubility in the aluminium matrix, almost all Fe present in ENAA 6xxx alloys will bind the excess of Si and the abundant Al to form typically one volume percent of Fe-containing intermetallics. During solidification, these intermetallics form at the edges of the aluminium dendrites by an eutectic reaction, which explains their plate-like shape. Most of these intermetallics are plate-like β -AlFeSi phase while a small fraction of the phases can be cubic α -AlFeMnSi phase, more rounded. These Fe-containing intermetallics do not dissolve and remain as a separate phase in the aluminium matrix even after long homogenization times, although they may change in phase composition and phase morphology. The three most prevalent intermetallics in ENAA 6xxx aluminium alloys are the monoclinic β -AlFeSi phase, the hexagonal α_h -AlFeSi phase and the cubic α_c -AlFeMnSi phase.

The monoclinic β phase

The β -AlFeSi has a monoclinic crystal structure. This is an important phase in as-cast aluminium ENAA 6xxx alloys, where it has a plate-like morphology with a length up to 20 μm and a thickness of 0.1-2 μm . The appropriate stoichiometry of this phase is Al_5FeSi . In contrast to the α phase, no manganese can be present in the β phase.

The hexagonal α_h phase

The stoichiometry of this phase is approximately $\text{Al}_8\text{Fe}_2\text{Si}$. The α_h phase forms in the ENAA 6xxx series alloys with Mn, V and Cr concentrations less than ~ 0.01 wt.%. Higher concentrations of these elements lead to stabilisation of the

cubic α_c phase. Since industrial alloys mostly have small additions of Mn and Cr, this transformation is rarely observed in industrial practice and usually the β -Al₅FeSi phase transforms to the stabilized α_c -Al₁₂(FeMn)₃Si phase.

The cubic α_c phase

In typical ENAA 6xxx aluminium alloys extrusion, small additions of V, Cr, and/or Mn are required to form α_c during homogenization. In this case, the α_c phase seems to be the thermodynamically stable phase since it is also observed after long homogenization times. In this phase, the Fe atoms are interchangeable with V, Cr, and/or Mn atoms. This phase has approximately the Al₁₂(Fe_xMn_{1-x})₃Si stoichiometry. Three different types of cubic intermetallic phases can be present in the ENAA 6xxx series alloys: (1) formed during casting, (2) formed as dispersoids, (3) formed by the β -to- α transformation. Although the crystal structures of those types are all cubic, all three types have prominent differences in morphology, size and distribution:

1. α_c formed during casting: The morphology of these particles is often called "Chinese script" morphology, since in two dimensional sections, the eutectic has the morphology of Chinese characters. The morphology is rounded, has a large variation in length and thickness and have a size of 5 μ m. These particles have a high Fe/Mn ratio.
2. α_c as dispersoids: These dispersoids are formed in the aluminium matrix during homogenization. They have sizes of 50-200 nm and are uniformly distributed. The dispersoids have a low Fe/Mn ratio and their stoichiometry is approximately equal to that of α_c -Al₁₂Mn₃Si.
3. α_c formed after the β -to- α transformation: The transformed α_c particles have a size of approximately 1 μ m and are present as strings of rounded particles located on the previous location of the β particles. They have an intermediate Fe/Mn ratio, since Mn diffuses into the α_c particles during homogenization.

1.3.2 Morphological changes

The initial state of the AlMgSi aluminium alloys is constituted of a 3D network of Fe-bearing intermetallic particles as shown in Figure 1.4. The morphology change, of the β -AlFeSi phase during the β -to- α phase transformation in the ENAA 6xxx series of alloys is shown in Figure 1.5.

The plate-like β particles transform to a string of multiple smaller and more rounded cubic or hexagonal α particles. Although many papers have been published that describe the change of intermetallic phase, nobody agrees about

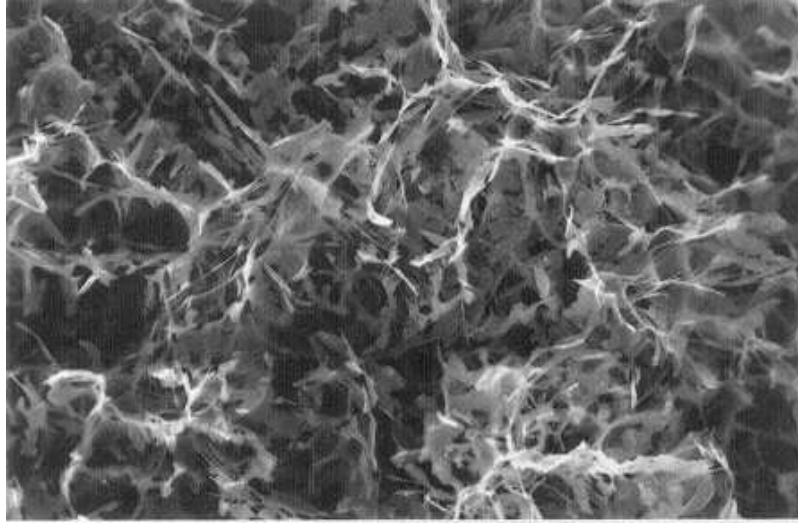


Figure 1.4 – The β network in as-cast AlMgSi alloys.

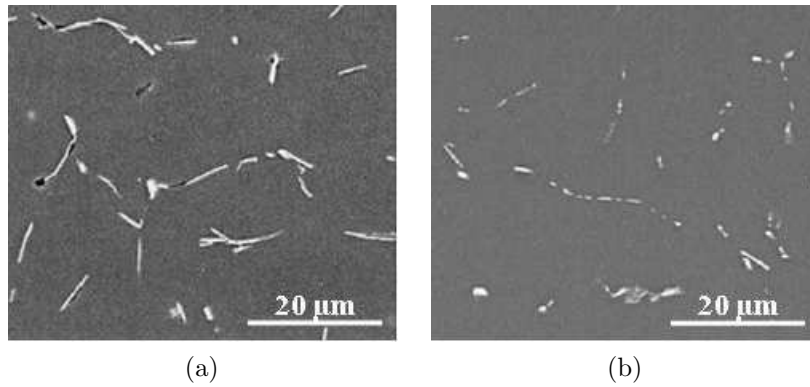


Figure 1.5 – The β -to- α transformation in AlMgSi aluminium alloys (a) β particles in the as-cast state (b) α particles after homogenization at 580°C for 3h30.

the morphological change mechanism. As reported by Kuijpers [52], some authors comment briefly on α particles that nucleate at the beginning of the transformation on the boundary of the β -phase. Zajac [97] observed that the β plates are gradually replaced by uniform strings of cubic and/or hexagonal α -AlFeSi particles, or that the long plate-like intermetallic particles break up into a necklace structure. They found that individual platelets, in an intermediate homogenization state, exhibit partial transformation to the α -phase. The islands of α -phase particles then coarsen and spheroidise at the expense of the remaining β -phase particles. The remaining α particles coarsen when the homogenization process takes longer than 10 hours. Other authors as Duncan Alexander, the α phase nucleation proceeds by eutectoid decomposition of the β phase [3]. For him, the fragmentation of the particles occurs during homogenization. Then, the chemical transition from one phase to another completes progressively.

1.3.3 Influence of the alloy content

The chemical composition of the ENAA 6xxx alloys influences the β -to- α transformation rate as well as the stability of the different intermetallic phases. It was found that both Mn and Si have a significant effect on the transformation rate. Mn acts as a catalyst for the transformation, accelerating the rate. For alloys with a low Mn content (≤ 0.01 wt.%), it is observed that the β plates first transform to the cubic α_c -phase and subsequently transform to the hexagonal α_h -phase, which is the thermodynamically stable phase in this case. For high Mn content (~ 0.02 - 0.1 wt.%) it is observed that the β plates transform to the cubic α -phase only. The Si content has a significant effect on the transformation rate also. The β -AlFeSi phase is indeed thermodynamically stable in alloys containing high levels of Si (≥ 1 wt.%). The high Si content alloy will thus hardly transform.

1.3.4 Improvement of extrudability

The word "extrudability" can be defined as the maximum production speed attainable for a given press capacity while still obtaining the desired mechanical properties, surface quality and geometric tolerance of the extrudate. As described earlier, the extrudability can improve thanks to the β -to- α transformation. It is therefore useful to define a parameter that quantifies the degree of β -to- α transformation of a billet after homogenization. This parameter can be the ratio of the α volume and the total volume of intermetallics. It is found that a relative α fraction of at least 85% is required to get an optimal extrudability. The increase in extrudability with the relative α fraction is caused both by the improvement of the ductility and of the surface defects.

Various types of surface defects may occur during the extrusion process. So far,

Melting temperature	Reaction
555°C	$\text{Al} + \text{Mg}_2\text{Si} + \text{Si} \longrightarrow \text{Liquid}$
576°C	$\text{Al} + \beta\text{-AlFeSi} + \text{Mg}_2\text{Si} \longrightarrow \text{Liquid} + \alpha_h\text{-AlFeSi}$
577°C	$\text{Al} + \text{Si} \longrightarrow \text{Liquid}$
578°C	$\text{Al} + \beta\text{-AlFeSi} + \text{Si} \longrightarrow \text{Liquid}$
587°C	$\text{Al} + \text{Mg}_2\text{Si} \longrightarrow \text{Liquid}$
612°C	$\text{Al} + \beta\text{-AlFeSi} \longrightarrow \text{Liquid} + \alpha_h\text{-AlFeMnSi}$
630°C	$\text{Al} + \alpha_h\text{-AlFeSi} \longrightarrow \text{Liquid} + \text{Al}_3\text{Fe}$

Table 1.1 – Some eutectic melting temperatures in AlMgSi alloys.

it is not yet clear which of these are the most plausible. The main assumptions are summarized below.

1. The weak adhesion of the β intermetallics to the Al matrix causes these particles to become lost from the matrix. During extrusion, these lost β particles stick to the die surface and scratch the aluminium surface.
2. The elongated β particles initiate damage and micro-cracks during the deformation, and therefore start cracking the aluminium surface. The transformed α particles are smaller and more rounded causing less local damage at the surface.
3. Local melting leads to pick-up at the aluminium surface. Table 1.1 shows some relevant eutectic melting reactions and their temperatures. The eutectic melting temperature of homogenised material containing α particles (630°C) is higher than the temperature at the die, which will not result in the formation of pick-up defects.

1.4 Surface quality considerations

It is accepted that the process variables, temperature and speed (strain rate), determine the acceptability of surface quality. During extrusion of aluminium alloys the temperature term appears to be dominant. The surface quality in most extrusions depends also on the stress conditions near the die regions. If the tensile force exceeds the fracture stress of materials, then some tearing is encountered. Additionally, if the heat generation near the die area increases the local temperature in excess of the solidus point, localised melting can occur, which causes severe cracking of the surface. This temperature generation is a function of the alloy chemistry, extrusion speed, extrusion ratio, container temperature and the initial billet temperature. Furthermore, those who have spent time near the press will know that the die can play a significant part in

determining the surface quality. The end results of this is that extrusion tests carried out to identify the critical metallurgical conditions for improved surface finish are difficult to design and are often inconclusive due to the complex interaction of all these factors. Furthermore, extruded surfaces are difficult to qualify and assessment of what is good and bad is often subjective. As a result, **the problem of surface quality is still far from falling off the list of extrusions problems.** Quality requirements still continue to increase, shapes continue to get thinner and the drive for increasing extrusion productivity all make the understanding of surface generation important.

There are numerous defects which occur during the production of aluminium alloys extrusions and, of these, it is surface cracking, pick-up and die lines which present the largest problem for the extruder.

1.4.1 Surface cracking

Surface cracking is most commonly associated with high strength aerospace aluminium alloys, but it is also observed in the more dilute architectural and structural alloys of the ENAA 6xxx series. Reiso [76, 77] has reported that the extrudability of the AlMgSi alloys, on an industrial scale extrusion plant, is strongly influenced by the Mg and Si content and the homogenization practice. The extrudability reduces with increased amount of Mg and Si in solid solution, resulting from either increasing cooling rate from homogenization temperature or increasing the alloy content. The surface cracks are often reported to be caused by tearing in the aluminium matrix.

It is also suggested that a second type of crack initiation mechanism occurs when slow cooling rates from the homogenization temperature are employed. In this case the presence of coarse Mg_2Si precipitates in the subcutaneous layer represented a region of local weakness in the structure which is unable to withstand the stresses at the die. The weakened structure subsequently shears, leaving a pore in the structure which acts as a crack initiation point. This emphasises the importance of the thermal history and the choice of the alloy composition.

1.4.2 Pick-up and die-lines

Pick-up and die lines are very important defects observed in the common alloys ENAA 6060 and ENAA 6063. Despite the commercial importance of such defects, there is surprisingly little documented research on the origins of their formation, especially in the case of *die lines*. Present evidence suggests that during extrusion a thin film of extrudate material adheres to the die land surface, and it is this interaction that results in the formation of these defects. The Aluminium Association has defined die lines as "longitudinal depressions

or protrusions formed at the surface of the extruded material due to imperfection on the die surface". Although extrudate-die interaction is clearly a major cause of the die line formation, an alternative mechanism of generation has been observed to give rise to micro-die lines. The two types of die line generation operate simultaneously during extrusion. Nevertheless, the first one is minimum when the billet temperature is between 425°C and 475°C, whereas the second one appears from 350°C to 550°C with the same intensity. The variation of the surface roughness can be directly related to the aluminium film on the die land area. This film has two characteristic features. At the front portion of the die, the newly formed extrudate chokes the die throat. The extrudate surface and the die area are in intimate contact, preventing exposure to the atmosphere. After leaving the choked area, the small amount of die deflection causes the extrudate to dissociate from initial contact, permitting oxide formation on the surface. This interaction creates the film development. Once generated, the rear portion of the die land serves only to deteriorate the surface finish by the imposed ironing and galling of the extrusion product. The micro-die lines are thinner and less deep. Their origins lie in some other mechanisms. Elongated Fe-containing precipitates have been identified in the subcutaneous layer and have been clearly associated with surface scoring. These precipitates were in fact fragments of larger precipitates interspersed with considerable cavitation. This cavitation links each fragment linearly and it is this string of voids which appears as micro-die lines on the surface.

The *pick-up* defect is usually thought to be enhanced by inclusions in the cast billet, inadequate homogenization treatment and die deflection. The defect is also temperature sensitive. It is observed as intermittent score lines of varying lengths between 3 mm and 12 mm and often terminates in a fleck of aluminium debris which is referred to a "pick-up deposit".

1.5 Micro-mechanisms of ductile fracture

This section is devoted to an introduction on damage micro-mechanisms. This is related to the necessity of a sound understanding of the physical mechanisms of damage before dealing with modeling of these complex processes. It is probably also the only way to design new materials and to improve mechanical properties of existing materials.

Ductile fracture results from the nucleation, growth and coalescence of cavities as shown in Figure 1.6. This failure mode occurs in metals provided that these materials are loaded at sufficiently high deformation, temperatures and strain rates. Large improvements in the resistance of ductile fracture and in fracture toughness could be achieved if cavity nucleation could be postponed. It is therefore important to investigate the material variables and the mechanical factors controlling this first step of ductile fracture. Considering a smooth

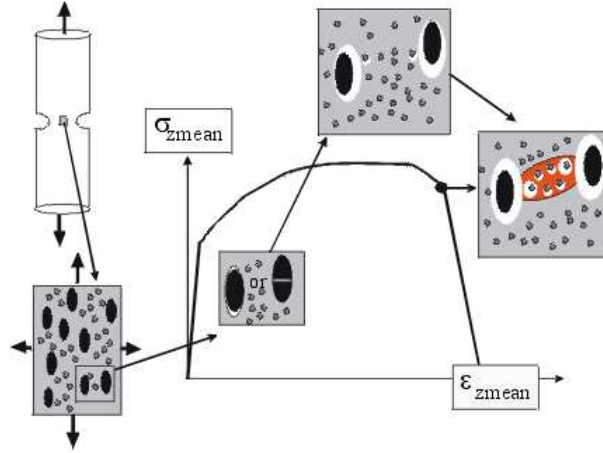


Figure 1.6 – Physical sequence of damage mechanisms in aluminium alloys.

tensile specimen, at the maximum load a local necking appears when the strain hardening of the material is not matching anymore the reduction of the load bearing section owing to plastic deformation. This plastic instability leads to the separation of the specimen in two pieces, in some cases by complete extent of the neck down to a point. In most cases, however, the fracture starts sooner by the development of a crack in the mid section of the neck. Looking down at the crack surface, we can see the presence of dimples as shown in Figure 1.7. Thus the fracture in the mid section results from the growth of cavities which join together.

In metallic materials, cavity initiation sites are usually associated with second phase particles or non-metallic inclusions. However in very pure single phase metals, there is some evidence that cavities can be homogeneously nucleated. As a general rule, cavity nucleation results from the inhomogeneity in plastic deformation between the matrix and the inclusions. Several approaches to this problem have been proposed, based either on dislocation theory or on pure continuum mechanics. Cavity formation cannot occur unless the elastic energy released from the particle by interfacial separation is at least equal to the surface energy created. A criterion based on the achievement of a critical stress at the interface or inside the particle must be satisfied. In many circumstances nucleation is not instantaneous but occurs continuously during plastic deformation. In classical alloys, void nucleation stems from the fracture of brittle phases or by the interface decohesion between two phases.

Once voids are formed they grow until they reach the coalescence stage. Void coalescence is the sudden transition from the void growth stage driven by dif-

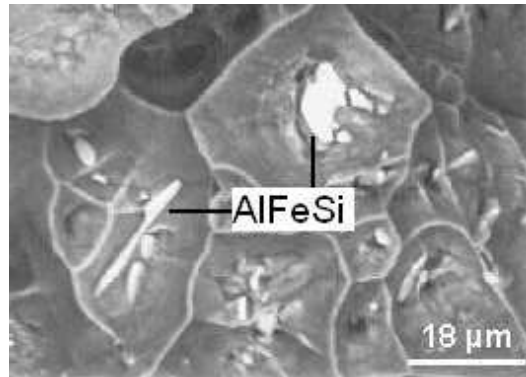


Figure 1.7 – Dimples on the fracture surface of an ENAA 6060 tensile specimen with second phase particles at the bottom responsible for damage nucleation.

fuse plastic yielding around the void to a localised mode of plastic deformation in the ligament between voids either normal to the main loading direction (coalescence by internal necking) or in shear (void sheet coalescence mechanism). Two broad classes of behavior must be distinguished at this stage. In the first class which is observed in a number of materials with a "single" microstructure, cavity growth occurs continuously until the voids impinge against one another. In this case, only one population of well-formed dimples are observed on the fracture surfaces. In the second class which corresponds to many structural materials with complex microstructures, cavity growth process initiated from large second phase particles is bypassed by the formation of shear bands between growing cavities. In these localisation bands, smaller cavities are initiated from smaller precipitates (hardening precipitates in Al alloys, carbide in steels).

1.6 Micromechanics-based constitutive model for ductile fracture

The section is devoted to a small summary of the history and development of the **Gurson model** in order to motivate the use of this model for modeling ductile fracture on ENAA 6xxx aluminium alloys.

1.6.1 Local approach to fracture

In normal elastoplastic analysis, it is commonly assumed that hydrostatic stress has no effect on plastic yield and that plastic deformation is incompressible. This assumption is based on physical considerations and is experimentally well

verified, except for conditions close to ductile fracture. The true reason for the failure of conventional fracture mechanics is that they completely neglect the presence of microfracturing process in the heavily stressed region. When microvoids are present in ductile material, studies have indicated that the hydrostatic components of stress can cause macroscopic dilatation through the mechanism of void growth. Over the years, several plasticity theories for void containing solids have been developed to model the void growth under hydrostatic tension.

The outstanding difference between classical plasticity yield equations, for example von Mises model, and micromechanical void containing elastic-plastic yield modes, for example the Gurson-Tvergaard model is that the stress triaxiality has been incorporated into the latter ones. In other words, such models have become pressure-dependent. One significant advantage of local approaches is that it is not necessary to assume that a crack pre-exists in engineering components. It has long been recognised that ductile fracture occurs in plastically deforming metals through the nucleation, growth and coalescence of small internal voids or cavities at the sites of inclusions and second phase particles. It was natural to develop a fracture model based on the modeling of these three steps.

1.6.1.a Void nucleation

In structural metals, void nucleation primarily occurs either by debonding or cracking of second phase particles and/or inclusions. The fracture of a particle or of an interface is assumed to occur when the maximum principal stress in the particle or at the interface reaches a critical value:

$$\sigma_{princ}^{particle\ max} = \sigma_c^{bulk\ or\ interf} \quad (1.1)$$

which is different for each mechanism. Following the Eshelby theory [29] and the secant modulus extension to plastically deforming matrix proposed by Berveiller and Zaoui [15], the maximum principal stress in an elastic inclusion (and at the interface) $\sigma_{princ}^{particle\ max}$ can be related to the overall stress state by using:

$$\sigma_{princ}^{particle\ max} = \sigma_{princ}^{max} + k_s(\sigma_e - \sigma_0) \quad (1.2)$$

where σ_{princ}^{max} is the maximum overall principal stress and k_s is a parameter of order unity which is a function of the inclusion shape and of the loading direction. This void nucleation criterion was initially proposed by the Beremin group [13] who also identified k_s from experimental data. They found that the values of k_s predicted by the theory were about two times higher than the experimental values because of an overstiff response of the homogenization scheme.

The rate of increase of the void volume fraction associated to the nucleation of new voids from a population of particles by particle fracture or decohesion is taken as a function of the plastic strain rate:

$$\dot{f}_{nucl} = g(\bar{\epsilon}^p) \dot{\bar{\epsilon}}^p \quad (1.3)$$

where $\dot{\bar{\epsilon}}^p$ is the effective plastic strain rate of the matrix material. A polynomial form for the function $g(\bar{\epsilon}^p)$ is chosen:

$$g(\bar{\epsilon}^p) = a_1(\bar{\epsilon}^p)^4 + a_2(\bar{\epsilon}^p)^2 + a_3 \quad (1.4)$$

When the condition eqn. 1.2 is fulfilled, with the corresponding effective plastic strain noted $\bar{\epsilon}^p = \bar{\epsilon}_c^p$, the nucleation starts and takes place during a range of strains $\Delta\bar{\epsilon}^p$.

The main motivation for the void nucleation condition eqn.1.1 is that most inclusions, reinforcements or precipitates in metal alloys can be considered as brittle solids (this statement is not true in alloys involving two ductile phases such as in duplex steels). A critical maximum principal stress corresponds to the critical stress in the particle required to reach the critical stress intensity factor for the propagation of the nanoscale internal defects present within the particles [51]. A condition for the fracture of the interface between the particle and the matrix should also ideally include a second necessary condition stating that the energy be larger than the interface toughness [80, 7]. As mentioned above, more advanced homogenization scheme or the use of tabulated stress concentration factors [61] would deliver more accurate estimate of the stress in the particle. Also, the validity of the micro-macro condition eqn.1.2 when rate dependent effects becomes significant, i.e. when typically $m > 0.05$, is questionable and homogenization schemes for viscoplastic materials are required. In conclusion, this void nucleation condition should only be seen as a qualitative model that approximately account for the dependence on the mode of loading, on the particle shape and on the mode of nucleation.

1.6.1.b Growth of isolated void

Several researchers have devoted great attention to void growth models. Among them, McClintock [62, 63] developed a void growth model based on his analysis of cylindrical void in an infinite matrix subjected to axial and transverse stresses. An exponential dependence of the void growth rate on biaxial stress was obtained. The most successful and versatile model for void growth in a plastic flow field was developed by Rice and Tracey [79] for the case of a spherical void of radius R_0 in a remote uniform strain-rate field (infinite matrix). It leads to the following expression for the ratio between the deformed void radius and its initial value R_0

$$\int_{void\ initiation} 0.283 \exp\left(\frac{3\sigma_h}{2\sigma_y}\right) d\epsilon_e^p = \ln\left(\frac{R}{R_0}\right) \quad (1.5)$$

where σ_h is the average macroscopic Cauchy stress, σ_y the flow stress representing the actual microscopic stress state in the matrix material and ϵ_e^p the equivalent plastic strain. Subsequent investigators found that this equation could be approximately modified for strain hardening by replacing the yield strength with σ_e , the effective stress [4].

Since the Rice and Tracey model is based on a single void, it does not account for interactions between voids, nor does it predict ultimate failure. A separate failure criterion must be applied to characterize microvoid coalescence. Although, this model does not account for the feed-back of the void growth to the constitutive behavior of the material, it has been proved to give a fairly accurate description of ductile fracture processes in a number of applications.

1.6.1.c Micromechanical model by Gurson for porous solids

The void growth stage of ductile fracture consists in the stable expansion of voids within a material undergoing tensile plastic deformation. There are two aspects of this stage that must be considered:

1. The void expansion and change in shape during deformation.
2. The degradation in the material's load carrying capacity due to the presence of the voids.

The critical void growth model by Rice and Tracey has only considered the first aspect of the stable void expansion stage. Dilatational constitutive functions which can take into account of the degradation of the load carrying capacity by the presence of porosity are therefore a desirable component of a mathematical model of the ductile fracture process [98].

The Gurson model [38] analyzes the plastic flow in a porous medium by assuming that the material behaves as a continuum. Voids appear in the model indirectly through their influence on the global behavior. The effect of the voids is averaged through the material, which is assumed to be continuous and homogeneous. The main difference between Gurson model and classical plasticity is that the yield surface in the former exhibits a hydrostatic stress dependence, while the classical plasticity assumes that yielding is independent of this hydrostatic stress. This modification to conventional plasticity has the effect on introducing a strain softening term [4].

For a porous solid with a randomly distributed volume fraction f of voids, Gurson has suggested the use of an approximate yield function of the form $\phi(\sigma_h, f, \sigma_y) = 0$. Gurson theory is endowed with a yield condition, a flow law, a measure of void volume fraction, a rule for nucleating voids and a law for evolution of the voids. The approximate yield locus is obtained by the following procedures:

1. von Mises condition is used to characterise the yield and flow of the matrix material
2. a rigid-plastic model is assumed valid because of the large strain involved in ductile fracture
3. a form is assumed for the velocity in the aggregate, which allows the voids to grow but requires incompressibility of the matrix. This velocity field must also meet kinematic boundary corresponding to deformation rates on the surfaces [98].

Based on the above rigid-plastic upper-bound analysis of spherical voids, Gurson obtained the following yield function ($q_1 = q_2 = 1$):

$$\Phi(\sigma_h, f, \sigma_y) = \frac{\sigma_e^2}{\sigma_y^2} + 2q_1 f \cosh\left(\frac{3q_2\sigma_h}{2\sigma_y}\right) - 1 - (q_1 f)^2 \quad (1.6)$$

Where σ_e is the von Mises equivalent stress. The implication of the Gurson model is that voids are assumed to be randomly distributed, so that the macroscopic response is isotropic. It is easy to see that if $f = 0$, this constitutive relation reduces to the classical isotropic hardening plasticity. The yield surface was extended to hardening materials by regarding σ_y as a measure of the effective flow stress of the matrix material in the current state. Due to the presence of microvoids, the plastic flow is dilatational and pressure sensitive. Furthermore, although the matrix material continues to harden, the aggregate can soften.

Constants q_1 and q_2 were introduced by Tvergaard [90, 91] to bring the predictions of the model into closer agreement with full numerical analysis of a periodic array of voids. Tvergaard has investigated the macroscopic shear band instability behavior, based on a numerical model which fully accounts for the non uniform stress field around each void and also for the interaction between neighboring voids. Good qualitative agreement was found between the predictions of the full numerical model and the Gurson model for the onset of localization. Based on this comparison, for both plane strain and axisymmetric conditions, Tvergaard suggested that $q_1 = 1.5$ should be used. The modified Gurson model is sometimes called the Gurson-Tvergaard model. According to this modification, the material loses load carrying capacity if f reaches a limit $\frac{1}{q_1}$, because all the stresses have to vanish in order to satisfy the flow surface equation. The advantage of Gurson-based models is that fracture could arise as a natural outcome of the deformation process. However, even if $q_1 = 1.5$ as proposed by Tvergaard, the void volume fraction $f = \frac{1}{1.5}$ is still too large to be realistic in practice to simulate the final material failure. Therefore, an extra criterion in G-T model is needed to model the material failure, typically by void coalescence. Three different failure criteria have been proposed in the literature [98].

1.6.1.d Influence of the void shape

Although good agreement with a range of experiments and void cell computations has been observed, the G-T model as it currently stands still suffers from significant limitations:

1. The transfer of experimental data from non-cracked specimens for the modeling of cracked structures, and vice versa. Many problems of ductile fracture in non-cracked structures occur at low to intermediate stress triaxiality. In such applications, the model does not properly predict fracture using a set of parameters identified at high triaxiality on cracked specimens.
2. Non-spherical void can only be accounted for in an *ad hoc* manner by introduction of an effective porosity. Even when the cavities are initially spherical, void shape effect can be significant upon growth, especially at low triaxiality.
3. The significant stress triaxiality dependence of the coalescence condition is not captured by current models [72].

To account for the void shape effect and its influence on void growth and coalescence, Gologanu-Leblond-Devaux [36] have proposed an extension of the Gurson model. This extended model addresses the problem of theoretically predicting growth and coalescence of cavities in periodically voided ductile solids. They consider a cylindrical representative volume element containing an initially spheroidal void (spheric, prolate or oblate) and subjected to some axisymmetric loading. They have retained the original structure of the model and introduce one more parameter and its evolution law: the void shape.

1.6.1.e Void coalescence conditions

The critical void growth ratio criterion by Rice and Tracey

Although the void growth model proposed by Rice and Tracey [79] does not itself constitute a fracture criterion, it has been showed in the literature that, as a first approximation, the deformation at fracture in tension is dependent of the size and distance between voids and only depends on void growth ratio. With this observation, a fracture criterion based on the assumption of a critical ratio of void growth ($\frac{R_{mean}}{R_0}$), specific to the material for a given direction of the load, has been formulated and widely used in the local approaches to fracture. In general, the critical void growth criterion modified to take into account the hardening and non-constant stress triaxiality case can be written:

$$\int_{\epsilon_n}^{\epsilon_c} 0.283 \exp\left(\frac{3\sigma_h}{2\sigma_y}\right)_{vonMises} d\epsilon_e^p = \ln\left(\frac{R_{mean}}{R_0}\right)_c = R_c \quad (1.7)$$

where ϵ_n and ϵ_c are the strain at void nucleation and void coalescence respectively. The value $(\frac{R_{mean}}{R_0})_c$ is usually determined through simple uniaxial or axisymmetric tests and then applied to more complex stress states, for example, notched or cracked specimens.

The constant critical void volume fraction criterion

In this approach to be used with a constitutive model for porous materials, a modification replacing f by f^* as follows in order to account for void coalescence effect on final failure has been proposed by Tvergaard and Needleman [66]:

$$f_c + K_f(f - f_c) \left. \begin{array}{l} f \quad \text{if } f \leq f_c \\ \text{if } f > f_c \end{array} \right\} \Rightarrow f^* \quad (1.8)$$

Here, f_c is the critical void volume fraction at which voids coalesce and K_f is a constant determined from the void volume fraction at final failure of the material f_F , which is much smaller than $\frac{1}{q_1}$:

$$K_f = \frac{f_u^* - f_c}{f_F - f_c} \quad (1.9)$$

where f_F is the ultimate void volume fraction and $f_u^* = \frac{1}{q_1}$. In the absence of physical proof and in line with mathematical convenience this modification has induced the constant critical void volume fraction criterion, which is perhaps one of the most widely applied criteria.

The plastic limit-load criterion by Thomason

Thomason emphasised the necessity of modeling the ductile fracture process in terms of dual plastic constitutive responses for a void-containing solid [87]. After a detailed analysis of the mechanics of ductile fracture by void coalescence, Thomason observed that the sudden transformation from a macroscopically homogeneous state of plastic flow, to a highly localised internal necking of the intervoid matrix across a single weakest sheet of voids coincide with the attainment of the plastic limit-load condition for localised plastic failure of the intervoid matrix. After the limit-load has been reached, the strain localizes in the ligament and the material fails with little additional strain outside the ligament. Based on this information, Thomason has defined two dilatational yield surfaces: the weak dilatational yield surface, which represents the stable homogeneous macroscopic plastic flow yield, and the strong dilatational surface, which signifies the virtual unstable model of incipient void coalescence. A critical condition for incipient void coalescence by internal necking failure of the intervoid matrix can therefore be given by:

$$\sigma_{strong} = \sigma_{weak} \quad (1.10)$$

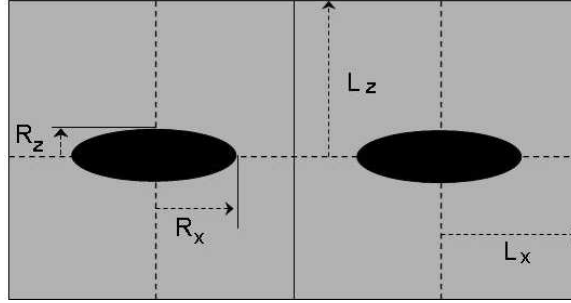


Figure 1.8 – Unit cell geometry representing volume element that the model aims at describing.

where σ_{weak} is the applied maximum principal stress on the current stable yield surface and σ_{strong} is the virtual maximum principal stress required to initiate the localised internal necking of the intervaid matrix material.

1.6.2 Unified extended model for void growth and coalescence

Pardoen and Hutchinson [73, 72] have proposed an enhanced Gurson model integrating two contributions proposed by the literature. The first one is the model of Gologanu-Leblond-Devaux extending the Gurson model to void shape effects. The second one is the approach of Thomason for the onset of void coalescence. Each of these has been extended heuristically to account for strain hardening. In addition, a micromechanically-based simple constitutive model for the void coalescence stage is proposed to supplement the criterion for the onset of coalescence. The fully enhanced Gurson model depends on the flow properties of the material and the dimensional ratios of the void-cell representative volume element. Phenomenological parameters such as critical porosities are not employed in the enhanced model. It incorporates the effect of void shape, relative void spacing, strain hardening and porosity [72].

As depicted on Figure 1.8, the representative volume element geometry that the model aims at describing is a matrix characterised by a mean yield stress σ_y , containing spheroidal voids ($R_z = R_y$) with porosity f , void aspect ratio $W = \frac{R_z}{R_x}$, the relative void spacing $\lambda = \frac{L_z}{L_x}$. The parameter $\chi = \frac{L_z}{R_x}$ (the relative void spacing) will be used more often than λ . It is univocally related to f , W and λ through:

$$\chi = \left(\frac{3f\lambda}{2W} \right)^{\frac{1}{3}} \quad (1.11)$$

The model is thus based on two different solutions for the expansion of a void in an elasto-plastic material: one is called "void growth" (ϕ_{growth}) corresponding to diffuse plasticity around the void and the other is called "void coalescence" ($\phi_{coalescence}$) corresponding to localised plasticity in the intervoid ligament.

These two solutions can be presented in the form of two distinct plastic yield surfaces supplemented by evolution laws for the internal variables of the model and the normality rule for the plastic strain increment. These two yield surfaces are two modes of deformation in competition for an elasto-plastic material containing voids:

$$\Phi_{growth} = \frac{C}{\sigma_y^2} \|s + \eta\sigma_h X\|^2 +$$

$$2q(g+1)(g+f) \cosh\left(\kappa \frac{\sum h}{\sigma_y}\right) - (g+1)^2 - q^2(g+f)^2 \equiv 0 \quad (1.12)$$

$$\Phi_{coalescence} = \frac{\sigma_e}{\sigma_y} + \frac{3}{2} \frac{|\sigma_h|}{\sigma_y} - F(W, \chi) \equiv 0. \quad (1.13)$$

The first yield surface Φ_{growth} is a Gurson type surface derived by Gologanu-Leblond-Devaux [36] and extended to strain hardening materials in Pardoen and Hutchinson [71]. The yield surface $\Phi_{coalescence}$ has been developed in the spirit of seminal work by Thomason [87] extended to the full coalescence response and to strain hardening by Pardoen and Hutchinson [72]. The model is by nature anisotropic through the account of void shape (and the evolution law for the shape that depends on the orientation of the symmetry axis of the void).

The homogenised material switches from one plasticity solution to the other when the two yield loci meet at the current loading point. The first yield surface to be reached is Φ_{growth} . In the beginning of the deformation, the voids are small and the spacing between them is relatively large, resulting in a diffuse plastic deformation. With increasing deformation, Φ_{growth} first tends to expand due to hardening and then to contract due to void growth softening. Void growth and ligament reduction also induces a contraction of $\Phi_{coalescence}$. When the two yield surfaces intersect at the current loading point, the transition to coalescence occurs. With increasing deformation, the coalescence yield surface tends to contract very rapidly towards the zero stress state [71].

Some very ductile materials fail by complete void impingement, which corresponds in the model to the shrinking of the coalescence yield surface to a point. Other materials tend to involve premature ligament failure owing to the growth of a second population of voids or owing to microcleavage. In that case, the coalescence mechanism is suddenly interrupted and only very limited amount

of energy is spent during the final ligament failure. Pardoen and Hutchinson have thus introduced a third stage of damage called "final failure". A simple phenomenological criterion based on a critical ligament reduction $\chi = \chi_c$ has been implemented. Traction is ramped to zero in few steps. χ_c is the only purely phenomenological parameter of the model that must be adjusted experimentally except when final coalescence by void impingement is observed. In that case, $\chi_c = 1$.

2

The starting point

First industrial full scale extrusion tests

Chapter 2

The starting point

First industrial full scale extrusion tests

This first step of the research relates to the manufacture of shaped aluminium profiles. It aims at understanding and at controlling certain metallurgical mechanisms concerned within various stages of the process. The industrial objective is the optimization of the mechanical properties of the alloys at various temperatures, which will make it possible to reduce the risk of cracking or tearing during extrusion. To improve the capacity of deformation without initiating damage at the extrusion temperatures, the alloys undergo a preliminary heat treatment. Subtle changes of the microstructure occur at this time. The optimization of the temperatures and holding times during the homogenization, as well as the cooling rate after homogenization allows, in fine, to extrude healthy profiles at higher rates. By now, the extrudability problems are solved in majority by "tests and errors" thanks to the experience and the intuition of technicians and experienced engineers. The objective of this chapter is to study the existing relationship between parameters of heat treatment, the microstructure of the materials and the defects of cracking during extrusion, in order to develop a robust strategy of optimization of the homogenization and extrusion conditions. This objective goes hand in hand with the acquisition by the company Sapa RC Profile in Ghlin, Belgium, of a new continuous homogenization furnace for which it is advisable to control the parameters of the thermal cycle applied to each type of material.

2.1 Introduction on industrial extrusion

It is well established that homogenized aluminium alloys billets extrude easier and faster and give better surface finish than as-cast billets. However, there are limits to how much a homogenization treatment can improve the performance of the billet on the press. There are several features that must be imparted to the billet before homogenization. The billet chemistry has to be optimized in accordance with the needs and expectations of the extruder. A cast billet should also have fine grain and cell structure uniformly distributed over its cross-section, no coarse intermetallics, minimum surface segregation, and an acceptable surface finish. When properly homogenized, such a billet will give high throughput rates, low breakout pressures, desired shape and uniform surface finish free from defects. It is assumed that the process variables, temperature and speed (strain rate), determine the acceptability of the surface quality. The surface quality in most extrusions depends upon the stress conditions obtaining near the die land regions. If the tensile friction force exceeds the fracture stress of the materials, then some tearing is encountered. Additionally, if the heat generation near the die increases the local temperature in excess of the solidus point, localised melting occurs, which can cause severe cracking of the surface. These mechanisms severely increase when second phase particles restrict the ductility of the material or cause eutectic melting at lower temperature than the solidus point. The temperature generation during extrusion is a function of the alloy chemistry, extrusion speed, extrusion ratio, aspect ratio, container temperature and the initial billet temperature. It is obvious that the heat generation increases with an increase in the extrusion ratio and the ram velocity. The major effect of this heat generation is to restrict the speed of operation at high temperatures. Furthermore, the danger of cracking increases in shaped extrusions near re-entrant corners. In an extreme case, there is a danger of corners disintegrating.

An industrial **homogenization** practice typically consists in a soaking treatment which is followed by cooling at a determined rate. Several processes take place during soaking. The interdendritic network of the plate-like β -AlFeSi intermetallics are replaced by the more rounded discrete α -AlFeMnSi particles. The Mg_2Si particles and coarse eutectic are also solutionised in a soaked billet while the coring inherited from the as-cast microstructure is leveled out in favor of a more homogenized distribution of the solute Mg and Si. Following the soaking at high temperature, the cooling to room temperature needs also to be controlled. Slow cooling tends to produce coarse Mg_2Si particles while rapid cooling traps the Mg and Si in solution with little or no Mg_2Si precipitation. Coarse β - Mg_2Si particles lead to incipient melting and surface tearing during extrusion giving poor surface quality. Mg and Si in solution, on the other hand, have an adverse effect on the flow stress of the alloy and thus increase its resistance to deformation. Another extrusion process parameter that needs to be

controlled is **the reheating to the extrusion temperature**. Indeed, as the hot extrusion of aluminium alloys asks for billets typically between 400°C and 470°C, the material is heated through the temperature range favorable for the precipitation of the different Mg₂Si particles.

As the productivity always requires higher rates and better surface aspect, the microstructural origin of the surface defects appearing during extrusion and the correct mechanisms responsible for their appearance need to be better studied. This study relates to the implementation of ingots for the manufacture of aluminium profiles. A better knowledge of the fundamentals mechanisms of hot cracking and tearing off of material during extrusion is necessary in order to optimize the choice of the technological parameters to apply to each type of alloy. This first step aims at understanding the surface cracking during the extrusion of ENAA 6060 aluminium alloys.

This study consists in the realization of full-scale industrial extrusion tests in order to observe the macroscopic response of different homogenization conditions on the maximum extrusion speed and on the surface defects appearance. Following this, an important work is carried out to study the microstructure evolution of the alloys at the different steps of the process and to study the different surface defects in order to determine their origins.

2.2 Material and Industrial testing

The production of the studied aluminium alloys, their thermal treatments and the different extrusion tests are performed in a full-scale industrial plant of Sapa RC Profile in Ghlin, Belgium. Systematic extrusions at increasing ram speed are carried out for differently homogenized billets in order to correlate the defects intensity with the homogenization temperature and soaking time. In order to be able to detect and measure the microstructure change effects on the defects appearance, we point out our interest in analyzing very accentuated extrusion defects. An extrusion die is thus chosen thanks to which extrusion tests at very high rates could be carried out without disturbing the production by burning die (a die is said "burned" when a non uniform layer of aluminium sits on its surface, spoiling the profile surface).

2.2.1 Material

Logs with a diameter of 8 inches are cast and treated in an industrial continuous homogenization furnace. The alloy under investigation is a standard industrial ENAA 6060 aluminium alloy. Its chemical composition is given in Table 2.1.

Al	Mg	Si	Fe	Mn
98.84	0.49	0.43	0.22	0.02

Table 2.1 – Chemical composition (wt.%) of the aluminium alloy ENAA 6060 used during the industrial tests.

Homogenization conditions			
Alloy	Temperature(°C)	Soaking time (h)	Cooling rate (°C/h)
1	570	2.5	410
2	585	2.5	410
3	585	3.5	410
4	585	4.5	410
5	585	4.5	320

Table 2.2 – Different homogenization parameters used for extrusion tests.

2.2.2 Homogenization tests

Five combinations of homogenization temperatures, soaking times and cooling rates are applied to the material in order to study the effect of the microstructure evolution on the surface defects appearance. Table 2.2 shows the different homogenization conditions. The alloy homogenized with the homogenization conditions 1 is named alloy 6060₁, and so on for the homogenization conditions 2,3,4 and 5. The homogenization conditions 1 to 4 are applied here to modify the intermetallic particles content whereas the conditions 5 is applied with a slower cooling rate in order to increase the Mg₂Si re-precipitation during the cooling to room temperature after homogenization. The as-cast alloy is identified as alloy 6060₀. These homogenization tests are carried out in the new continuous homogenization furnace of Sapa Rc Profile in Ghlin.

2.2.3 Extrusion tests

The extrusion trials are performed with an industrial 1800T press represented in Figure 2.1. The billets are preheated around 460°C in a gas furnace before being extruded at increasing ram speed. This re-heating time is in the range of 25 to 30 minutes. The container temperature is maintained around 465°C. The geometry of the extruded section is presented in Figure 2.2.

This geometry is chosen because of its edges and protuberances, which are critical zones for the appearance of surface defects without excessive burning of the extrusion die. Indeed, as we changed the ram speed at each extruded billets, we want to avoid any trouble caused by the die surface. We signal also that this die could extrude two profiles at the same time, one upside of the other one. The results presented in the next sections compare each time the



Figure 2.1 – The industrial 1800T press used during the extrusion tests.

defects intensities appeared on each profile (the upper profile UP and the lower profile LP). The main difference between these two profiles is the temperature reached during extrusion. The lower profile is known to meet more problem to evacuate its accumulated heat and its temperature is in general higher.

The different billets are extruded with a relative ram speed increasing from 1 to 1.53 (1 being the standard industrial ram speed for this specific profile), in order to determine the maximum extrusion speed before the appearance of surface defects (*critical extrusion speed*). All the extruded billets are compared each time to a standard billet to ensure the reproducibility of the tests. The following parameters are measured during the extrusion tests:

1. Billet temperature
2. Profile temperature (at the very output of the die)
3. Extrusion speed
4. Surface defects intensity

2.3 Results of the extrusion tests

During these full-scale extrusion tests, two type of surface defects are observed on the extruded profiles, the relative intensities of which depend on the homogenization conditions and ram speed. The defect named *defect A* appeared on the outside edges of the profiles, and the defect named *defect B* appeared at an inside protuberance of the profiles. We can see in Figure 2.3 both surface defects and their situation on the profile.

The places where the defects appear, are very critical in term of temperature increase and stress state. The next figures show the evolution of both defects

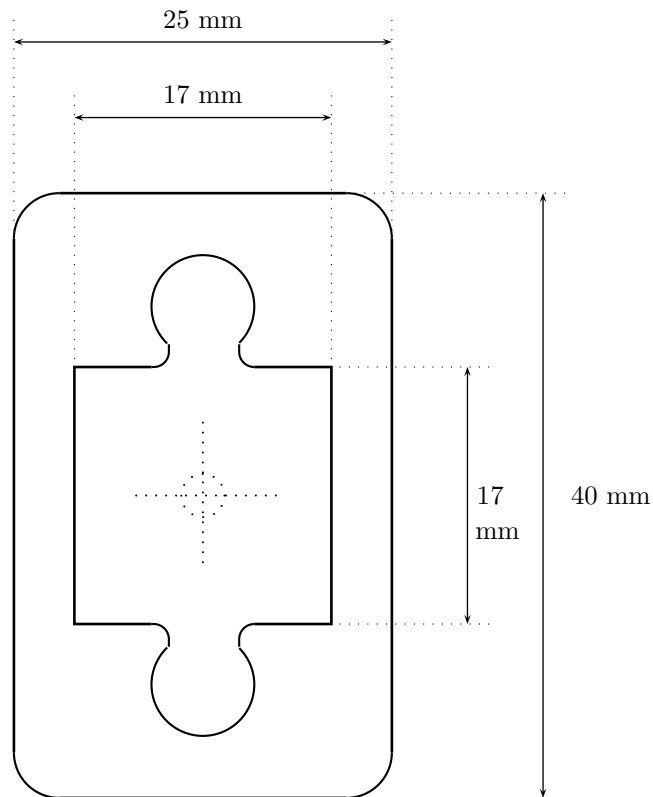


Figure 2.2 – Shape of the extruded profile.

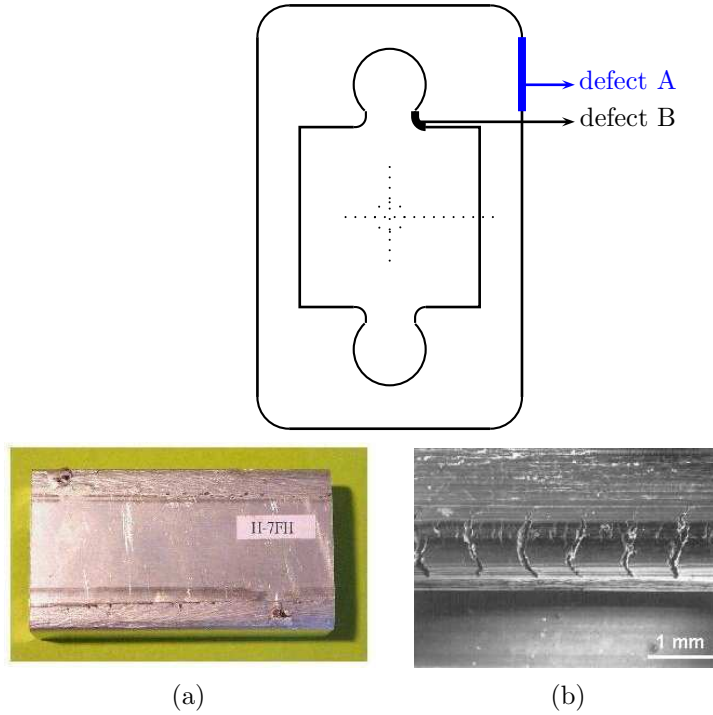


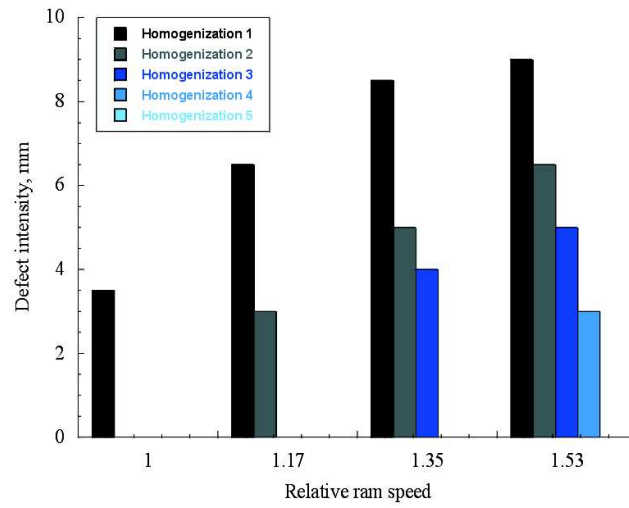
Figure 2.3 – Surface defects appearing during the extrusion tests: (a) *defect A* appears on the outside edges of the profiles (b) *defect B* appears at an inside protuberance of the profiles.

intensities, as well as the other parameters measured during the tests. We compare each time the defect evolution for the upper profile and for the lower profile as the die allowed to extrude two profiles at the same time.

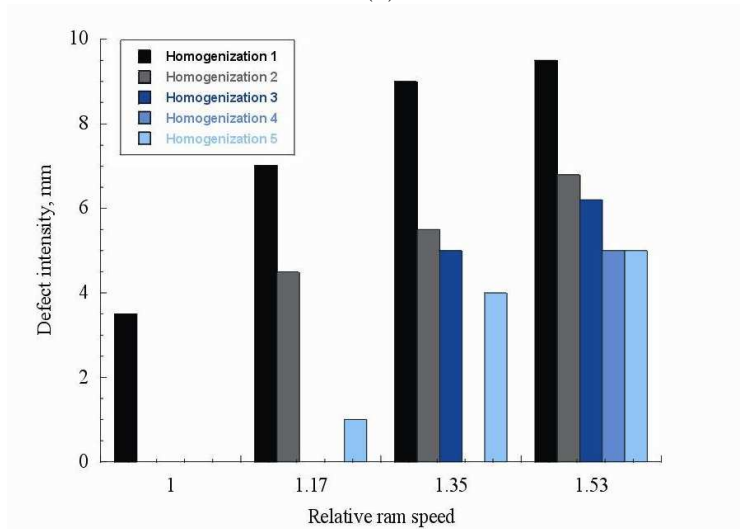
2.3.1 Surface defect A

The intensity of the defect A, which appears on the outside edges of the profiles, is quantitatively measured as the width of the tearing. This defect is shown to increase from the beginning to the end of the profiles and with ram speed. Figure 2.4 shows the evolution of the defect A mean intensity with ram speed for the five different homogenization treatments and for the upper and the lower profile.

As expected, we observe that the defect intensity increases with ram speed and decreases with an increasing degree of homogenization quality. The homogenization conditions 4 leads to an increase of the extrudability by 53% in



(a)



(b)

Figure 2.4 – Evolution of the defect A intensity with ram speed for different homogenization treatments: (a) the upper profile and (b) the lower profile.

terms of ram speed when compared to conditions 1. The extrusion speed (as well as the extrusion temperature which is linked to the speed) governs thus the surface cracking as well as the homogenization quality (thus as the β -to-

α transformation). Note that the presence of the defect at the corner of the profile obviously confirms that the local stress state and the local deformation temperature related to the geometry of the component is also a first order effect not addressed in this study devoted to a single profile. We clearly see that this defect intensity is still higher for the same profile extruded by the lower orifice of the die. The only parameter that is anticipated to change between both orifices is the temperature which is higher for the lower ones since the heat can not escape as easily as for the upper ones.

We can conclude that the defect A is sensitive to the β -to- α transformation of the Fe bearing intermetallic and sensitive to the temperature. A better homogenization practice allows to avoid this tearing at higher ram speed.

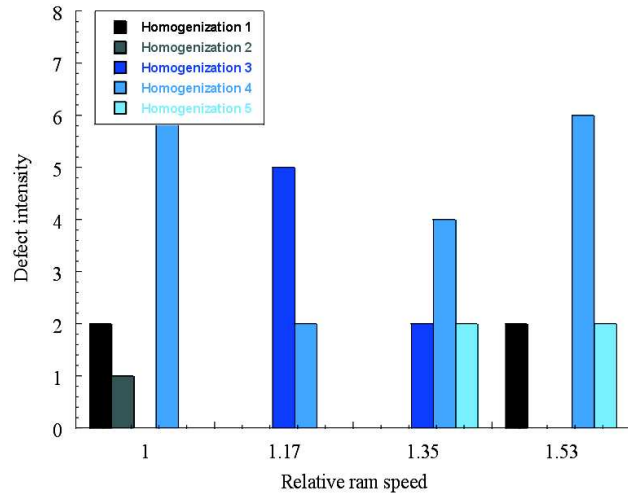
2.3.2 Surface defect B

The evolution of the surface defect B with ram speed is less clear than for the first defect at least for the four first homogenization conditions. Figure 2.5 shows the evolution of the intensity of the defect B with ram speed for the five different homogenization treatments and for both profiles (up and down). A marked effect can be observed only between the homogenization condition 5 and the other ones. Indeed, the condition 5 with a lower cooling rate after homogenization leads to a large increase in the defect B intensity. It means that this defect is probably linked to the presence of Mg_2Si -phases, which seems to be the only phase that can be influenced by the cooling rate.

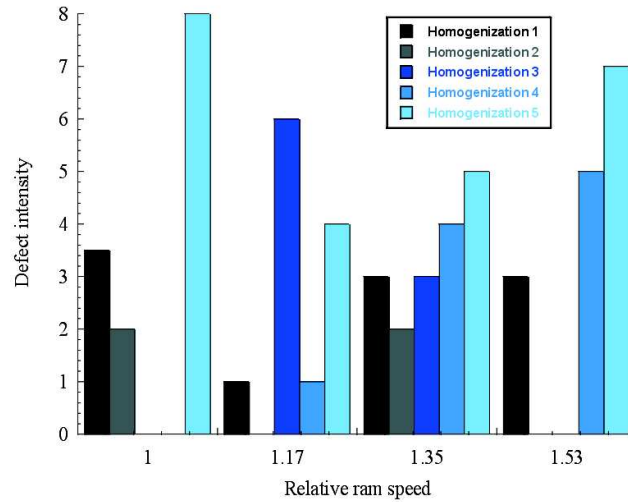
There is no reason to conclude that the defect B is sensitive to the β -to- α transformation of the Fe bearing intermetallic. Nevertheless, it is sensitive to the cooling rate after homogenization with a marked increase of the defect intensity with a slower cooling rate.

2.3.3 Evolution of the extrusion temperature

The evolution of the extrusion temperature is measured at the very exit of the extrusion press on the profile surface thanks to an infrared pyrometer. The results are presented in Figure 2.6 in order to see if there exists a link between this parameter and the defects intensity. We can see that the billets homogenized at a lower temperature or with shorter holding times (thus possessing a lower homogenization quality) present higher value of the extrusion temperature. This temperature reaches in those cases values above the eutectic melting temperature that can be encountered in this alloy as summarized in Table 2.3. This means that, if the microstructural state allows such eutectic reactions to take place, melting can be seen as an hypothetical cause for surface cracking. Nevertheless, as the initial temperatures has never been exactly similar for all the tests, we have to stay careful with these last results.



(a)



(b)

Figure 2.5 – Evolution of the defect B intensity with ram speed for different homogenization treatments: (a) the upper profile and (b) the lower profile.

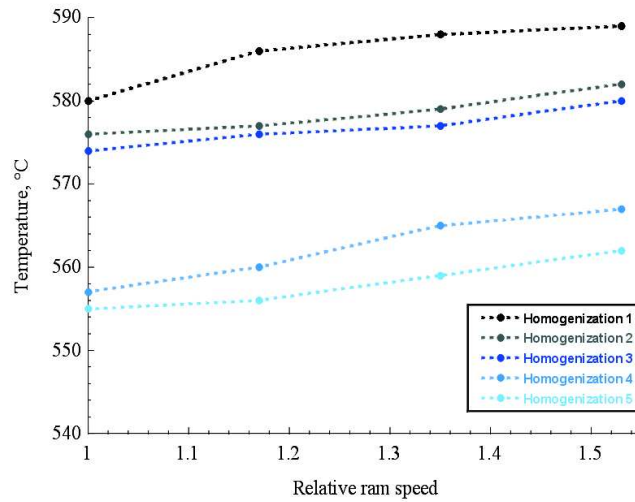


Figure 2.6 – Evolution of the extrusion temperature with ram speed for the different homogenization conditions.

Melting temperature	Reaction
555°C	$\text{Al} + \text{Mg}_2\text{Si} + \text{Si} \longrightarrow \text{Liquid}$
576°C	$\text{Al} + \beta\text{-AlFeSi} + \text{Mg}_2\text{Si} \longrightarrow \text{Liquid} + \alpha\text{-AlFeSi}$
577°C	$\text{Al} + \text{Si} \longrightarrow \text{Liquid}$
578°C	$\text{Al} + \beta\text{-AlFeSi} + \text{Si} \longrightarrow \text{Liquid}$
587°C	$\text{Al} + \text{Mg}_2\text{Si} \longrightarrow \text{Liquid}$

Table 2.3 – Some eutectic melting temperatures in AlMgSi alloys.

2.4 Microstructure investigation around the surface defects

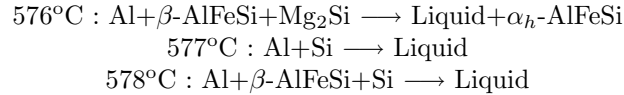
The microstructure state at the surface defects places is investigated by means of transmission electron microscopy (TEM) and differential scanning calorimetry (DSC). The goal is to look for relationships between the presence of the particles of the different phases and the occurrence of tearing.

2.4.1 TEM investigation at the defects locations

Material samples are firstly cut in thin foils before being polished until we obtain a thickness of 100-150 μm . Then, circular samples of 3 mm in diameter are cut from the thin foils. Transmission electron microscopy (TEM) samples

are finally prepared by double jet electro-polishing in $\text{HNO}_3 - \text{CH}_3\text{OH}$ (volume ratio 1:3) at a temperature of -30°C and a voltage of 9 V. TEM analyses are performed at 200 keV. Many samples from the extruded profiles are analyzed in zones close to the surface problems. The micrographs presented in Figure 2.7 show typical examples of the microstructure discovered near the defect A at the outside edges of the extruded profiles. We can see typical β -AlFeSi particles in Figure 2.7(a) to Figure 2.7(b). Some of these particles are cracked over all their length (a), others present just a small initiated microcrack at one edge (b). In addition to these intermetallic particles, pure silicon inclusions are found along grain boundaries and in the aluminium matrix in Figure 2.7(c) to (e). Micro-cracks are also observed at the interface of some of these inclusions (c). It is thus possible that these micro-cracks point to the presence of bigger ones at locations of very high stress and temperature such as the surface of the profiles edges.

As said before, cracked AlFeSi particles are found near the defect, but the main difference with the zones which do not present any defect lies in the number of silicon-rich inclusions (which are located near the billet surface after casting). Some melting reactions are possible in this range of temperature as presented in the introduction:



The accumulation of these inclusions near the surface due to casting or due to the diffusion of a large quantity of silicon during the β -to- α -AlFeSi transformation, combined with the high temperature level at the edge of the profile can be responsible for the tearing initiation at the surface. The cleavage of the second phase particles such as AlFeSi can also induce damage near the surface.

Concerning the surface defect B, the microstructural origin seems different. As shown in Figure 2.8, many coarse Mg_2Si particles are observed in this zone of the profiles at the grain boundaries. The presence of such particles can lead to melting at high temperature:



2.4.2 DSC investigation at the defects locations

DSC measurements were carried out at the TU Delft. These experiments aim at highlighting eutectic meltings, which could occur in the temperature range reached in the profile during extrusion.

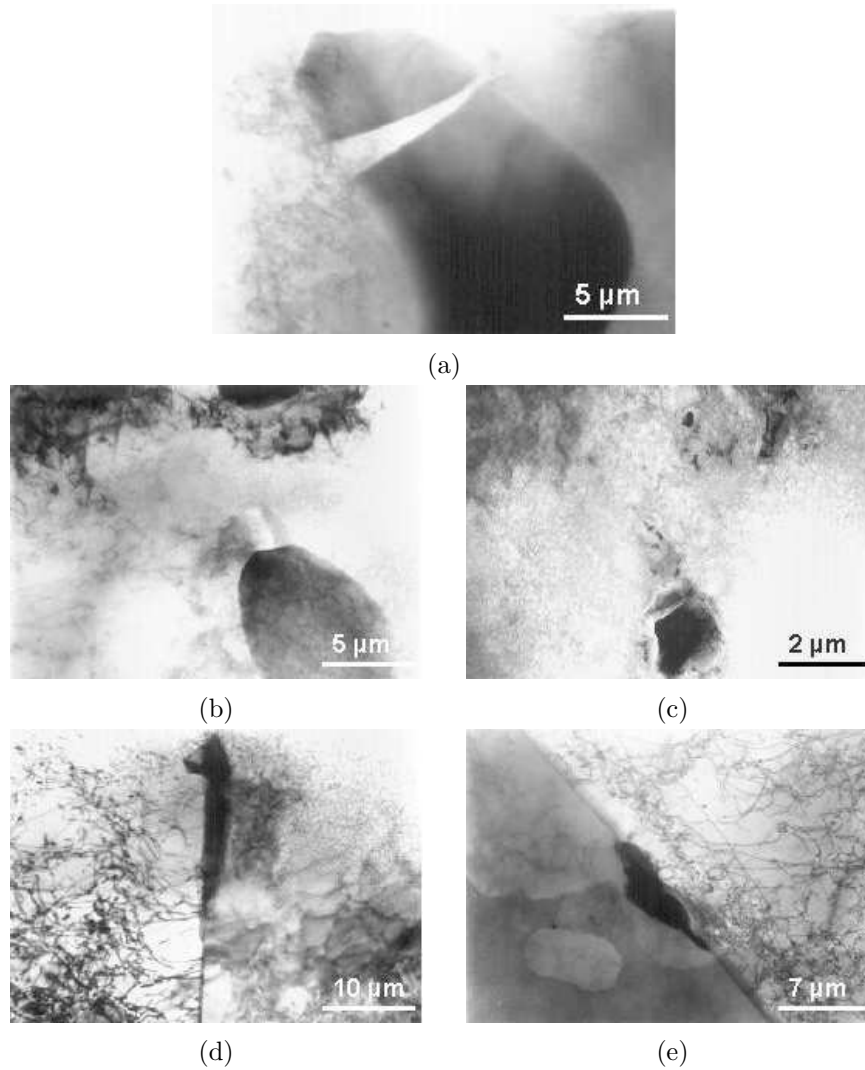


Figure 2.7 – TEM micrographs of samples close to the surface defects A locations: (a-b) AlFeSi cracked particles and (c-e) pure silicon inclusions.

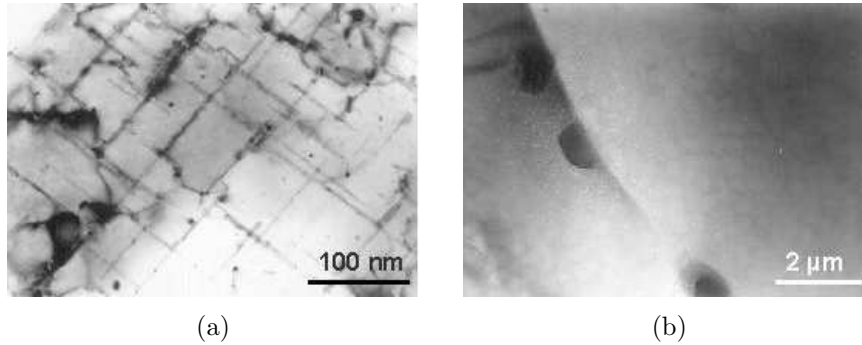


Figure 2.8 – TEM micrographs of samples close to the surface defects B locations: evidence of Mg_2Si precipitations.

2.4.2.a The DSC methodology

The DSC measurements were performed with a Perkin-Elmer DSC7. The theory of operation is based on the "power-compensated null balance" principle in which energy absorbed or released by the sample is compensated by adding or subtracting an equivalent amount of electrical energy to a heater located in the sample holder. Platinum heaters and thermometers are used in the DSC7 to measure energy and temperature. The continuum and automatic adjustment of heater power (energy per unit of time) necessary to keep the sample holder temperature identical to that of the reference holder, provides a varying electrical signal equivalent to the varying thermal behavior of the sample. This system is represented in Figure 2.9. This measurement is made directly in differential power units (mW), providing true electrical energy measurements of peak areas.

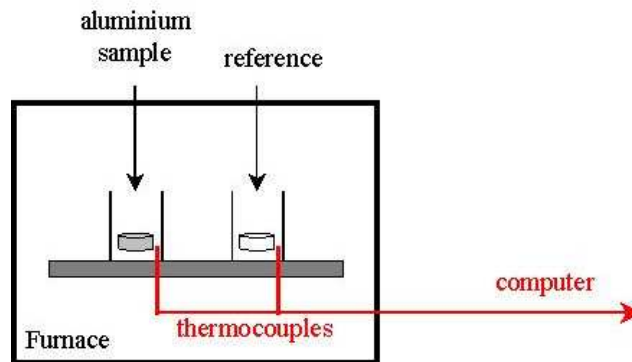


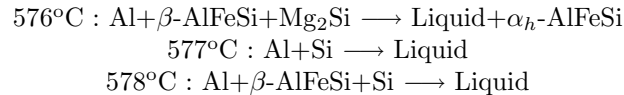
Figure 2.9 – Sketch of the power-compensated null balance principle of a DSC.

2.4.2.b DSC measurements

Experiments were carried out with a sample weight of approximately 53 mg. Graphite sample pans are used to allow a better thermal transfer up to high temperature. They have indeed extremely good heat transfer properties that yield to sharp transition curves and they allow to heat the samples at higher temperature than the aluminium melting point. The calibration of the DSC7 for temperature and energy is accomplished by running high purity standard and reference materials with known temperature and energy transitions. The data obtained after running these materials are used in programs to calibrate automatically the DSC. Potassium sulfate is used in this case, because of its transition point at $585 \pm 0.5^\circ\text{C}$ with a corresponding enthalpy transition of 33.26 J/g which allows an accurate calibration in the temperature range of interest. Temperature scans are made from 20°C to 640°C with heating rates of 5, 10, 20, 40, 60, 80, and $120^\circ\text{C}/\text{min}$. A baseline is obtained by fitting a polynomial on the points of the curve where no reaction is observed.

The tests aim at extrapolating the melting points onset temperature to the hypothetical null heating rate, in order to get the absolute melting temperatures. The scans related to samples taken at the surface defect A are presented in Figure 2.10(a). The area of interest of these scans is zoomed in in Figure 2.10(b).

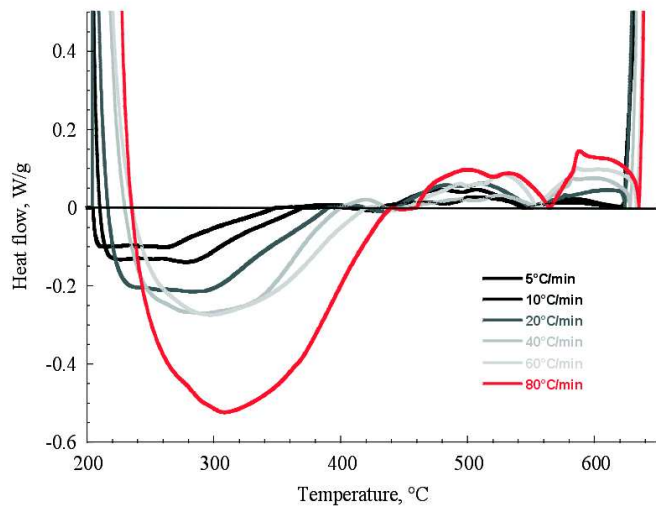
We can clearly see in these figures the different peaks around $580\text{-}590^\circ\text{C}$ corresponding to eutectic melting. This peak is clearly visible for the heating rates higher than $20^\circ\text{C}/\text{min}$ if we report now the melting onset temperatures on a graph versus the corresponding heating rates and we extrapolate this onset temperature to $0^\circ\text{C}/\text{min}$, we get directly the absolute melting temperature corresponding to this transformation. The result is shown in Figure 2.11. The eutectic melting temperature found is around 576°C . According to the literature, this temperature can correspond to different eutectic reactions as mentioned earlier:



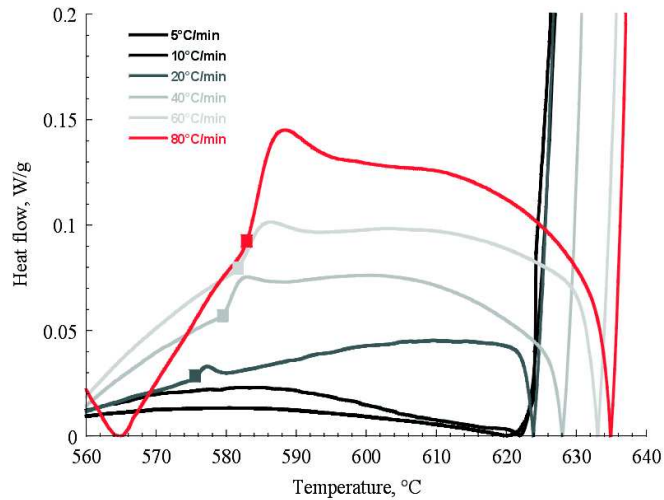
This confirms the presence of the $\beta\text{-AlFeSi}$ particles at the defect position as well as the presence of silicon (silicon inclusion or silicon agregate present in the vicinity of the intermetallic particle and resulting from diffusion of silicon during the $\beta\text{-to-}\alpha$ transformation).

2.5 First conclusions

The homogenization temperature and time and the ram speed are critical parameters for extrusion. In this study, the effect of these parameters is studied in



(a)



(b)

Figure 2.10 – (a) DSC scans of the samples taken at the surface defect A place with heating rates from 5 to 80°C/min, (b) zoom in the temperature range of interest.

a specific case in order to determine the microstructural origins of one surface defect. This is done using scanning electron microscopy (SEM), transmission electron microscopy (TEM), and differential scanning calorimetry (DSC) to al-

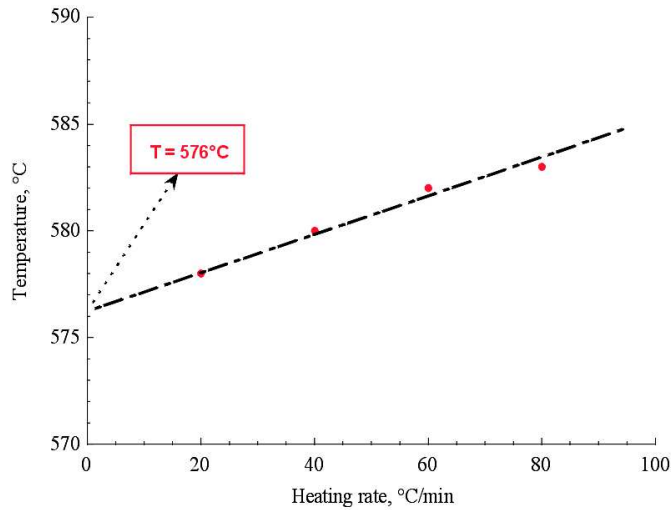


Figure 2.11 – Extrapolation of the eutectic melting onset temperature to infinite slow heating rate.

low an optimization of the process parameters. The analysis of the defects shows that:

1. Improving the heat treatment while using a higher homogenization temperature and a longer soaking time allows to shift the extrusion critical speed to higher value. We obtain a gain of 35% with a temperature increase of 15°C and a soaking period increase of 40%.
2. The surface defect A is shown to be due to the cracking of brittle β -AlFeSi and pure Si second phase particles and/or due to the incipient melting caused by the eutectic reaction $\text{Al} + \beta\text{-AlFeSi} + \text{Si} \rightarrow \text{liquid}$, (578°C).

Focusing on a general optimization of the extrusion process and on the modeling of the hot mechanical behavior and of the prediction of fracture during extrusion, the above results indicate that:

1. The homogenization temperature and time need to be increased. 585°C for 4h30 is surely necessary if we want to avoid the problem caused by the β -AlFeSi phase.
2. The temperature gradient between the billet and the container needs to be modified. It is generally accepted that a container temperature lower than the billet temperature prevents the billet surface to flow in the extrusion direction.

3. Two different origins of damage leading to fracture will be studied when predicting the hot fracture during extrusion: the first one is the breaking of the β -AlFeSi phase and the second one is a melting caused by the same phase in the presence of Si at temperature higher than 578°C.

3

Microstructure evolution during homogenization

Chapter 3

Microstructure evolution during homogenization

The effect of the homogenization treatment conditions on the evolution of surface quality has been presented in the previous part. In this chapter, the behavior of intermetallic compounds with various homogenization treatment conditions is examined through laboratory homogenization treatments tests. We will now focus on the effect of the homogenization conditions on the evolution of the microstructure and particularly on the β -to- α Fe-bearing intermetallics transformation for the ENAA 6060 and the ENAA 6005A alloys currently extruded by Sapa RC Profile.

3.1 Introduction

For architectural and structural applications, the ENAA 6xxx alloys of choice are mainly the ENAA 6060 and ENAA 6005A for Sapa RC Profile. Figure 3.1 shows a graphical comparison of the major alloy additions of these two aluminium alloys. ENAA6005A contains a higher level of addition elements, and an excess of silicon to increase the aging response.

The extrudability (hot deformation capability) of AlMgSi alloys depends on many factors, including chemical composition and casting but is largely determined by the subsequent homogenization treatment the material receives. During extrusion, the material would preferably need to have its softest conditions. Usually, the surface problems are determined in these alloys by the interaction between the matrix and the second phases precipitates such as Mg_2Si and AlFeSi system inclusions. The distribution and the type of intermetallic

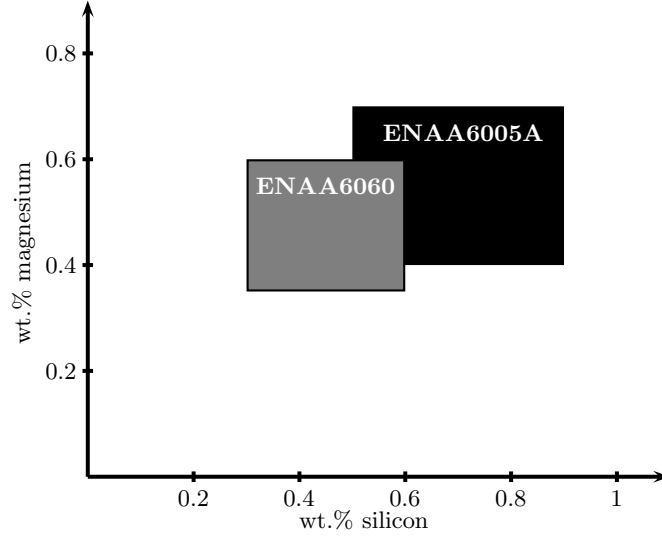


Figure 3.1 – Graphical representation of ENAA6060 and ENAA6005A chemistry limits.

compounds are important to the surface quality of extruded aluminium alloys.

During the homogenization process the transformation of the brittle plate-like β -AlFeSi phase into the more rounded α -AlFeMnSi phase takes place. The β -AlFeSi phase influences the deformation of the material in a negative way. Most producers claim that they need a transformation rate of at least 90 percent to avoid surface problem at a reasonable extrusion speed. This transformation occurs as a slow rate, and appears to demand more homogenizing capacity than is required for the redistribution of magnesium and silicon. Furthermore, in alloys containing higher percentages of silicon, the required holding time is said to be longer since the silicon increases the stability of the β -AlFeSi phase. Small additions of manganese are reported to shorten the necessary homogenization time shifting the α -phase in the direction of lower iron/silicon ratios.

In order to analyze the extrusion quality of homogenized ENAA 6000 aluminium alloys, it is useful to have an accurate idea of the evolution of the microstructure during the homogenization process as well as an accurate method for the quantification of the amount of β -AlFeSi and α -AlFeSi particles inside the material. This β -to- α transformation is here quantitatively characterized using SEM in combination with EDS measurements and image analysis. We note here that the analysis performed by the company Sapa to study the β -to- α transformation is different. There, the samples are dissolved in absolute butanol at 117 °C. Then, the chemical composition, the structure, the shape

Alloy	Mg	Si	Fe	Mn	Al
ENAA 6060	0.49	0.43	0.22	0.02	balance
ENAA 6005A-1	0.56	0.59	0.20	0.04	balance
ENAA 6005A-2	0.50	0.62	0.19	0.10	balance

Table 3.1 – Chemical composition of the alloy (wt%) homogenized in laboratory.

and the size of the undissolved particles are determined by means of x-ray fluorescence and x-ray diffraction. This technique has not been selected in this case, because not controlled in our laboratory.

3.2 Materials and Experimental techniques

This section is dedicated to the presentation of the materials studied in this work and of the investigation methods employed to analyze and quantify the microstructure evolution during thermal treatments as well as the methods used to analyze the different extrusion surface defects. Materials in the as-cast and extruded states have been provided by Sapa RC Profile, Ghlin, Belgium.

3.2.1 Material

The alloys selected for this study are the commercial AlMgSi alloys: ENAA 6060 and ENAA 6005A. These alloys have been provided by Sapa RC Profile both as as-cast logs. They are chosen to examine the effect of the silicon and magnesium content as well as the effect of manganese additions on the homogenization quality. The nominal chemical compositions of the alloys studied here are given in Table 3.1.

The alloy ENAA 6060 is considered as a low to low-medium strength alloy. It has a very high extrudability and can be used for many applications. The use is quite varied due to the alloys good surface finish and excellent response to anodizing. Typical applications for dilute ENAA 6060 have been for profiles where shape is more important than strength. It can be used for light wall architectural sections as well as general purpose extrusions. Its advantage is that lower levels of Mg can be used which improves extrudability, but at the expense of mechanical properties. By increasing the level of excess Si, the mechanical properties are increased.

The alloy ENAA 6005A is a medium strength alloy with a moderate to a high excess of Si. The applications for which it is suited include profiles such as flag poles, ladder parts and light yacht mast sections. Alloy ENAA 6005A-2 contains more Mn additions than ENAA 6005A-1 in order to study the effect of this element on the kinetics of transformation of the intermetallic phases

during homogenization.

The as-cast materials are treated in a laboratory furnace. The homogenization treatment conditions for control of the nature of intermetallic compounds are as follows:

1. Temperature: 585°C and 600°C
2. Holding time: 0 minute to 300 minutes
3. Cooling method: water quenching

The level of transformation of the Fe-bearing inclusions from the β -AlFeSi phase to the α -AlFeMnSi phase is then observed and quantified with a combination of SEM and X-ray diffraction analysis as explained further.

3.2.2 Experimental techniques for microstructure analysis

3.2.2.a Scanning Electron Microscopy (SEM)

Scanning Electron Microscopy (SEM) is firstly used to study qualitatively the microstructure of the material in its initial state and after the homogenization treatments. This technique is used thanks to the good atomic number contrast which can exist between aluminium and iron. The back-scattered electron detector allows thus to obtain good information about the composition of the different phases in presence. The Fe rich particles are easily distinguished from the aluminium matrix. The samples are prepared with standard metallographic techniques. All the polishing is done on wet polishing papers to avoid particles from this paper from getting embedded in the soft aluminium matrix. This polishing on papers goes on until 1200 grit size. Following this, diamond suspension is used as abrasive medium. This is continued until 3 μm suspension. Finally, the polishing is carried out with 0.6 μm colloidal silica suspensions to get the required metallographic finish. The samples are then observed in an unetched condition.

3.2.2.b Quantification of the relative α -AlFeMnSi and β -AlFeSi fraction by SEM and EDS

The transformation of the intermetallic particles from the plate-like β -AlFeSi phase to the more rounded α -AlFeMnSi phase is quantitatively characterized. In order to use an accurate and systematic method of quantification, SEM is used in combination with EDS on polished samples, with a relatively high voltage of 20kV to improve the contrast between intermetallics and the aluminium matrix. Spot size during the EDS measurements is approximately 2 μm , which is in most cases larger than the size of the intermetallics. Therefore also some Al x-ray signal from the matrix is detected. 250 intermetallic particles randomly chosen were analyzed on each sample. Discrimination between

the α -Al₁₂(FeMn)₃Si and the β -Al₅FeSi particles and quantification is made on the S_{ratio} defined as

$$S_{ratio} = \frac{at.\%_{Fe} + at.\%_{Mn}}{at.\%_{Si}}. \quad (3.1)$$

The theoretical S_{ratio} of the α -Al₁₂(FeMn)₃Si and the β -Al₅FeSi is equal to 3 and 1 respectively. In order to eliminate particles which might be incorrectly identified as α -Al₁₂(FeMn)₃Si or β -Al₅FeSi intermetallics, the particles for which the X-ray intensities of minor elements such as Ti, V, Cr, Cu and Pb were higher than 10% of one of the intensities of Si, Fe or Mn, are rejected. Also, particles with relative intensities of Si, Mn and Fe below the noise level are eliminated. The non-rejected particles are considered to be α -Al₁₂(FeMn)₃Si or β -Al₅FeSi.

In order to quantify the β -to- α transformation, we define a critical S_{ratio} , called S_{crit} . If $S < S_{crit}$, the particle is considered to be a β -Al₅FeSi and otherwise to be a α -Al₁₂(FeMn)₃Si. Having specified the classification criteria we can now analyze the degree of transformation. The true relative intermetallic α -Al₁₂(FeMn)₃Si fraction is defined as

$$f_{\alpha} \equiv \frac{n_{\alpha}}{n_{\alpha} + n_{\beta}} \quad (3.2)$$

where n_{α} and n_{β} are the total number of α -Al(FeMn)Si and β -AlFeSi particles respectively. The true relative fraction of β -AlFeSi is equal to $f_{\beta} = 1 - f_{\alpha}$.

Now, we want a close estimate of these true relative fractions from the experimental measurements. To get an accurate estimate of the true α -Al(FeMn)Si fraction transformed, the following procedure is applied [53]. First, the distribution of the parameter S_{ratio} is measured for two calibration samples containing purely α -Al(FeMn)Si (reference α) and purely β -AlFeSi (reference β) respectively. The value of the critical parameter S_{crit} for the allocation of α or β particles is chosen such that for the error made by incorrectly assigning α -Al(FeMn)Si as β -AlFeSi particles in the reference sample α is equal to the error made by incorrectly assigning β -AlFeSi as α -Al(FeMn)Si particles in the reference sample β .

For this purpose, the apparent relative α fractions, $f_{\alpha \text{ apparent}}$, are determined by varying the S_{crit} parameter. The error made by incorrect assignment in the reference sample α is expressed by

$$\Delta f_{\alpha} = 1 - f_{\alpha \text{ apparent}}. \quad (3.3)$$

The same procedure is followed for the reference sample β . It is clear that increasing the value of S_{crit} reduces the error made by incorrect allocation for the reference sample β , whereas at the same time it increases the error made

for the reference sample α . Finally, the correct critical parameter S_{crit} for an optimal allocation of the different intermetallics is offered by the value which equalizes the errors made for both reference samples.

3.2.2.c Measurements of the intermetallics shape by Image analysis (IA)

An image analyzer program named *Visilog* is used to get information on the evolution of the intermetallic particles shape during the homogenization treatments. For each polished sample, five pictures obtained by SEM at a magnification of 500x are digitized and then analyzed. We measure the Feret diameters of the different particles under varying angles and the particles surface. The Feret diameter is the length of a straight line which passes through the gravity center of the particle and intercepts its boundaries. These data allow us to get the length (maximum Feret diameter) and the width (minimum Feret diameter) of the particles and their mean aspect ratio (width/length).

The first step in such an analysis is to build a binary image which is coded on a single bit with two associated colors: blue (=1) for the objects of interest, black (=0) for the other parts of the image. In practice, we have to determine a brightness threshold in order to allow the program to distinguish the bright intermetallics from the dark aluminium matrix. This is a non-objective step depending in particular on the brightness of the initial SEM picture and which can have a significant impact on the results arising from this analysis. Nevertheless, all these parameters are kept constant for all the studied samples.

3.3 Results

As a first step of this study and before the quantification of the β -to- α transformation, the microstructural state is simply observed and characterized thanks to SEM observations. This investigation is presented here in order to give an idea of the microstructure evolution during homogenization.

3.3.1 SEM investigations of the microstructure evolution

Figure 3.2 shows the as-cast microstructure of the investigated billets. The typical as-cast structure of ENAA 6060 and ENAA 6005A consists of a mixture of β -AlFeSi and α -AlFeMnSi intermetallic distributed at cell boundaries, connected sometimes with coarse Mg_2Si , and a solid solution within the cells. Additionally, small round eutectic particles can also be observed inside grains. Clear differences between the β -AlFeSi and α -AlFeMnSi phases are seen concerning their sizes and their shapes.

These as-cast samples here contain mainly elongated β -AlFeSi particles. Both

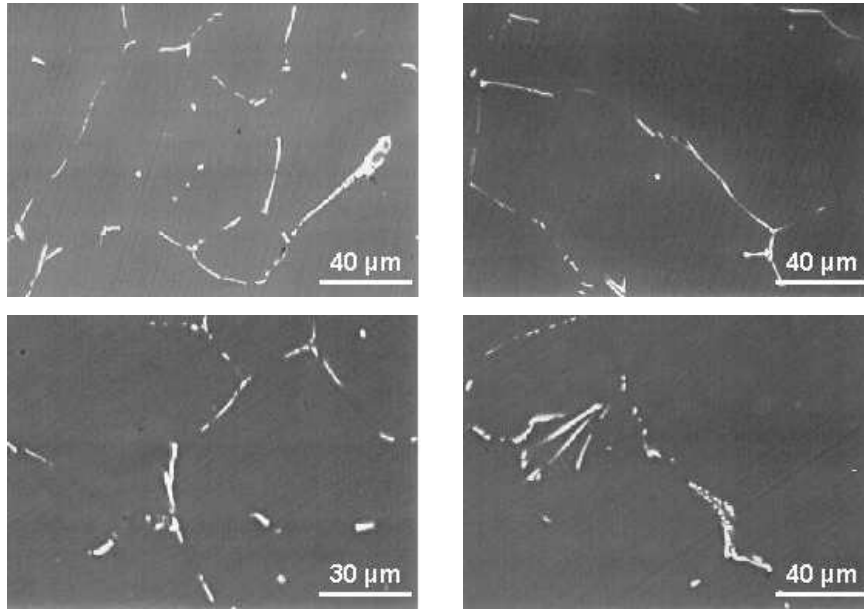


Figure 3.2 – Various SEM micrographs showing β intermetallic β -AlFeSi particles in as-cast AlMgSi alloys.

type of alloys, ENAA 6060 and ENAA 6005A, present similar microstructure. This hard, eutectic phase severely restricts hot workability and must be modified during homogenization heat treatment prior to extrusion.

As expected, during homogenization, one can clearly observe in Figure 3.3 that the plate-like intermetallic break up into necklaces of smaller particles which get rounder and rounder as long as the homogenization time increases. The effect of homogenization holding time on the evolution of AlFeSi particles is shown in Figure 3.3 for a homogenization temperature of 585°C with the alloy ENAA 6060.

After a homogenization of 120 minutes at 585°C, the break-up and spheroidization of the iron phases are already clearly observed even if we can still distinguish the grain boundaries distribution and the orientation of the parent β -phase. The long particles located on the grain boundaries in the as-cast structure break down to smaller ones. We can also observed that the particles are getting smaller and rounder with an increase of the homogenization holding time. Furthermore, segregations of Mg and Si seem to be eliminated during the heat treatment at high temperature slightly above the alloy solvus.

Figure 3.4 presents the micrographs of the microstructure evolution of the

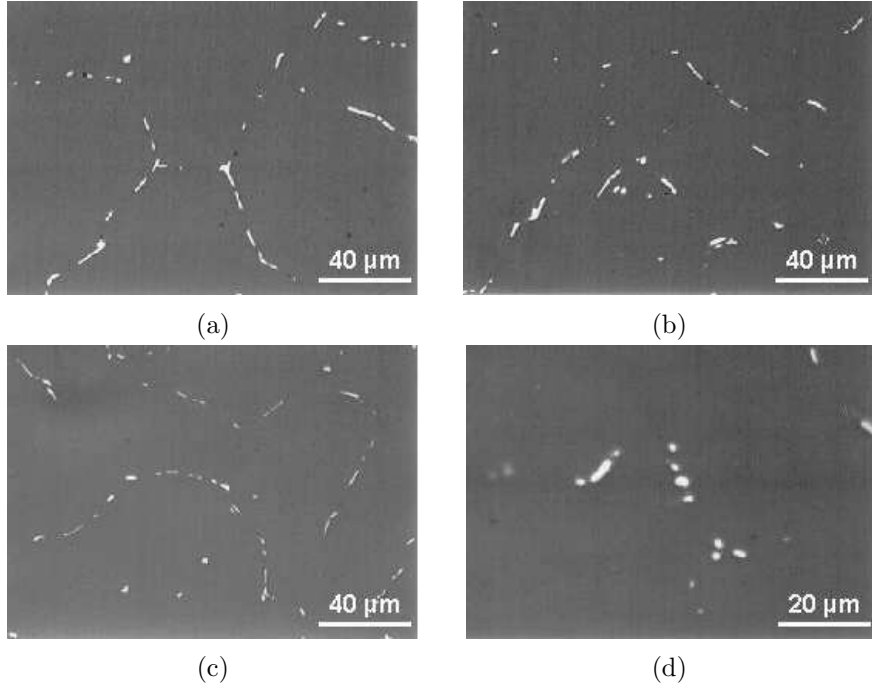


Figure 3.3 – Microstructure of the ENAA 6060 alloy after homogenization at 585°C: (a) 120 minutes, (b) 180 minutes, (c) 240 minutes, (d) 300 minutes.

ENAA 6060 alloys during a homogenization at 600°C. In this case, the same observations can be made, but with a large increase of the intermetallic transformation kinetics. The particles are indeed already short and rounded even after 60 minutes.

Similar conclusions are made for the aluminium alloy ENAA 6005A, but with a difference in kinetics. The higher level of silicon in this alloy makes the iron phase transformation slower. Nevertheless, this effect will be more explicitly quantified in the next section.

3.3.2 Quantification of the microstructure evolution

The transformation of the intermetallic particles from the plate-like β -AlFeSi phase to the more rounded α -AlFeMnSi phase is studied here. Figure 3.5 shows the x-ray relative intensities I_{Fe} and I_{Si} versus I_{Al} of the particles in an as-cast sample of the ENAA 6060 and in a sample of the same alloy homogenized for 180 minutes at 585°C. Figure 3.5(a) clearly shows that the ratio of I_{Fe} and I_{Si} is approximately unity, which corresponds to the β -AlFeSi stoichiometry.

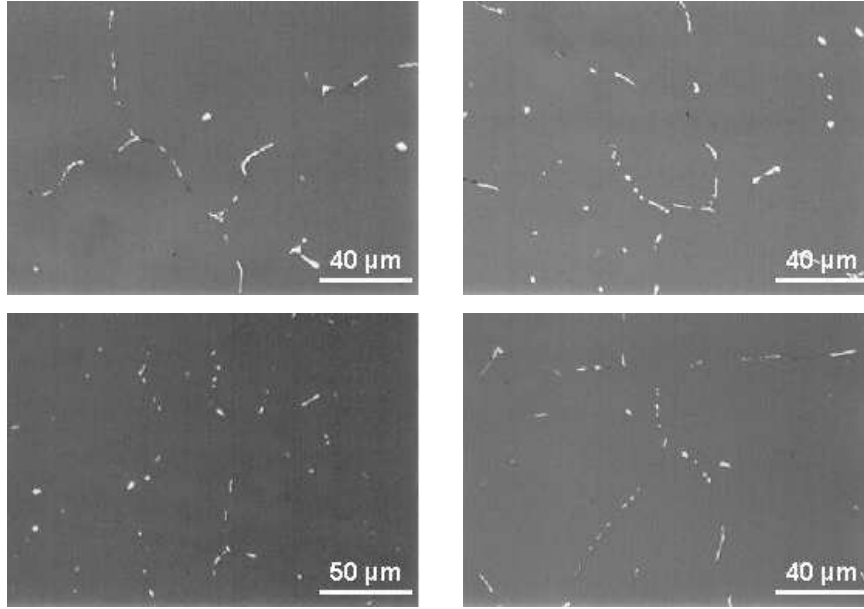
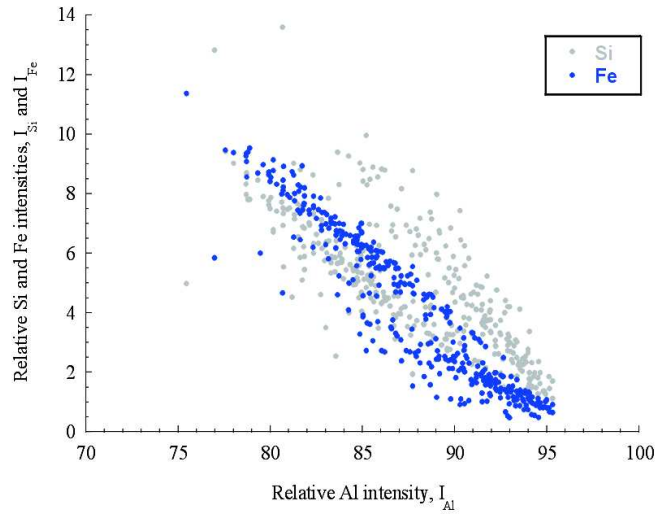


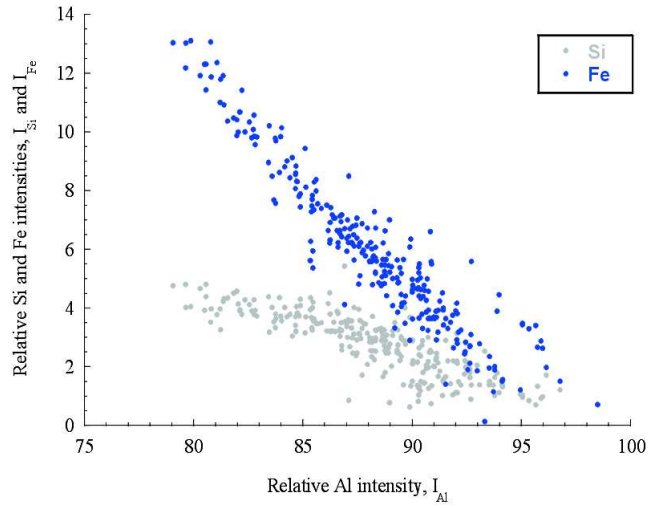
Figure 3.4 – Microstructure of the ENAA 6060 alloy after homogenization at 600°C: (a) 30 minutes, (b) 60 minutes, (c) 90 minutes, (d) 120 minutes.

Figure 3.5(b) shows the same relative intensities of the sample homogenized. The ratio between I_{Fe} and I_{Si} is closer to three in this case, which corresponds to a good transformation of the intermetallic compounds to the α -AlFeMnSi phase. This previous results give important information of the homogenization quality, but not really in a quantitative way.

The transformation of the intermetallic particles from the plate-like β -AlFeSi phase to the more rounded α -AlFeMnSi phase is quantitatively characterized by following the methodology that is explained previously in this chapter. At least 250 intermetallic particles randomly chosen are analyzed on each sample. Discrimination between the α -Al₁₂(FeMn)₃Si and the β -Al₅FeSi particles is made on the S_{ratio} defined as eqn. (3.1). The theoretical S_{ratio} of the α -Al₁₂(FeMn)₃Si and the β -Al₅FeSi is equal to 3 and 1 respectively. For this purpose, we defined a critical S_{ratio} , S_{crit} . If $S < S_{crit}$, the particle is considered to be a β -Al₅FeSi and otherwise to be a α -Al₁₂(FeMn)₃Si. Having specified the classification criteria we can now analyze the degree of transformation. In a first step, the several particles are analyzed and are discretized in different classes of S_{ratio} values. The distribution of the particles stoichiometries is showed in Figure 3.6 for the as-cast sample of ENAA 6060, for a fully homogenized sample of the same alloy (24h at 585°C), and for samples homog-



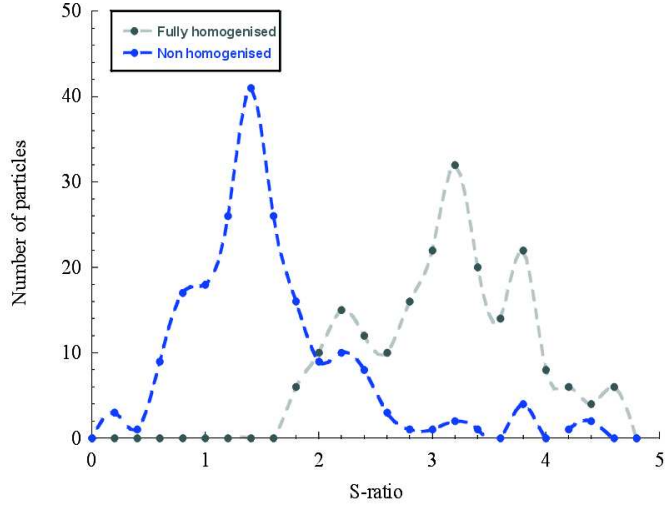
(a)



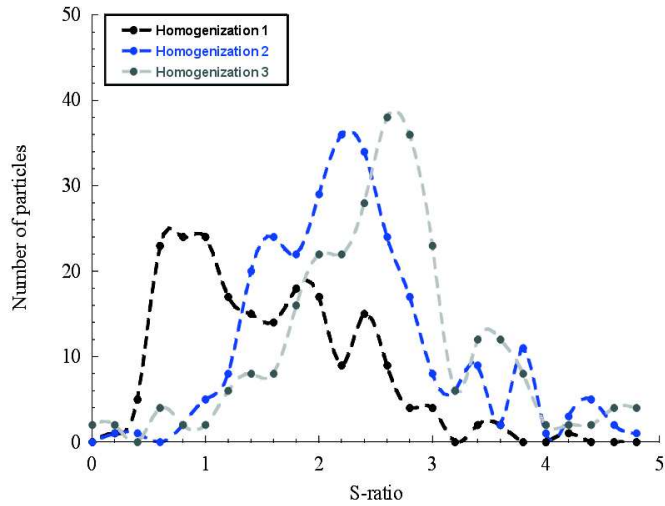
(b)

Figure 3.5 – Assembly of EDX measurements on (a) as-cast sample and (b) homogenized sample 3h30 at 585°C.

enized 150 minutes, 240 minutes and 300 minutes at 585°C. The S_{ratio} values



(a)



(b)

Figure 3.6 – S-ratio distribution of iron bearing intermetallic in ENAA 6060 for (a) an as-cast sample and a fully homogenized sample, (b) for samples homogenized 150 minutes, 240 minutes and 300 minutes at 585°C.

are close to 1 for the as-cast sample, but are divided in different classes around

3 in the fully homogenized sample. Figure 3.6(b), which shows the distribution of S-ratio value at different homogenized states indicates a clear evolution of the mean S_{ratio} value from 1 to 3.

Now, to get a close estimate of these true relative fractions from the experimental measurements, we apply the method exposed previously. The apparent relative α fractions, $f_{\alpha \text{ apparent}}$, are determined by varying the S_{crit} parameter. It is clear that increasing the value of S_{crit} reduces the error made by incorrect allocation for the reference sample β , whereas at the same time it increases the error made for the reference sample α . Figure 3.7 represents the results of the SEM/EDX analysis based on the measured S_{ratio} .

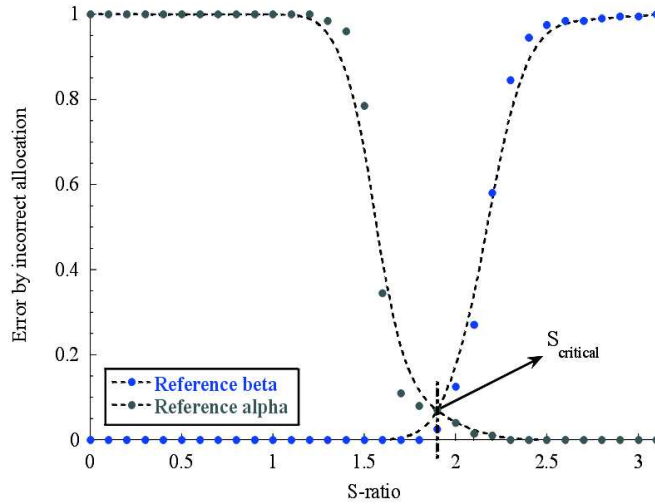


Figure 3.7 – Absolute error of $f_{\alpha \text{ apparent}}$ made by incorrect allocation of α -AlFeMnSi or β -AlFeSi particles, as a function of the critical S_{ratio} , called S_{crit} .

The value Δf_{α} (absolute error of $f_{\alpha \text{ apparent}}$ made by incorrect allocation of α -AlFeMnSi or β -AlFeSi particles) is plotted as a function of S_{crit} for the alloy ENAA 6060 (a) and ENAA 6005A (b). One curve corresponds to the as-cast sample whereas the second curve corresponds to the fully homogenized sample. The correct critical parameter S_{crit} for an optimal allocation of the different intermetallics is offered by the value which equalizes the errors made for both reference samples. These results show that the minimised Δf_{α} values are found for $S_{crit} = 1.8$ and $S_{crit} = 1.91$ for the alloys ENAA 6060 and ENAA 6005A respectively.

Using these values for S_{crit} , it is now obvious to quantify the β -to- α transformation of the intermetallic phases. The different kinetics are presented in Figure 3.8 and 3.9. These figures present the evolution of the α particles ratio for the three alloys studied in this chapter at 585°C and 600°C respectively.

We can observe different things. Firstly, the as-cast sample of the ENAA 6060 alloy contains more α -AlFeMnSi particles than the equivalent sample in ENAA 6005A (more or less 20% for 10%). The transformation kinetic for the ENAA 6060 is more rapid than the ENAA 6005A, but we see that an increase in the manganese content in this last alloy can help the transformation a lot, bypassing even the evolution in the ENAA 6060 alloy after 200 minutes. We can also observe that an increase of the homogenization temperature by only 15°C to 600°C allows to nearly double the transformation kinetics of the intermetallic compounds.

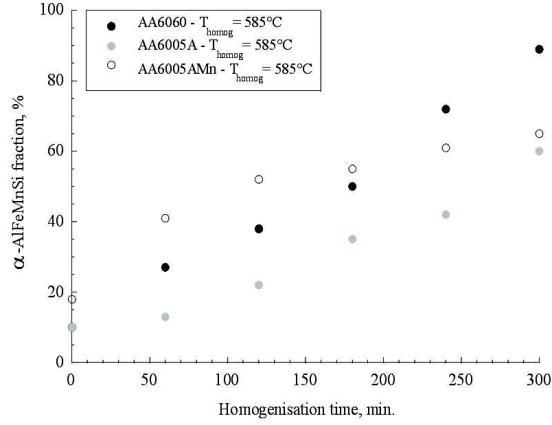
The image analyzer *Visilog* is used to get information on the evolution of the intermetallic particles shape during the homogenization treatments. The length (maximum Feret diameter) and the width (minimum Feret diameter) of the particles and their mean aspect ratio (width/length) have been measured.

Figure 3.9 presents the evolution of the mean aspect ratio of the AlFeSi particles for the different alloys at both homogenization temperature used. The conclusions are quite similar as for the evolution of the α content. The alloy ENAA 6060 presents less elongated particles in the as-cast state than the alloy ENAA 6005A and the spheroidisation in the 6060 is more rapid than in the ENAA 6005A excepted for the ENAA 6005A containing more manganese which presents more rounded particles than the other alloy after 200 minutes at 585°C or after 130 minutes at 600°C. The mean initial aspect ratio, W , of the AlFeSi particles are approximately 0.11, 0.09 and 0.2 for the alloys ENAA 6060, ENAA 6005A-1 and ENAA 6005A-2 respectively.

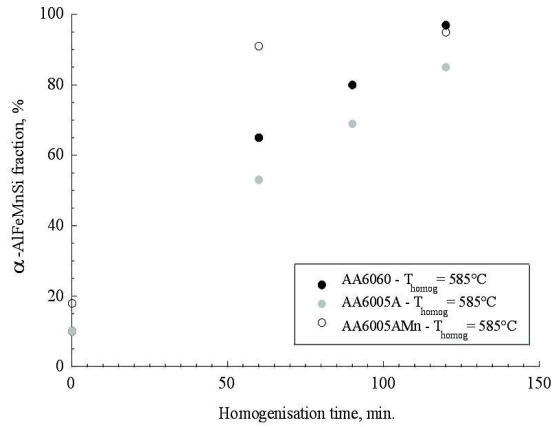
3.4 Conclusions

The main information arising from the experimental investigation described in this chapter is the kinetics of the β -to- α transformation and the evolution of the particles shape during this thermal treatment. On the basis of these two microstructural parameters, it is possible to compare the influence of the homogenization parameters and of the alloy composition.

These as-cast ENAA 6xxx samples contain mainly elongated β -AlFeSi particles which severely restrict hot workability and is thus modified during homogenization heat treatment prior to extrusion. During homogenization, the plate-like intermetallic particles break up into necklaces of smaller particles which get increasingly round as the homogenization time increases.



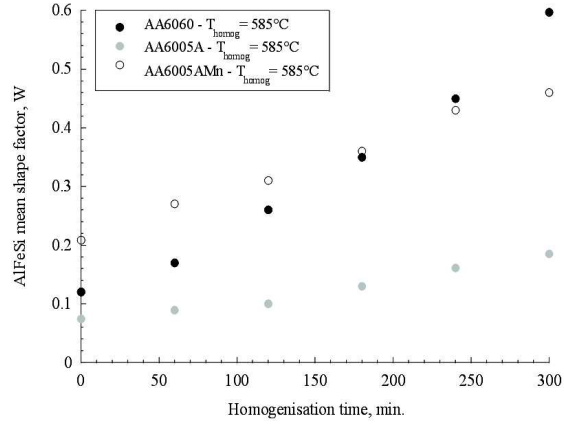
(a)



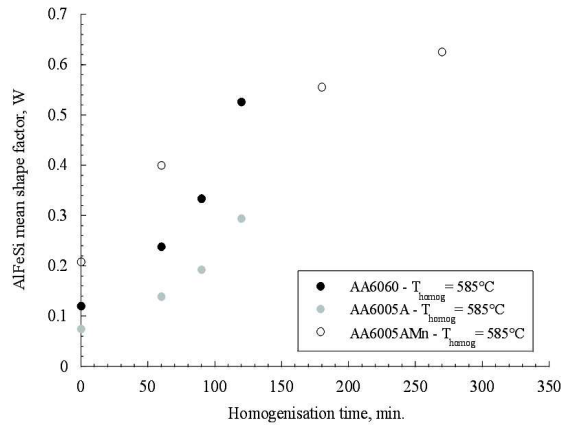
(b)

Figure 3.8 – Evolution of the α -AlFeMnSi particles ratio during homogenization (a) at 585°C and (b) at 600°C for the three studied alloy.

The quantification of the transformation of the intermetallic particles from the plate-like β -AlFeSi phase to the more rounded α -AlFeMnSi phase is studied here thanks to discrimination between the α -Al₁₂(FeMn)₃Si and the β -Al₅FeSi



(a)



(b)

Figure 3.9 – Evolution of the intermetallic particles mean aspect ratio during homogenization (a) at 585°C and (b) at 600°C for the three studied alloy.

particles with the S_{ratio} . Different behaviours are observed. The kinetics of the AlFeSi phases transformation are different for the different alloys. The first difference lies into the α -AlFeMnSi particles content of the as-cast alloys.

The ENAA 6060 contains already more α -AlFeMnSi than the as-cast sample of ENAA 6005A (more or less 20% and 10% respectively). Then, during homogenization, the transformation kinetics for the ENAA 6060 is more rapid than for the ENAA 6005A with low level of Mn. Nevertheless, an increase in the Mn content in this last alloy accelerates the transformation a lot, bypassing even the evolution in the ENAA 6060 alloy after 200 minutes at 585°C. We can also observe that an increase of the homogenization temperature by only 15°C (up to 600°C) allows a reduction of the homogenization time of 50% at least.

The evolution of the shape of the AlFeSi particles has also been measured after various homogenization treatments. This parameters is very important in terms of fracture initiation (more important than the stoichiometry of the particles even though these two parameters are linked). The conclusions concerning the kinetics of spheroidization of the particles are quite similar as for the evolution of the α content. The alloy ENAA 6060 presents less elongated particles than the alloy ENAA 6005A even in the as-cast state (the mean initial aspect ratio, W , of the AlFeSi particles is approximately 0.11, 0.09 and 0.2 for the alloys ENAA 6060, ENAA 6005A-1 and ENAA 6005A-2 respectively) and the spheroidisation of these intermetallics is more rapid for the ENAA 6060 alloy than for the ENAA 6005A. We see, however, an exception for the alloy ENAA 6005A containing more manganese. This last one presents more rounded particles than the other alloy after 200 minutes at 585°C or after 130 minutes at 600°C. All these results give us already many indications concerning the difference in mechanical behavior which will exist between the two types of alloys. The improvement of resistance to cracking being dependent on the contents in intermetallic particles, it will evolve in a very different way during the various heat treatments for both alloys.

4

Growth and coalescence of
penny-shaped voids

Chapter 4

Growth and coalescence of penny-shaped voids

As we will see in the next chapter, damage at room temperature in the 6xxx aluminium alloys occurs through the nucleation of relatively flat voids that then grow and coalesce. A theoretical study has been made to address this specific mechanism in details. From a generic viewpoint, the goal is to better understand this mechanism and to develop and validate a constitutive model for the next chapter. This chapter has thus a particular state in the thesis as it does not directly link with the extrusion process nor with the aluminium alloys. The chapter is almost identical to the paper submitted by D. Lassance, F. Scheyvaerts and T. Pardoen [57].

The growth and coalescence of penny-shaped voids resulting from particle fracture is a common damage process for many metallic alloys. A three steps modeling strategy has been followed to investigate this failure process. Finite element void cell calculations involving very flat voids surrounded or not by a particle have been performed in order to enlighten the specific features of a damage mechanism starting with initially flat voids with respect to more rounded voids. An extended Gurson-type constitutive model supplemented by micromechanics-based criteria for both void nucleation and void coalescence is assessed for the limit of very flat voids towards the FE calculations. The constitutive model is then used to generate a parametric study of the effects of the stress state, the microstructure and the mechanical properties on the ductility. Based on these results, a simple model for the ductility is finally proposed.

4.1 Introduction

Materials scientists are usually interested in capturing the effect of complex microstructure in order to guide the processing of better alloys and composites. If the methodology of the micromechanics or local approach of ductile fracture has not much evolved over the years (i.e. from the contributions by McClintock, Rice, Needleman, Pineau, Gurson, Argon, Embury, Hutchinson, Tvergaard, and coworkers [62, 63, 79, 78, 38, 14, 13, 58, 21, 65, 23, 90, 91, 66, 5, 19, 20]), new efforts are currently made to incorporate more physics into the models, which will obviously have also a positive impact on the structural integrity analysis (e.g. see a selection of contributions in recent years [10, 11, 75, 12, 43, 47, 35, 83, 73, 80, 33, 30, 88, 46, 71]). The goal of the present study is to contribute to that effort by addressing in details the specific problem of the growth and coalescence of initially penny-shaped voids resulting from the fracture of particles.

At room temperature, the nucleation of voids in metallic alloys occurs either by the decohesion or the fracture of second phase particles, e.g. [13, 61]. In the case of elongated particles when the main loading axis is perpendicular to the long diameter, particles separation from the matrix by decohesion is frequently observed and, when loaded parallel to the long diameter, particles are usually more prone to fracture, sometimes into several fragments. No general trends can be formulated for equiaxed particles: the competition between decohesion and particle fracture is not only governed by the fracture properties of the interface and of the particle but also by the stress state and the accompanied level of the plastic strains, see [81, 61, 7]. When nucleation results from particle fracture, the void is initially extremely flat. Partial decohesion of particle also lead to flat voids, e.g. [22]. The sequence of damage events, starting with the nucleation of flat voids by particle fracture, is represented in Figure 4.1.

With plastic deformation, the initially flat void opens and becomes more and more rounded. At some point, strong interactions take place between neighboring voids leading to the localization of the plastic flow within the ligament, which constitutes the onset of the void coalescence process. Aluminium alloys with elongated intermetallic particle (such as dual or multiphase steels with hard brittle martensite islands, ferritic steels with long MnS inclusions, cast Al alloys with brittle Si particles, Ti α/β alloys with a platen type α -phase, and metal matrix composites) exhibit this fracture sequence starting with initially flat voids.

State-of-the art models rely on a simple approach which consists in assimilating the initially flat void to an equivalent spherical void, leading to the definition of an effective initial porosity, e.g. [45]. This approach neglects the particular initial shape of the void which affects both the void growth rates and, later, the fulfillment of the coalescence condition. As a matter of fact, when the void

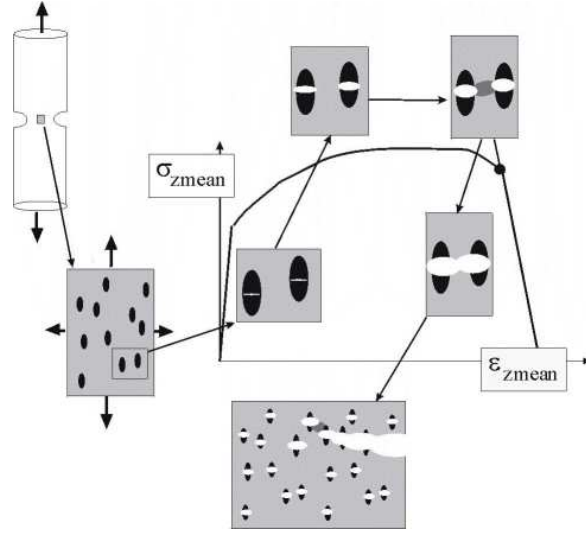


Figure 4.1 – Sequence of damage mechanisms starting with particle fracture, followed by a stable void growth stage from an initially very flat geometry, void coalescence, and crack propagation; the sequence is related to the overall stress strain curve associated to a representative volume of material.

is initially very flat, the concept of initial porosity is, from a physical point of view, not well suited: the initial state of damage is much better characterized by the *relative void spacing*. The limits of validity of the concept of effective porosity have not been systematically quantified. This is an important issue considering the large number of systems that exhibit this type of damage sequence. More importantly, the particular features associated to the growth and coalescence of voids from an initial penny shape are up to now simply not well understood.

In this work, the response of elastoplastic solids involving initially penny-shaped voids, resulting either from particle fracture, from partial decohesion, from total decohesion of flat particles, or from other damage mechanisms (processing defects, fatigue microcracks) is studied in the case of spheroidal void geometry and axisymmetric loading conditions. As shown in Figure 4.2, the material is idealized by a periodic packing of simple unit cells containing spheroidal particles of volume fraction f_p , aspect ratio $W_p = R_{pz}/R_{px}$, and particle anisotropy distribution parameter $\lambda = L_{pz}/L_{px}$ with the symmetry axis z oriented parallel to the main loading direction. The fracture of the particle gives rise to spheroidal voids characterized by the three non dimensional quantities : $W_0 = R_{0z}/R_{0x}$, $\lambda_0 = \lambda_p$ and initial porosity f_0 . The initial relative void spacing $\chi_0 = R_{0x}/L_{0x}$

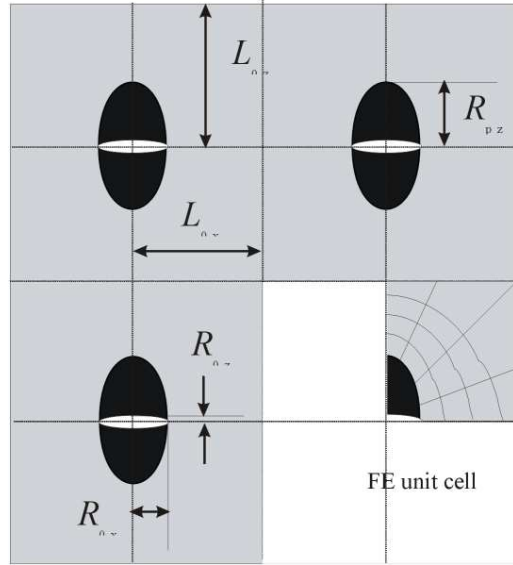


Figure 4.2 – Model material consisting of a periodic packing of unit cells involving one particle. The unit cell is approximated by a cylindrical cell to simplify the numerical analysis.

is related to these three quantities through the following expression:

$$\chi_0 = \frac{R_{0x}}{L_{0x}} = \left(\frac{R_{0x}^3}{L_{0x}^3} \right)^{\frac{1}{3}} = \left(\frac{R_{0x}^2 R_{0z} R_{0x} L_{0z}}{L_{0x}^2 L_{0z} R_{0z} L_{0x}} \right)^{\frac{1}{3}} = \left(\frac{f_0}{\gamma} \frac{\lambda_0}{W_0} \right)^{\frac{1}{3}} \quad (4.1)$$

where γ is a geometric factor which depends on the arrangement of voids : $\gamma = \pi/6 = 0.523$ for a periodic simple cubic array, $\gamma = \sqrt{3}\pi/6 = 0.605$ for a periodic hexagonal distribution and $\gamma = 2/3 = 0.666$ for a void surrounded by a cylindrical matrix (note that for particle fracture along the equatorial plane, $R_{px} = R_{0x}$). The initial void volume fraction for a single void located on the equatorial plane of the particle is related to the particle volume fraction through

$$f_0 = \frac{W_0}{W_p} f_p \quad (4.2)$$

Hence, the initial relative void spacing χ_0 also writes

$$\chi_0 = \left(\frac{f_p}{\gamma} \frac{\lambda_p}{W_p} \right)^{\frac{1}{3}} \quad (4.3)$$

A J_2 isotropic hardening elastic-viscoplastic response is assumed for the matrix, characterized by the following representation in uniaxial tension

$$\frac{\sigma}{\sigma_0} = \frac{E}{\sigma_0} \epsilon \quad \text{for } \sigma < \sigma_0 \quad (4.4)$$

$$\frac{\sigma}{\sigma_0} = \left(1 + \frac{E}{\sigma_0} \epsilon^p\right)^n \left(1 + \frac{\dot{\epsilon}^p}{\dot{\epsilon}_0}\right)^m \quad \text{for } \sigma > \sigma_0 \quad (4.5)$$

where E is the Young's modulus, σ_0 is the initial yield stress, n is the strain hardening exponent, m is the strain rate sensitivity exponent, ϵ_0 is a reference plastic strain rate. The present paper will only focus on the limit of rate independent solids (i.e. $m \rightarrow 0$). The Poisson ratio of the matrix ν is always taken equal to 0.3. The particle is elastic with Young's modulus E_p and Poisson ratio ν_p equal to 0.3.

The main quantity of interest in this study is the ductility. There are several ways of defining ductility. This study addresses the attainment of a critical state of damage. For the sake of convenience, we will define the ductility as the strain corresponding to the onset of void coalescence. Defining the ductility as the final fracture strain would have been more appealing from a physical point of view. Nevertheless, these two "reference strains" are usually very close to each other: the strain at final fracture is rapidly attained after the onset of coalescence, at least under low to moderate stress triaxiality, see [72]. Furthermore, this definition avoids dealing with the complex problem of modeling the material response during coalescence. Even though models have been proposed for the damage evolution during void coalescence when final failure occurs by void impingement [11, 72], many metals involve fine scale micromechanisms that accelerate or interrupt the coalescence process for instance through the growth of a second population of voids, through microcleavages, or through localized shear banding within the ligament. The modeling of these micromechanisms is outside the scope of the present study.

A three-step modeling methodology has been followed:

Section 2 - unit cell calculations. Selected results obtained with finite element void cell calculations will be analyzed in order to better understand: (i) the damage evolution of voids which are initially flat; (ii) the effect of the surrounding particle on the void growth rate.

Section 3 - constitutive model. A constitutive model for the nucleation, growth and coalescence of voids is presented and assessed towards the void cell calculations for the limit of flat voids. This model is very similar to the model derived in [72], while introducing also the void nucleation stage. A first experimental validation of the application of the model to a material involving initially penny-shaped voids has been reported elsewhere [43].

Section 4 - parametric study and discussion. A parametric study emphasizing the couplings between the microstructure, the applied stress state, the flow properties of the matrix, and the critical stress for void nucleation is proposed. Special attention will be paid (i) to the occurrence of void coalescence under very low stress triaxiality conditions, which will turn out to be a specific feature of materials involving initially very flat voids and (ii) to the conditions for void nucleation controlled ductility versus void growth controlled ductility. A last subsection is devoted to a very simple, closed-form model for the ductility of materials exhibiting initially very flat voids.

4.2 Void cell calculations with initially penny-shaped voids

4.2.1 Numerical procedures

The unit cell calculations performed in this study follow a long history of finite element analyses of void growth in plastically deforming materials, initiated by the work of Needleman in 1972 [65], and pursued by many others [90, 91, 47, 88, 46, 72, 50, 41, 40, 96, 18, 86, 34, 32, 54, 72]. Figure 4.2 shows the unit cell used to simulate the growth and coalescence of initially penny-shaped voids under axisymmetric loading conditions.

For the sake of simplicity, a cylindrical unit cell is assumed. The validity of this assumption has been checked repetitively in the literature, e.g. [96, 54]. Owing to the symmetry of the problem, only one quarter of the cell is simulated. The periodic boundary conditions are enforced by keeping the outer cylinder and top surface straight and parallel to the z and x axis, respectively. The void nucleation step will not be considered in this study (see Faleskog et al. [32] for an example of FE cell calculations involving the fracture of particles, within the context of cleavage). The voids are thus considered to be present from the beginning of the loading, surrounded or not by a particle. Figure 4.3 presents example of meshes used for the cell calculation with and without the presence of a particle.

The general purpose FE code Abaqus [39] is used within a finite strain set up. Displacement rates \dot{U}_z and \dot{U}_x with $\dot{U}_z > \dot{U}_x$ are applied on the edges of the cell. The Riks method is employed to enforce a constant stress triaxiality ratio T which is defined as the ratio σ_h/σ_e where σ_h is the hydrostatic stress and σ_e is von Mises stress. The J_2 isotropic hardening elastic-viscoplastic response characterized by (4.4) and (4.5) is applied for the matrix material.

The overall stress and strain rates are directly computed from the reaction forces and the applied displacement rates. The porosity is calculated by subtracting, from the current volume of the cell, the sum of the current volume of

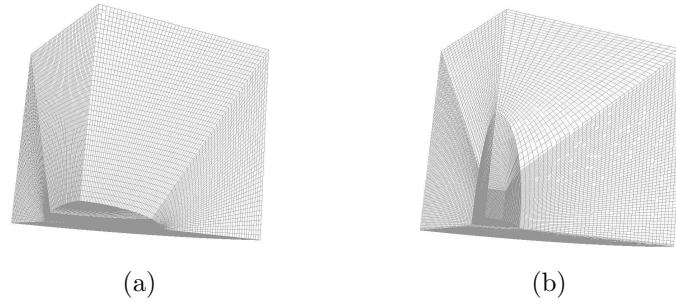


Figure 4.3 – Fine initial meshes used to model unit cell (a) without and (b) with the presence of a particle.

each solid element (accounting thus for the elastic volume change) and dividing by the current volume of the cell. This method, requiring some effort on the data post-processing, was preferred over the more simple and frequently used relationship proposed by Koplik and Needleman [50] which is too approximate when large volume fraction of particles are considered. The onset of void coalescence corresponds to a localization of the plastic deformation inside the ligament between the voids, see [72, 50]. It is thus detected by a sudden change in the mode of deformation: in one or two load increments, the transverse strain rate changes abruptly and becomes very small, especially at low stress triaxiality. The onset of void coalescence also leads to a marked change in the evolution of the porosity and void shape, as well as a drop in the load carrying capacity.

Very refined meshes are used at the tip of the flat void in order to capture the large strain gradients. Ideally, void remeshing should have been used to resolve the important mesh distortion near the tip of the flat void. Nevertheless, the mesh refinement studies, repeated for each set of calculations involving different initial geometries, have always lead to converged solutions. Several initial void shapes, void volume fractions, particle properties and stress triaxialities have been analyzed in order to provide a fairly general picture of the problem and a large basis for the assessment of the constitutive model.

4.2.2 Results of the unit cell calculations without particle

The first set of calculations does not involve particles. For the sake of generality in the presentation and discussion, we will consider that the voids are still surrounded by particles having elastic-plastic properties identical to the matrix material. The void (or particle) anisotropy distribution parameter $\lambda_p = \lambda_0$ is kept equal to 1. Three "virtual" volume fractions of spherical particles ($W_p = 1$) are considered : $f_p = 0.1\%$, 1% and 10% , which is similar to prescribing the

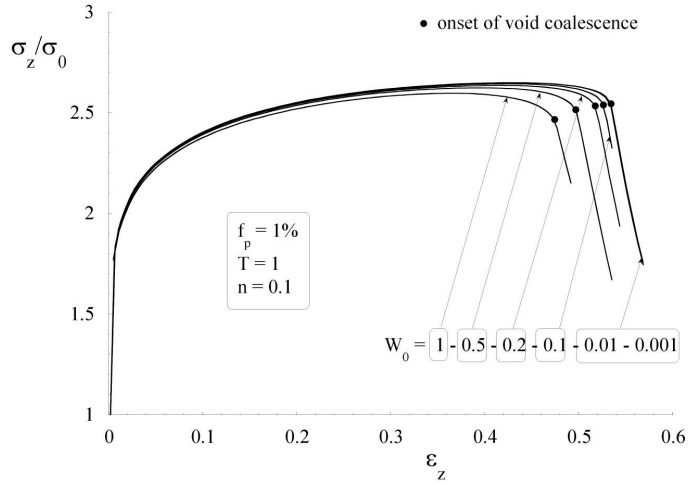
relative void spacing $\chi_0 = 0.114, 0.247,$ and $0.531,$ respectively. The initial void aspect ratio W_0 ranges between 0.001 and 2. The initial void volume fraction is given by (4.2). Figure 4.4 gathers the results obtained for $f_p = 1\%$ (a,b,c) and $f_p = 10\%$ (d,e,f) at a prescribed stress triaxiality equal to 1, in terms of (a,d) the overall stress - overall strain curves corresponding to the z direction, (b,e) the evolution of the porosity, and (c,f) the evolution of the void aspect ratio.

A stress triaxiality equal to 1 can be considered as an intermediate value between the low stress triaxiality of uniaxial tension ($T = 1/3$) and the high stress triaxiality of a highly constrained volume element, e.g. $T > 3$ in front of a crack tip.

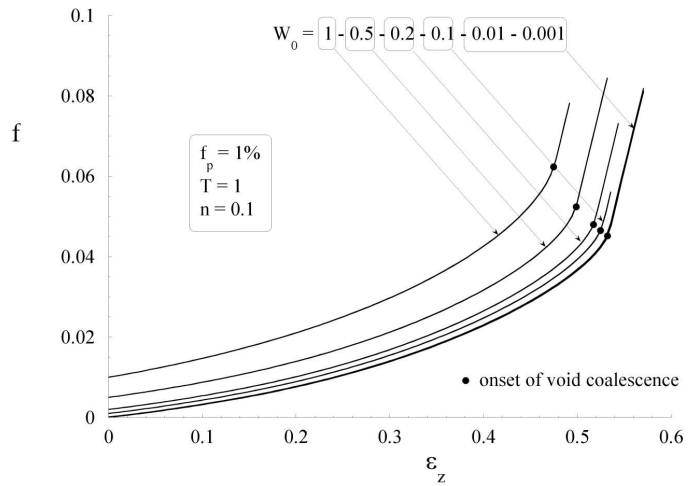
The most important result emerging from Figure 4.4 is that the evolution with straining of the overall stress, porosity, and void shape is independent of the initial void aspect ratio W_0 if W_0 is typically lower than 0.01. This shows that for flat voids, the key parameter controlling the damage evolution process is the relative void spacing χ_0 . By comparing Figure 4.4(a) and 4.4(d), it is clear that the assumption of taking the effective initial porosity as equal to the porosity associated to an equivalent spherical void is acceptable as long as the particle volume fraction is sufficiently low ($f_p = 1\%$) but not when the volume fraction is large ($f_p = 10\%$). The stress-strain curves, and the porosity and void shape evolutions are much more dependent on the initial void shape (when $W_0 > 0.1$) when $f_p = 10\%$ than when $f_p = 1\%$. The fact, for instance, that the peak stresses in Figure 4.4(d) are very much affected by the change of W_0 is explained by the large values of f_0 when $f_p = 10\%$ and $W_0 > 0.1$ (leading to $f_0 > 1\%$).

Figure 4.5 shows the variation of the ductility as a function of the initial void aspect ratio (a) for various volume fractions of particles f_p and a stress triaxiality T equal to 1, and (b) for various stress triaxialities and $f_p = 1\%$.

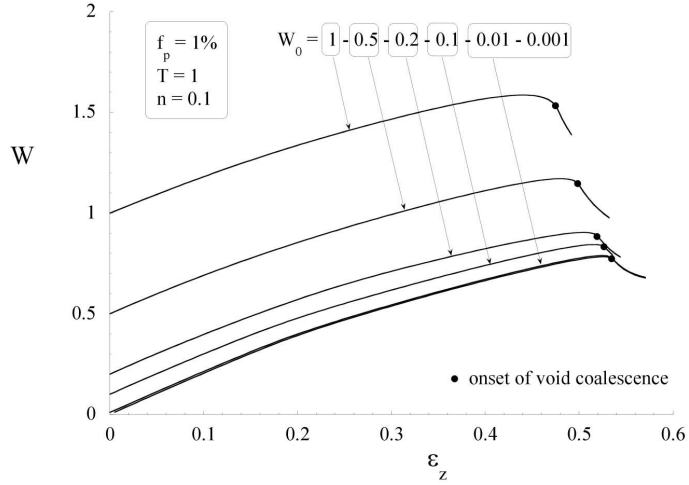
Figure 4.5(b) shows that the ductility is independent of W_0 whatever the imposed stress triaxiality as long as W_0 is sufficiently small. Note also that the ductility does not always decrease with increasing W_0 (and thus increasing f_0 proportionally). As discussed in the introduction, the definition of ductility as the strain corresponding to the onset of void coalescence can raise some discussion. For instance, the unloading slopes after the onset of coalescence for large f_p (see Figure 4.4(d)) are smaller at large W_0 than at low W_0 . This would indicate that, for a coalescence process by full void impingement, the ductilities defined on the final fracture strains would be closer than when defined at the onset of void coalescence. This effect is specific to the very large initial porosity analyzed in that example, which is not encountered in most industrial materials.



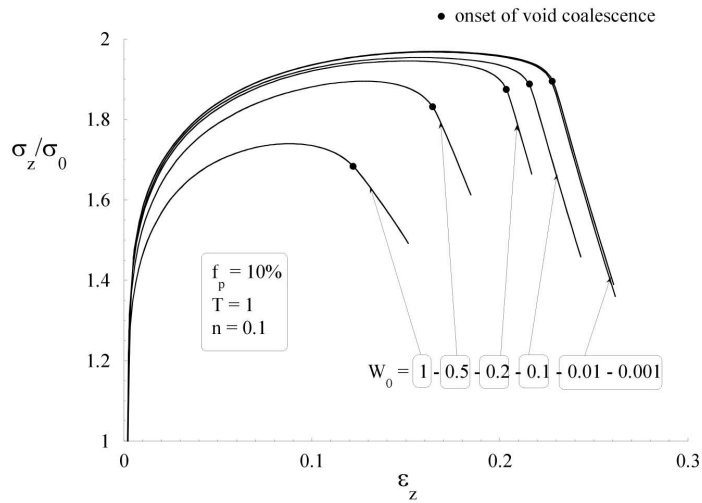
(a)



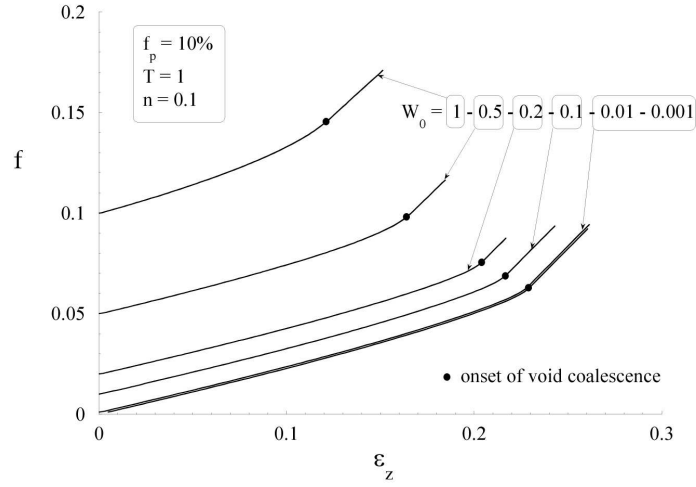
(b)



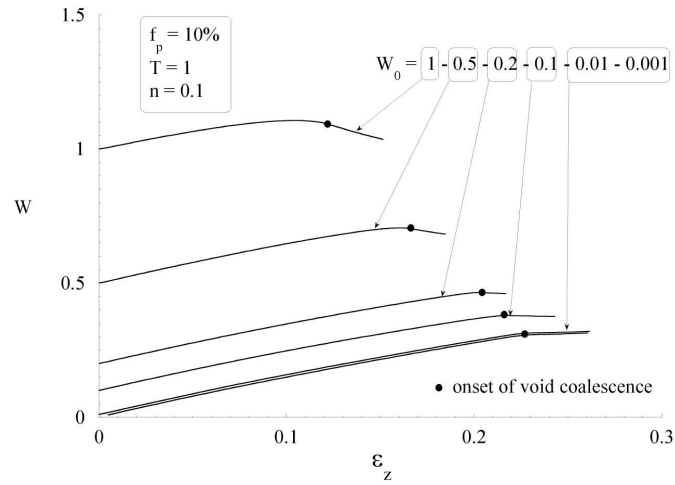
(c)



(d)

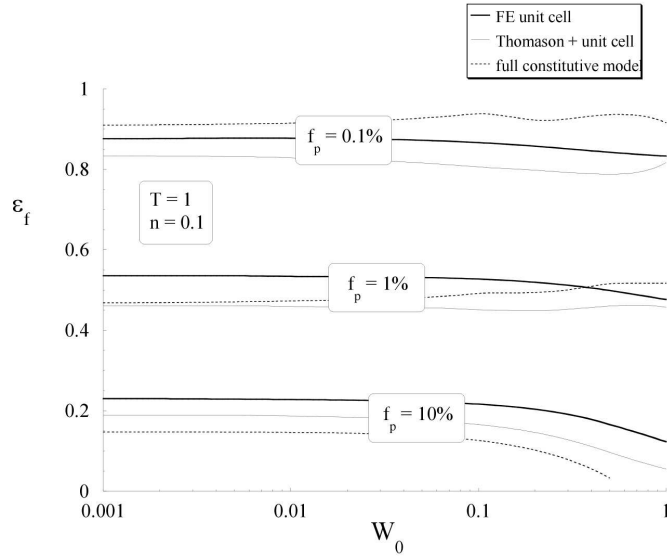


(e)

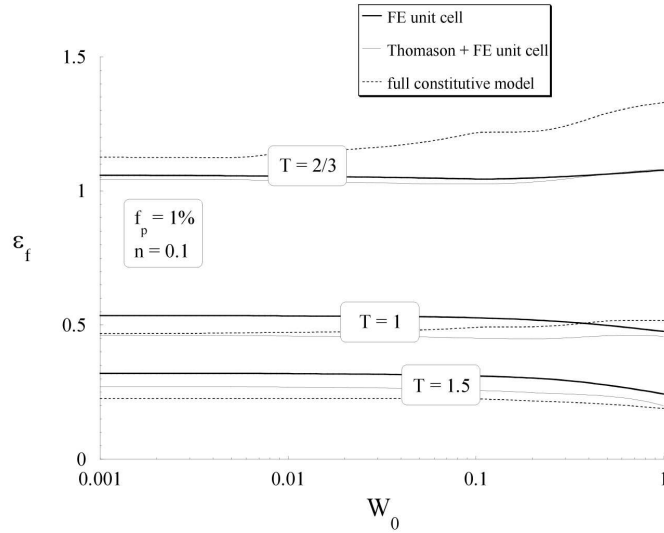


(f)

Figure 4.4 – Results of the FE unit cell calculations for various initial void aspect ratio W_0 ranging between 0.001 and 1, under a constant stress triaxiality $T = 1$, with $n = 0.1$ and $E/\sigma_0 = 500$, for (a,b,c) $f_p = 1\%$ and (d,e,f) for $f_p = 10\%$; (a,d) overall axial stress versus axial strain curves; (b,e) evolution of the porosity as a function of the axial strain; (c,f) evolution of the void aspect ratio as a function of the axial strain. The onset of coalescence is indicated by a bullet.



(a)



(b)

Figure 4.5 – Variation of the ductility ϵ_f as a function of the void aspect ratio W_0 for $n = 0.1$; (a) for different particle volume fraction $f_p = 0.1, 1$ and 10% with a stress triaxiality $T = 1$, (b) for different stress triaxiality $T = 2/3, 1$ and 1.5 with $f_p = 1\%$. The results obtained from the FE unit cell simulations are compared to the predictions of the void coalescence condition using the evolution of the state variables calculated either by the FE unit cell method or by the constitutive model.

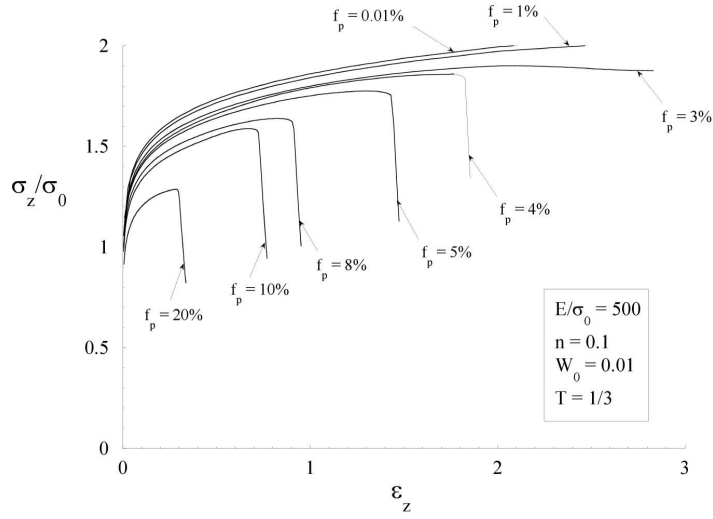
Now, a set of unit cell calculations is presented for the specific case of a stress triaxiality equal to $1/3$, i.e. for pure uniaxial tension conditions. Figure 4.6 gathers, for various particle volume fractions, the variation with the overall axial strain of (a) the overall axial stress, (b) the void volume fraction and (c) the void aspect ratio.

For low particle volume fraction, the porosity saturates after some amount of growth to a porosity f_s . The saturation occurs at large strains (> 2). No transition to coalescence is observed following saturation. The explanation for this saturation is provided by the evolution of both the void aspect ratio and of the void radii. After some amount of growth, the void contracts in the x direction enough to compensate exactly the elongation in the z direction. When the void has become sufficiently elongated, like a needle, plastic flow can occur as if there was no void in the material because there is no stress to open the void transversely. The saturation is thus the result of volume conservation for the overall cell when the void has become very elongated in the direction of loading. If the particle volume fraction is larger than a threshold value f_p^* , neighboring voids are sufficiently close to each other initially to allow, after some amount of void growth, to meet the coalescence condition before saturation takes place. We will come back to the peculiarities of void growth and coalescence in the very low triaxiality regime in section 4.4 and look into more details at the threshold particle volume fraction f_p^* .

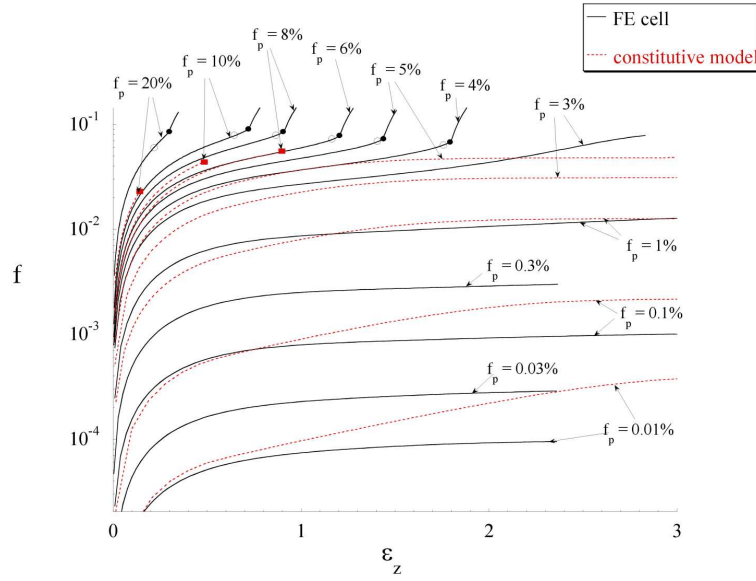
4.2.3 Results of the unit cell calculations with particle

Figure 4.7 compares the response of a porous material involving flat voids ($W_0 = 0.01$) with and without the presence of a surrounding particle, in terms of (a) the overall stress - strain curves, (b) the evolution of the porosity, (c) the evolution of the void aspect ratio.

As in the previous section, the anisotropy distribution parameter $\lambda_p = \lambda_0$ is kept equal to 1 and three volume fractions of spherical particles ($W_p = 1$) are analyzed : $f_p = 0.1\%$, 1% , and 10% . The Young's modulus of the particle E_p is taken much larger than the Young's modulus of the matrix : $E_p = 10E$, which is a realistic choice for intermetallic particles in aluminum for instance. Two stress triaxialities are considered : $1/3$ and 1 . The only first order effect associated to the presence of the particles is the composite effect consisting of a marked increase of the material strength when the volume fraction is high enough ($f_p = 10\%$). Regarding damage evolution, the presence of the particle affects only moderately the void growth rate. At the intermediate stress triaxiality $T = 1$, the void growth rate is smaller when the void is not surrounded by a particle, which puts a constraint on the radial expansion. At low stress triaxiality ($T = 1/3$), the opposite effect occurs: in the absence of particle, the void is free to contract while the presence of the particle constraints the



(a)



(b)

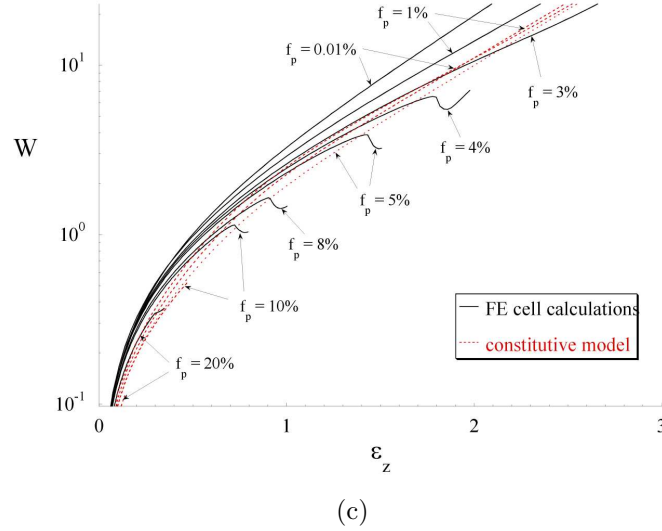
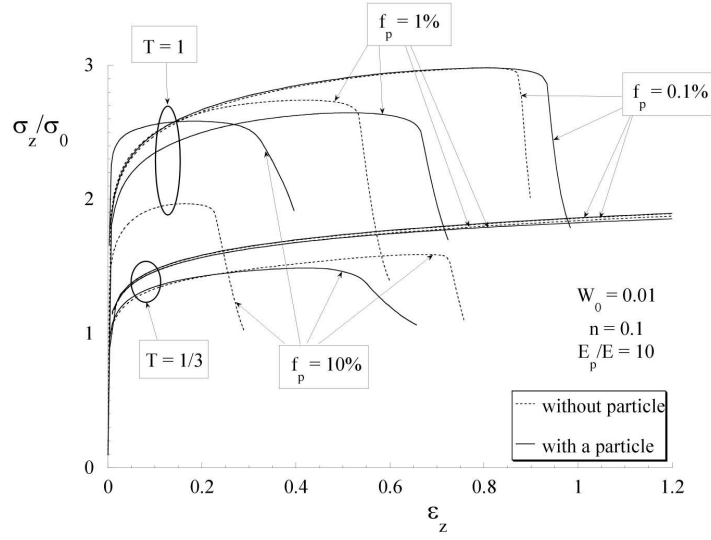


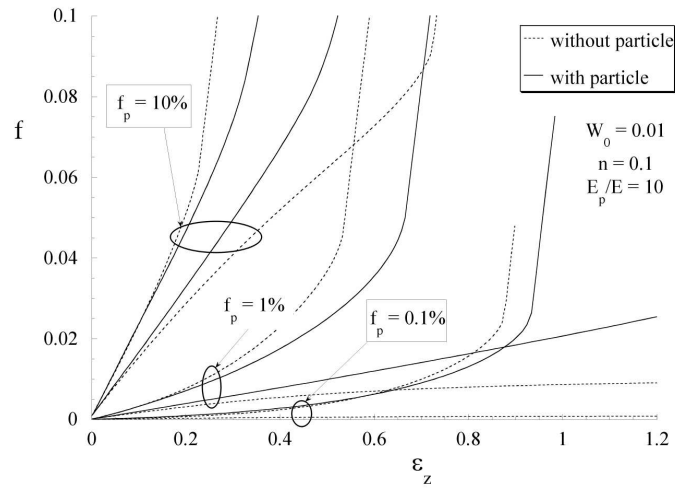
Figure 4.6 – Results of the FE cell calculations for uniaxial tension conditions, i.e. $T = 1/3$, very flat initial voids $W_0 = 0.01$, and various particle volume fractions f_p ; (a) axial stress versus axial strain curves; (b) evolution of the porosity; (c) evolution of the void aspect ratio.

transverse contraction. The main reason for the limited effect of the presence of the particle on the damage evolution is that the void growth rate and void aspect ratio change is essentially controlled by the opening of the void in the z direction, which is driven by plastic deformation in front of the penny void tip (a mechanism similar to the blunting of a sharp macro-crack). The presence of the particle does not significantly perturb the plastic flow in that region. The picture is different for more rounded voids which involve also plastic flow on the upper side of the void.

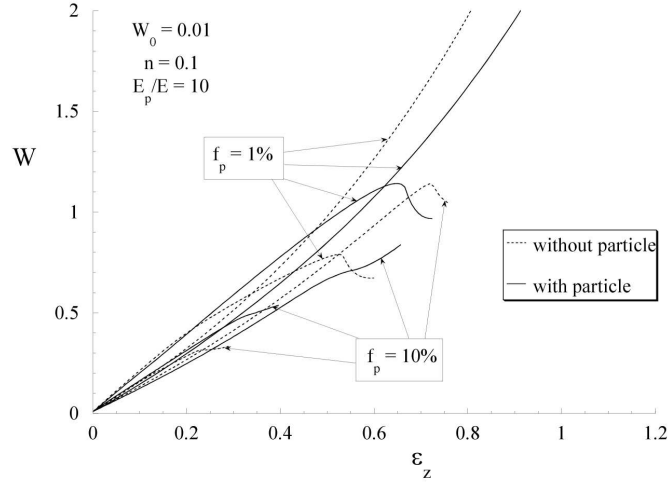
Figure 4.8 compares the responses obtained for different elastic mismatch between the particle and the matrix $E_p/E = 1, 2, 4, \text{ and } 10$. The results of Figure 4.7 are confirmed: the presence of the particle has a second order effect on the ductility. We note here that the difference between the evolution of the overall axial stress for the case without particle and with a particle presenting identical stiffness than the matrix, is due to the fact that the particles has always an elastic behavior unlike the matrix which is elasto-plastic.



(a)



(b)



(c)

Figure 4.7 – Results of the FE unit cell calculations with and without the presence of particles surrounding a flat initial void ($W_0 = 0.01$) for two different stress triaxialities (1/3 and 1) and three different particle volume fractions $f_p = 0.1, 1$ and 10%, with $n = 0.1$ and $E/\sigma_0 = 500$; (a) axial stress - axial strain curves; (b) evolution of the porosity as a function of the axial strain; (c) evolution of the void aspect ratio as a function of the axial strain.

Hence, we conclude from this sub-section that proper account of the presence of the particle on the response of the material is not essential for semi-quantitative ductility predictions.

4.3 The constitutive model

A constitutive model for the nucleation, growth and coalescence of voids in plastically deforming material

The emphasis in this study is on the growth and coalescence of initially flat voids. Nevertheless, interesting couplings take place when considering also the void nucleation stage. Thus, although void nucleation was not considered in the FE unit cell calculations, mostly because of the extra complexity involved

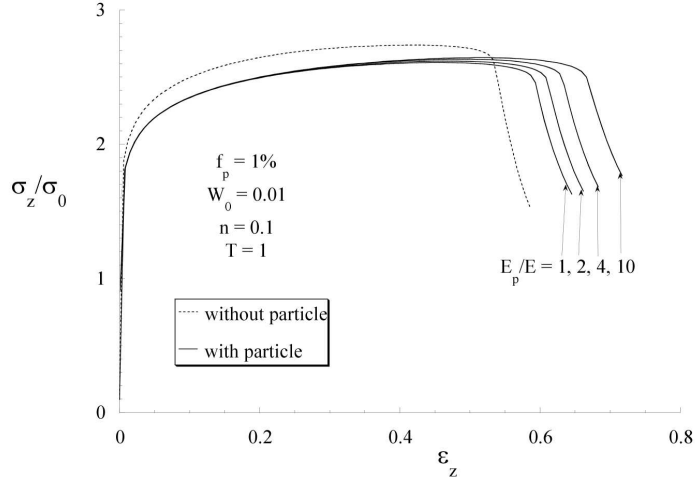


Figure 4.8 – Variation of the overall axial stress as a function of the overall axial strain predicted by FE unit cell calculations for flat voids ($W_0 = 0.01$) surrounded by particles with different stiffness ($E_p/E = 1, 2, 4, 10$). The volume fraction of particles is $f_p = 1\%$. The particles are spherical, i.e. $W_p = 1$. The plastic properties of the matrix are described by $n = 0.1$ and $E/\sigma_0 = 500$.

in such kind of simulations, a nucleation condition will be introduced in the constitutive model. This nucleation condition relies on an approximate model for the stress transfer within the particle. Note that no effect of the presence of the particle on the flow behavior is introduced in this version of the model.

4.3.1 The model

4.3.1.a Before void nucleation

The material is assumed to behave as an isotropic hardening J_2 elastic-viscoplastic material with effective flow properties in uniaxial tension described by (4.5). For large volume fraction of particles ($f_p > 5-10\%$), a micro-macro type constitutive model homogenization such as the incremental mean field model of Doghri and Ouaar [26] would obviously be more appropriate to describe the response of the composite material under general loading histories.

4.3.1.b Void nucleation condition

The fracture of the particles (which is the main source of penny-shaped voids) is assumed to occur when the maximum principal stress in the particle reaches a critical value noted σ_c :

$$\sigma_{princ}^{particle\ max} = \sigma_c \quad (4.6)$$

The motivation for such a simple void nucleation condition is that most inclusions or precipitates in aluminium alloys can be considered as brittle solids. A critical maximum principal stress corresponds to the critical stress in the particle required to reach the critical stress intensity factor for the propagation of the internal defects present within the particles [51, 7]. Following the Es-helby theory [29] and the "secant modulus" extension to plastically deforming matrix proposed by Berveiller and Zaoui [15], the maximum principal stress in an elastic inclusion $\sigma_{princ}^{particle\ max}$ can be related to the overall stress state by the following expression:

$$\sigma_{princ}^{particle\ max} = \sigma_{princ}^{max} + k(\sigma_e - \sigma_0) \quad (4.7)$$

where σ_{princ}^{max} is the maximum overall principal stress and k is a parameter of order unity which is a function of the inclusion shape and loading direction. This void nucleation criterion was initially proposed by the Beremin group [13] who also identified k from experimental data. They found that the values of k predicted by the theory were about two times higher than the experimental values because of an over stiff response of the homogenization scheme. As mentioned above, more advanced homogenization scheme or the use of tabulated stress concentration factors (e.g. see the comprehensive analysis of Lee and Mear [61]) would deliver more accurate estimate of the stress in the particle (note that such model must also account for the drop of the particle reinforcement effect after void nucleation). In this paper, absolute prediction of the ductility is not a primary issue and the void nucleation stage (for instance, the effect of the particle shape) will thus not be investigated in details, hence k is simply taken equal to 1.

The rate of increase of the void volume fraction associated to the nucleation of new voids is taken as a function of the plastic strain rate:

$$\dot{f}_{nucl} = g(\bar{\epsilon}^p) \bar{\epsilon}^p \quad (4.8)$$

where $\bar{\epsilon}^p$ is the effective plastic strain rate of the matrix material. A polynomial form for the function $g(\bar{\epsilon}^p)$ is chosen:

$$g(\bar{\epsilon}^p) = a_1(\bar{\epsilon}^p)^4 + a_2(\bar{\epsilon}^p)^2 + a_3 \quad (4.9)$$

When the condition (4.8) is fulfilled, with the corresponding effective plastic strain noted $\bar{\epsilon}^p = \bar{\epsilon}_c^p$, the nucleation starts and takes place during a range of

strains $\Delta\bar{\epsilon}^p$. The parameters a_i are chosen in such a way as to avoid discontinuities in the porosity evolution: both $g(\bar{\epsilon}_c^p)$ and $g(\bar{\epsilon}_c^p + \Delta\bar{\epsilon}^p)$ as well as their first derivatives are taken equal to 0. In the present study, nucleation is assumed to occur simultaneously on all particles and $\Delta\bar{\epsilon}^p$ is equal to 0.001.

4.3.1.c Void growth model

As soon as voids nucleation starts, the accumulation of plastic deformation causes the enlargement of the voids and an increase of the void volume fraction which, by stating volume conservation, writes:

$$\dot{f}_{growth} = (1 - f)\dot{\epsilon}_{ij}^p \quad (4.10)$$

where $\dot{\epsilon}_{ij}^p$ are the ij components of the overall plastic strain rate tensor. The full evolution law for the void volume fraction writes

$$\dot{f} = \dot{f}_{growth} + \dot{f}_{nucl} \quad (4.11)$$

The initially flat voids progressively open with plastic flow leading to a change of the void aspect ratio $W = R_z/R_x$ while assuming that the void remain spheroidal with the current void radii noted $R_x = R_y$ and R_z . The evolution law for W is

$$\frac{\dot{W}}{W} = \frac{3}{2}(1 + h_1) \left(\dot{\epsilon}^p - \frac{\dot{\epsilon}_{kk}^p}{3}\delta \right) : P + h_2\dot{\epsilon}_{kk}^p \quad (4.12)$$

This evolution law has been derived by Gologanu *et al.*, see [36], from a micromechanical analysis of the growth of a spheroidal void in a J_2 perfectly plastic material. This analysis, completed by subsequent works, leads to expressions for h_1 and h_2 as a function of W , f and n (see for the full expressions [72, 36]). P is a projector tensor, defined by $e_z \otimes e_z$ and e_z is a unit vector parallel to the main cavity axis; δ is the Kronecker tensor. In this study, devoted to axisymmetric loading conditions, the main void axis e_z does not rotate and remains parallel to the maximal principal stress.

The plastic strain rate is taken normal to the flow potential:

$$\dot{\epsilon}_{ij}^p = \dot{\gamma} \frac{\partial \Phi}{\partial \sigma_{ij}} \quad (4.13)$$

where Φ is the flow potential proposed by Gologanu *et al.* [35] for a porous materials involving spheroidal voids. This flow potential writes

$$\Phi = \frac{C}{\sigma_y^2} \|\sigma' + \eta\sigma_h^g X\|^2 + 2q(g+1)(g+f) \cosh \left(\kappa \frac{\sigma_h^g}{\sigma_y} \right) - (g+1)^2 - q^2(g+f)^2 = \text{04.14}$$

where σ' is the deviatoric part of the Cauchy stress tensor; σ_h^g is a generalized hydrostatic stress defined by $\sigma_h^g = \sigma : J$; J is a tensor associated to the void axis and defined by $(1 - 2\alpha_2)e_z \otimes e_z + \alpha_2 e_x \otimes e_x + \alpha_2 e_y \otimes e_y$; X is a tensor associated to the void axis and defined by $2/3e_z \otimes e_z - 1/3e_x \otimes e_x - 1/3e_y \otimes e_y$; $\|\cdot\|$ is the von Mises norm; $C, \eta, g, \kappa, \alpha_2$ are analytical functions of the state variables W and f ; q is a parameter that has been calibrated as a function of f_0, W_0 , and n (see [72] for complete expressions). The only differences in the version of the model used in the present study is that q is kept constant during deformation and that the dependence in W_0 is not maintained for $W_0 < 0.1$: if $W_0 < 0.1$, q is taken equal to $q(W_0 = 0.1)$.

The plastic dissipation in the matrix material is related to the overall rate of plastic work through the energy balance initially proposed by Gurson [38]:

$$\sigma_y \dot{\epsilon}^p (1 - f) = \sigma_{ij} \dot{\epsilon}_{ij}^p \quad (4.15)$$

which, combined with eqns (4.5) and (4.13), determines the plastic multiplier γ . The stress rate tensor is then directly evaluated from

$$\dot{\sigma}_{ij} = L_{ijkl} (\dot{\epsilon}_{kl} - \dot{\epsilon}_{kl}^p) \quad (4.16)$$

where the L_{ijkl} are the elastic moduli. This void growth model has been worked out and validated elsewhere [72, 36] for the limit of rate independent solids ($m = 0$). In the present study, the viscoplastic formalism is used but only the limit of rate independent solids will be addressed. The strain rate exponent m will be taken equal to 0.01 in all calculations. It is important to underline that the present model, described by eqns (4.10) to (4.16), cannot be used as such for truly viscoplastic solids, i.e. when m significantly departs from 0. The velocity fields used to derive the flow potential eqn. (4.14) are relevant only in the elastoplastic limit. An analysis of truly viscoplastic behaviour leads to different flow potentials, which still keep a form similar to the Gurson solution, but explicitly introduces an effect of the strain rate exponent m [60]. The recent work of Klocker and Tvergaard [47] has shown that not only the flow potential has to be adapted, but also the void aspect evolution law is significantly affected by the viscoplastic contribution.

4.3.1.d Void coalescence condition

The process of void growth by relatively homogenous plastic deformation of the matrix surrounding the voids is, at some point, interrupted by the localization of the plastic flow in the ligament between the voids. This localization corresponds to the onset of coalescence. Thomason [87] proposed the following condition for the onset of coalescence:

$$\frac{\sigma_z}{\sigma_y} = \frac{2}{3}(1 - \chi^2) \left[\alpha \left(\frac{1 - \chi}{\chi W} \right)^2 + 1.24 \sqrt{\frac{1}{\chi}} \right] \quad (4.17)$$

where the parameter α has been fitted as a function of the average value of the strain hardening exponent n : $\alpha(n) = 0.1 + 0.22n + 4.8n^2$ ($0 \leq n \leq 0.3$), see [72]. Criterion (4.17) states that coalescence occurs when the stress normal to the localization plane reaches a critical value and this critical value decreases as the voids open (W increases) and get closer to each other (χ increases). The key parameter controlling the transition to the coalescence mode is the relative void spacing χ . The porosity affects the coalescence because it is related to the void spacing χ and because it has a softening effect on the applied stress σ_z and on the strength σ_y . In more advanced applications of this model [69], the localization condition (4.17) is tested in all possible directions which requires to define χ and W as a function of the orientation of the localization plane. In the present study, coalescence always occurs in a band normal the main void axis.

4.3.2 Assessment of the model

4.3.2.a Assessment of the void coalescence condition

The validity of the coalescence condition (4.17) can be assessed directly using the results provided by the FE unit cell calculations. Indeed, the variables entering relationship (4.17) are direct outcome of the simulations except for the current yield stress of the matrix material σ_y which can be computed using the energy balance (4.15). The energy balance (4.15) is accurate as long as the strain hardening exponent is not too large (n typically lower than 0.15, see [59]). The predictions obtained with the coalescence model are compared in Figures 4.5(a) and 4.5(b) to the predictions of the onset of coalescence given by the unit cell calculations (if the prediction made by (4.17) for the onset of coalescence takes place after the onset of coalescence in the unit cell, care is taken to extrapolate as accurately as possible the variables appearing in (4.17) from their evolution before the onset of coalescence predicted by the cell calculations). The agreement is good for the whole range of stress triaxialities, initial void shape and particle volume fractions. For pure uniaxial tension, Figure 4.6 shows that condition (4.17) (open circles) predicts also very well the onset of void coalescence as given by the unit cell calculations (plain circles). Furthermore, in agreement with the unit cell calculations, no coalescence is predicted when $f_p < 4\% = f_p^*$. The result of this assessment reinforces the statement made previously (in [72]) that the criterion (4.17), although relatively simple, is quite robust.

4.3.2.b Assessment of the void growth model

The validity of the void growth model has been carefully assessed for void aspect ratios ranging between 1/6 and 6 in ref [72]. Further assessment is provided by the comparisons in Figures 4.6(a) and 4.6(b), showing the variations

of the porosity and of the void aspect ratio, respectively, for uniaxial tension conditions. Among others, the extended Gurson model properly captures the saturation of the porosity under low initial porosity.

Figure 4.5 also involves an indirect validity check of the void growth model by directly looking at the predictions of the full model in terms of the variation of the ductility as a function of the initial void aspect ratio, stress triaxiality and particle volume fraction (or, equivalently, relative void spacing χ_0). The error resulting only from the void growth model on the prediction can be inferred by comparing the predictions of the Thomason model based on the evolution laws extracted from the FE calculations and the predictions with the full constitutive model. The main point here is that the full constitutive model correctly predicts that the ductility is independent of the initial void aspect ratio W_0 as long as the initial porosity is identified from relationship (4.2).

The full constitutive model provides reliable predictions, but even if the model is already quite complex, some quantitative discrepancies still persist. More accurate predictions require additional fitting and adjustment of the void shape evolution law based on the numerical cell calculations such as recently illustrated by Klocker and Tvergaard [47].

4.4 Parametric study and discussion

The ductility of metals with penny-shaped voids

The purpose of the three first subsections is to provide a relatively comprehensive study of the relationships between the ductility, the stress triaxiality, the flow properties, i.e. the strain hardening exponent n and the ratio E/σ_0 , and the microstructure, i.e. the particle volume fraction f_p (or equivalently χ_0) and the anisotropy distribution parameter λ_p . The focus is mainly on materials involving penny-shaped voids ($W_0 = 0.01$ is used throughout). Calculations with other initial void shapes are proposed only when useful for better revealing the peculiarities of a damage process involving penny-shaped voids. The constitutive model presented and assessed in the previous sections has been used to run all the calculations, allowing looking at the effect of void nucleation. We discuss independently (i) the ductility of metals in the absence of nucleation stage; (ii) the ductility of metals in the absence of nucleation stage in the case of very low stress triaxiality; (iii) the ductility of metals when void nucleation occurs after some amount of straining. In a fourth subsection, a simple closed-form model will be developed that incorporates assumptions and approximations motivated by the results generated in the previous sections.

4.4.1 No nucleation stage - low to large stress triaxiality

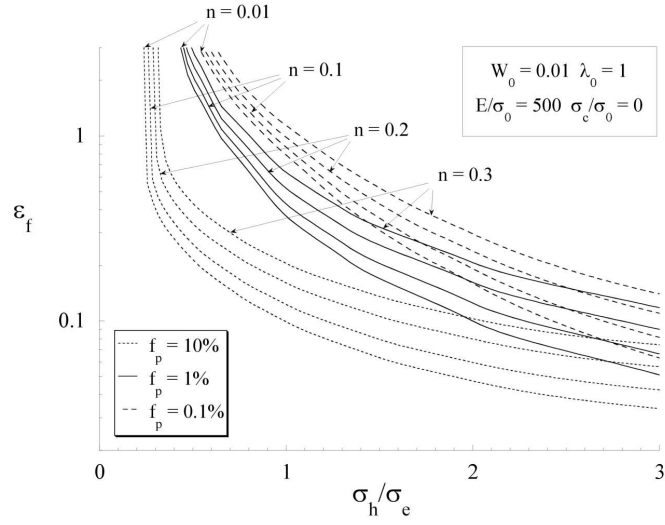
Figure 4.9 shows the variation of the ductility with the stress triaxiality for three volume fractions of particles $f_p = 0.1\%$, 1% and 10% , while varying also in Figure 4.9(a) the strain hardening exponent n , in Figure 4.9(b) the ratio E/σ_0 and in Figure 4.9c the anisotropy distribution factor λ_0 . Figure 4.9(a) shows that strain hardening has a secondary effect on the ductility when the ductility is controlled by a mechanism of stable void growth followed by void coalescence.

Changing for instance the strain hardening exponent n from 0.1 to 0.2 by proper thermal treatment will not markedly improve the ductility as such. Of course, an enhanced strain hardening capacity will, in practical structural loading conditions, delay necking and shear banding which significantly contributes to improving the ductility by postponing the rise of the stress triaxiality, e.g. [43]. Those last effects are geometric and not a result of an intrinsic influence of the strain hardening on the damage evolution. Note also that in the practice, strain hardening can hardly be changed without affecting the strength (one important exception is given by aluminum alloys which show at low temperature a change of the strain hardening capacity without much variation of the yield stress).

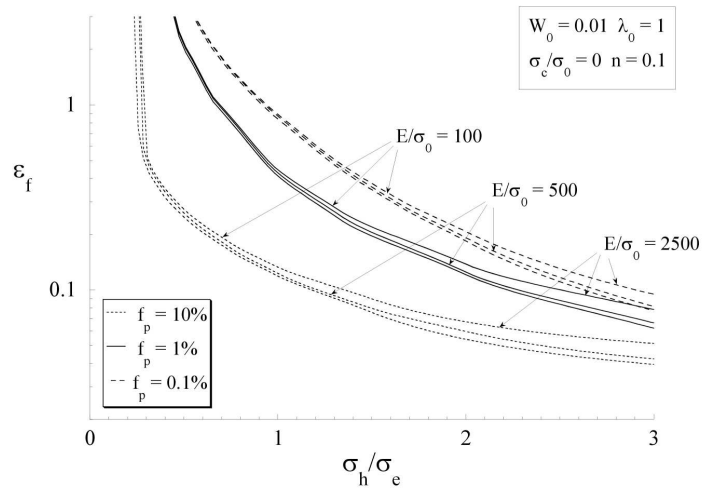
The effect of the particle volume fraction depicted in Figure 4.9 is trivial: larger f_0 corresponds to larger relative void spacing χ_0 which is the primary parameter controlling the onset of coalescence (4.17). The effect of the anisotropy distribution parameter λ_0 is more difficult to grasp. First, Figure 4.9c shows the variation of the ductility with stress triaxiality for different λ_0 . Here different λ_0 , for the same f_p , means different χ_0 . This plot is interesting because it approximately quantifies the maximum level of anisotropy in the ductility that can be expected for a material with $\lambda_0 = 2$ in one symmetry direction, which, loaded in the orthogonal direction, would be characterized by $\lambda_0 = 1/2$. A material with such an anisotropic void distribution will involve significantly different ductility when deformed in the two transverse direction (examples of anisotropic particle distribution function can be found after severe plastic deformation typical of many forming operations: oxide columns in extruded copper bars, potassium bubbles columns in tungsten wires, columns of broken intermetallic particles in rolled aluminum sheets).

To supplement the information provided by Figure 4.9(c), Figure 4.10 shows the variation of the ductility as a function of anisotropy distribution parameter λ_0 but now keeping the relative void spacing χ_0 constant ($\chi_0 = 0.114, 0.247$, or 0.531).

Keeping the void aspect ratio W_0 constant ($W_0 = 0.01$) and χ_0 constant, while varying λ_0 means that the initial porosity f_0 changes (see eqn (4.1)). An increase in λ_0 (accompanied with a proportional decrease of f_0) leads to lower



(a)



(b)

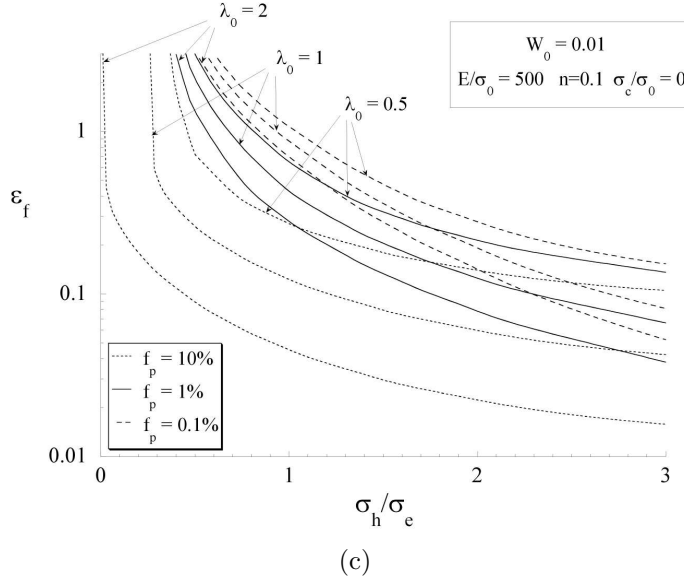


Figure 4.9 – Variation of the ductility as a function of the stress triaxiality for penny-shaped voids of aspect ratio $W_0 = 0.01$ and for three volume fractions of particles $f_p = 0.1\%$, 1% and 10% , considering (a) different strain hardening exponents $n = 0.01, 0.1, 0.2, 0.3$ with $E/\sigma_0 = 500$ and $\lambda_0 = 1$; (b) different ratios $E/\sigma_0 = 100, 500, 2500$ with $n = 0.1$ and $\sigma_0 = 1$; (c) three different anisotropy distribution parameters $\lambda_0 = , 1, \text{ and } 2$, with $E/\sigma_0 = 500$ and $n = 0.1$.

ductility which is apparently counterintuitive. The ductility becomes insensitive to the value of λ_0 when it becomes very large and f_0 very small. The limit $\lambda_0 \rightarrow 0$ corresponds to a single plane of voids in an infinite solid. The limit to very small λ_0 is not physical as voids then tend to touch each other in the axial direction. This effect of the void distribution was already presented in [72] for initially spherical voids but without providing in depth explanation. As it is not a focal point of this study, the detailed explanation for the trends shown in Figure 4.10 is given in Appendix A.

To summarize, the parameters that primarily control the ductility, in the absence of delayed void nucleation, are the stress triaxiality T and the relative void spacing χ_0 . These two parameters can be responsible for significant drop or increase of the ductility. For instance, moving from a low stress triaxiality of $T = 0.66 - 1$ typical of a plane strain tension specimen or a shallow notched structure to a high stress triaxiality typical of crack tip region, i.e. $T > 3$, leads

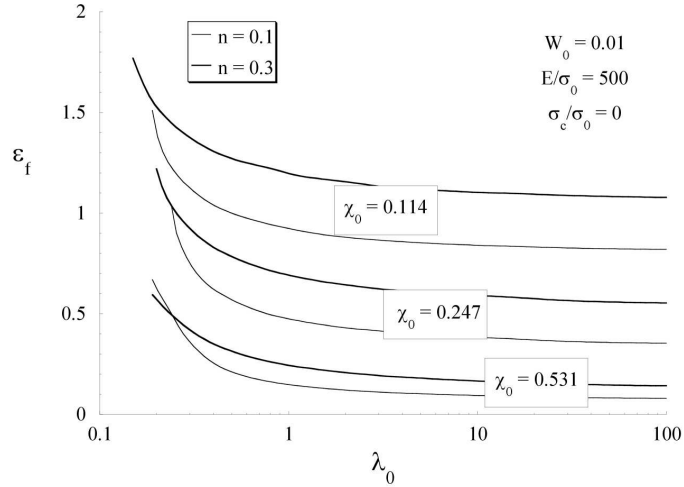


Figure 4.10 – Variation of the ductility as a function of the anisotropy distribution parameters λ_0 for penny-shaped voids of aspect ratio $W_0 = 0.01$, for three relative void spacings $\chi_0 = 0.114, 0.247, \text{ or } 0.531$, two strain hardening exponents $n = 0.1$ and 0.3 , and a stress triaxiality T equal to 1 .

to one order of magnitude drop in the ductility (see Figures 4.9). Processing cleaner materials with lower second phase inclusions content and avoiding stress concentration remain thus the best routes to improve ductility. A change of the initial porosity f_0 at constant relative void spacing and void aspect ratio (meaning a change of the void distribution parameter λ_0) moderately affects the ductility as by influencing both the void growth rates and stress softening. A change of the initial void aspect ratio W_0 constant χ_0 and λ_0 (i.e. at constant f_p) with f_0 directly related to W_0 through eqn (4.4) affects the ductility only if the initial porosity f_0 is large enough (typically $f_0 > 1\%$). The strain hardening capacity has, intrinsically, only a moderate effect on the ductility, but can obviously play a major role in postponing localization at the structural level and reducing stress concentration. The ratio E/σ_0 has no effect on the ductility.

4.4.2 No nucleation stage - very low stress triaxiality

Figure 4.9 shows that in the very low stress triaxiality regime, slight changes in stress triaxiality lead to marked changes in ductility. Figure 4.6 exhibited a

minimum particle volume fraction, f_p^* , under which the void growth rate saturates to a value f_s . Void coalescence never takes place after saturation. The saturation corresponds to a stage during which the void elongates as much as it contracts in the transverse direction. The damage evolution under very low stress triaxiality is particular to flat voids and is investigated in more details in this sub-section.

Figure 4.11 shows the variation of the ratio f_s/f_p as a function of f_p for two different strain hardening exponents $n = 0.1$ and 0.3 , a stress triaxiality $T = 1$ and very flat initial voids. The threshold value f_p^* is also indicated.

A saturation porosity is predicted by the constitutive model for $f_p > f_p^*$ when

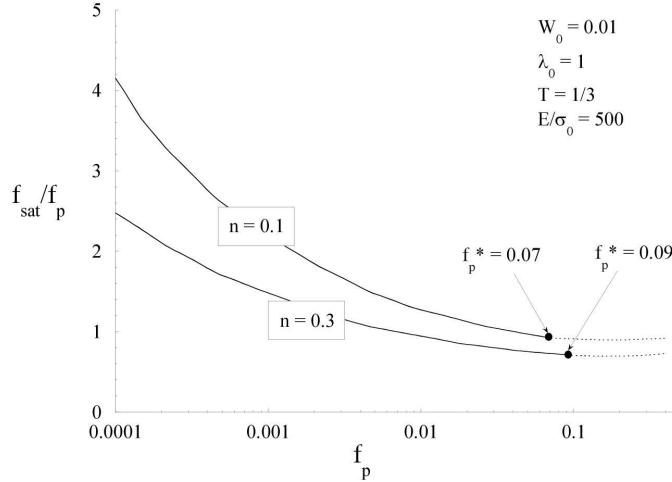


Figure 4.11 – Variation of the saturation porosity attained under uniaxial tension condition, normalized by the particle volume fraction, as a function of the particle volume fraction for initially flat voids ($W_0 = 0.01$) and two different strain hardening exponents $n = 0.1$ and 0.3 . The threshold particle volume fraction f_p^* under which no coalescence takes place is also indicated on the figure .

the coalescence condition is turned off, but this prediction is not physically meaningful (dotted line in Figure 4.11). The saturation porosity is on the order of magnitude of the particle volume fraction, especially when the particle volume fraction becomes close to the threshold.

Figure 4.12 shows the variation of the threshold value f_p^* as a function of the

stress triaxiality. The stress triaxiality is noted T_{trans} to signify, for the corresponding particle volume fraction, the transition between a regime of void elongation without coalescence for a lower triaxiality to the classical regime of void growth followed by coalescence for larger stress triaxiality.

Of course, the threshold increases when the stress triaxiality decreases. Note

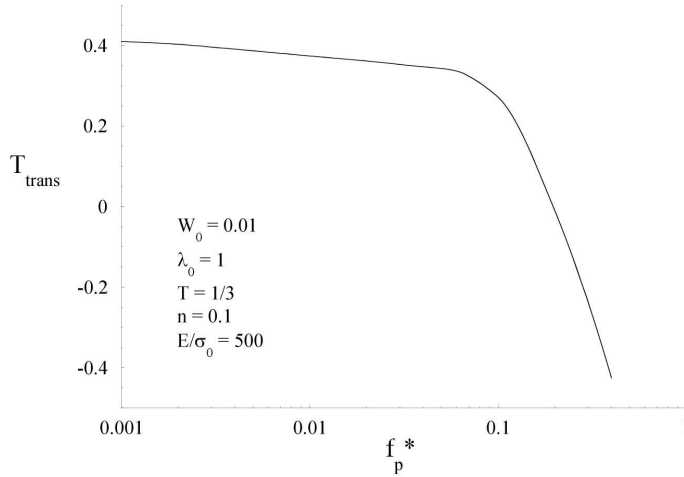


Figure 4.12 – Variation of the transition stress triaxiality as a function of the particle volume fraction for initially flat voids ($W_0 = 0.01$) and $n = 0.1$. The transition stress triaxiality is the stress triaxiality under which, for a given volume fraction of particles, no void coalescence takes place (the porosity either saturates with straining or decreases). This figure can also be interpreted as giving the variation of the threshold particle volume fraction as a function of the stress triaxiality .

that when the particle volume fraction gets large, the transition stress triaxiality becomes negative. The compression is due to negative highly transverse stresses while the material element still deforms in the axial direction under positive axial stresses. The void, initially very flat, first opens before collapsing quickly in the transverse direction at larger strains. Hence, for a stress triaxiality lower than $1/3$, the porosity first increases and then decreases. The saturation behavior is thus only observed at $T = 1/3$. If the initial porosity (or the initial relative void spacing χ_0) is sufficiently large, the increase of the void aspect ratio in the beginning of the deformation is enough to compensate the decrease of the relative void spacing and to satisfy the localization condition

(4.17).

Figure 4.13 supplements the results of Figure 4.11 and 4.12 by showing the variation of the ductility as a function of the particle volume fraction for different initial void shapes, considering uniaxial tension conditions ($T = 1/3$).

The threshold porosity f_p^* is also indicated. This figure clearly shows that,

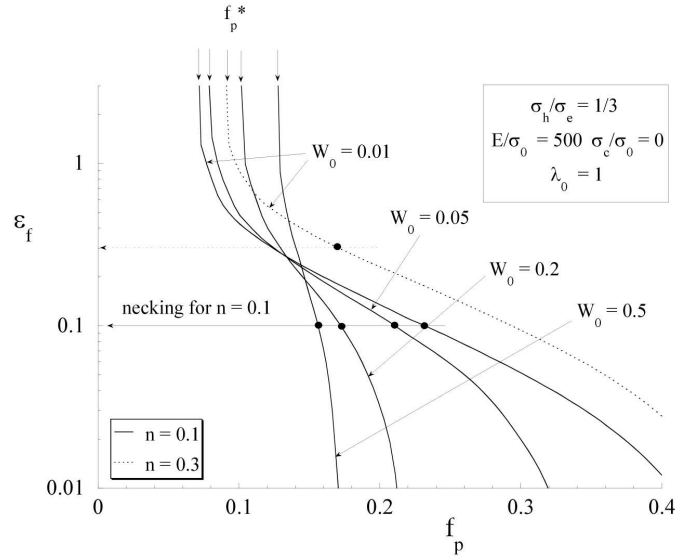


Figure 4.13 – Variation of the ductility as a function of the particle volume fraction for different initial void aspect ratios $W_0 = 0.01, 0.05, 0.2, 0.5$, strain hardening exponent $n = 0.1$ or 0.3 and a stress triaxiality equal to $1/3$. The necking condition predicted by the Considere criterion is indicated on the figure to show the range of particle volume fraction for which fracture can be expected before the occurrence of necking under uniaxial tension conditions .

for initially flat voids, a wide range of particle volume fraction gives rise to a process of stable void growth followed by void coalescence, at this low stress triaxiality. In contrast, more rounded voids involve a much more abrupt transition : under f_p^* no coalescence takes place while above f_p^* coalescence is almost immediate without any stable void growth stage.

Another interesting outcome of the calculations presented in Figure 4.13 is that void coalescence, and thus ductile fracture, is possible under purely uniaxial tension conditions, i.e. before the occurrence of necking. Using the Considere condition, necking starts in the absence of geometric or material imperfection

when $\epsilon = n$. Hence, for $n = 0.1$ and $n = 0.3$, fracture takes place before necking if $f_p > 23\%$ and $f_p > 17\%$, respectively.

As explained in section 4.2 (Void cell calculations with initially penny-shaped voids), the presence of a particle surrounding the void puts a moderate constraint on the void contraction and can delay the saturation of the void growth rate. The problem is different for voids nucleated by full particle decohesion [73, 22]. In that case, the particle prevents the void collapse in the transverse direction which might significantly affect the ductility.

4.4.3 Delayed void nucleation

Figure 4.14 shows the variations of the nucleation strain and of the ductility as a function of the stress triaxiality for a material involving 1% of spherical particles of stiffness $E_p/E = 10$ giving rise to penny-shaped voids ($W_0 = 0.01$) when a nucleation stress σ_c is attained (Beremin criterion (4.7)). Let us define the "void growth strain" ϵ_g as the strain increment required to bring freshly nucleated void to coalescence, i.e. $\epsilon_g = \epsilon_f - \epsilon_n$. In Figure 4.14(a), the results are plotted for various nucleation stresses $\sigma_c/\sigma_0 = 0, 4, 5,$ and 6 with $n = 0.1$. The main conclusion is that the increase of the ductility ϵ_f with increasing nucleation stress is smaller than the increase of the void nucleation strain ϵ_n . In other words, the void growth strain decreases with increasing resistance to void nucleation. The main reason for this effect is that the mean spacing between particles in the plane normal to the principal loading direction decreases before void nucleation. Hence, the initial value of the relative void spacing χ_0 at nucleation gets larger when the nucleation takes place later. At very low stress triaxiality, this effect can be very substantial and lead to the unexpected trend that the ductility can, in some circumstances, be lower when nucleation is delayed. The argument is related to the discussion of the previous subsection about the transverse contraction of the voids at low stress triaxiality: voids nucleated early with a low χ_0 might undergo void growth saturation while voids nucleated later with a larger χ_0 will reach the coalescence condition before saturation.

The coupling between the strain hardening capacity and the void nucleation process is illustrated in Figure 4.14(b) for two nucleation stresses $\sigma_c/\sigma_0 = 0, 5$ and two different strain hardening exponents $n = 0.1$ and 0.2 . Figure 4.14(b) shows that the main effect of the strain hardening capacity is to accelerate the attainment of the nucleation stress. Hence, improving the strain hardening capacity is beneficial for the ductility only when it is not controlled by the void nucleation step. Note that the couplings between strain hardening, damage evolution and the occurrence of macroscopic necking were already discussed in [43].

Figure 4.15 presents the variation of the ratio ϵ_g/ϵ_n , as a function of the stress

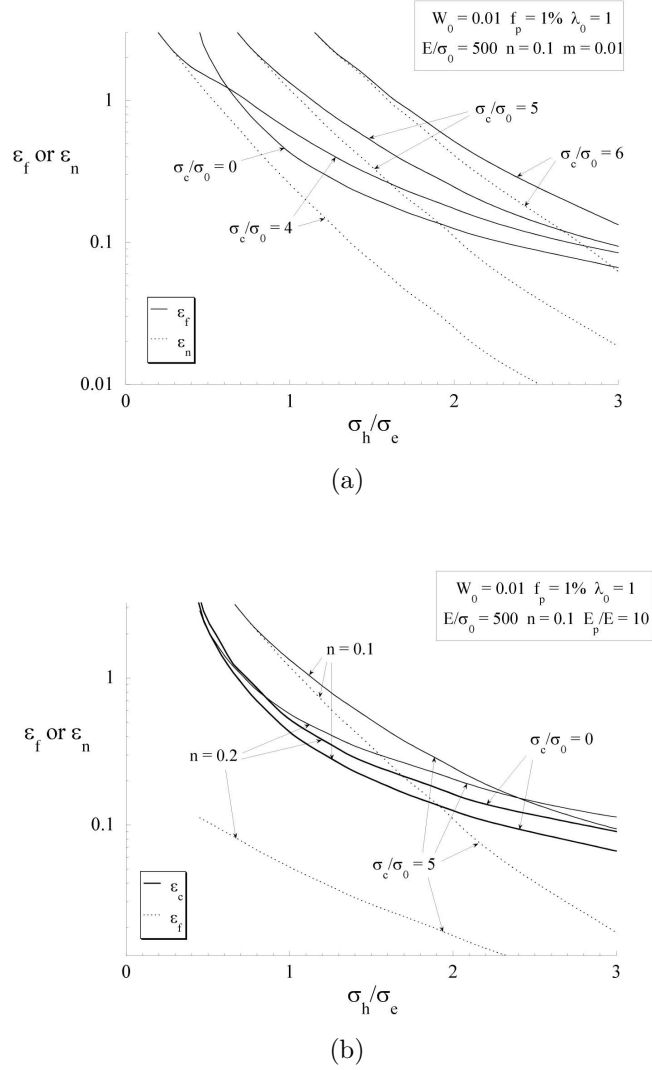


Figure 4.14 – Variation of the ductility and nucleation strain vs. triaxiality for a material involving 1% of spherical particles of stiffness $E_p/E = 10$ giving rise to penny-shaped voids ($W_0 = 0.01$) when a nucleation stress σ_c is attained; (a) for various nucleation stresses $\sigma_c/\sigma_0 = 0, 4, 5, 6$ and $n = 0.1$; (b) for two nucleation stresses $\sigma_c/\sigma_0 = 0, 5$ and two strain hardening exponents $n = 0.1$ and 0.2 .

triaxiality for different nucleation stresses and for two different initial void shapes : penny shape ($W_0 = 0.01$) and spherical ($W_0 = 1$).

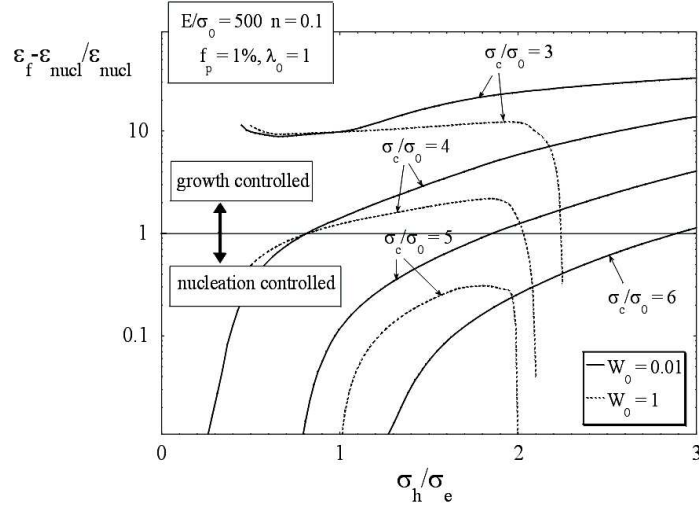


Figure 4.15 – Variation of the normalized void growth strain (i.e. the strain increment from void nucleation to void coalescence) normalized by the nucleation strain as a function of the stress triaxiality for various void nucleation stress σ_c/σ_0 and for two different initial void aspect ratios $W_0 = 0.01$ (penny shape void) and 1 (spherical void). This plot can be seen as a failure map that determines whether the fracture is controlled more by the void nucleation stage or by the void growth stage.

This plot is a sort of failure map which reveals, for a given set of material parameters and stress states, whether the fracture is void growth or void nucleation controlled. The initial penny-shaped character of the voids tends to favour a void growth controlled mechanism. Indeed, all microstructural parameters taken constant, the void coalescence condition (4.17) is satisfied later for flat voids (even though, flat voids lead to larger void growth rates (an incorrect statement is made in ref [43] about that point. The Thomason coalescence condition does lead to smaller localization stresses for larger void aspect ratio)). Note also that for initially spherical voids, void growth controlled fracture is favored only at intermediate stress triaxiality, while for flat voids, the propensity towards a void growth controlled fracture mode keeps increasing with increasing stress triaxiality. Note that the effect of the particle volume fraction was already analyzed elsewhere [43], showing that for large particle volume fraction, the void growth strain is always small simply because the ductility is small :

nucleation is rapidly followed by void coalescence.

The results of Figures 4.13, 4.14 and 4.15 provide a reasonable explanation for the low ductility of some metallic alloys, such as dual phase steels or peak aged Al alloys, but still exhibiting a transgranular fracture mechanism dominated by a voiding process. In those materials, the ductility, even though mainly controlled by the void nucleation stage, involves some amount of stable void growth before void coalescence, see e.g. [30, 74]. The combination of an initial penny shape and of a sufficiently high volume fraction of particles is certainly an important factor that explains the low ductility of these metals. For instance, the results of Figure 4.13 can explain the poor ductility (smaller than the "potential" ultimate tensile strain) measured in some metal matrix composites containing large volume fraction of a brittle reinforcement, e.g. [34]. Other arguments invoked to explain the low ductility of some metallic alloys rely on either (i) a transition in the void coalescence mode from internal necking to void sheeting and/or (ii) the presence of a second population of voids, and/or (iii) void clustering effects.

4.4.4 Simple model for the ductility of metals with penny shape voids

A simple closed-form model can be formulated based on the recognition that, for flat voids, the ductility is essentially controlled by the initial relative void spacing. The goal of this model is to provide an estimate of the effect of the key parameters of the problem, i.e. stress triaxiality, initial void spacing, strain hardening exponent, without having to either run FE simulations or integrate the complex constitutive model developed in section 4.2. We assume

1. *a small volume fraction of particle f_p* (i.e. typically smaller than 1-3%) in order to neglect the effect of the void on the overall response of the material;
2. the J_2 *flow theory* in order to compute the stress and hardening evolution;
3. *rigid plastic behavior* (the ductility is always much larger than elastic strains):

$$\epsilon_{ij}^p = \epsilon_{ij} \quad (4.18)$$

4. *axisymmetric loading conditions* which, combined to volume conservation, leads to

$$\epsilon_x = \epsilon_y = \frac{-\epsilon_z}{2} \quad (4.19)$$

$$\bar{\epsilon} = \epsilon_z \quad (4.20)$$

5. a constant stress triaxiality T , which together with the previous assumption leads to

$$\frac{\sigma_z}{\sigma_y} = T + \frac{2}{3} \quad (4.21)$$

6. a simple mapping between the evolution of the void aspect ratio W and the cell aspect ratio evolution:

$$W = \frac{R_z}{R_x} = \frac{R_{z0} + \Delta R_z}{R_{x0} + \Delta R_x} = \frac{\Delta R_z}{R_{x0} + \Delta R_x} = \frac{\Delta L_z}{L_{x0} + \Delta L_x} = \lambda_0 \frac{\exp(\epsilon_z) - 1}{\exp(\frac{-\epsilon_x}{2})} \quad (4.22)$$

The validity of this last assumption is checked in Figure 4.16 by comparing the void shape evolution towards unit cell calculations. As shown in Figure 4.16, when the void is initially very flat it evolves mostly by opening in the z -direction, independently of the level of stress triaxiality for a large range of deformation. This mapping unfortunately does not work for voids that are not initially flat which would avoid the complexity involved in the void shape evolution law (see Section 4.2).

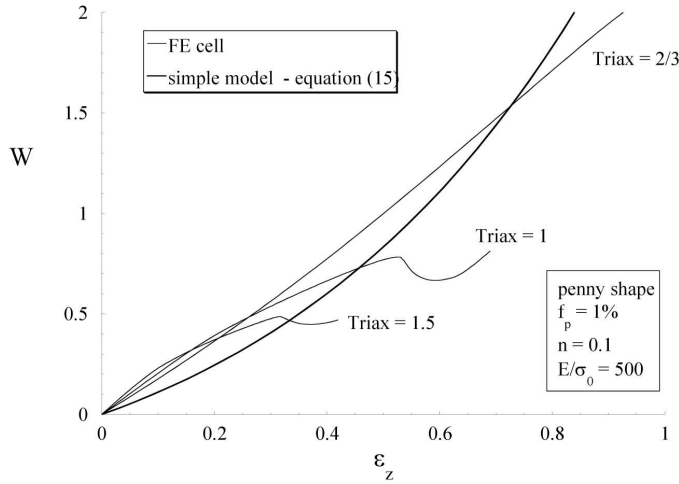


Figure 4.16 – Variation of the void aspect ratio of initially penny-shaped voids as a function of the overall strain for three different stress triaxialities: comparison between the simple evolution law (19) (which is independent of the stress triaxiality) and the FE predictions.

Indeed, rounded voids tend to become prolate at low stress triaxiality and oblate at larger stress triaxiality, conforming thus not with the overall cell kinematics (see [21, 72, 36]). The mapping (4.22) works well for larger stress triaxiality because coalescence then takes place before that the void becomes too rounded and is pushed to evolve towards an oblate shape.

7. the *Rice and Tracey evolution law for the radial evolution of the void radius under constant stress triaxiality* :

$$\frac{R_x}{R_{x0}} = \frac{1}{C} [(C - 1) \exp(C\epsilon_z) - 1] \quad (4.23)$$

where

$$C = 0.427 \exp\left(\frac{3}{2}T\right) \quad (4.24)$$

Relationships (4.23) and (4.24) have been assessed by several authors, e.g. [96]. They give satisfactory predictions as long as the volume fraction is sufficiently small which is the basic assumption of the Rice and Tracey analysis dealing with isolated void [79]. The factor "0.427" appearing in (4.24), instead of "0.283" as initially proposed by Rice and Tracey, has been computed by Huang [42] when reworking the numerics.

The evolution of the relative void spacing is obtained directly from 4.16

$$\chi = \frac{R_X}{L_X} = \frac{R_X}{R_{X0}} \frac{R_{X0}}{L_{X0}} \frac{L_{X0}}{L_X} = \frac{R_X}{R_{X0}} \chi_0 \exp\left(\frac{\epsilon_Z}{2}\right) \quad (4.25)$$

The value of the ductility ϵ_f can be estimated by plugging relationships (4.21), (4.22) and (4.25) into the void coalescence condition (4.14). The equations of the model are summarized in Table 4.1, while introducing also a nucleation strain ϵ_{nucl} . The input parameters of the model are: the stress triaxiality, T , the initial relative void spacing and void distribution parameter, χ_0 and λ_0 , respectively (or, alternatively, the particle volume fraction f_p), the nucleation strain ϵ_{nucl} , and the strain hardening exponent n . The model can be solved for instance by using a simple data analyzer software (the procedure requires to create a column with a serie of ϵ_z ranging between 0 and 5, a second column with W (4.29), a third column with χ (4.28), a fourth column with the left hand side of (4.26), a fifth column for the right hand side (4.26) and finally plot column 4 and 5 as a function of ϵ_z and determine the intersection, ϵ_f). The model is assessed in Figure 4.17 by comparing the predictions to the FE unit cell calculations for various stress triaxiality and particle volume fraction f_p . The predictions usually underestimate the FE cell results but the trends are well reproduced.

$$\frac{\left(\frac{3}{2}T + 1\right)}{(1 - \chi^2)} = \left[\alpha \left(\frac{1 - \chi}{\chi W} \right)^2 + 1.24 \sqrt{\frac{1}{\chi}} \right] \quad (4.26)$$

$$\alpha(n) = 0.1 + 0.22n + 4.8n^2 (0 \leq n \leq 3) \quad (4.27)$$

$$\chi = \chi_0 \frac{\left[(0.427 \exp(\frac{3}{2}T) - 1) \exp(0.427 \exp(\frac{3}{2}T)(\epsilon_z - \epsilon_{nucl})) - 1 \right] \exp(\frac{\epsilon_z}{2})}{0.427 \exp(\frac{3}{2}T)} \quad (4.28)$$

$$W = \lambda_0 \frac{\exp(\epsilon_z - \epsilon_{nucl}) - 1}{\exp(\frac{\epsilon_z - \epsilon_{nucl}}{2})} \quad (4.29)$$

Table 4.1 – Summary of the equations of the simple model for the ductility

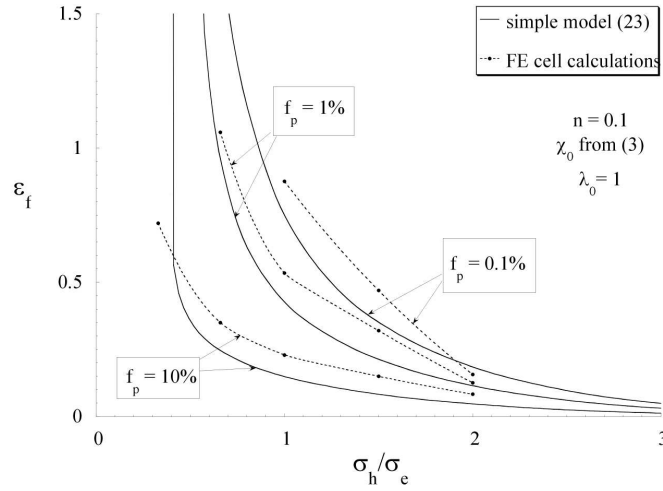


Figure 4.17 – Variation of the ductility as a function of the stress triaxiality for three particle volume fractions in the case of initially penny-shaped voids : comparison between the simple model (23) and the FE predictions.

4.5 Conclusions

This study takes part to an effort to enhance the micromechanical models of ductile fracture by incorporating more physics in order to (i) guide advanced

materials processing strategy, (ii) to optimize forming operation limited by ductile damage phenomena, and (iii) to enhance structural integrity assessment methods. In this theoretical study, the effect of the initial penny shape of the voids resulting from particle fracture or partial decohesion on the ductility has been carefully analyzed, leading to the following conclusions

1. The ductility of a material failing by the fracture of particles followed by void growth and void coalescence stages, is primarily controlled by the relative particle spacing, the stress triaxiality, and by the, possible, anisotropy in the particle distribution.
2. Hence, when working with a damage model accounting for the initial shape of the voids, the predicted response is independent of the choice of the initial porosity as long as it is related to the particle volume fraction f_p and initial void and particle aspect ratio W_0 and W_p , respectively, through the relationship $f_0 = (W_0/W_p)f_p$ while imposing a value for W_0 sufficiently small ($W_0 < 0.03$ is always safe).
3. If one uses a "regular" version of the Gurson model assuming spherical voids, the definition of an effective initial porosity $f_0 = f_p/W_p$ is a good approximation for low particle volume fraction ($f_p < 1-2\%$) but becomes less and less accurate for larger particle volume fractions.
4. The strain hardening capacity has, intrinsically, only a moderate effect on the ductility, although it will obviously play a major role at the structural level for postponing localization and reducing stress concentration. The ratio of the Young's modulus over the yield stress E/σ_0 has no effect on the ductility.
5. A particle surrounding a cavity has a minor effect on the void opening and puts a moderate constraint on the transverse void radius evolution: under low stress triaxiality ($T < 0.5$), the void contraction in the transverse is impeded leading to lower ductility than without the presence of a particle, while the opposite effect takes place under larger stress triaxiality. Neglecting the presence of the particle in the modeling of ductile fracture is a valid approximation.
6. Void coalescence following a stable void growth stage can occur before the onset of necking under purely uniaxial tension condition if the volume fraction of particles is high enough and/or the strain hardening exponent is large enough.
7. Void nucleation controlled ductile fracture is favored when the particle volume fraction is large, the nucleation stress is large, and the stress triaxiality is low.

8. Based on these conclusions, a closed-form very simple model as been developed for predicting the ductility of materials with a damage process starting with very flat voids, based only on the applied stress triaxiality, initial relative void spacing and initial distribution anisotropy.

Although much work remains to be done to carefully assess these conclusions on experimental data, some of them have already been validated, either quantitatively based on a relatively ideal system (cast Al alloys involving brittle Si particles, see [43]) or qualitatively based on results found in the literature (e.g. results on MMC such as given in ref [22]).

5

Micromechanics of low and high temperature fracture in 6xxx Al alloys

Chapter 5

Micromechanics of low and high temperature fracture in 6xxx Al alloys

The understanding and modeling of the deformation and fracture behavior of aluminium alloys at room and at hot working temperature is very important for optimizing manufacturing processes such as extrusion. The ductility of 6xxx aluminium alloys can be directly related to chemical composition and to the microstructural evolution occurring during the heat treatment procedures preceding extrusion if proper physics based deformation and fracture models are used. In this Chapter, room temperature and hot tensile tests are adopted to address this problem experimentally. Uniaxial tensile tests allow measurements of the flow properties for various deformation temperatures and microstructural states. The effect of the stress triaxiality, which is the key stress state parameter affecting the ductility, is studied using notched tensile tests at various temperatures and strain rates varying in the range 0.02 to 2 s^{-1} . SEM analyses of tensile specimens are carried out to study the damage evolution mechanisms at various temperatures. A micromechanics based model of the Gurson type considering several populations of cavities nucleated by different second phase particles groups is developed on the basis of the experimental observations. This model allows relating quantitatively microstructure and ductility at various temperatures, strain rates and stress triaxialities. Finite element simulations based on an enhanced micromechanics-based model are used to identify the unknown parameters of the model, to validate the model on data not used for the identification.

5.1 Introduction

Low and medium strength AlMgSi alloys are commonly processed by extrusion. Their extrudability depends to a large extent on chemical composition, casting practice, and homogenization treatment, which determine the microstructure of the billet before extrusion. A modern vision of process optimization is through setting up intelligent manufacturing strategies. Such strategies heavily depend on the capacity to integrate the various steps of the process in a chain of models. New solutions can be rapidly inserted owing to the potential to directly relate downstream problems to upstream problems. Here, the problem in mind is to relate the damage and fracture of profiles during extrusion to the chemical composition and homogenization treatment. One important ingredient of the problem is the development of predictive models that relate the microstructure to the damage properties. This field was mainly led by the structural community for two decades (80's and 90's) but has been more recently transferred to the materials and processes community. This transfer has required lots of new progress to adapt existing approaches to the reality of complex materials and complex loading conditions typical of forming operations [62, 63, 79, 38, 14, 58, 21, 65, 23, 90, 5, 19, 20, 10, 75, 12, 43, 47, 35, 83, 73, 80, 33, 30, 88, 46, 71]. The purpose of this chapter is to adapt and extend existing micromechanics based methodology to the problem of low and high temperature damage of 6xxx alloys. The next chapter will then be devoted to the problem of linking this scheme with real extrusion parameters, such as the maximum extrusion speed.

As discussed in details in previous chapters, aluminum alloys ENAA 6xxx contain a large amount of various intermetallic particles (typically 1%) with sizes typically ranging between 1 to 10 micrometers. These coarse particles have a first order effect on the formability and mechanical properties. The most typical are intermetallic compound particles such as plate-like β -Al₅FeSi and rounded α -Al₁₂(FeMn)₃Si. The brittle monoclinic β -Al₅FeSi phase, which is insoluble during solution heat treatment, is associated to poor workability and cause a poor surface finish [97, 2, 27, 48, 89, 28, 82, 67]. Damage initiation occurs by decohesion or fracture of these inclusions as referred by Agarwal, Toda and Kobayashi [2, 1, 49, 89]. The resistance to failure depends thus directly on the second phase particles content. The negative effect of the β -Al₅FeSi particles can be mitigated by performing a long homogenization heat treatment at a sufficiently high temperature, by which the β -Al₅FeSi phase transforms into the more rounded meta-stable cubic α -Al₁₂(FeMn)₃Si phase or into the equilibrium hexagonal α' phase. The optimization of the extrusion process depends on a thorough understanding of the homogenization kinetics and, in particular, in the link between the morphological evolution of the intermetallic inclusions during the homogenization process and the resulting gain in ductility.

The hot-working capability of aluminium alloys is thus dependent on both intrinsic parameters, e.g. materials microstructure, inclusions and constitutive properties, as well as extrinsic factors of the processing, e.g. temperature, strain rate, strain path and tooling. Currently, data on constitutive behavior as a function of homogenization parameters, forming strain rate and temperature are limited and/or incomplete, and usually based on very phenomenological approaches. The present investigation is aimed to probe the effects of the homogenization conditions on the room temperature and hot-working potential of two 6xxx series aluminium alloys ENAA 6060 and ENAA 6005A.

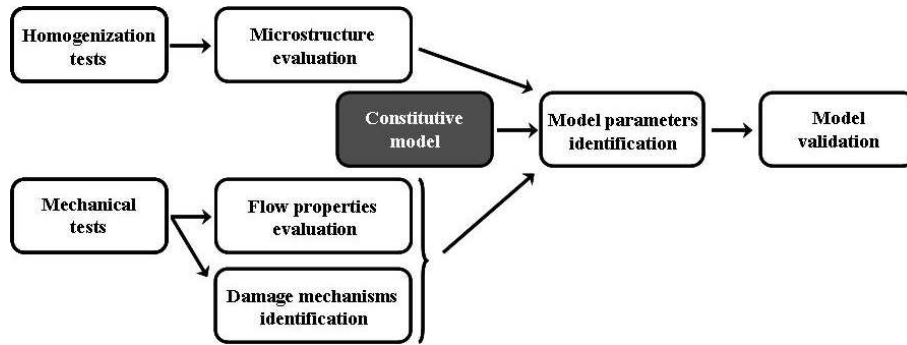
The methodology followed to build, identify and validate the ductility model requires the steps described hereafter, which will constitute the outline of the chapter:

1. The first part of the chapter summarizes the main data obtained for both 6060 and 6005 alloys material, which consist of industrial direct-chill cast aluminium alloys logs containing a volume fraction of intermetallic inclusions around 1%. The α/β -AlFeSi ratio is varied using different homogenization conditions. The microstructural evolution (β -to- α transformation) is studied by energy dispersive X-ray analysis (EDS) coupled with scanning electron microscopy (SEM). The accompanying morphology change is measured by image analysis. These results have already been presented in a previous chapter. Nevertheless, as this chapter is intended to be published, it asked to show again some microstructure data.
2. The hot ductility is measured from a campaign of uniaxial tests on smooth and notched cylindrical rods at various deformation temperatures and strain rates with different second phase particles contents. Among various screening tests, uniaxial tension test is the most common one since it also provides constitutive properties of materials and allows comparison between maximum ductility and microstructure analysis. It is also the easiest to adapt and control test at elevated temperatures. The constitutive behavior obtained from uniaxial tension is important in estimating the effects of various factors influencing the workability under more complex loading conditions.
3. The microstructure and the fracture surface of the tested specimens have been examined using scanning electron microscopy in an attempt to correlate tensile properties with changes in microstructure at high temperature. In situ tensile tests have been performed directly within a SEM at room temperature to observe the influence of second phase particles on damage mechanisms.
4. The model is a Gurson type constitutive model considering three different populations of cavities as motivated by the observations made during the

in-situ tensile tests and an advanced micromechanics based coalescence model. The material parameters are the volume fractions of particles, shapes of particles, critical stress for void nucleation and the elastoviscoplastic properties of the aluminium matrix.

- Furthermore, FE simulations based on an enhanced micromechanics-based model are used to relate quantitatively microstructure and ductility. First of all, they are used to identify the unknown parameters (nucleation stresses) of the model. Then, they are used to validate the model on experimental data not used for the identification. The validation is made on the prediction of the average fracture strain as a function of the deformation temperature, homogenization conditions, triaxiality state and alloy composition.

These steps and the methodology of this chapter are summarized in the following diagram.



5.2 Materials, Experimental methods and Mechanical data reduction scheme

5.2.1 Materials

The materials consist of industrial direct-chill casts of ENAA 6060 and ENAA 6005A aluminium alloys that are supplied in the form of 8 inches-diameter logs. The chemical composition is provided in Table 5.1.

The as-cast aluminium matrix contains ellipsoidal intermetallic β -AlFeSi inclusions mainly located along the grain boundaries. The different logs were subjected to a solution homogenization heat treatment in order to transform these particles into the rounded α -AlFeMnSi phase. The homogenization was performed at 585°C with different holding times. Both alloys have different levels of Mg, Si, Mn and Fe resulting in different homogenization kinetics and

Alloy	Mg	Si	Mn	Fe	Al
ENAA 6060	0.49	0.43	0.02	0.21	bal.
ENAA 6005A	0.56	0.59	0.04	0.18	bal.

Table 5.1 – Chemical composition (wt.%) of the aluminium alloys studied.

different mechanical behaviors.

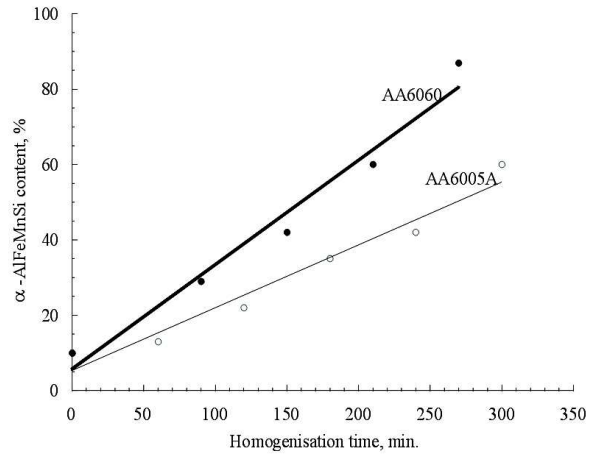
The quantitative chemical and morphological characterization of the intermetallic inclusions was performed using image analyses (IA) measurements coupled with scanning electron microscopy (SEM) observations and EDS measurements following a procedure described in [53] and in [56]. The volume fractions of AlFeSi inclusions were measured by IA, giving the values of 1% and 1.2% for the ENAA 6060 and ENAA 6005A, respectively. The evolutions of the α -AlFeSi particles content and of the particles average aspect ratio (aspect ratio = average particle width/average particle length) for an homogenization treatment performed at 585°C are presented in Figure 5.1(a) and (b) for the alloys ENAA 6060 and ENAA 6005A.

The quantitative evaluation of intermetallic particles transformation revealed that the relative proportion of α -AlFeMnSi phase varied systematically with homogenization treatment, such that this phase becomes increasingly dominant while increasing the homogenization soaking times at a fixed temperature. The aluminium alloy with the lowest Si and Mg content (ENAA 6060) leads to faster β -to- α transformation. The higher Si content has a stabilizing effect on the β -AlFeSi phase [97]. Consequently, the α particle content of the two alloys differs by more than 30% after 4h30 at 585°C.

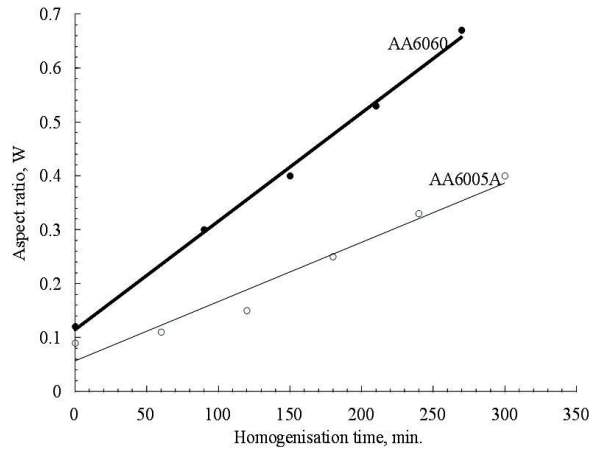
The initial value of the average aspect ratio (W) of the intermetallic particles, are almost the same for the two alloys: $W = 0.09$ for the alloy ENAA 6005A and $W = 0.11$ for the alloy ENAA 6060. During homogenization, as the β -to- α transformation takes place, the mean aspect ratio increases because of the spheroidisation process.

5.2.2 Characterization of the damage nucleation and evolution

Seminal contributions to the understanding of the mechanisms of ductile fracture have established that non-metallic inclusions and second phase particles play a fundamental role in the ductile fracture of metal alloys as the source of the voids which then grow by plastic deformation until final coalescence, e.g. [5]. The problem of void nucleation has received less attention than the problem of void growth, especially from an experimental point of view. The most common modes of nucleation are the complete or partial interfacial de-



(a)



(b)

Figure 5.1 – Evolution of the transformation of the β -AlFeSi particles into α -AlFeSi particles during homogenization at 585°C; (a) volume fraction of α -AlFeSi particles; (b) mean aspect ratio.

cohesion of the inclusion or the fracture of the inclusion [12, 14, 13]. In some materials, nucleation starts early after the beginning of loading whereas, in some other materials, fracture is controlled by nucleation, i.e. void nucleation is delayed and rapidly followed by the propagation of a macroscopic crack or plastic instability. Voids nucleation depends on the size, orientation, location and interfacial strength of the inclusion. Voids usually nucleate first on larger inclusions. Elongated inclusions tend to break in one or several fragments when their major axis is aligned in the direction of the maximum stress while interface decohesion takes place when the direction of the maximum stress is perpendicular to the major axis of the inclusion. The nucleation mode is thus influenced by the stress state as well as the attainment of the critical condition nucleation [12, 14, 13]. In order to study and characterize the damage nucleation modes in both ENAA 6060 and ENAA 6005 alloys at high temperature, metallographically prepared sections of unloaded damaged specimens were analyzed using a 25 keV Scanning Electron Microscope (SEM) after having imposed different levels of straining. Small samples were machined out of the necking region and grinded following planes parallel to the loading direction. These specimens were then polished using standard metallographic techniques.

At room temperature, the nucleation of the voids were analyzed during in-situ tensile tests performed within the SEM. The specimens have a thickness of 2 mm and an initial width of 3 mm. A smooth notch was machined in order to localize the damage and fracture phenomena in the center of the specimen. Specimens were polished before testing. Obviously, the characterization of the damage nucleation also provides interesting observations about the growth and coalescence regime when the deformation is further increased.

5.2.3 Tensile tests

Smooth round bars with a diameter of 9 mm and a gage length of 40 mm were machined from the homogenized logs parallel to the casting direction. The specimens were always extracted from a zone located at least 30 mm away from the ingots surface. Notches were machined in part of the specimens with notch radii of 2 mm and 5 mm, respectively in order to impose higher levels of stress triaxiality than in smooth tensile bars. The geometry and dimensions of the smooth and notched specimens are shown in Figure 5.2. The tests were performed on a screw-driven universal machine by imposing strain rates varying between 0.02 to 2 s⁻¹ and temperatures between 20°C and 590°C. An average true fracture strain measure is used to quantify the ductility, defined as

$$\epsilon_f = \ln \frac{A_0}{A_f} \quad (5.1)$$

where A_0 and A_f are the initial and final macroscopic areas, respectively. The final cross-sectional area is obtained by reconstructing the broken specimen and

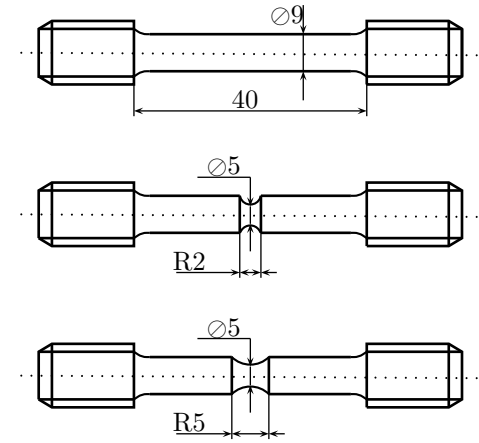


Figure 5.2 – Geometry of the test specimens, dimensions in mm: smooth and notched round bars.

measuring the diameter of the minimum cross section along several position.

5.2.4 Inverse procedure to determine uniaxial flow properties

The flow curves obtained from uniaxial tensile testing are directly useful only before the onset of necking. With increasing temperature, necking starts early due to the low strain hardening exponent and it becomes increasingly unreliable to extrapolate the flow curve up to large strains. Different options are available to determine the flow properties after the onset of necking, such as the use of the Bridgman correction [70] or the use of compression or torsion tests. The Bridgman correction requires the measurement, of at least, the current minimum cross-sectional area. As the evolution of the specimen section reduction could not be measured during testing due to the presence of the furnace device, no correction for necking could be made on the tensile curves. The experimental campaign being already quite extensive, we preferred not to perform other type of mechanical tests but to develop an inverse procedure. The procedure is based on the comparison between the experimental tensile curves and finite element calculations of the uniaxial tensile test in order to get, after several iterations, the flow properties of the non-damaged material up to very large strains. Finite element simulations of the uniaxial tensile test are carried out using a first guessed extrapolation of the experimental flow curve beyond the necking start point (beginning with a linear extrapolation). This method has been initially proposed by Norris et al. [68] and used later by several authors,

e.g. Pardoen and Delannay [70], Zhang et al. [98]. The iterative procedure is repeated until good agreement between experimental and numerical stress-strain curves is obtained as illustrated in Figure 5.3.

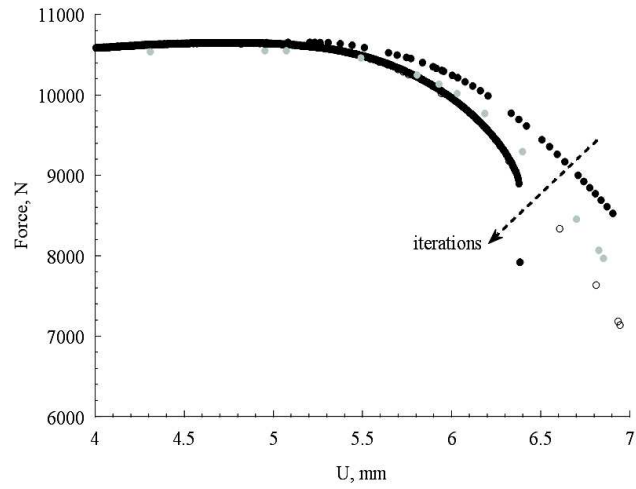
The simulations were performed using the general-purpose finite element code ABAQUS within a finite strain set up. Figure 5.4 shows a 3D representation of the finite element mesh. In order to take benefits of the symmetry of the problem, axisymmetric four noded elements were used with 41 elements along the radius of the bars. This large number of elements was found necessary in order to ensure fully converged results, in terms of the mesh discretization error. In order to trigger necking, a small initial diameter reduction of 5 μm was introduced in the cross-section located on the symmetry plane. All results presented in this chapter are obtained using those meshes. The procedure followed to identify the flow properties of the sound material up to large strains is slightly different for room temperature and high temperature.

At room temperature, damage is nucleated very early during testing. As the damage evolution slightly influences the force-displacement curve from the beginning of straining, we take it into account by using an extended Gurson type [73] constitutive model (see further for more details about the Gurson model and its extensions). For each alloy, the simulation is made by imposing an initial porosity as well as an average shape factor resulting from the microstructural characterization (see later). These simulations assume that damage nucleates mainly from the β -AlFeSi second phase particles at the beginning of plastic straining. In these simulations, the void coalescence condition is turned off as the interest at this stage was only on the flow properties.

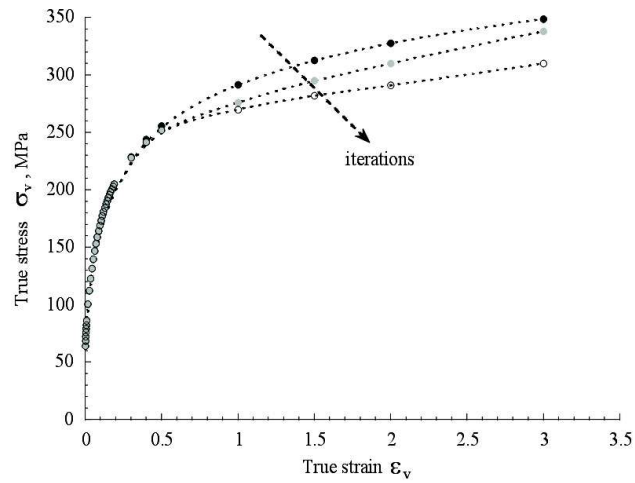
At high temperature, the procedure is quite different since, on the one hand, damage nucleates very late during straining, which makes the analysis more simple, and since, on the other hand, strain rate effects have to be taken into account, which makes the analysis more difficult. The damage mechanism was thus neglected at high temperature and the viscoplastic version of the J_2 flow theory was used for all the simulations. In order to simplify the identification, a fixed mathematical description of the flow curve was used at high temperature to describe the behaviour of the material (while at room temperature, no specific mathematical representation of the stress strain curve was imposed):

$$\frac{\sigma}{\sigma_0} = \left(1 + \frac{E}{\sigma_0} \epsilon^p\right)^n \left(1 + \frac{\dot{\epsilon}^p}{\dot{\epsilon}_0}\right)^m \quad (5.2)$$

The goal is thus to find n and m (hardening coefficient and strain rate sensitivity respectively) that allow the best match between the experimental and numerical stress-strain curves for the main part of these flow curves.



(a)



(b)

Figure 5.3 – Illustration of the iterative inverse identification procedure applied to the alloy ENAA 6060 at 20°C; (a) comparison between the experimental and simulated load-displacement curves (for three different iterations) and (b) the corresponding true stress-true strain curves.

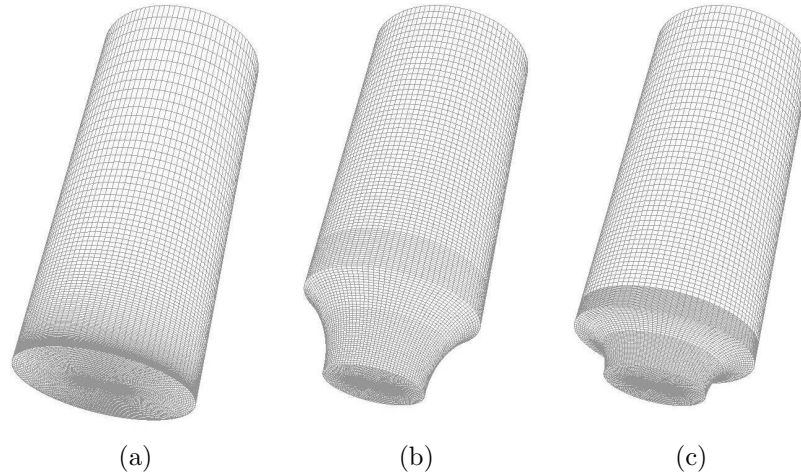


Figure 5.4 – 3D representation of the finite element meshes used to simulate the tensile tests on the smooth and notched round bars; (a) smooth specimen (b) notched specimen with a notch radius equal to 5mm (c) notched specimen with a notch radius equal to 2mm.

5.3 Experimental results

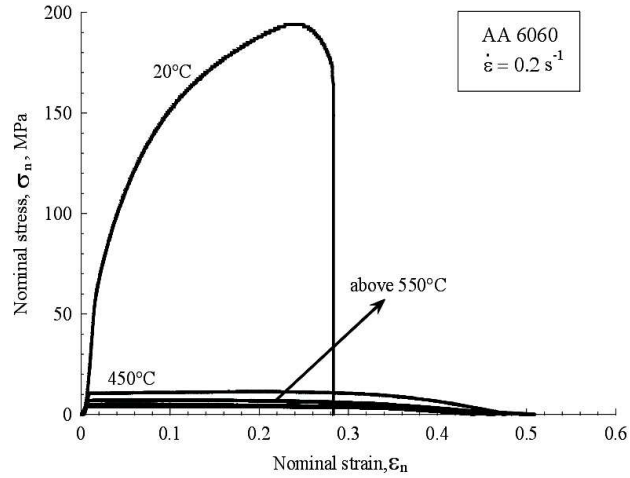
5.3.1 Mechanical tensile tests

5.3.1.a Nominal stress-strain relationships

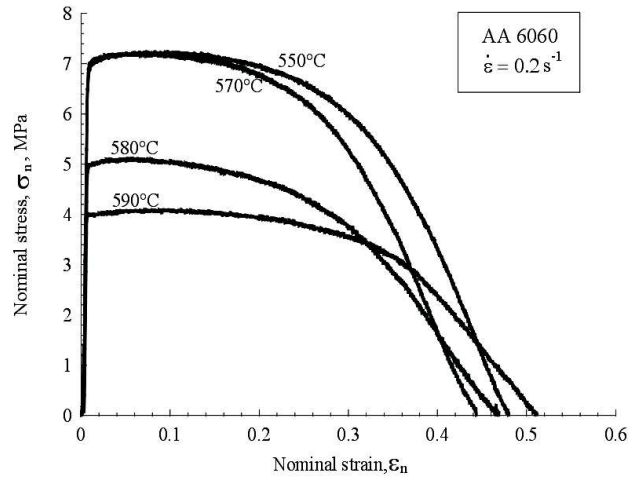
Figure 5.5 and Figure 5.6 show selected nominal stress-nominal strain curves obtained for the whole range of test temperatures (20-450-550-570-580-590°C).

Figure 5.5 belongs to the alloy ENAA 6060 while Figure 5.6 belongs to alloy ENAA 6005A. For both alloys, the homogenization condition was 2h30 at 585°C. The strain rates were always equal to 0.2 s^{-1} . The curves corresponding to the deformation temperatures superior to 550°C are repeated in Figures 5.5(b) and 5.6(b). The decrease of the strength with temperature is of course very marked. As shown in these figures, the flow properties as well as the total elongation differ between the two alloys. The alloy ENAA 6060 involves lower strength but is more ductile than the alloy ENAA 6005A when compared at identical test temperatures.

The effect of the homogenization conditions on the nominal uniaxial response is shown in Figures 5.7 and 5.8, for the alloys ENAA 6060 and ENAA 6005A, respectively, in the case of a deformation temperature of 550°C. Three homogenization times are compared for the alloy 6060: 2h30, 3h30 and 4h30, respectively, at 585°C. The volume fraction of the α -AlFeMnSi for these three

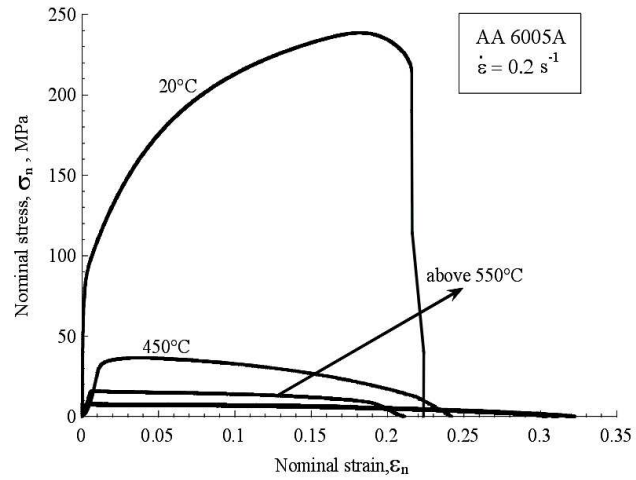


(a)

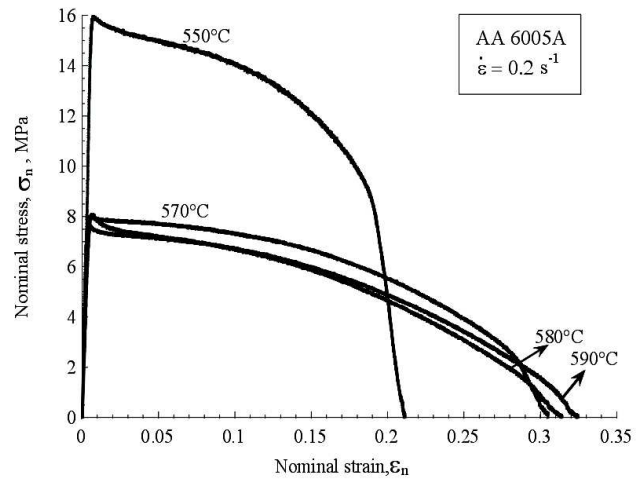


(b)

Figure 5.5 – Nominal stress- strain curves for the alloy ENAA 6060 homogenized at 585°C for 2h30 and deformed at different temperatures ranging 20°C to 590°C, at a strain rate of 0.2 s⁻¹ (a) all curves; (b) only the curves corresponding to temperatures larger than 550°C.



(a)



(b)

Figure 5.6 – Nominal stress- strain curves for the alloy ENAA 6005A homogenized at 585°C for 2h30 and deformed at different temperatures ranging 20°C to 590°C, at a strain rate of 0.2 s⁻¹ (a) all curves; (b) only the the curves corresponding to temperatures larger than 550°C.

conditions is equal to 32%, 40% and 72%, respectively. Again, three ho-

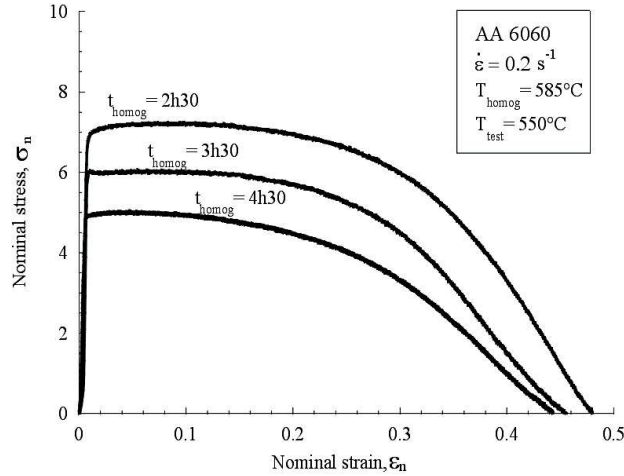


Figure 5.7 – Nominal stress-nominal strain curves for the alloy ENAA 6060 homogenized at 585°C with different holding times (2h30, 3h30 and 4h30) and deformed at 550°C, under a strain rate of 0.2 s⁻¹.

mogenization times are compared for the alloy 6005A: 2h30, 3h30 and 4h30, respectively, at 585°C. The volume fraction of the α -AlFeMnSi for these three conditions is equal to 19%, 28% and 42%, respectively. The flow strength decreases with increasing homogenization quality, i.e. with increasing conversion of the β -AlFeSi particles into α -AlFeMnSi particles (The β -AlFeSi particles have a larger strengthening effect than the α -AlFeSi particles).

Figure 5.8 also qualitatively shows that the ductility (elongation at fracture) of the alloy ENAA 6005A increases when the α -AlFeSi particles content increases.

While the room temperature strain rate sensitivity is known to be negligible for aluminium alloys, the rate sensitivity at high temperature can become very large [16, 84]. Figure 5.9 shows the nominal stress-strain curves obtained at 550°C under three different strain rates (0.02, 0.2 and 2 s⁻¹) for (a) ENAA 6060; (b) ENAA 6005A. The homogenization conditions are specified in the figure. The flow stress level significantly increases with strain rate, especially for the alloy ENAA 6060. Qualitatively, the ductility, seen here through the elongation at fracture, increases with increasing strain rate, which is unusual at least from the perspective of low temperature ductility.

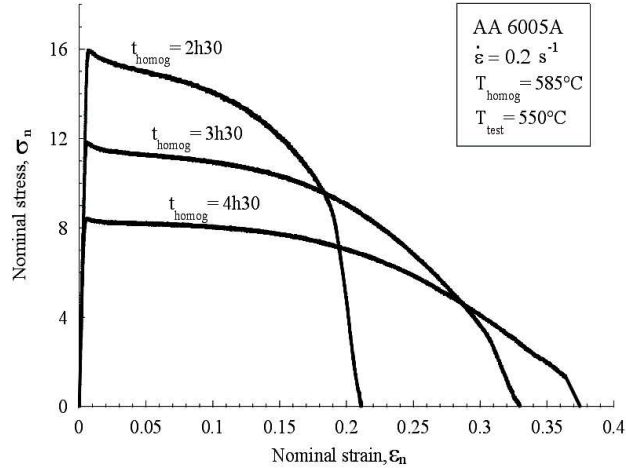


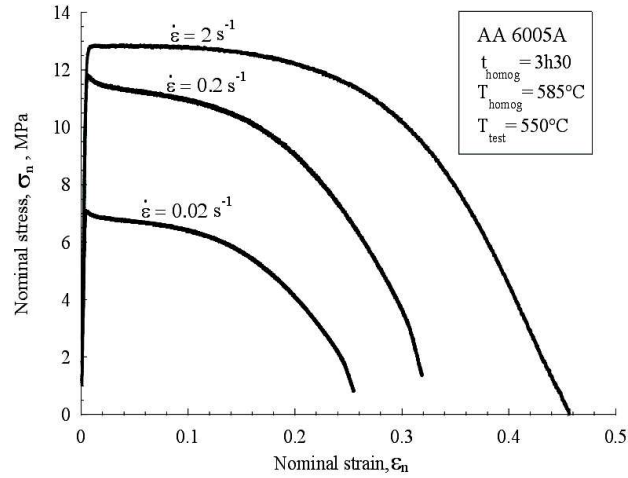
Figure 5.8 – Nominal stress-nominal strain curves for the alloy ENAA 6005A homogenized at 585°C with different holding times (2h30, 3h30 and 4h30) and deformed at 550°C, under a strain rate of 0.2 s⁻¹.

5.3.1.b Yield stress evolution

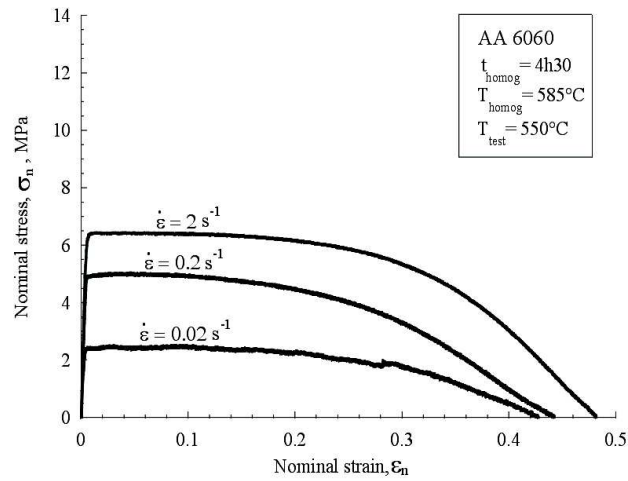
The evolution of the yield stress with the test temperature has been plotted in Figure 5.10 for the alloys (a) ENAA 6060 and (b) ENAA 6005 for three different homogenization conditions. As explained above, the yield stress systematically decreases with deformation temperature and with homogenization time, i.e. with a decrease of the β -AlFeSi particles content.

5.3.1.c Uniform elongation - Hardening behavior

The true strain at maximum load, ϵ_u is an indicator of the strain hardening capacity at least for small or moderate plastic deformation (i.e. up to ϵ_u). Figure 5.11 shows the variation of ϵ_u as a function of test temperature for both alloys homogenized at 585°C for different soaking times. At low or moderate temperature (20 to 450°C), the strain at maximum load is a good indicator of the onset of necking. At large temperature, the effect of m tends to stabilize necking and thus ϵ_u is not anymore a good indicator of the capacity to harden (e.g. [44]). For each alloy, ϵ_u decreases with increasing test temperature and, for a fixed temperature, it decreases with increasing homogenization time. Thus, the presence of β particles not only increases the yield strength but also the strain



(a)



(b)

Figure 5.9 – Nominal stress-nominal strain curves obtained at three different strain rates: 0.02, 0.2 and 2 s^{-1} for the alloys (a) ENAA 6060 homogenized at 585°C for 4h30 and (b) ENAA 6005A homogenized at 585°C for 3h30. Both alloys are deformed at 550°C .

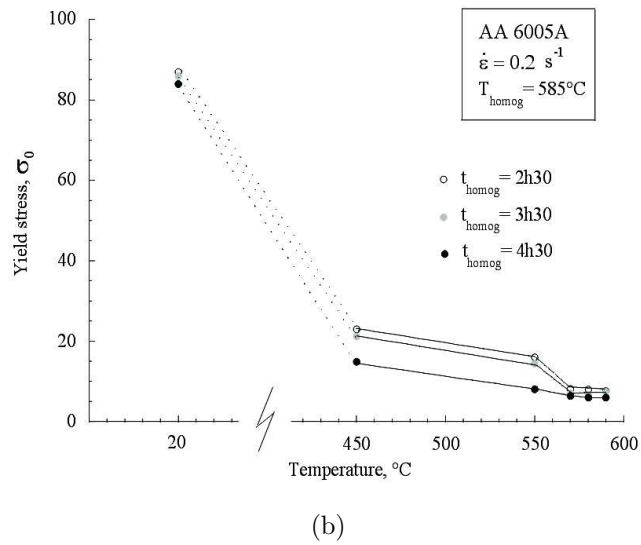
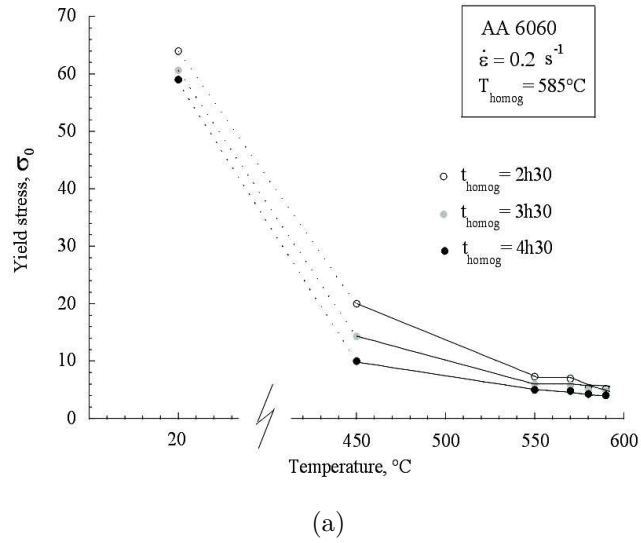


Figure 5.10 – Variation of the yield stress as a function of the deformation temperature for aluminium alloys (a) ENAA 6060 and (b) ENAA 6005A. Both alloys were homogenized at 585°C for three different holding times and deformed at a strain rate of 0.2 s^{-1} .

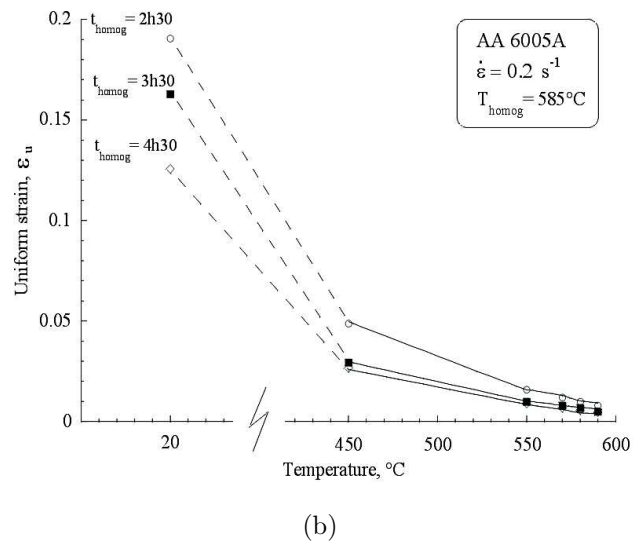
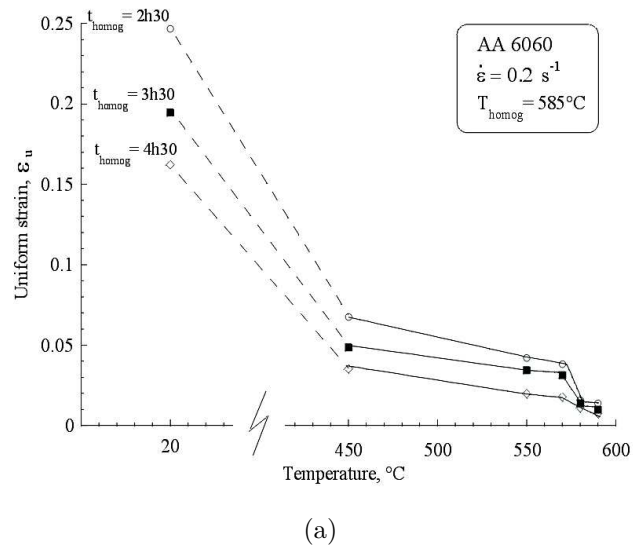


Figure 5.11 – Variation of the (true) uniform strain as a function of test temperature for alloys (a) ENAA 6060 and (b) ENAA 6005A. Both alloys were homogenized at 585°C with different holding times (2h30, 3h30 and 4h30) and deformed at a strain rate of 0.2 s⁻¹.

hardening capacity. As reported previously by Zajac [97], the work hardening exponent which is attributable to dislocation accumulation at the particles, is a function of particle size. Zajac showed that above a critical particle diameter ($6 \mu\text{m}$), dislocations accumulate at the particle as geometrically necessary dislocations, leading to a complex dislocations structure responsible for an increase of the work hardening rate. At the opposite, in structures dominated by well spheroidized $\alpha\text{-AlFeMnSi}$ particles, the dislocations are able to pass such particles via a climbing process and therefore the well homogenized alloys have a low work hardening coefficient and superior extrudability; both the increase of yield strength and of the strain hardening rate are detrimental for extrusion as they involve increasing extrusion pressure. At room temperature, the strain corresponding to the onset of necking ϵ_u is higher in the alloy 6005A alloy than in the alloy ENAA 6060.

5.3.1.d Inverse identification of the materials flow curves

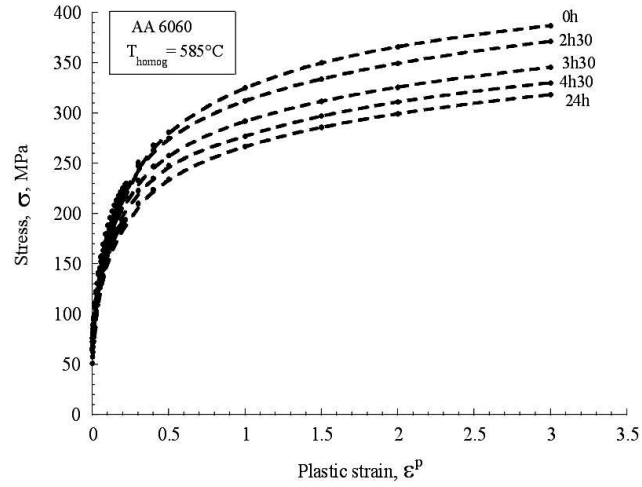
The inverse procedure described in section 5.2.4 has been applied to generate the flow properties of non-damaged material up to large strains. Figure 5.12 presents the room temperature flow curves for the alloys ENAA 6060 and ENAA 6005A corresponding to different homogenization conditions. As explained above, the strength levels decrease with increasing homogenization time as a result of a decrease of the solute content in the matrix. The alloy ENAA 6005A is systematically 20% stronger than the alloy ENAA 6060.

At higher deformation temperatures, the identification of the flow curves consisted in finding the strain hardening exponent n and strain rate sensitivity exponent m that provided the best match between the mathematical description (5.2) and the experimental results. Examples of flow curves identified for two temperatures, 450°C and 550°C , are given in Figure 5.13 for the alloys (a,b) ENAA 6060 and (c,d) ENAA 6005A. The rest of these flow curves can be found in Appendix E.

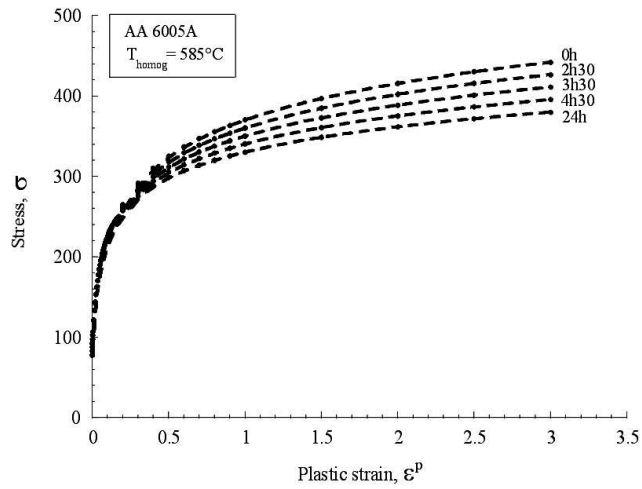
The full identification procedure was performed for only one homogenization condition (24 hours). We will thus assume in the modeling part hereafter that, at high temperature, n and m are independent of the homogenization time. Figure 5.14 shows the variation of the average n and m as a function of the deformation temperature. These values are also summarized in Table 5.2.

5.3.1.e True average fracture strain ϵ_f

The average true fracture strain defined by equ. (5.1) is the most physical experimental indicator to quantify the resistance to damage and fracture of a material under tensile loading conditions. In Figure 5.15, the true fracture strain corresponding to different homogenization times is plotted as a function of the deformation temperature for the alloys (a) ENAA 6060 and (b) ENAA

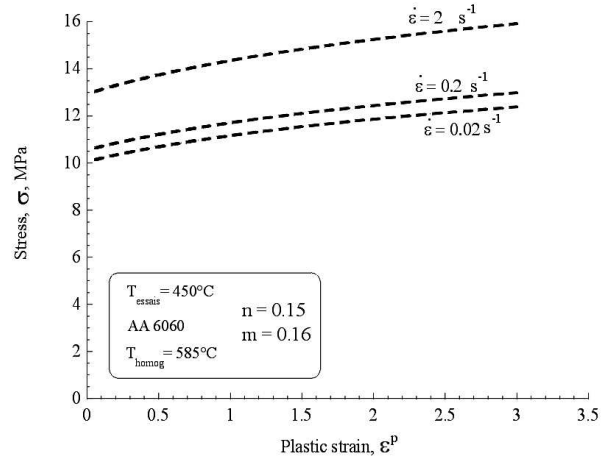


(a)

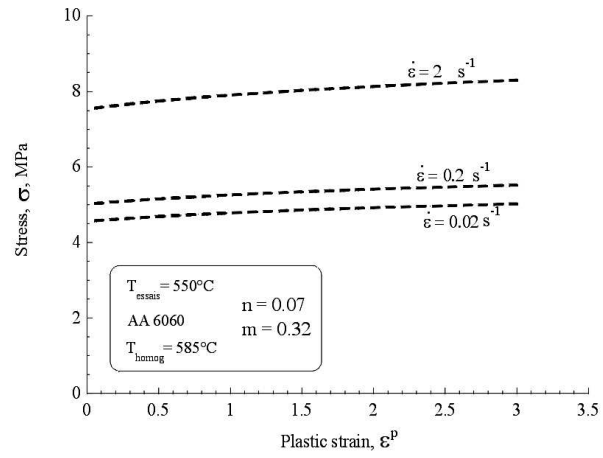


(b)

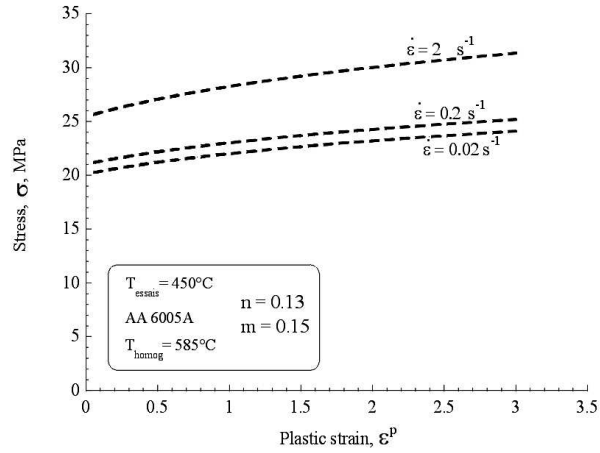
Figure 5.12 – True stress-true plastic strain flow curves at 20°C obtained after inverse identification for the alloys (a) ENAA 6060 and (b) ENAA 6005A. Both alloys were homogenized at 585°C for different holding times.



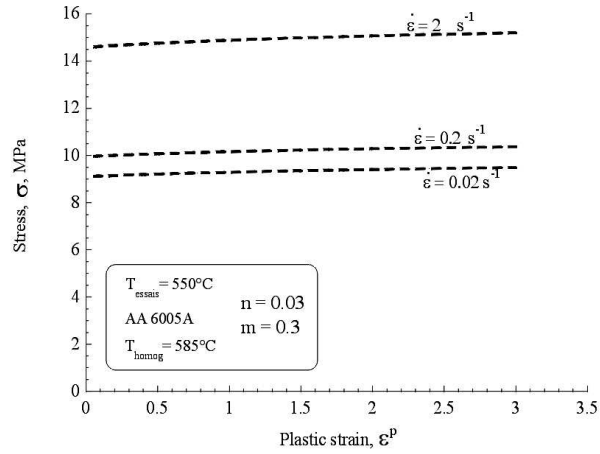
(a)



(b)



(c)



(d)

Figure 5.13 – True stress-true plastic strain flow curves for different strain rates equal to 0.02, 0.2 and 2 s⁻¹ at (a,c) 450°C and (b,d) 550°C for the alloys (a,b) ENAA 6060 and (c,d) ENAA 6005A. Both alloys were homogenized at 585°C.

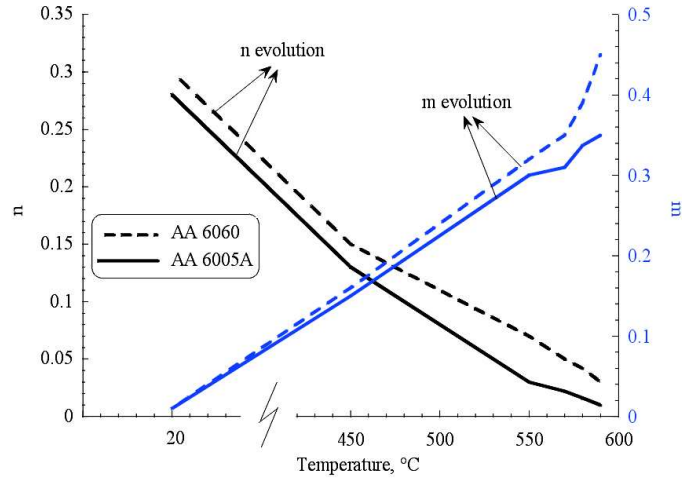


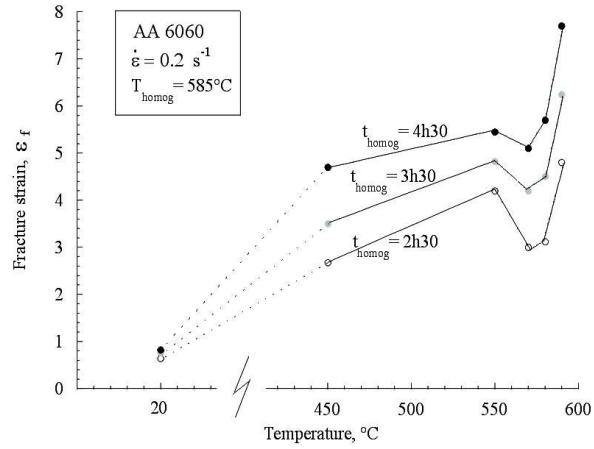
Figure 5.14 – Variation of the strain hardening exponent n and strain rate sensitivity exponent m identified with the iterative inverse procedure as a function of the test temperature for the alloys ENAA 6060 and ENAA 6005A, both homogenized at 585°C for 24h.

Temperature (°C)	ENAA 6060		ENAA 6005A	
	n	m	n	m
20	0.3	0.01	0.28	0.01
450	0.15	0.16	0.13	0.15
550	0.07	0.32	0.03	0.3
570	0.05	0.35	0.022	0.31
580	0.042	0.39	0.016	0.337
590	0.03	0.45	0.01	0.35

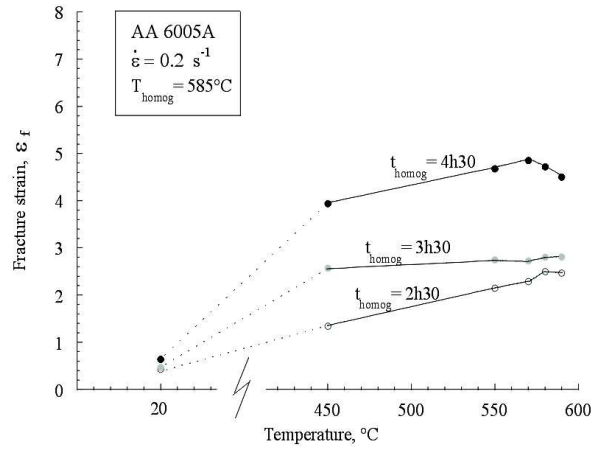
Table 5.2 – Values of the strain hardening exponent n and strain rate sensitivity exponent m identified with the iterative inverse procedure as a function of the test temperature for the alloys ENAA 6060 and ENAA 6005A, both homogenized at 585°C for 24h.

6005A.

As expected, the fracture strain significantly increases with temperature. The conversion of the elongated β particles into the more rounded α particles has also an extremely beneficial effect on the ductility, especially at high temper-



(a)



(b)

Figure 5.15 – Variation of the average true fracture strain ϵ_f as a function of the test temperature for the alloys (a) ENAA 6060 and (b) ENAA 6005A homogenized at 585°C for different holding times (2h30, 3h30 and 4h30).

ature. The larger ductility of the alloy ENAA 6060 is easily explained by the lower magnesium and silicon contents. The total volume fraction of intermetallic particles is also lower in the alloy ENAA 6060. Also, as shown in Figure 5.1, the conversion of the β particles into α particles is faster in the alloy ENAA 6060. Comparing the two alloys at the same homogenization time is thus not fair for the alloy ENAA 6005.

There are some details in the high temperature ductility that are worth commenting further. The alloy ENAA 6005A, shows a decrease in the ductility above a certain threshold temperature for the longest homogenization time. The true fracture strain in the alloy ENAA 6060 involves a marked drop around 570-580°C before increasing again at 590°C. The difference in the ductility evolution between both alloys probably reflects the differences in constituents present in the material. The drop in the ductility of the alloy ENAA 6060 around 570-580°C will be further discussed in the light of the fracture surface analysis (see further).

Figure 5.16 shows the effect of strain rate on the variation of true fracture strain of the alloy ENAA 6005 as a function of the test temperature. The fracture

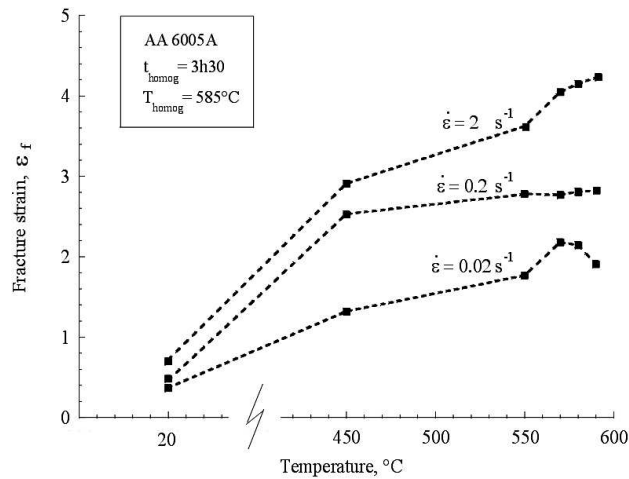


Figure 5.16 – Variation of the true fracture strain ϵ_f for different strain rates as a function of the deformation temperature for the alloy ENAA 6005A homogenized at 585°C for 3h30 (28% α -AlFeSi).

strain significantly increases with increasing strain rate. More strikingly, large

strain rates tend to suppress the decrease of the ductility at high temperature. The increasing rate can have two effects : a local increase of the temperature and an effect of preventing the diffusion related phenomena to occur.

The effect of the stress triaxiality on the fracture strain has been investigated for both alloys ENAA 6060 and ENAA 6005A using notched specimens. Figure 5.17 shows the variation of the fracture strain for the different specimen configurations as a function of the test temperature for the alloy (a) ENAA 6060 and (b) ENAA 6005A.

For the sake of comparison, an average value of the stress triaxiality was extracted from the FE simulations of the tests. The true fracture strain markedly decreases with increasing stress triaxiality whatever the temperature. The alloy ENAA 6005A seems to be more influenced by a change of stress triaxiality than the alloy ENAA 6060. But, we should note that the alloys are not compared at a similar amount of α particles. The drop in ductility of the alloy ENAA 6060 around 570°C appears also at larger stress triaxiality.

5.3.2 Fracture mechanisms

5.3.2.a In situ tensile tests at room temperature

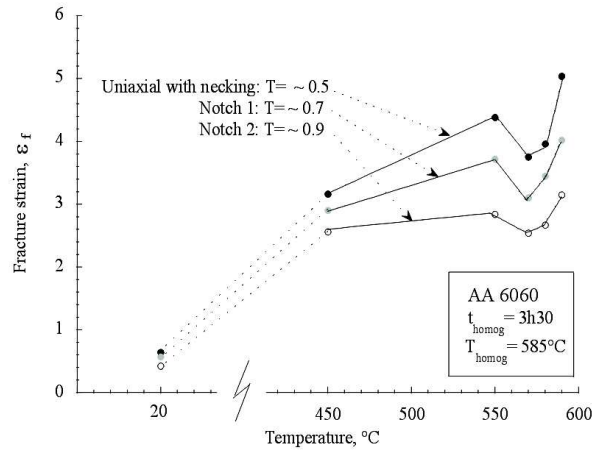
Void nucleation

The room temperature damage process up to fracture was characterized by performing in-situ tensile tests on polished micro tensile test specimens within the scanning electron microscope. These surface observations are known to be relevant to qualitatively determine the damage sequence but not to quantitatively study the damage evolution [7, 6]. Figure 5.18 shows representative damage sites at low strains.

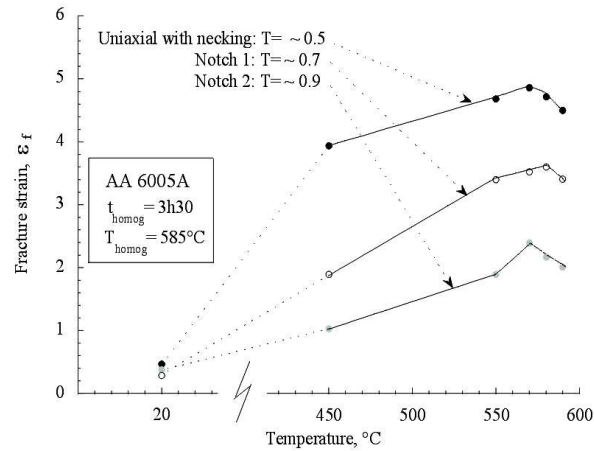
Both particle fracture and particle/matrix decohesion are observed. More or less all the particles of brittle second phases give rise to micro-void nucleation at the very beginning of straining.

Figure 5.19 shows how the fracture mode depends on the particle orientation. The majority of the particles oriented in the range of 0° to 45° with respect to the loading direction lead to particle fracture whereas the majority of the particles oriented in the range of 45° to 90° lead to particle/matrix interface decohesion.

The elongated particles aligned along the main loading direction break into several fragments. The cracks in the particles are normal to the macroscopic tension axis. The number of fragments increases with increasing particle length. The mean number of particle cracks estimated on a representative number of broken particles is equal to 3.35. The occurrence of such a marked degree of progressive multiple cracking suggests that the particle-matrix interface is strong at room temperature, since a second fracture can only occur under loads



(a)



(b)

Figure 5.17 – Variation of the fracture strain ϵ_f for various notch radius as a function of the test temperature for the alloys (a) ENAA 6060 and (b) ENAA 6005A homogenized at 585°C for 4h30 and deformed.

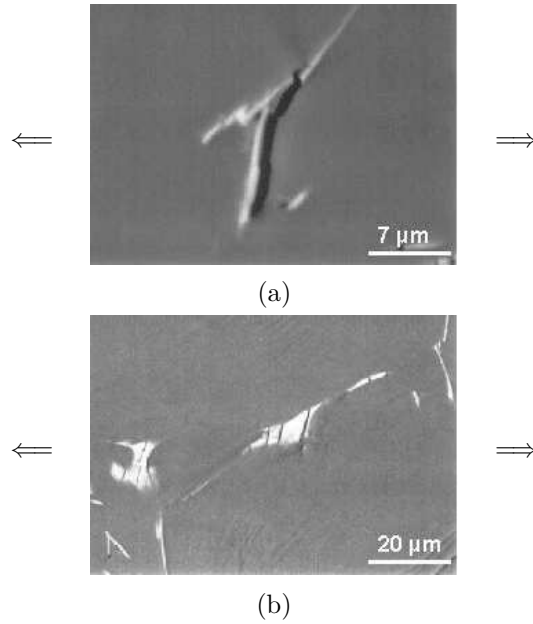


Figure 5.18 – SEM micrographs taken during in situ uniaxial testing of the alloy ENAA 6060 at low strains. Two damage nucleation mechanisms are observed (a) particle/matrix decohesion and (b) particle fracture.

transferred by shear across the particle sides and through normal stresses at one end [94, 95]. A complete description of damage mechanisms at room temperature is exposed here below.

Void growth

After nucleation, the initially flat voids resulting from interface decohesion or particle fracture open by plastic deformation of the surrounding matrix. As shown in Figure 5.20, the micro-cracks nucleated by particle cracking grow mostly in the direction of the applied stress.

The presence slip bands reveals the plastic yielding mechanism required to grow the voids. Micro-cracks formation and growth goes along with further particle cracking and particle decohesion. As the straining continues, the brittle Fe-rich inclusions rotate as the ductile matrix deforms. This rotation can bring new Fe-rich second phase particles into morphological orientations that may facilitate particle cracking. This can also affect the damage progression leading to higher damage level.

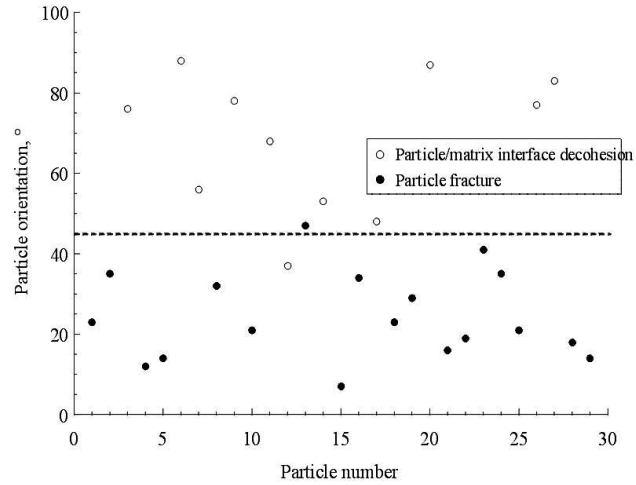


Figure 5.19 – Dependence of the fracture mode on the orientation of the long axis of the intermetallic particles with respect to the loading direction.

Void coalescence

The process of "independent" growth of the voids, as if they were alone within a sound matrix, continues up to a point where the voids have grown so much that they start interacting with each other and the plasticity tend to the localize in the intervold ligament. Figure 5.21 presents a set of micrographs of voids that are on the verge of coalescing or right after linking up.

Some voids have become almost equiaxed when coalescing. Micrograph 5.21(c) and 5.21(d) show the interactions between the large voids nucleated by interface decohesion and the serie of smaller voids nucleated by particle fragmentation .

5.3.2.b Interrupted tensile tests at high temperature

Some of the uniaxial tensile tests performed at 550°C were interrupted after various amount of straining. Figure 5.22 presents typical micrographs showing the damage evolution at 550°C in the alloy ENAA 6060 alloys. The first occurrences of damage at this temperature are observed only at large strains (i.e. > 0.3). The nucleation always occurs through debonding along the particle/matrix interfaces. The nucleation proceeds by partial debonding. Full debonding require additional straining.

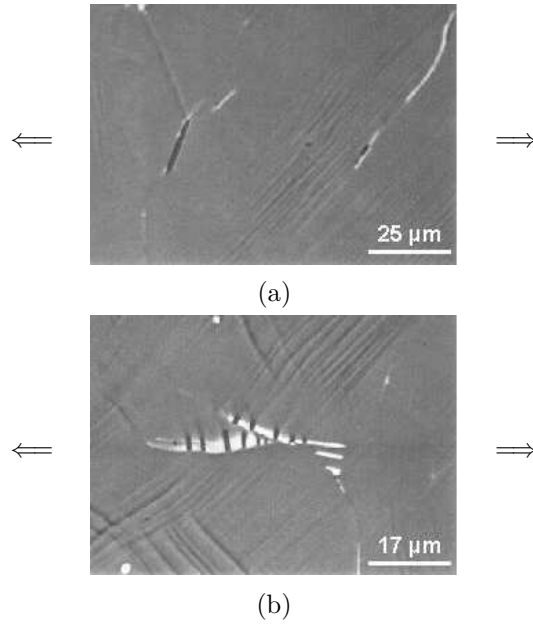


Figure 5.20 – SEM micrographs taken during in-situ tensile test performed at room temperature on the alloy ENAA 6060 and showing the opening of the voids for (a) voids nucleated by interface decohesion, (b) voids nucleated by particle fragmentation.

5.3.2.c Fracture surface

The fracture surfaces presented hereafter belong to the alloy 6060 with 72% of α -AlFeSi inclusions. The differences observed when compared to the alloy 6005 or other homogenization treatment will be mentioned in the text. Up to 550°C, the fracture surfaces present the classic ductile profile with dimples. Figure 5.23 shows the presence of particles inside the dimples. EDS measurements have confirmed that these particles are β -AlFeSi inclusions, which act as void nucleation sites. The sizes and shapes also match the analysis of the β particles. Figure 5.23(a) shows the existence of two different dimple sizes, which can be related to the presence of the two populations of voids (resulting from the two different void nucleation modes).

At 570°C and 580°C, the fracture surfaces are quite different as shown in Figure 5.24 for the alloy ENAA 6060. Intergranular and shear like fracture surfaces are observed without well defined dimples. This observation can be directly related to the fall in ductility in this temperature range, see Figure 5.15(a). This fracture mechanism is typical of fracture due to incipient melting along grain boundaries (liquid metal embrittlement) inside an alloy [97, 24, 25, 64].

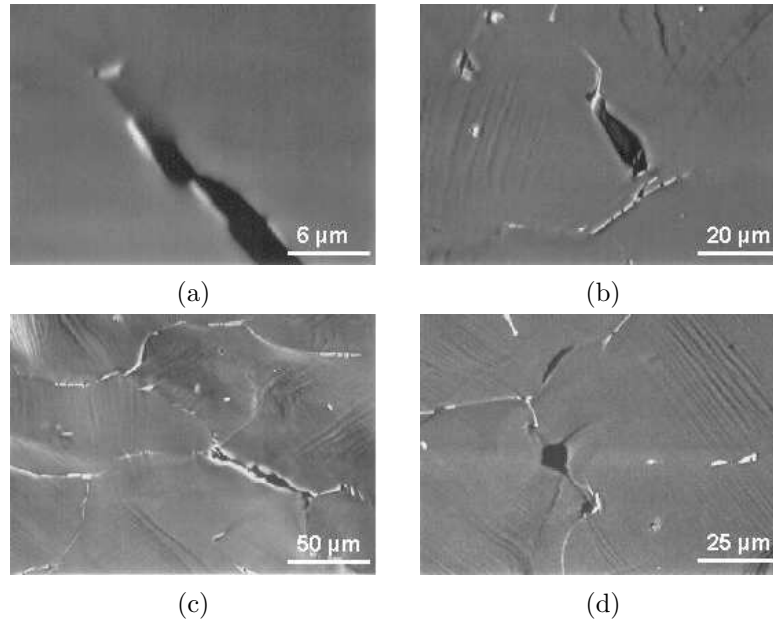


Figure 5.21 – SEM micrographs taken during in-situ tensile test performed at room temperature on the alloy ENAA 6060 and showing the end of the opening of the void at the end of the damage process, the interactions between the large voids initially nucleated by particle decohesion and the interactions between the large voids and the smaller voids nucleated by particle fragmentation.

It corresponds to the observations previously made on the same composition [56], where TEM and DSC analysis revealed the presence of Mg_2Si and pure silicon inclusions combined with the presence of $\beta-AlFeSi$ particles. The eutectic melting reaction $Al + Si (Mg_2Si) + \beta-AlFeSi \rightarrow liquid$ occurring at $578^\circ C$ can explain the observed behaviour. The drop of ductility associated to this local melting process is already observed for the samples tested at $570^\circ C$, presumably because of the plasticity-induced heating. Figure 5.25 indicates that, at $590^\circ C$, the fracture is again ductile in the alloy ENAA 6060. This figure shows that at large temperatures, the fracture surfaces is made of a few very big voids. A very stable void growth process is thus possible at these temperatures. Local melting was never observed for the alloy ENAA6005A which always exhibits a classical ductile fracture surface with dimples. The difference between both alloys concerning this phenomenon lies in the presence or not of Mg_2Si and Si precipitates. The casting and the homogenization conditions imposed during the production of the ENAA 6005A alloys prevented the presence of these phases.

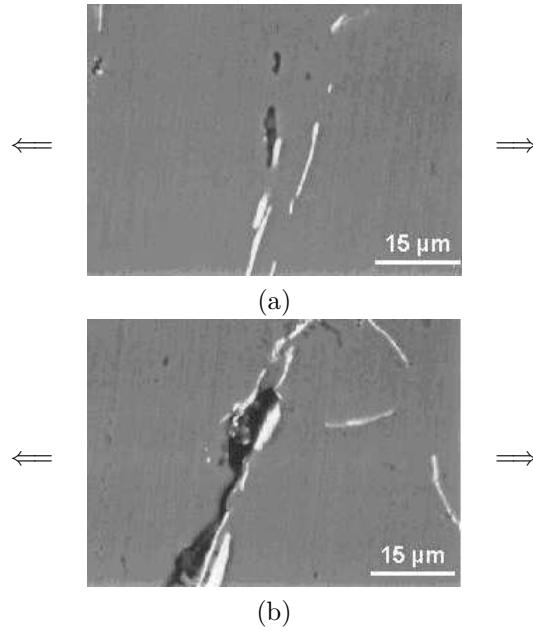


Figure 5.22 – SEM micrographs showing some features of the process of (a) void nucleation and growth and (b) void growth and coalescence, the alloy ENAA 6060, deformed at 550°C (samples machined and polished from prestrained unloaded specimens). Only particle/matrix interface decohesion is observed.

5.4 Micromechanical modeling

5.4.1 Physical model

A physical model, schematically illustrated in Figure 5.26, can be formulated based on the characterization of the damage evolution presented in the previous section.

At room temperature, the intermetallic β -AlFeSi particles oriented in the range 0° to 45° with respect to the loading direction lead to particle fragmentation. The voids initially present a penny shape. A specific analysis of the growth and coalescence of penny shape voids has been presented in chapter 4. The intermetallic β -AlFeSi particles, which are oriented between 45° to 90° with respect to the loading direction lead to particle/matrix interface decohesion. The initial void volume fraction associated to this mechanism is equal to the volume fraction of particles with an aspect ratio W_p equal to about 0.1. Considering that the majority of the intermetallic particles are uniformly distributed along the grain boundaries and that almost all give rise to voids, one can assume

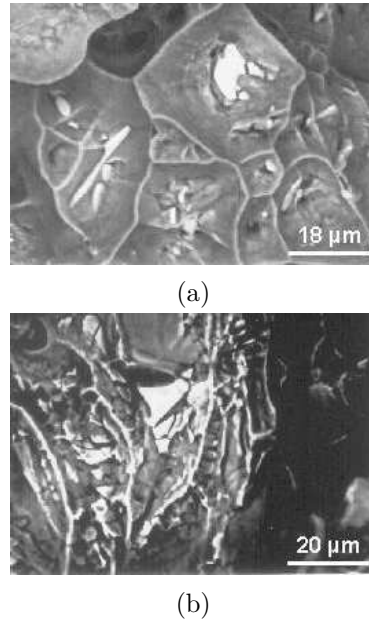
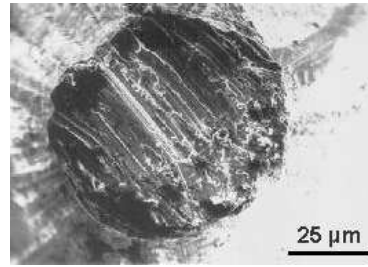


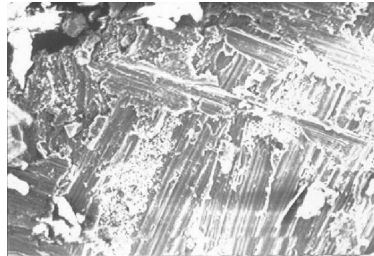
Figure 5.23 – Fractographies showing the presence of the intermetallic particles within the dimples.

that 50% lead to particle multiple fractures whereas the other 50% lead to particle/matrix interface decohesion. The more rounded α -AlFeMnSi particles create also damage but only by particle/matrix interface decohesion. At room temperature, all this damage is nucleated in the very beginning of straining. The large voids nucleated by interface decohesion dominate the damage process. The coalescence of the large voids is definitely accelerated by the presence of the smaller voids resulting from particle fragmentation.

At high temperature (above 450°C), the stresses undergone by the intermetallic particles is much smaller and damage is mainly nucleated by β -AlFeSi particle/matrix decohesion driven by accumulation of plastic strains along the interfaces. Furthermore, the voids do not nucleate at the beginning of straining but only when the stress triaxiality has reached a higher value (after necking). The small particles do not play a role in this mechanism. At high temperature, only the large voids play a role in the damage process. Viscoplastic effects result in very stable void growth process, postponing to very large strains the coalescence process. The melting of the particles in the alloy ENAA 6060 at temperature around 580°C can be, as a first approximation, seen as a void nucleation process occurring at the beginning of the loading.



(a)



(b)

Figure 5.24 – Fracture surfaces of ENAA6060 specimens deformed at 570°C and 580°C revealing the change of fracture mode resulting from the melting of at least some of the intermetallic particles.

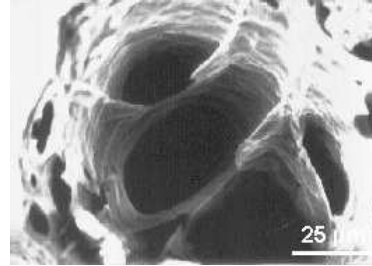


Figure 5.25 – Fracture surface observed at 590°C for the alloy ENAA 6060.

Based on this physical model, the necessary ingredients for a micromechanics based constitutive models should :

1. A void nucleation condition that takes into account three possible populations of voids and two different modes of nucleation. By assuming that the critical condition for nucleation do not change too much with temperature, the disappearance of particle fragmentation at high temperature is expected to be outcome of the model, without adding any

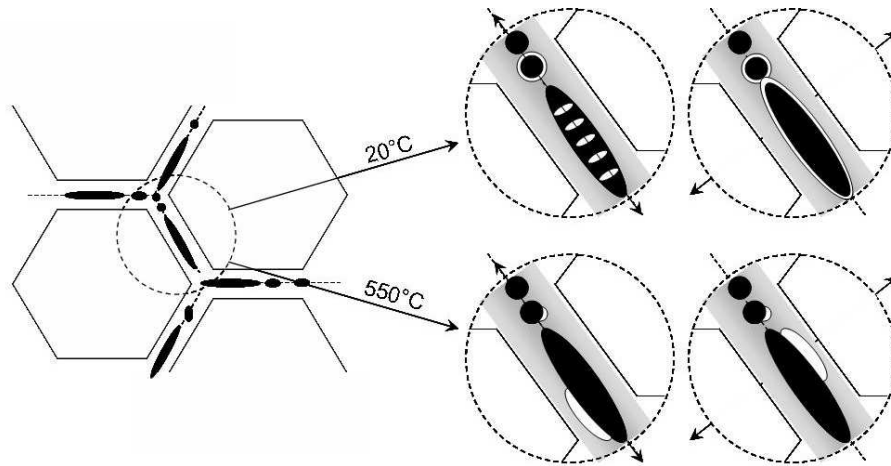


Figure 5.26 – Damage initiation mechanisms in aluminium alloys ENAA 6xxx at room temperature and at high temperature.

ad-hoc assumption.

2. The void growth model should account for the effect of the initial flat void shape of the large voids which is known to affect the void growth kinetic (as seen in chapter 4 and in [57]) as well as the attainment of the void coalescence condition. Properly accounting for void shape effect is known to be essential for encompassing various stress triaxiality levels, in the regime of low stress triaxiality [73, 11, 72].
3. The presence of the smaller voids (nucleated by particle fragmentation) which grow in between the large voids should be accounted for in a way or another, at least through their effect on the coalescence mechanism.
4. Viscoplastic effects have to be taken into account in order to encompass different temperatures and the effect of the strain rate.

5.4.2 Micromechanics-based full constitutive model

5.4.2.a Introduction

The goal of the present model is to address the different aspects described above through a micromechanical description of the three stages of void nucleation, growth and coalescence in an elasto-viscoplastic solid. We start by providing a general presentation of the model before showing how it has been adapted to the specific problem of the damage and fracture of the 6xxx alloys studied in

this work. The range of application of this model is for describing the damage evolution in elasto-viscoplastic materials involving *small volume fraction of particles giving rise to primary spheroidal voids and a secondary population of cavities*. The extent to which the model properly accounts for the presence *several populations of primary voids* and for the effect of a *second population of voids (involving the definition of what is considered as a second population)* is described in the presentation.

As shown in Figure 5.27, the particles giving rise to one first population of primary voids are characterized by the two principal radii R_{pz} and R_{px} and two spacings L_{pz} and L_{px} (for the sake of simplicity, we do not introduce index i to distinguish between different populations of primary voids, the distinction will be made later). The volume fraction of the large particles is noted f_{1p} with

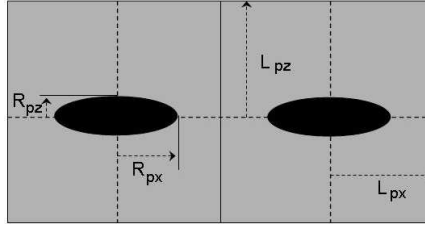


Figure 5.27 – Model material for first population of primary particles.

aspect ratio $W_{1pi} = R_{pz}/R_{px}$ and particle anisotropy distribution parameter $\lambda_{1pi} = L_{pz}/L_{px}$. The volume fraction of particles which will give rise to the second population of voids (only one second population) is noted f_{2p} with a shape W_{2p} , assuming an isotropic distribution, i.e. $\lambda_{1p} = 1$. If the primary voids nucleate by full decohesion, the initial void volume fraction f_{10} is equal to f_{1p} and $W_{10} = W_{1p}$. If the primary voids nucleate as a result of particle fracture or from partial decohesion, the initial void aspect ratio W_{10} is arbitrarily fixed to $W_{10} = 0.01$ and the initial void volume fraction is then uniquely determined. The initial anisotropy distribution parameter of the primary voids λ_{10} is equal to λ_{1p} . The initial relative void spacing $\chi_{10} = R_{0x}/L_{px}$ is related to the three other non-dimensional quantities f_{10} , W_{10} and λ_{10} through the following expression:

$$\chi_{10} = \frac{R_{0x}}{L_{px}} = \left(\frac{R_{0x}^3}{L_{px}^3} \right)^{\frac{1}{3}} = \left(\frac{R_{0x}^2 R_{0z} R_{0x} L_{pz}}{L_{px}^2 L_{pz} R_{0z} L_{px}} \right)^{\frac{1}{3}} = \left(\frac{f_{10} \lambda_{10}}{\gamma W_{10}} \right)^{\frac{1}{3}} \quad (5.3)$$

where γ is a geometric factor which depends on the arrangement of the voids (see Chapter4, section 4.1). For the sake of simplicity, the secondary voids will be assumed initially spherical, i.e. $W_{20} = 1$, which will require to define an effective initial porosity f_{20} (see chapter 4).

A J_2 isotropic hardening elastic-viscoplastic response is assumed for the matrix surrounding the particles, characterized by the mathematical representation eqn. (5.2) during plastic deformation.

The Poisson ratio of the matrix ν is always taken equal to 0.3. The flow properties of real materials do obviously follow more complex evolutions than eqn. (5.2) especially at high temperature due to microstructure evolution involving complex hardening and softening mechanisms. There is no difficulty in extending the present model to any other type of flow representation.

5.4.2.b Before void nucleation

Before the nucleation of the first voids, the material is assumed to behave as an isotropic hardening J_2 elastic-viscoplastic material with effective flow properties in uniaxial tension described eqn. (5.2). For large volume fraction of particles ($f_p > 5-10\%$), a micro-macro type constitutive model homogenization such as the incremental mean field model of Doghri and Ouair [26] would obviously be more appropriate to describe the response of the composite material under general loading histories. The current version of the model is thus intrinsically limited to materials involving low particle volume fractions.

5.4.2.c Void nucleation condition

The fracture of a particle or of an interface is assumed to occur when the maximum principal stress in the particle or at the interface reaches a critical value:

$$\sigma_{princ}^{particle\ max} = \sigma_{ci}^{bulk} \text{ or } \sigma_{ci}^{interf} \quad (5.4)$$

which is different for each mechanism. The indice i designates one specific population of particle. Following the Eshelby theory [29] and the secant modulus extension to plastically deforming matrix proposed by Berveiller and Zaoui [15], the maximum principal stress in an elastic inclusion (and at the interface) $\sigma_{princ}^{particle\ max}$ can be related to the overall stress state by using:

$$\sigma_{princ}^{particle\ max} = \sigma_{princ}^{max} + k_s(\sigma_e - \sigma_0) \quad (5.5)$$

where σ_{princ}^{max} is the maximum overall principal stress and k_s is a parameter of order unity which is a function of the inclusion shape and of the loading direction. This void nucleation criterion was initially proposed by the Beremin group [14] who also identified k_s from experimental data. They found that the values of k_s predicted by the theory were about two times higher than the experimental values because of an overstiff response of the homogenization scheme.

The rate of increase of the void volume fraction associated to the nucleation of

new voids from a population i of particles by particle fracture or decohesion is taken as a function of the plastic strain rate:

$$\dot{f}_{nucli} = g_i(\bar{\epsilon}^p) \bar{\epsilon}^p \quad (5.6)$$

where $\bar{\epsilon}^p$ is the effective plastic strain rate of the matrix material. A polynomial form for the function $g_i(\bar{\epsilon}^p)$ is chosen:

$$g_i(\bar{\epsilon}^p) = a_{1i}(\bar{\epsilon}^p)^4 + a_{2i}(\bar{\epsilon}^p)^2 + a_{3i} \quad (5.7)$$

When the condition eqn. (5.5) is fulfilled, with the corresponding effective plastic strain noted $\bar{\epsilon}^p = \bar{\epsilon}_{ci}^p$, the nucleation starts and takes place during a range of strains $\Delta\bar{\epsilon}_i^p$. The parameters a_{ni} are chosen in such a way as to avoid discontinuities in the porosity evolution: both $g_i(\bar{\epsilon}_{ci}^p)$ and $g_i(\bar{\epsilon}_{ci}^p + \Delta\bar{\epsilon}_i^p)$ as well as their first derivatives are taken equal to 0.

The void nucleation condition eqn. (5.4) applies when the inclusions, reinforcements or precipitates can be considered as brittle solids. A critical maximum principal stress corresponds to the critical stress in the particle required to reach the critical stress intensity factor for the propagation of the nanoscale internal defects present within the particles [51]. A condition for the fracture of the interface between the particle and the matrix should also ideally include a second necessary condition stating that the energy be larger than the interface toughness [80, 7]. As mentioned above, more advanced homogenization scheme or the use of tabulated stress concentration factors [61] (e.g. see the comprehensive analysis of Lee and Mear, 1999) would deliver more accurate estimate of the stress in the particle. Also, the validity of the micro-macro condition eqn. (5.5) is questionable when rate dependent effects become significant, i.e. when typically $m > 0.05$, and homogenization schemes for viscoplastic materials are required, see Montheillet [17]. In conclusion, this void nucleation condition should only be seen as a qualitative model that approximately accounts for the dependence on the mode of loading, on the particle shape and on the mode of nucleation.

5.4.2.d Void growth model

1. Evolution law for the void volume fraction f

As soon as voids nucleation starts for one family of particles, the accumulation of plastic deformation causes the enlargement of the voids and an increase of the void volume fraction which, by volume conservation, writes

$$\dot{f}_{growth} = (1 - f) \dot{\epsilon}_{ii}^p \quad (5.8)$$

where $\dot{\epsilon}_{ii}^p$ are the ij components of the overall plastic strain rate tensor. The full evolution law for the void volume fraction writes

$$\dot{f} = \dot{f}_{growth} + \sum_i \dot{f}_{nucl} \quad (5.9)$$

in which the nucleation of new voids from the i family of particles is accounted for. At this stage, the model does not distinguish anymore between the different families of primary voids and merge all the contributions into one global void volume fraction.

2. Evolution law for the void aspect ratio W

From a micromechanical analysis of the growth of a spheroidal void in a rate independent ($m = 0$) J_2 perfectly plastic material ($n = 0$), Gologanu et al. [35, 36] derived the following evolution law for W :

$$\left. \frac{\dot{W}}{W} \right|_{m=0} = \frac{3}{2}(1 + h_1) \left[\dot{\epsilon}^p - \frac{\dot{\epsilon}_{kk}^p}{3} \delta \right] : P + h_2 \dot{\epsilon}_{kk}^p \quad (5.10)$$

This analysis, completed by subsequent works [73, 72, 11], leads to expressions for h_1 and h_2 as a function of W , f and n . The full expressions are provided in Appendix C. P is a projector tensor, defined by $e_z \otimes e_z$ and e_z is a unit vector parallel to the main cavity axis; δ is the Kronecker tensor. In this version of the model, the main void axis e_z does not rotate and remains parallel to the maximal principal stress (see Scheyvaerts et al. [69] for a discussion about the void rotation effects).

Klocker and Tvergaard [47] showed that the evolution of the void aspect ratio in rate sensitive matrices departs significantly from eqn. (5.10). The void aspect ratio increases more rapidly for large rate sensitivity m than for small m . We have used the results of the void cell simulations of Klocker and Tvergaard [47] to introduce a correction to eqn. (5.10) depending on the value of m . In their work, a void aspect parameter k is defined such that

$$k = \frac{1}{W_0} \frac{\dot{R}_z}{\dot{R}_x} = \frac{W}{W_0} \left(\frac{\dot{\epsilon}_z + 2\dot{\epsilon}_x + \frac{\dot{f}}{f} + 2 \left. \frac{\dot{W}}{W} \right|_{m=0}}{\dot{\epsilon}_z + 2\dot{\epsilon}_x + \frac{\dot{f}}{f} - \left. \frac{\dot{W}}{W} \right|_{m=0}} \right) \quad (5.11)$$

where use was made of the relationships presented in Appendix D to express everything in terms of the primary variables of the model. From the results of their void cell calculations, Klocker and Tvergaard [47] suggest the following empirical law for k :

$$k = k_0(T, W_0) + m k_m(T, W_0) \quad (5.12)$$

where k_m and k_0 are fitted functions of the initial void shape W_0 and stress triaxiality, optimized numerically. Here, k_0 is not evaluated from the fit of Klocker and Tvergaard [47] but directly from eqn. (5.11) using eqn. (5.10). The correction term for the rate sensitivity k_m in eqn. (5.12) does not vary much for a relatively wide range of stress triaxiality ($T < 2$) and W_0 values

with an average value $k_m = 6 (\pm 2.5) k_0$. As a first approximation, the rate sensitivity effect is well captured using $k_m = 6k_0^2$ (the more accurate correction from Klocker and Tvergaard [47] is proposed in Appendix D). For larger stress triaxiality, k_m may significantly depart from $6k_0$ but in that case an accurate description of the void evolution law is much less important with respect to the evolution of the void volume fraction. After some elementary algebra (see Appendix B), the void aspect ratio evolution law finally writes

$$\frac{\dot{W}}{W} = \frac{[W_0 k_0 (1 + 6m) - W]}{[W_0 k_0 (1 + 6m) + 2W]} \left(\frac{\dot{f}}{f} + \dot{\epsilon}_z + 2\dot{\epsilon}_x \right) \quad (5.13)$$

Finally, it is important to note that cavities in this model nucleate with an initial shape equal to the mean shape of the already growing voids (whatever the population it belongs to). Circumventing this limitation of the model would require significant extra complexity for an improvement which, we believe, is minor, except perhaps in very specific problems. We will provide in the identification section 5.4.4.a an approximate method to account for that effect by correcting the initial porosity into an effective porosity.

3. Evaluation of the plastic strain rate

The plastic strain rate is taken normal to the flow potential:

$$\dot{\epsilon}_{ij}^p = \dot{\gamma} \frac{\partial \Phi}{\partial \sigma_{ij}} \quad (5.14)$$

where Φ is the flow potential proposed by Gologanu et al. [36] for a porous materials involving spheroidal voids and corrected by Klocker and Tvergaard [47] for the rate sensitivity. This flow potential writes

$$\Phi = \frac{C}{\sigma_y^g} \|\sigma' + \eta \sigma_h^g X\|^2 + 2q(g+1)(g+f)p_m \left(\kappa \frac{\sigma_h^g}{\sigma_y} \right) - (g+1)^2 - q^2 \left(g + \frac{1-m}{1+m} f \right)^2 = 0 \quad (5.15)$$

where

1. σ' is the deviatoric part of the Cauchy stress tensor;
2. σ_h^g is a generalized hydrostatic stress defined by ;
3. J is a tensor associated to the void axis and defined by $(1 - 2\alpha_2)e_z \otimes e_z + \alpha_2 e_x \otimes e_x + \alpha_2 e_y \otimes e_y$;
4. X is a tensor associated to the void axis and defined by $2/3e_z \otimes e_z - 1/3e_x \otimes e_x - 1/3e_y \otimes e_y$;

5. $\|\cdot\|$ is the von Mises norm;
6. $C, \eta, g, \kappa, \alpha_2$ are analytical functions of the state variables W and f provided in Appendix C;
7. q is a parameter which has been calibrated has a function of f_0, W_0 , and n (see [72]):

$$q = \frac{1}{2} + q_1 \left(\frac{q_b - 1}{\pi} \right) + \frac{1}{2} q_b \quad (5.16)$$

with

$$q_b = 1 + (0.65 - 1.75n - \frac{1}{2}f_0^{1/4}) \left(\frac{1}{2} + \frac{\tan^{-1}(2.4 - 2\ln(W_0))}{\pi} - \frac{1}{44W_0} \right) \quad (5.17)$$

where q_1 is usually taken as equal to 1.5 (slightly more accurate predictions can be obtained if one introduces a dependence of q_1 in the stress triaxiality T , see [72]). This expression is valid for $W_0 > 0.1$. If $W_0 < 0.1$, q is taken equal $q(W_0 = 0.1)$ from eqns (5.16) and (5.17).

8. The function p_m writes

$$p_m(x) = h_m(x) + \frac{1-m}{1+m} \frac{m}{h_m(x)}, \quad h_m(x) = (1 + mx^{1+m})^{1/m} \quad (5.18)$$

This function converges towards the *cosh* function of Gurson [38] and Gologanu et al. [36] for elastoplastic materials ($m \rightarrow 0$)

The plastic dissipation in the matrix material is related to the overall rate of plastic work through the energy balance initially proposed by Gurson [38]:

$$\sigma_y \bar{\epsilon}^{\dot{p}} (1 - f) = \sigma_{ij} \epsilon_{ij}^{\dot{p}} \quad (5.19)$$

which, combined with eqns (5.3) and (5.14), determines the plastic multiplier $\dot{\gamma}$. The stress rate tensor is then directly evaluated from

$$\dot{\sigma}_{ij} = L_{ijkl} (\epsilon_{kl}^{\dot{p}} - \epsilon_{kl}^{\dot{p}}) \quad (5.20)$$

where the L_{ijkl} are the elastic moduli. The variation of the yield stress σ_y of the matrix material is obtained using the consistency condition $\dot{\Phi}=0$.

Note finally that the effect of the particle on the void growth rate is not taken into account. In the case, of particle decohesion, the particle affects the void growth rate only under very low stress triaxiality by preventing the contraction of the void in the direction transverse to the main loading direction or under large shear strains because of the void rotation (see [90, 86, 85, 83]).

5.4.2.e Onset of void coalescence

The first stage of void growth by relatively homogeneous plastic deformation of the matrix surrounding the voids is interrupted by the localization of the plastic flow in the ligament between the voids. This localization corresponds to the onset of coalescence. From that point on, a second mode of void growth, called void coalescence, starts, driven by plasticity localized between the primary voids. The problem is quite similar to an internal necking process at a microscale. Thomason [87] proposed the following condition for the onset of coalescence:

$$\frac{\sigma_z}{(1-f_2)\sigma_y} \frac{1}{1-\chi^2} = \frac{2}{3} \left[\alpha \left(\frac{1-\chi}{\chi W} \right)^2 + 1.24 \sqrt{\frac{1}{\chi}} \right] \quad (5.21)$$

where $f_2 = 0$ in the original criterion and the parameter α has been fitted as a function of the average value of the strain hardening exponent n : $\alpha(n) = 0.1 + 0.22n + 4.8n^2$ ($0 \leq n \leq 0.3$), see Pardoen and Hutchinson, [72]. Criterion (5.21) states that coalescence occurs when the stress normal to the localization plane reaches a critical value. This critical value decreases as the voids open (W increases) and get closer to each other (χ increases). The dominant parameter controlling the transition to the coalescence mode is the relative void spacing χ . The porosity affects the coalescence indirectly through the obvious link with the void spacing χ and through its softening effect on the applied stress σ_z . In the present study, coalescence always occurs in a band normal the main void axis. In more advanced applications of this model (Scheyvaerts et al., [69]), the localization condition eqn. (5.21) is tested in all possible directions, which requires to generalize the definition of χ and W as a function of the orientation of the localization plane. No correction is made for the rate sensitivity effect, which anyway plays a role by influencing the evolution of the internal variables σ , σ_y , χ and W .

It has been repetitively reported in the literature (e.g. Cox and Low, [32, 60, 59, 91]) that the nucleation and growth of a second population of voids might very significantly accelerate the damage process and cut down the ductility. Our assumption here is that this secondary voids will have mainly an effect on the onset of void coalescence. If we consider that the presence of secondary voids within the ligament between two large primary voids does not influence the growth of the primary voids nor the overall response of the material, the only possible effect of these small voids is through a local softening that will accelerate the onset of coalescence. This softening was introduced heuristically into eqn. (5.21) by multiplying the current mean yield stress of the matrix material by $(1-f_2)$. Motivated by FE void cell simulations involving both large primary voids and small secondary voids modelled as a regular Gurson continuum (see [31]), it was found that the localization process was triggered by the local value of f_2 in the most damaged region of the ligament and thus by

the associated local softening. In other words, if the cell calculations are used to evaluate both f_2 in the most damaged part of the ligament and σ_z , σ_y , W and χ , then eqn. (5.21) provides relatively accurate predictions of the onset void coalescence. The most damaged region was always found next to the surface of the primary voids in the minimum section of the ligament. Consequently, f_2 in eqn. (5.21) should be seen as the local value of f_2 next to the surface of the primary voids.

Now, an estimate of the evolution of f_2 in the region next to the surface of the primary void is required in order to couple the void coalescence condition eqn. (5.21) to the void growth model presented in the previous section. The state of deformation adjacent to the surface of the primary voids can be described in the following way. The local circumferential strain rate on the equatorial section of the void surface ($z = 0$) is directly related to the transverse rate of the void growth through:

$$\dot{\epsilon}_{\theta\theta}^S = \frac{\dot{R}_x}{R_x} = \frac{1}{3} \left(\dot{\epsilon}_z + 2\dot{\epsilon}_x + \frac{\dot{f}}{f} - \frac{\dot{W}}{W} \right) \quad (5.22)$$

where use was made of the relationships presented in Appendix B. In order to estimate the local strain rate $\dot{\epsilon}_{zz}^S$, an arc of the ellipsoid was mapped onto the z-axis while assuming that the rate of straining along this line is uniform. This means that $\dot{\epsilon}_{zz}^S$ is the largest in the plane $z = 0$ and decreases monotonously when moving to the pole at $x = 0$, $z = R_z$. The motivation for this assumption is to capture the concentration of plastic deformation along the equatorial plane of the void. The local strain rate $\dot{\epsilon}_{zz}^S$ at $z = 0$ thus writes :

$$\dot{\epsilon}_{ZZ}^S = \frac{\dot{R}_z}{R_z} \frac{P_e}{4R_z} \quad (5.23)$$

Using the approximate solution for the perimeter of the ellipse

$$P_e \approx 2\pi\sqrt{0.5(R_x^2 + R_z^2)}$$

and the relationships of Appendix B, (eqn.5.23) becomes :

$$\dot{\epsilon}_{zz}^S = \left(\dot{\epsilon}_z + 2\dot{\epsilon}_x + \frac{\dot{f}}{f} + 2\frac{\dot{W}}{W} \right) \left(\frac{\pi}{2} \sqrt{\frac{1}{2} \left(\frac{1}{W^2} + 1 \right)} \right) \quad (5.24)$$

Finally, using the fact that $\dot{\sigma}_{rr}^S = 0$ at the surface of the void (because $\sigma_{rr}^S = 0$), together with eqns (5.21) and (5.22), the evolution of f_2 can be computed using relationships (5.9)-(5.15)-(5.19)-(5.20) particularized to spherical voids after the voids have started to nucleate following the relationships presented in section 5.4.2.c.

The coalescence model used here involves only one extra parameters: the initial void spacing, which has a physical meaning and can be related to microstructural measurements.

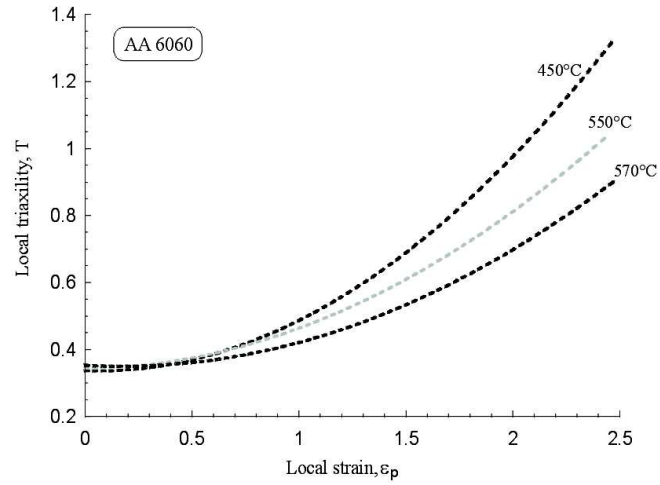
5.4.2.f Void coalescence

The modelling of the material response during the coalescence phase is not addressed here. This phase is unimportant when dealing only with the fracture strain in low stress triaxiality problems. However, adequate modelling of the final stage of the drop of the load carrying capacity becomes essential for properly simulating ductile tearing (see [37]). Various coalescence models, i.e. empirical or micromechanical descriptions of the material behavior during the coalescence phase, have been worked out by [66, 72, 11, 69].

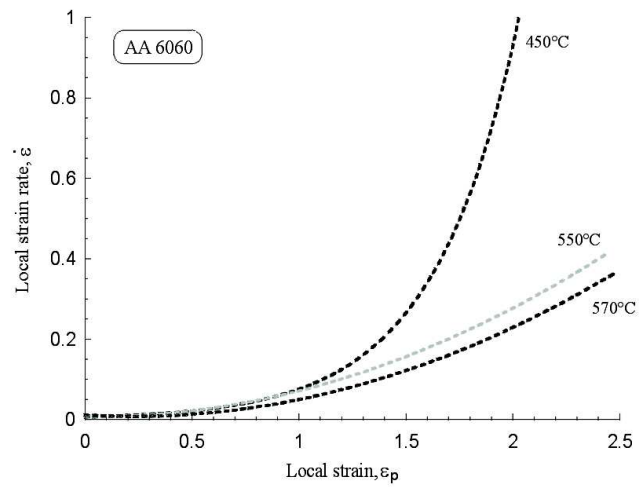
5.4.3 Numerical method and problem formulation

A Fortran program has been developed in order to integrate the constitutive model presented in the previous section under homogenous loading conditions. Axisymmetric loading conditions are prescribed in terms of a stress triaxiality history and effective strain rate history. In order to simplify the analysis, use was made of that code to simulate the response of the material point located in the most damaged region of the specimens tested experimentally. The methodology consisted in extracting from the FE simulations described in section 5.2.4 the stress triaxiality history and effective strain rate history in the element located at the centre of the minimum section of each specimen. These simulations were performed assuming a J_2 elasto-viscoplastic response. Then, the loading history is applied to the Fortran program in order to determine the local fracture strain. Finally the correspondance is made between the local fracture strain and the reduction of section calculated with the FE simulation. This methodology allows to accelerate the identification procedure as well the parametric study. An implementation of the rate independent version of the model into the code Abaqus Standard, using the UMAT sub-routine capabilities has been used to check the validity of that methodology. The influence of ductile damage on the macroscopic behavior of a non cracked structure is negligible until cracking initiates. From that point, fracture occurs with limited additional deformation. Neglecting the coupling between the mechanical fields and the damage is thus acceptable up to the point of fracture initiation and fracture initiation is an excellent indicator of the end-of-life of non-cracked specimens.

For the sake of illustration, Figure 5.28 shows the evolution of the stress triaxiality and strain rate as a function of the local equivalent strain for the central element of an initially smooth bar of the alloy ENAA 6060. The evolution of triaxiality is provided for different test temperatures in Figure 5.28(a) and the evolution of strain rate is provided in Figure 5.28(b). These evolutions already provide interesting information to qualitatively understand the variations of the ductility. Increasing the temperature leads to decreasing stress triaxiality, mainly because increasing the strain rate sensitivity very much smooth down



(a)



(b)

Figure 5.28 – Evolution of the local triaxiality (a) and local strain rate (b) as a function of the local plastic strain during FE calculations of the uniaxial tensile tests in the more loaded central element.

the sharpness of the neck. An increase in the deformation temperature also leads to a decrease of the local strain rate.

5.4.4 Results of the modeling

After identification of the free parameters, the micromechanical model and numerical scheme exposed in the previous section are used to predict the fracture strain for the conditions tested experimentally. The results are presented first for the low temperature conditions and then for the whole range of temperatures.

5.4.4.a Parameters identification

There are three types of parameters to identify:

1. the flow properties of the sound material,
2. the geometrical parameters defining the microstructure,
3. the critical stresses for the different modes of void nucleation.

The identification of the flow properties has been described in details in section 5.2.4.

Concerning the microstructure, three parameters must be defined: the initial void volume fraction of each population of voids, the initial void aspect ratio for each population of voids and the void distribution parameter for each population of voids.

A smart average initial shape W_0 for the two primary populations has first to be defined. It is indeed the transformation of the β -AlFeSi into α -AlFeMnSi which we speculate to be essential in controlling the improvement of ductility. A simple rule of mixture is used

$$W_0 = \frac{f_{10}^A W_{10}^A + f_{10}^B W_{10}^B}{f_{10}^A + f_{10}^B} \quad (5.25)$$

Both populations of primary voids result from interface decohesion and the initial void shape can thus be identified to the intermetallic particles aspect ratio. Based on the characterization of the β -AlFeSi and α -AlFeSi, one thus gets

$$\begin{aligned} W_{10}^A &= 0.1 \\ W_{10}^B &= 1 \end{aligned}$$

The initial void volume fractions f_{0i} can be related to the volume fraction of particles initiating damage. The *most important population of primary voids*, f_{10}^A , is created by the decohesion of the interface of the β -AlFeSi particles oriented with the long axis perpendicular to the main loading direction, which,

as shown in Figure 5.19, corresponds to half the volume fraction of β -AlFeSi particles, hence

$$f_{10}^A = 0.5 f_{\beta\text{-AlFeSi}}$$

The *other population of primary voids*, f_{10}^B , results from the α -AlFeMnSi particle/matrix decohesion. The fact that the model allows for the nucleation of different "main" populations, but with an initial void aspect ratio corresponding to the void aspect ratio of the already growing voids, leads to a subtlety in the identification of the initial volume fraction of a population that will nucleate voids with very different initial shapes. This is the case here because the α -AlFeMnSi particles are spherical. Based on the results presented in chapter 4, an effective porosity that accounts for the fact that the voids nucleate with a shape different than spherical is defined as

$$f_{10}^B = f_{\alpha\text{-AlFeSi}} W_{10}^\beta(\epsilon_{\text{nucleation}})$$

The voids initiated by the multiple fractures of the elongated β particles are considered here as a *secondary population* f_{20} which will only affect the coalescence of the primary voids. An effective initial volume fraction has to be used in order to account for the initial penny shape of the voids into the regular version of the Gurson model that only deals with spherical voids (the regular version of the Gurson model is used for taking into account the growth of the second population). Experimentally, it was found that, on the average, each particle gives rise to 3.35 voids, hence:

$$f_{20} = \frac{0.5 f_{\beta\text{-AlFeSi}} W_0^{\text{second population}} 3.35}{W_{\beta\text{-AlFeSi}}}$$

Only the initial void distribution index λ_0 is taken equal to 1 in all cases as there is no preferential distribution or orientation of the intermetallic phases in the homogenized aluminium alloys.

As the damage nucleation mode has been identified as very dependent of deformation temperature, very different initial parameters are used in the model as a function of temperature.

Finally, the two free parameters of the model that have to be adjusted are the critical stress values entering the void nucleation law (5.4). First we assume that the critical stress is the same for the interface fracture in the case of the β and α particles. Then, we also assume, as a first guess, that the critical stress does not change with temperature and is the same in both alloys. The assumptions are extremely strong and will be discussed later. They are used to assess the robustness of the model, using the minimum amount of adjustment. The critical stresses have been determined to fit a single experimental result in order to provide the best match between the experimental and predicted fracture strains. The uniaxial tensile test fracture strain of ENAA6060 containing

40% of α -AlFeSi (homogenized 3h30 at 585°C) and deformed at 550°C has been chosen for that purpose, because it involves an average behaviour. In order to account for the void nucleation, the criterion proposed by Beremin and defined earlier is used with different k_s shape parameters for the different void populations: 0.904, 0.416 and 1.67 for the cavities nucleated by β elongated particles decohesion, α rounded particles decohesion and particles cracking, respectively.

The nucleation stress are identified as equal to $\sigma = 15$ MPa for void nucleated by particle decohesion and $\sigma = 35$ MPa for void nucleated by particle cracking. This last stress is identified as the minimum nucleation stress, which will never be reached during deformation above 450°C whereas it is reached directly at room temperature.

5.4.4.b Deformation at room temperature

The predictions of the model at room temperature are presented first. Figure 5.29 shows the evolution of the fracture strain as a function of the volume fraction of α -particles for test performed under different stress triaxiality conditions, for the alloys (a) ENAA 6060 and (b) ENAA 6005A. For both aluminium alloys, all the experimental evolutions in terms of the effect of the stress triaxiality and importance of the β/α transformation are very well captured. The ductility is generally overestimated. The reason for this overestimation can have many origins. It does not come from the identification of the critical stress for void nucleation because, at room temperature, with such critical stress values, the nucleation is immediate for all the populations. Delayed nucleation could only increase the ductility. One physical origin for the overestimation is that we consider that the particles are uniformly distributed ($\lambda_0 = 1$) even though there are located along the grain boundaries. A previous similar study with a similar model but which did not take account for the effect of the second population of voids, leads us to impose a particle distribution factor $\lambda_0 = 7$ in order to obtain a good correspondence with experiments [55]. Of course, all the approximations underlying the model play a role here. We believe that the predictions are excellent considering that all the parameters have been derived from the microstructure analysis.

In order to give an idea of the gain obtained while using different void populations, the Figure 5.30 compares the calculated ductility at room temperature with the new model and with a similar model but where all the void contribution have been mixed in a single population. This shows the big influence of the presence of a second void population on the attainment of the coalescence stage, and thus of the fracture.

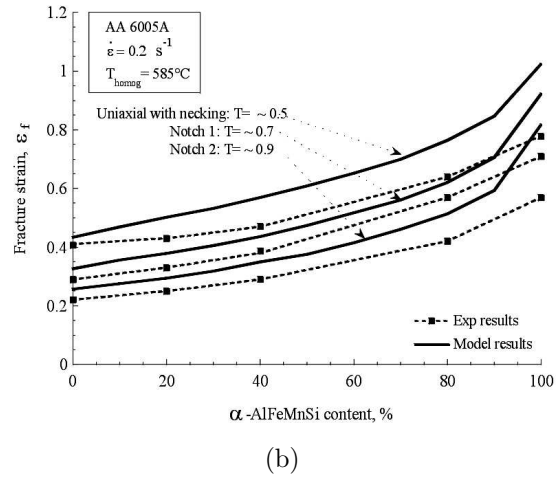
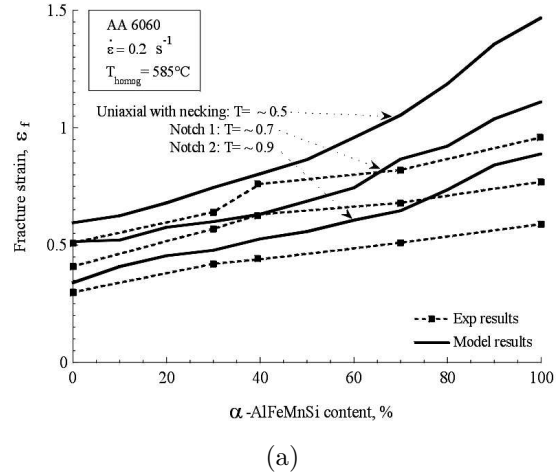


Figure 5.29 – Evolution of the calculated ductility (fracture strain) as a function of the α -AlFeMnSi content for aluminium alloys ENAA 6060 (a) and ENAA 6005A (b) deformed at 20°C with different tensile specimen geometries: uniaxial tension with necking, notch 1 with radius of 5 mm and notch 2 with radius of 2 mm.

5.4.4.c Deformation at high temperature

At high temperature, only nucleation by interface decohesion of the long β -AlFeSi particles occurs. In this case, when the nucleation stress is reached,

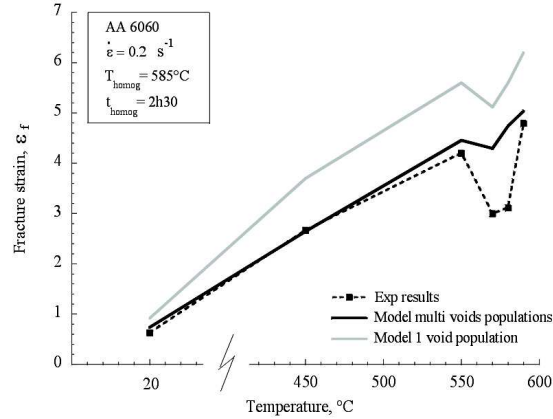
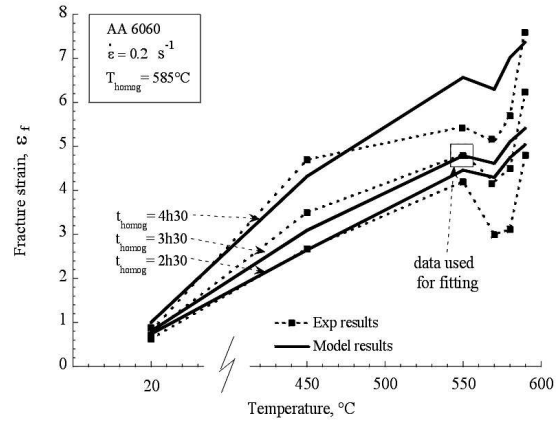


Figure 5.30 – Comparison between models with one population and with several populations for aluminium alloys ENAA 6060 deformed at 20°C with uniaxial tensile specimen geometries.

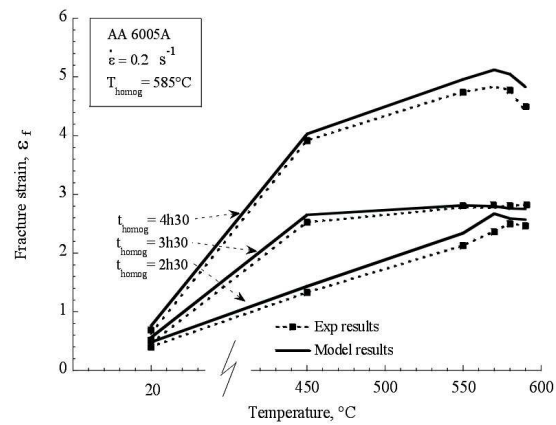
the damage is nucleated in a deformation interval equal to $\Delta\epsilon_{nucleation} = 0.5$. Above 570°C, in order to take into account the fact that eutectic melting associated with the presence of β particles occurs, the nucleation stress is taken equal to 0 as the melting of the particles induces directly void nucleation.

Figure 5.31 shows the variation of the fracture strain as a function of the temperature of deformation for tests performed under uniaxial stress triaxiality conditions, for the alloys (a) ENAA 6060 and (b) ENAA 6005A. The results are in excellent agreement with the experimental values, especially for the ENAA 6005A alloy (although the adjustment of the nucleation stress was made for on the alloy ENAA 6060). The introduction of an immediate void nucleation above 570°C to mimic the melting of the β intermetallic particles allows reproducing in an approximate way the fall of ductility observed for the ENAA 6060. The quality of the predictions for the alloy ENAA6005 A at 590°C is conspicuous.

Figure 5.32 shows the variation of the fracture strain as a function of the α -AlFeMnSi content for different strain rates at a deformation temperature of 550°C, for the alloys (a) ENAA 6060 and (b) ENAA 6005A. Here again, the results are in quite good agreement with the experimental values. We note that, at low strain rate, the model always underestimates the fracture strain whereas it overestimates it at the highest strain rate (2 s^{-1}). Nevertheless, it



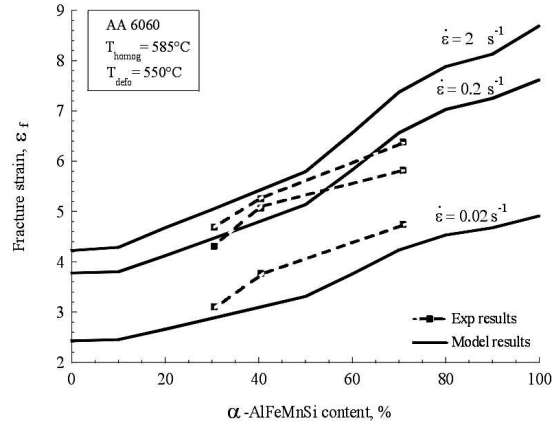
(a)



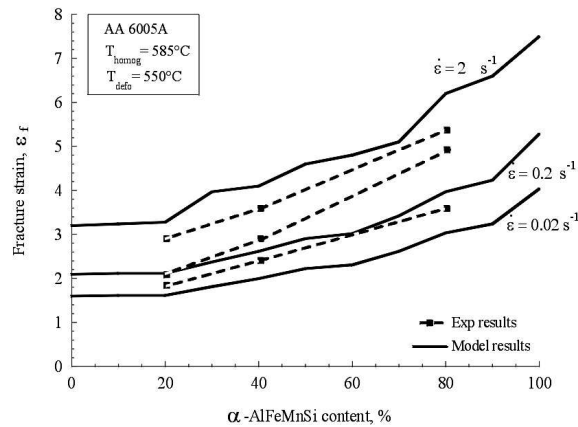
(b)

Figure 5.31 – Evolution of the ductility (fracture strain) as a function of the deformation temperature for the alloys (a) ENAA 6060 and (b) ENAA 6005A; for different homogenization conditions.

fits very well the reality at the intermediate strain rate where the nucleation stresses have been identified.



(a)



(b)

Figure 5.32 – Evolution of the ductility (fracture strain) as a function of α -AlFeMnSi content for aluminium alloys ENAA 6060 (a) and ENAA 6005A (b) deformed at 550°C with different strain rates: 0.02, 0.2 and 2 s⁻¹.

5.5 Discussion and conclusions

During extrusion of aluminium alloys, the maximum ram speed is usually limited by hot cracking, which may be associated to the embrittling effect of sec-

ond phases due to particles decohesion, particles fracture or eutectic melting reactions. The understanding and modeling of the deformation and fracture behavior of aluminium alloys at room and at hot working temperatures is very important for optimizing manufacturing processes such as extrusion. The ductility of 6xxx aluminium alloys can be directly related to chemical composition and to the microstructural evolution occurring during the heat treatment procedures preceding extrusion if proper physics based deformation and fracture models are used.

A micromechanics based model of the Gurson type considering several populations of cavities nucleated by different second phase particles groups has been developed here on the basis of experimental observations. This model allows to relate quantitatively microstructure and ductility.

As a first stage to the modeling, investigation of the mechanical behavior of the aluminium alloys (ENAA 6060 and ENAA 6005A) at different temperatures has been carried out in order to create an experimental data base to compare with the model predictions. In addition to providing the flow curves of the materials (thanks to a inverse procedure), it leads to the following observations:

1. The decrease of the strength with temperature is very marked. The flow properties as well as the total elongation differ between the two alloys. The alloy ENAA 6060 exhibits a lower strength but is more ductile than the alloy ENAA 6005A. The flow strength decreases with increasing homogenization quality, i.e. with increasing conversion of the β -AlFeSi particles into α -AlFeMnSi particles. All these results are consistent with a generally accepted view that a well homogenized material exhibits superior hot workability in terms of lower extrusion pressure. The flow stress level significantly increases with strain rate, especially for alloy ENAA 6060. Qualitatively, the ductility increases with increasing strain rate, which is unusual at least from the perspective of low temperature ductility.
2. For each alloy, ϵ_u (indicator of the hardening behavior) decreases with increasing test temperature, and, for a fixed temperature, it decreases with increasing homogenization time. Thus, the presence of β particles increases not only the yield strength but also the strain hardening capacity.
3. As expected, the fracture strain significantly increases with temperature. The conversion of the elongated β particles into the more rounded α particles has also an extremely beneficial effect on the ductility, especially at high temperature. The larger ductility of alloy ENAA 6060 is easily explained by the lower magnesium and silicon contents. The total volume fraction of intermetallic particles is also lower in alloy ENAA 6060. Concerning the high temperature ductility, alloy ENAA 6005A shows a

decrease in the ductility above a certain threshold temperature for the longest homogenization time. The true fracture strain in alloy ENAA 6060 involves a marked drop around 570-580°C before increasing again at 590°C. The difference in the ductility evolution between both alloys reflects the difference in constituents present in the material. The drop in the ductility of alloy ENAA 6060 around 570-580°C has been identified to be due to second phase eutectic melting.

4. The fracture strain significantly increases with increasing strain rate. More strikingly, large strain rates tend to suppress the decrease of the ductility at high temperature. An increase of strain rate can have two effects : a local increase of the temperature and an effect of preventing the diffusion related phenomena.
5. The true fracture strain markedly decreases with increasing stress triaxiality whatever the temperature. Alloy ENAA 6005A seems to be more influenced by a change of stress triaxiality than alloy ENAA 6060. The drop in ductility of alloy ENAA 6060 around 570°C appears also at larger stress triaxiality.

In order to model correctly the evolution of the maximum ductility using a void nucleation, growth and coalescence model, the nucleation step needs first to be correctly defined. Observations of the damage nucleation mechanisms have been carried out through in situ tensile tests at room temperature and interrupted tensile tests at higher temperature. This leads to the following conclusions:

1. At room temperature, the majority of the particles with the long axis oriented in the range of 0° to 45° with respect to the loading direction exhibit to particles fracture whereas the other particles lead to particle/matrix interface decohesion. All this happens directly at the beginning of straining.
2. At high temperature, general cavitation (nucleation of voids) occurs after an appreciable strain (i.e. 0.2-0.3). The nucleation of voids results from debonding along certain particle/matrix interfaces.

With all this knowledge and the identification of the microstructural parameters and of the critical stresses for the different modes of void nucleation, the model developed in this chapter was used to predict the maximum ductility before fracture of tensile specimens. This model is well suited for the present case as it incorporates void shape effects, which is key to capture the impact of the β -to- α transformation on ductility. For deformation at room temperature, different void populations (nucleated from different particles groups) have been defined: void nucleated by particle fracture, by β particle/matrix decohesion and by α particle/matrix decohesion. The pennyshape voids initiated by the

multiple fractures of elongated β particles are considered here as a population, which accelerates the damage progression. The void coalescence takes thus into account the effect of the second population which was found essential to generate quantitative predictions of the ductility without any tuning or adjustments.

At room temperature, for both aluminium alloys, all the experimental evolutions in terms of the effect of the stress triaxiality and effect of the β/α transformation are very well captured. The ductility is generally overestimated. The reason for this overestimation can have many origins. The ductility is overestimated mainly for the lowest triaxiality but the evolution of ductility with the α -AlFeMnSi particles content is properly predicted. The variations with the experimental values increase when the α -AlFeMnSi particles content increases. The order of magnitude of the variations between experimental and calculated fracture strains is the same for both alloys.

At high temperature, the results are in excellent agreement with the experimental values, especially for ENAA 6005A alloy (although the adjustment of the nucleation stress was made for alloy ENAA 6060). The introduction of an immediate void nucleation above 570°C to mimic the melting of the β intermetallic particles allows reproducing in an approximate way the fall of ductility observed for ENAA 6060. The quality of the predictions for alloy ENAA6005 A at 590°C is really surprising. The effect of the strain rate dependence of the fracture strain is also in good agreement with the experimental values.

The limitation of the model comes from the identification of the critical stresses for void nucleation. These stresses are determined in order to fit an experimental value but have to be taken very small compared to the nucleation stresses generally encountered in the literature (around 100 Mpa). These parameters thus contain all the errors brought by the different assumptions made during modeling. Furthermore, one physical origin for the error is that we consider that the particles are uniformly distributed ($\lambda_0 = 1$) even though there are specifically located along the grain boundaries. We note here that a previous similar study with a similar model but which did not take account for the effect of the second population of voids effects, lead us to impose a particle distribution factor ($\lambda_0 = 7$ in order to obtain a good correspondence with experiments [55]). Of course, all the approximations underlying the model play a role here. We consider that the predictions are excellent considering that all the parameters have been derived from the microstructure analysis. This work thus allows quantifying the gain or loss in ductility obtained for different homogenized states, hence with different microstructures. Even if the extrudability cannot be directly linked to tensile tests conditions, it definitely provides a strong correlation with the possible change of maximum ram speed for a determined change in intermetallic content due to change in homogenization process. Note that the methodology has been validated for different stress states by varying the stress triaxiality which is the first step towards the investigation of stress

states more representative of the extrusion conditions. The following chapter will try to correlate the evolution of the fracture strain with the maximum extrusion speed before the appearance of surface defects.

6

Parametric study and optimization of extrusion conditions

Chapter 6

Parametric study and optimization of extrusion conditions

This chapter discusses the effect of some key factors that determine the extrudability of aluminium. The effect of aluminium alloy composition in terms of Si, Mg, Mn and Fe contents is studied here as well as the effect of the homogenization parameters and re-heating rate to the extrusion temperature. As explained previously, this last re-heating stage is critical in terms of Mg_2Si re-precipitation or growth. Indeed, if this phase is present during extrusion, it will lead to deleterious melting at grain boundaries. The experimental results and industrial extrusion tests are used to provide a correlation between the ductility calculations in uniaxial tension and the maximum extrusion speed for the profile studied in Chapter 3.

6.1 Introduction

Workability is usually defined as the amount of deformation that a material can undergo without failure at a given temperature and strain rate. The failure is generally due to internal damage and cracking in many commercial cases leading to poor surface finish. Workability is a complicated engineering issue due to the fact that the states of stress and strain in a material undergoing a deformation process are not uniform. Improving workability means increasing the productivity by increasing the extrusion speed. Workability can be improved by optimizing the various heat treatments, i.e. the homogenization and the re-heating treatments of the aluminium billet to the extrusion temperature. Other parameters for controlling the workability not addressed in the thesis are the casting practices and the die optimization.

In billet extrusion, the limit of workability can be determined by the occurrence of cracking due to either second phase induced damage or melting. Eutectic melting temperature, deformation conditions, chemical composition, secondary phases, grain size, strain rate and some other parameters affects the workability. In the alloys studied here, voids form through cleavage or interface decohesion of the AlFeSi particles and through the melting of second phases such as Mg₂Si or Si. This leads to cracking of the material during deformation.

In chapter 5, we demonstrated the effect of the homogenization heat treatment on the ductility and our ability to model this property using a micromechanical void growth based constitutive model of the Gurson type. In order to get closer to industrial practice, our goal in the present chapter is to summarize explicitly the effects of the most effective parameters and to show their net effect on hot workability and extrusion speed.

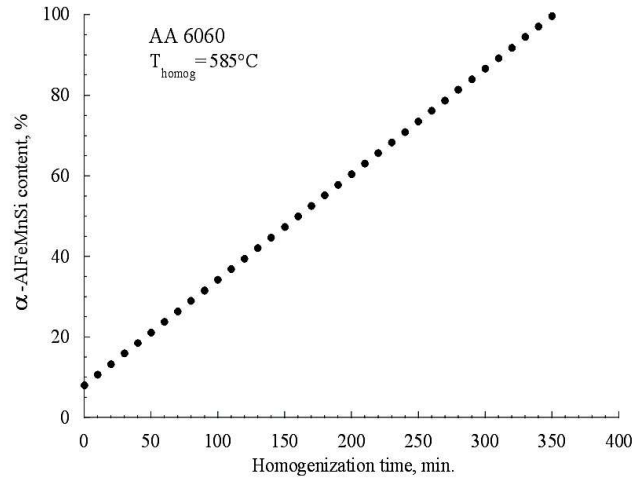
6.2 Influence of the homogenization temperature and holding time

Two different homogenization temperatures have been studied and compared experimentally through homogenization testing and microstructure analysis: 585°C and 600°C. This difference of 15°C in temperature leads to a large difference in kinetics of the β -AlFeSi to α -AlFeMnSi transformation, as explained in Chapter 3. This leads to different microstructures after similar homogenization soaking time and thus to differences in ductility for a constant deformation temperature. The microstructure evolution in terms of α -AlFeMnSi content has been extrapolated to different homogenization times; the result is presented in Figure 6.1(a) for a homogenization temperature of 585°C. This extrapolated evolution of the microstructural parameters (particles content and shapes) can be incorporated in the model in order to calculate the evolution of the fracture strain with homogenization conditions. The predicted evolution of the fracture strain is plotted in Figure 6.1(b) as a function of the homogenization time.

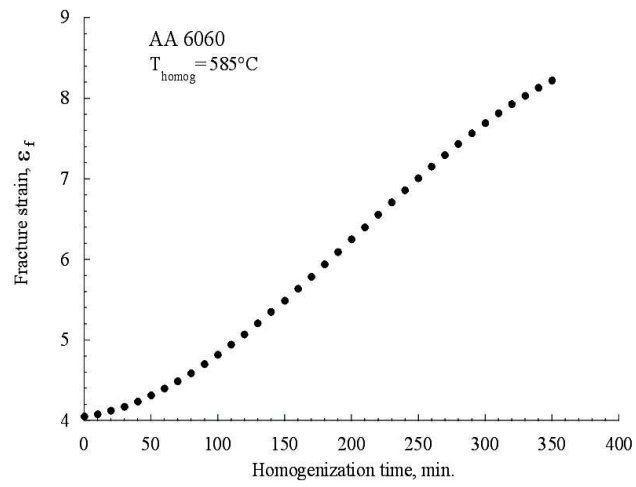
Figure 6.1(b) shows the gain in ductility ϵ_f brought about by an increase of the homogenization time. However, the ϵ_f values cannot be used directly for industrial purposes. We have thus related the fracture strain to the maximum extrusion speed by comparing the fracture strain and the ram speed of alloy ENAA 6060 measured during the industrial tests presented in Chapter 2.

A relationship can be established between the fracture strain (calculated for a deformation temperature of 580°C) and the maximum extrusion speed. From the results obtained for alloy 6060 homogenized at 585°C:

$$\text{Maximum speed } V_{max} = f(\epsilon_f \text{ model}) \quad (6.1)$$



(a)



(b)

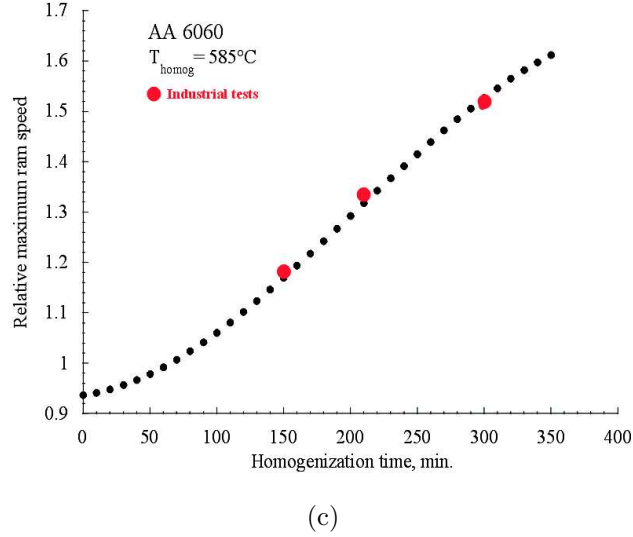


Figure 6.1 – Experimental and predicted evolution of the α -AlFeMnSi content (a), fracture strain (considering a maximum deformation temperature of 580°C) (b) and relative ram speed (c) with homogenization time for the aluminium alloy ENAA 6060 homogenized at 585°C .

This relationship is presented in Figure 6.1(c) and is valid only for the profile extruded in Chapter 2. Concerning the fracture strain modeling, we have taken into account the effects of the β particles on damage initiation but not the possible occurrence of melting. Figure 6.2 shows the ensuing prediction of the maximum ram speed evolution with homogenization time for alloy 6060 for two homogenization temperatures: 585°C and 600°C . It is predicted that increasing the homogenization temperature by 15°C allows a reduction of the homogenization time by nearly 70%. This relationship is then used to link the predictions of the fracture strain for alloy ENAA 6005A to extrusion speed in order to predict the maximum extrusion speed evolution with homogenization conditions.

6.3 Influence of the Mg and Si content

The coupled effect of the Mg and Si content is studied by comparing aluminium alloys ENAA 6060 and ENAA 6005A. The Mg and Si content of these alloys

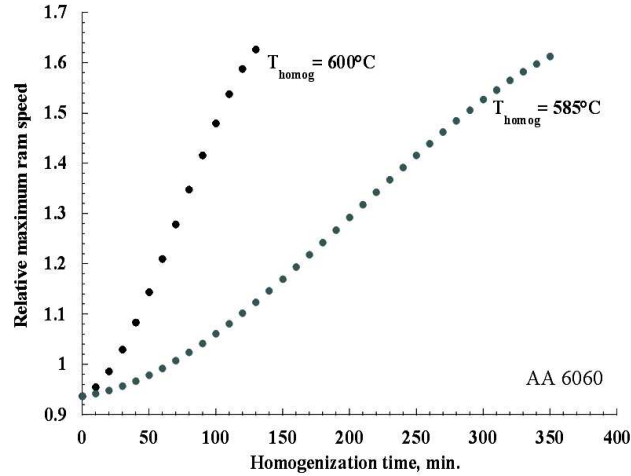


Figure 6.2 – Predicted evolution of the relative ram speed with homogenization time for the aluminium alloy ENAA 6060 homogenized at 585°C and at 600°C.

are 0.49-0.43 and 0.56-0.59 respectively. These alloying elements influence both the kinetics of transformation of the Fe-bearing second phase particles and the flow properties of the matrix. Figure 6.3 and Figure 6.4 show the evolution, as a function of the homogenization time, of α -AlFeMnSi content and of the predicted maximum ram speed respectively, for both alloys after homogenization at 585°C and 600°C .

An increase of the Si and Mg content significantly deteriorates the ductility hence the maximum extrusion speed. Unfortunately no industrial tests on the same profile has been made for alloy 6005A, but the predictions of the maximum ram speed for alloy ENAA 6005A correspond well with the trends given by the industrial partner.

6.4 Influence of the Mn content

The influence of the Mn content on the ductility is studied by considering that the Mn content has a negligible influence on the flow properties of the aluminium alloy matrix in comparison to its influence on the AlFeSi particle transformation kinetics. The microstructure evolution quantified in Chapter 3 for two aluminium alloys ENAA 6005A with 0.04 and 0.1 wt.% Mn is used to

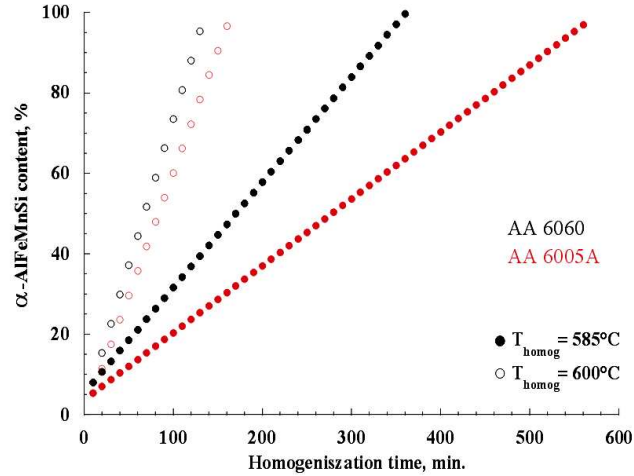


Figure 6.3 – Evolution of the α -AlFeMnSi content with homogenization time for the aluminium alloys ENAA 6060 and ENAA 6005A homogenized at 585°C and at 600°C.

study the evolution of the calculated ductility during homogenization at 585°C for different holding times. Figure 6.5 and 6.6 present the results of these calculations.

Doubling the manganese content permits to cut the homogenization time almost by a factor of two to get a similar maximum extrusion speed.

6.5 Influence of Fe content

Fe is present in aluminium alloys as an impurity (normally as a controlled impurity) due essentially to recycling. We study here the influence of the Fe content, and thus of the AlFeSi particles content on the maximum ductility. We suppose that the β - α -AlFeSi transformation kinetics are similar whatever the Fe content. Only the total volume fraction of AlFeSi particles is modified to take account of the evolution of the Fe content.

Figure 6.7 shows the evolution of the maximum extrusion speed for alloys ENAA 6060 and ENAA 6005A with Fe content for a homogenization at 585°C for 2h30. A major reduction of the extrusion speed would take place if the

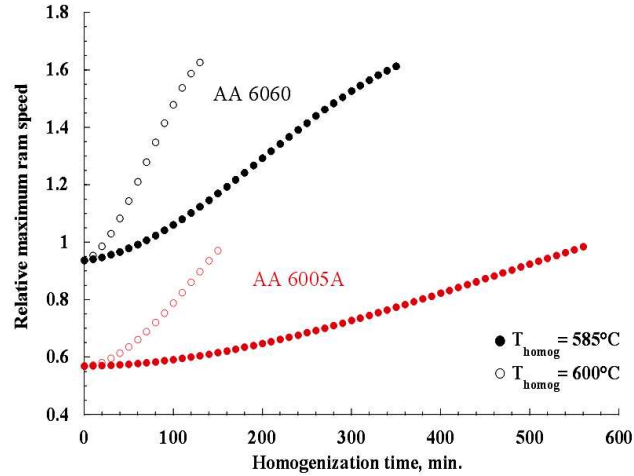


Figure 6.4 – Evolution of the relative ram speed with homogenization time for the aluminium alloys ENAA 6060 and ENAA 6005A homogenized at 585°C and at 600°C.

content of iron was increased. Nevertheless, the magnitude of the drop seems to decrease beyond 0.4wt.% of Fe.

6.6 Influence of the thermal treatment on Mg_2Si dissolution

In addition to the effect of the $AlFeSi$ particles on the workability of the $AlMgSi$ alloys, another important feature is the influence of large Mg_2Si precipitates during hot deformation. Indeed, a non-efficient cooling rate after homogenization or re-heating up to the extrusion temperature can have a huge influence on the appearance of internal or surface defects. A slow cooling rate as well as a slow re-heating rate at a too low temperature can induce undesirable precipitation and growing of the Mg_2Si phase, which cause damage due to melting at high temperature. A model of precipitation is used hereafter to predict the influence of these thermal parameters on the presence of this phase, which can significantly reduce the maximum ram speed if present before extrusion.

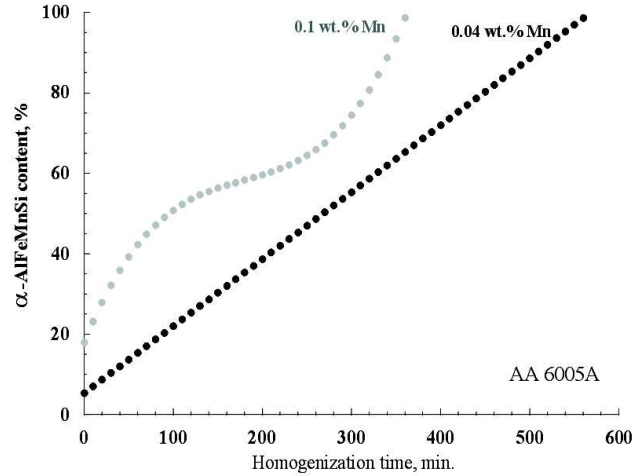


Figure 6.5 – Predicted evolution of the α -AlFeMnSi content with homogenization time for the aluminium alloys ENAA 6005A containing 0.04 and 0.1 wt.% Mn homogenized at 585°C.

6.6.1 Mg_2Si phase dissolution/growth

Several analytical models have been developed in order to quantify the kinetics of particle dissolution in metals and alloys at elevated temperature. The model provided by Vermolen, Vuik and Van der Zwaag [93, 92] is used here to describe particle dissolution and growth in multicomponents alloys with a given volume fraction of precipitates of different shapes under both isothermal and non-isothermal conditions. The following sections briefly presents the model and some selected results.

6.6.1.a The dissolution/growth model

The model for the dissolution of a stoichiometric second phase in a ternary alloy is presented in details elsewhere [93, 92]. The main points are introduced briefly with the appropriate nomenclature changes to adapt to model to the present analysis.

When all particles are nucleated simultaneously in a uniform, supersaturated solid solution, the particles grow independently until impingement occurs. Assuming a uniform spatial distribution of these particles, the model considers

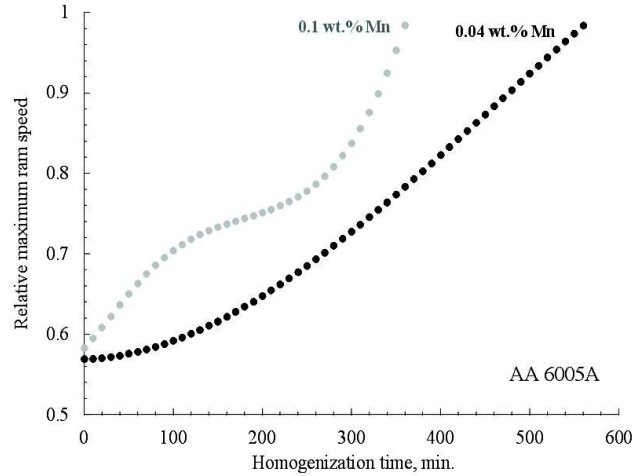


Figure 6.6 – Predicted evolution of the relative ram speed with homogenization time for the aluminium alloys ENAA 6005A containing 0.04 and 0.1 wt.% Mn homogenized at 585°C .

that precipitates dissolve within a finite cell of dimension determined by the average inter-particle distance. In each cell, the particle is surrounded by a solute-depleted matrix of uniform composition. There is no net flux of solute atoms between neighboring cells.

When a ternary alloy as AlMgSi is considered, local equilibrium is assumed at the matrix/particle interface at all times and dissolution kinetics of the particles is controlled by Mg and Si diffusion in the Al phase. The concentration $C_{\text{Mg,Si}}$ at the interface at annealing temperature must be such that mass conservation is satisfied at the interface moving at a velocity $v = dr/dt$. The basic formulation of Fick's second law describing multi-component diffusion is solved numerically with the boundary conditions satisfying the solubility product and the requirement that the interface velocity is identical for both alloying elements. In order to deal with particle dissolution during non-isothermal heating, the thermal cycle is divided into a number of discrete steps during which the diffusion coefficient is assumed to be constant and the boundary conditions are given by the solubility product appropriate at that temperature.

For the alloys studied here, assuming that the matrix/particle interface is in equilibrium at all time, the concentrations of Mg and Si in the matrix at the

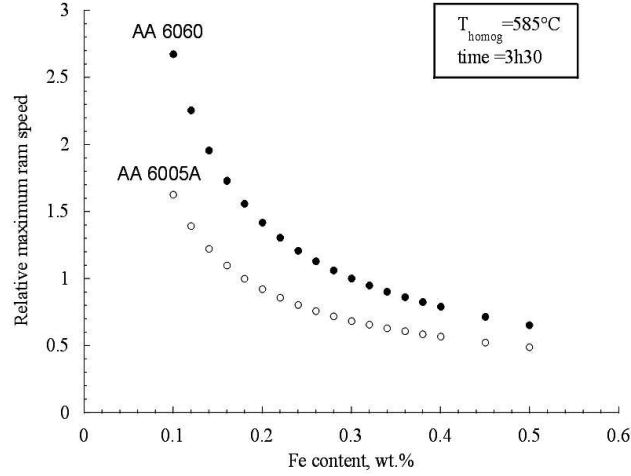


Figure 6.7 – Evolution of the relative ram speed with Fe wt.% content for the aluminium alloys ENAA 6060 and ENAA 6005A homogenized at 585°C for 3h30.

interface are given by the solubility product

$$\log[Mg]^2[Si] = A - \frac{B}{T} \quad (6.2)$$

in which A and B are constants and are taken as 5.85 and 5010 respectively for β -Mg₂Si particles.

When the particles are assumed to be of the same size and spacing, the matrix can be divided into equisized cells. The volume fraction of precipitates f_0 and the fraction dissolved x can then be written

$$f_0 = \frac{R^n}{M} \quad (6.3)$$

$$x = 1 - \frac{r(t)^n}{R} \quad (6.4)$$

where $r(t)$ is the radius of the particle at time t , R is the initial particle radius, M is the radius of the cell, n depends on the shape of particle and takes the

values 1, 2 and 3 for planar, cylindrical and spherical particles, respectively.

The equilibrium volume fraction of the precipitates f_0 , after a thermal treatment, can be calculated from a simple mass balance, assuming that the concentration in the matrix is given by the solvus boundary, and that the composition of the particle is constant and independent of temperature. The model can also be used for a material in which the particle radii are not equal. One has then a particle size distribution in space. The material is divided into spherical cells with a size distribution that matches the particles size distribution. Nevertheless, we will assumed here that all the particles have the same size.

6.6.1.b Results

The aluminium alloys addressed in this work contain 0.49% Mg and 0.43% Si for ENAA 6060 and 0.56% Mg and 0.59% Si for ENAA 6005A. These alloys are Si rich with respect to the stoichiometric composition. The Si is present in the as-cast alloys within the Mg₂Si particles and also within the AlFeSi intermetallics. Considering the upper-bound case where all Mg precipitates entirely into the Mg₂Si particles and that the AlFeSi intermetallics are present in the β phase, we can calculate the Si excess inside in the solid solution in the as-cast state.

$$C_{Si} \text{ in } Mg_2Si = 0.5C_{Mg} \frac{M_{Si}}{M_{Mg}} = 0.267 \quad (6.5)$$

$$C_{Si} \text{ in } AlFeSi = \frac{\frac{M_{Fe}}{M_{\beta-AlFeSi}}}{\frac{M_{Si}}{M_{\beta-AlFeSi}} C_{Fe}} = 0.1 \quad (6.6)$$

$$C_{Si} \text{ in excess} = 0.43 - 0.267 - 0.11 = 0.053 \quad (6.7)$$

After solidification, the casting is homogenized at high temperature. During this heat treatment, Mg and Si should re-enter into solid solution in order to optimize the hardening capacity of the extruded products. Solute atoms diffuse here down the composition gradient away from the interface and this loss of solute atoms causes the Mg₂Si phase to recede. The calculated particle dissolution characteristics are describe here assuming a monodisperse particle size distribution.

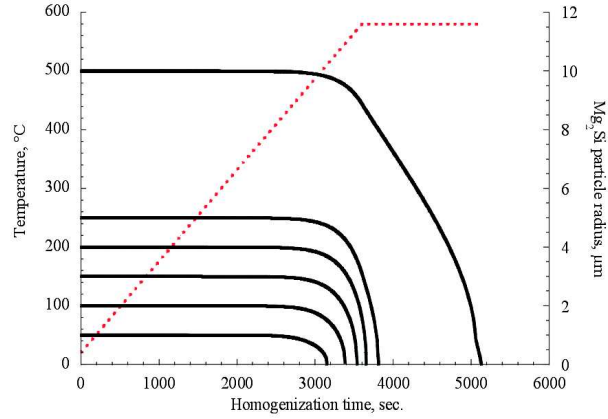
The homogenization treatment thermal profile is imposed here through model calculations for different particle sizes. The shape of the particles is likely to have a minor influence on dissolution kinetics when dissolution is controlled by volume diffusion. The precipitates will become increasingly spherical as they shrink and the dissolution time for a given shape of precipitate can be considered to be the same as for a sphere with identical volume. Assuming that all precipitates are spherical with a monodisperse size distribution, calculations are

performed with initial particle radii from 1 to 10 μm and different homogenization conditions: 1h heating to 585°C + 2h isothermal holding and 1h heating to 600°C + 2h isothermal holding. The results are presented in Figure 6.8.

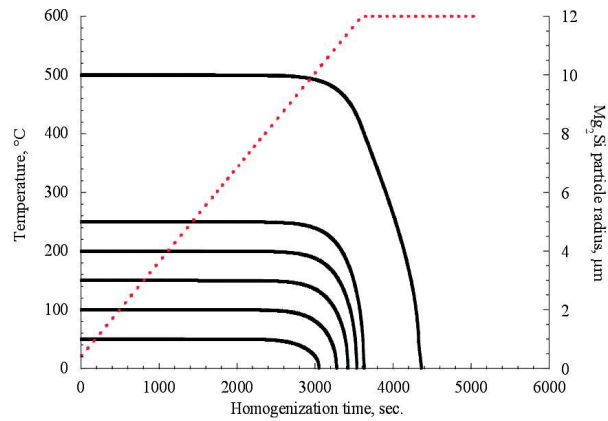
Of course, the smaller particles, with a size ranging between 1 and 5 μm dissolve first and need 1h heating to be completely dissolved. This means, that if a precipitation of Mg_2Si smaller than 5 μm can be controlled during solidification at casting, an homogenization holding temperature higher than the Mg_2Si melting temperature can be used (585°C). Nevertheless, we see that the bigger particles need a non negligible time to dissolve and exist even when the holding temperature is reached. In this case, we can imagine that the first step of the homogenization process could be carried out at 585°C until the biggest eutectic particles are dissolved before increasing the temperature in order to increase the intermetallic transformation kinetics and thus to reduce the total homogenization time.

After homogenization holding, the most critical step regarding the Mg_2Si phase is the cooling down to room temperature. If the cooling is not fast enough, coarse Mg_2Si particles can precipitate. The presence of this phase before extrusion is very detrimental as, on the one hand, it decreases the hardening capacity of the alloy while decreasing the Mg and Si content into solution, and, on the other hand, it induces fracture due to melting during extrusion. As the model does not deal with nucleation it was not possible to simulate this post-homogenization cooling. But, thanks to experimental observations, realistic assumptions are made concerning the volume fraction and the size of coarse Mg_2Si particles after cooling. This allows us to simulate the dissolution/growth behavior during the re-heating process up to the extrusion temperature.

The "mean" re-heating thermal profile used before extrusion is imposed here to determine the volume fraction of small Mg_2Si particles present before the extrusion step. In this case, we introduce another parameter which is the homogenization state. Indeed, the β/α content has an influence on the Si content in solid solution (excess of Si). Two hypothetical alloys with 80% β /20% α and 20% β /80% α are studied. The thermal profile imposed at this step of the process is not shown for confidential reason. This is a typical cycle used with gas furnace in industry to heat up the aluminium alloys billets to extrusion temperature around 450°C. We assume here a Mg_2Si content of 5% of the maximum content allowed by the Mg content. Different initial particle radii are compared ranging from 0.1 to 2 μm . The results of the calculations are presented below in Figure 6.9. According to these results, Mg_2Si particles with a radius bigger than 0.3 μm can not be completely dissolved with such a heat treatment. These particles first grow during the heating to the maximum temperature before they begin to dissolve until the end of the heating ramp. The slow reaction rate at the beginning of dissolution is due to the combined effect of a slow diffusion rate due to the low temperature and the small concentration



(a)



(b)

Figure 6.8 – Predicted evolution of the Mg₂Si particles radius (in μm) for different initial radii during homogenization at (a) 585°C and (b) 600°C.

gradient near the matrix/particle interface and the relatively small interfacial area to particle volume ratio. The dissolution rate is then increased due to temperature increase and to higher concentration gradient at the interface of

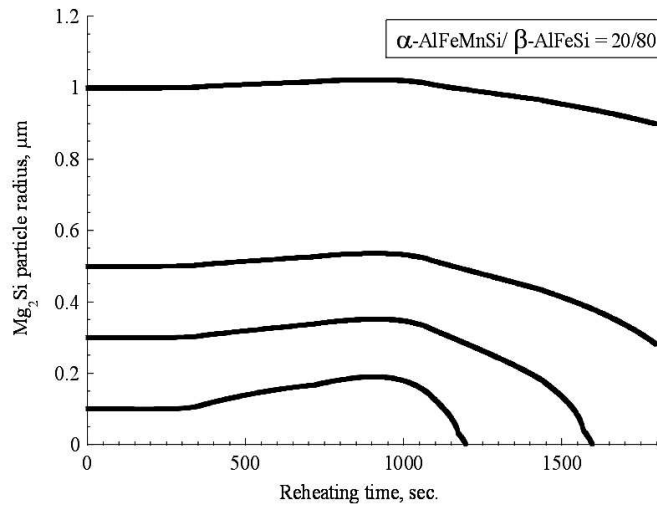
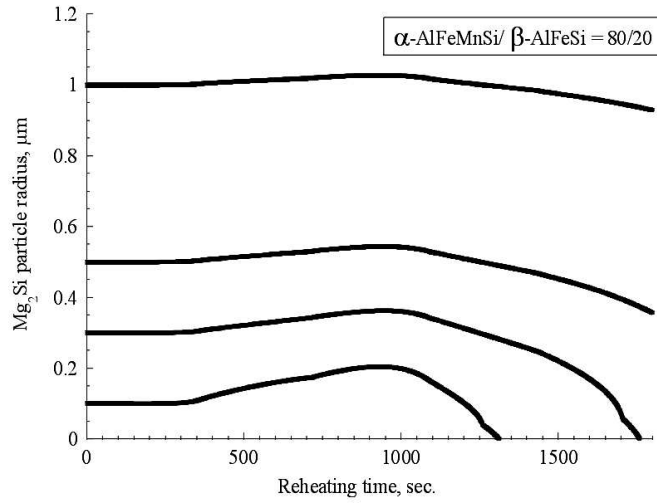


Figure 6.9 – Predicted evolution of the Mg_2Si particles radius (in μm) for different initial radii during reheating to the extrusion temperature for different α/β -AlFeSi initial contents: 20/80 (a) and 80/20 (b).

the particles. Increasing the initial particle radius shifts the dissolution initial temperature to higher values.

The study of the effect of the β/α -AlFeSi ratio indicates that increasing the β -AlFeSi content allows an increase of the dissolution kinetics. This is probably due to the associated lower Si excess which accelerates the dissolution through a higher concentration gradient.

The main conclusion from this study is that the re-heating should be as fast as possible in order to avoid the temperature range (400-430°C) where particles growth occurs. If the alloy still contains big Mg₂Si particles before extrusion, this phase will induce damage directly by melting, cutting down the maximum ram speed.

7

Conclusions

Chapter 7

Conclusions

Extrusion of aluminium alloys is a relatively efficient and cheap method for producing complex shapes. Nevertheless, the demand for increasing production rates with the best surface finish and the need to invest into quality improvement remains continuous. Surface problems usually originate from damage phenomena with a link to microstructure. It is well established that homogenized aluminium alloys billets extrude easier and faster and give better surface finish than as-cast billets. However, there are limits on the improvement that the homogenization treatment can provide to the performance of the billet on the press. This work, thanks to experimental observations and to the development of a micro-mechanical model allows a better understanding of the evolution of extrudability with the homogenization conditions.

AlFeSi intermetallic phases severely restrict hot workability when present as hard and brittle plate-like precipitates β -AlFeSi. Damage initiation occurs in these alloys by decohesion or fracture of these intermetallic inclusions. The β -AlFeSi-to- α -AlFeMnSi transformation obtained through a proper homogenization heat treatment, considerably improves the extrusion process of the aluminium since the conversion into α particles improves the ductility of the material and consequently the surface quality.

This research has allowed to characterize the effects of the heat treatments on the microstructure evolution and to establish a direct relationship between the process parameters and the behavior of the alloys during extrusion. In order to allow a quantitative understanding of how the microstructural features govern

the mechanical properties, it was necessary to elucidate the physics acting at the lower scales using a **micromechanical model**. This type of modeling aims at simulating the plasticity and damage of materials resulting from microstructural inhomogeneities. The microstructural inhomogeneities are associated here with the presence of second phase particles, which, being commonly present in the materials, play a very important role in triggering the fracture process and then in determining the mechanical response.

The present thesis shows that the local approach of fracture can give important information on the ductility and thus on fracture prediction in aluminium alloys at room and high temperature. This approach was successfully applied on both 6060 and 6005A alloys presenting different flow properties but similar microstructure.

The main achievements of the thesis are:

1. **A better understanding of the appearance of two extrusion surface defects in 6xxx aluminium alloys and their relationship with the homogenization process parameters and with the microstructure.**

Our work aimed at understanding and at controlling some metallurgical mechanisms concerned within various stages of the process. The relationship between the parameters of heat treatment and the cracking defects during extrusion was established. The analysis of the defects showed that:

- (a) The surface defects have two different microstructural origins. One is due to the cracking of brittle β -AlFeSi and pure Si second phase particles and/or due to the incipient melting caused by the eutectic reaction $\text{Al} + \beta\text{-AlFeSi} + \text{Si} \rightarrow \text{liquid}$, (578°C). The other one is due to a probable melting of the Mg_2Si phase at 585°C.
- (b) Improving the heat treatment while using a higher homogenization temperature and a longer soaking time allows to increase the critical extrusion speed. A gain of 35% was obtained with a temperature increase of 15°C and a soaking time increase of 40%.
- (c) The homogenization temperature and time must be increased. 585°C for 4h30 is surely necessary if we want to avoid the problem caused by the β -AlFeSi phase.

2. **The quantification of the effect of the homogenization temperature and time on the β -to- α transformation.**

We analyzed the influence of the homogenization parameters and of the alloy composition on the evolution of the particles phase and shape. As-cast

ENAA 6xxx samples contain mainly elongated β -AlFeSi particles. During homogenization of ENAA 6060 at 585°C, the plate-like intermetallics break up into necklaces of smaller round particles. We can also observe that the particles are getting smaller and rounder with an increase of the homogenization holding time. During a homogenization at 600°C, the same observations can be made, but with a large increase of the intermetallic transformation kinetics. Similar conclusions are made for the aluminium alloy ENAA 6005A, but with a difference in kinetics. The higher level of silicon in this alloy makes the iron phase transformation slower.

We noted that the as-cast sample of the ENAA 6060 alloy contain more α -AlFeMnSi particles than the equivalent sample in ENAA 6005A (more or less 20% for 10%). The transformation kinetics is more rapid for the ENAA 6060 than for the ENAA 6005A, but an increase of the manganese content in this last alloy significantly accelerates the transformation. An increase of the homogenization temperature by only 15°C to 600°C doubles the transformation kinetics of the intermetallic compounds.

Concerning the shape of the second phase particles, the conclusions are quite similar as for the evolution of the α content. Alloy ENAA 6060 presents less elongated particles in the as-cast state than alloy ENAA 6005A and the spheroidisation in alloy ENAA 6060 is more rapid than in alloy ENAA 6005A. The exception is alloy ENAA 6005A containing more manganese which presents more rounded particles than the other alloys after 200 minutes at 585°C or after 130 minutes at 600°C. The mean initial aspect ratio, W , of the AlFeSi particles are approximately 0.11, 0.09 and 0.2 for the alloys ENAA 6060, ENAA 6005A-1 and ENAA 6005A-2, respectively.

3. An analysis of the damage mechanisms associated with pennyshape voids (induced by the cleavage of the elongated β -AlFeSi intermetallic particles during straining) in order to introduce more physics into the micromechanical models. Among other, this study allows to formulate correct assumptions when describing a void population in a micro-mechanical void growth model when its results from particles fracture.

This theoretical study leads to the following conclusions:

- (a) The ductility of a material failing by the fracture of particles followed by void growth and void coalescence stages, is primarily controlled by the relative particle spacing, the stress triaxiality, and by the possible anisotropy of the particle distribution.

- (b) The predicted response is independent of the initial porosity as long as it is related to the particle volume fraction f_p and initial void and particle aspect ratio W_0 and W_p , respectively, through the relationship $f_0 = (W_0/W_p)f_p$ while imposing a value for W_0 sufficiently small ($W_0 < 0.03$ is always safe).
- (c) If one uses a "regular" version of the Gurson model assuming spherical voids, the definition of an effective initial porosity $f_0 = f_p/W_p$ is a good approximation for low particle volume fraction ($f_p < 1-2\%$) but becomes less and less accurate for larger particle volume fractions.
- (d) A particle surrounding a cavity has a minor effect on the void opening and puts a moderate constraint on the transverse void radius evolution: under low stress triaxiality ($T < 0.5$), the void contraction in the transverse direction is impeded leading to lower ductility than without the presence of a particle, while the opposite effect takes place under larger stress triaxiality. Neglecting the presence of the particle in the modeling of ductile fracture is a valid approximation.
- (e) Void nucleation controlled ductile fracture is favored when the particle volume fraction is large, the nucleation stress is large, and the stress triaxiality is low.

4. The development of a micromechanics-based void growth model to describe the effect of alloys microstructure on damage mechanisms. The model is a Gurson type constitutive model involving several enhancements: (1) proper account of the initial void shape and void shape change, (2) the incorporation of several void populations and (3) a proper treatment of the viscoplastic effect. Quantitative relationships are revealed between ductility and the volume fractions, sizes and shapes of the different phase particles.

Thanks to the identification of the microstructural parameters and of the critical stresses for the different modes of void nucleation, the model was used to predict the maximum ductility before fracture of tensile specimens. This model is well suited for the present case as it incorporates void shape effects, which is key to capture the impact of the β -to- α transformation on ductility. For deformation at room temperature, different void populations (nucleated from different particles groups) have been defined: void nucleated by particle fracture, by β particle/matrix decohesion and by α particle/matrix decohesion. The pennyshape voids initiated by the multiple fracture of elongated β particles are considered as a population,

which accelerates the damage progression. The void coalescence takes thus into account the effect of the second population which was found essential to generate quantitative predictions of the ductility without any tuning or adjustments.

At room temperature, for both aluminium alloys, all experimental evolutions in terms of the effect of the stress triaxiality and importance of the β/α transformation are very well captured. The ductility is generally overestimated. The reason for this overestimation can have many origin. The ductility is overestimated mainly for the lowest triaxiality but the evolution of ductility with the α -AlFeMnSi particles content is properly predicted. The variations with the experimental values increase when the α -AlFeMnSi particles content increases. The order of magnitude of the variations between experiments and calculated fracture strains is the same for both alloys.

At high temperature, the results are in excellent agreement with the experimental values, especially for alloy ENAA 6005 (although the adjustment of the nucleation stress was made for on alloy ENAA 6060). The introduction of an immediate void nucleation above 570°C to mimic the melting of the β intermetallic particles allows reproducing in an approximate way the fall of ductility observed for alloy ENAA 6060. The quality of the predictions for alloy ENAA6005 A at 590°C is conspicuous. The effect of the strain rate dependence of the fracture strain is also in good agreement with the experimental observations.

The limitation of the model comes from the identification of the critical stresses for void nucleation. These stresses are determined in order to fit an experimental value but has to be taken very small compared to the nucleation stresses generally encountered in the literature (around 100 MPa). These parameters contain all the errors brought by the different assumptions made by the modeling. Furthermore, one physical origin for the error is that we consider that the particles are uniformly distributed ($\lambda_0 = 1$) even though there are located along the grain boundaries. A previous similar study with a similar model but which did not take account for the effect of the second population of voids effects, required a particle distribution factor $\lambda_0 = 7$ in order to obtain a good correspondance with experiments [55]. Of course, all the approximations underlying the model play a role. Considering that all the parameters have been derived from the microstructure analysis, the predictions are excellent. This work aims thus at quantifying the gain or loss in ductility obtained for different homogenized states, hence with different microstructures. Even if the extrudability cannot be directly linked to tensile tests conditions, it definitely provides a strong correlation with the possible change of maximum ram speed for a determined change in intermetallic content due to

change in homogenization process. The last chapter of this work gives to the industrial partner indications about the evolution of the maximum ram speed as a function of the extrusion heat treatment parameters and chemical compositions variations.

5. A parametric study summarizing the effects of some relevant extrusion process parameters on the ductility of ENAA 6xxx alloys.

A modern vision of process optimization through setting up intelligent manufacturing strategies leads us to the **perspectives** of this work. Such strategies heavily depend on the capacity to integrate in a chain of models the various steps of the process. New solutions can be rapidly inserted owing to the potential to directly rely end downstream problems to upstreams problems. Here, the problem in mind was to relate the damage and fracture of profiles during extrusion to the chemical composition and homogenization treatment and it has given successful results through the development and the validation of a predictive model that relates the microstructure to the damage properties.

Other important ingredients of the problem in order to develop a full intelligent manufacturing approach concern the development of solidification and microstructure evolution models as shown in Figure 7.1. The development of these two other bricks would help in building a fully predictive model for the appearance of cracking during extrusion of 6xxx aluminium alloys. Furthermore,

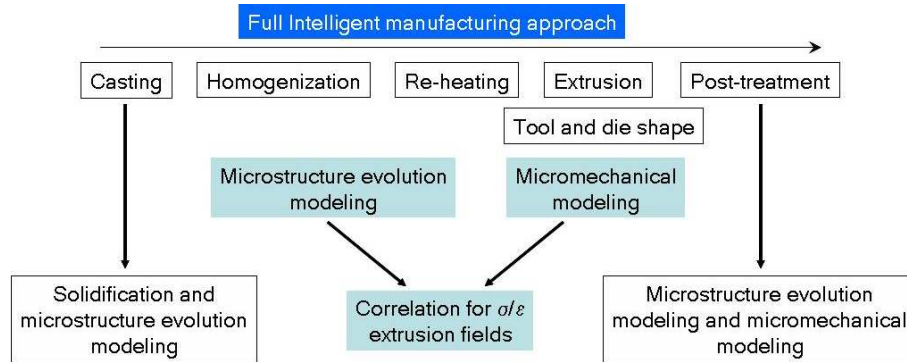


Figure 7.1 – Perspective leading to the development of a full intelligent manufacturing tool.

the predicted results concerning the evolution of the maximum ramp speed for alloy ENAA 6005 should be validated with experiments. Another important effect could aim to relate all these results with the complexity of the extrusion die in order to make this model valid for a larger number of profile shapes. We

could imagine to use a simple version of this model to run calculations with the entire tool modeled. It means to model the full shape and size of the extrusion die to study the effect of its complexity on the damage behaviour.

Some approximation of this work should also be assessed. As explained in the conclusions, one of the limitations of the model comes from the identification of the critical stresses for void nucleation, i.e. one remaining problem in the model concerns the modeling of the nucleation step. The nucleation stresses are determined in order to fit an experimental value but has to be taken very small compared to the nucleation stresses generally encountered in the literature (around 100 MPa). These parameters contain all the errors brought by the different assumptions made by the modeling. We could imagine to add a more complex nucleation model taking, theoretically, more accurately into account the nature, the size and the shape of the particles in the determination of the nucleation stresses.

A physical origin for the error made also in the model is that we consider that the particles are uniformly distributed ($\lambda_0 = 1$) even though there are located along the grain boundaries. An improvement could also be given while taking into account the fact that the intermetallic particles are found at grain boundaries and build together a network of interconnected particles, which has definitely an effect of the damage mechanisms, and thus study the effect of the void distribution and shape/size dispersion.

Finally, I think that the very good results obtained with this model should stimulate further research with other materials.

Bibliography

- [1] H. Agarwal, A.M. Gokhale, S. Graham, and M.F. Horstmeier. Quantitative characterization of three-dimensional damage evolution in a wrought al-alloy under tension and compression. *Metallurgical and Materials Transactions A*, 33A:2599–2606, 2002.
- [2] H. Agarwal, A.M. Gokhale, S. Graham, and M.F. Horstmeier. Void growth in 6061-aluminum alloy under triaxial stress state. *Materials Science and Engineering A*, 341(1-2):35–42, 2003.
- [3] D.T.L. Alexander and A.L. Geer. Particle break-up during heat treatment of 3000 series aluminium alloys. *Materials Science and Technology*, 21:955–960, 2005.
- [4] S.J. Andersen. Quantification of the mg_2si β'' and β' phases in al mg si alloys by transmission electron microscopy. *Metallurgical and Materials Transactions A*, 26A:1931–1937, 1995.
- [5] A.S. Argon. Formation of cavities from non deformable second-phase particles in low temperature ductile fracture. *J Engng Mater Tech*, 98:60–68, 1976.
- [6] L. Babout, Y. Brechet, E. Maire, and R. Fougères. On the competition between particle fracture and particle decohesion in metal matrix composites. *Acta Materialia*, 52(8):4517–4525, 2004.
- [7] L. Babout, E. Maire, and R. Fougères. Damage initiation in model metallic materials: X-ray tomography and modelling. *Acta Materialia*, 52(8):2475–2487, 2004.
- [8] D.H. Bae and A.K. Ghosh. Cavity formation and early growth in a superplastic al-mg alloy. *Acta Materialia*, 50:511–523, 2002.

- [9] A. Balasundaram, A.M. Gokhale, S. Graham, and M.F. Horstmeyer. Three-dimensional particle cracking damage development in an al-mg-base wrought alloy. *Materials Science and Engineering A*, 355:368–383, 2003.
- [10] A.A. Benzerga, J. Besson, and A. Pineau. Anisotropic ductile fracture - part i: experiments. *Acta Mat*, 52:4623–4638, 2004.
- [11] AA. Benzerga, J. Besson, and A. Pineau. Anisotropic ductile fracture - part ii: theory. *Acta Mater*, 52:4639–4650, 2004.
- [12] C. Berdin, J. Besson, S. Bugat, R. Desmorat, F. Feyel, S. Forest, E. Lorentz, E. Maire, T. Pardoen, A. Pineau, and B. Tanguy. *Local approach to fracture*. Collective book, Presses de l’Ecole des Mines de Paris, 2004.
- [13] F.M. Beremin. Cavity formation from inclusions in ductile fracture of a508 steel. *Metall Trans A*, 12:723–731, 1981.
- [14] F.M. Beremin. *Experimental and numerical study of the different stages in ductile rupture: application to crack initiation and stable crack growth*. Three-Dimensional Constitutive Relations and Ductile Fracture (S. Nemat-Nasser ed.) North-Holland Publishing Company, 1981.
- [15] M. Berveiller and A. Zaoui. An extension of the self-consistent scheme to plastically flowing polycrystals. *J Mech Phys Solids*, 26:325–340, 1979.
- [16] L. Blaz and E. Evangelista. Strain rate sensitivity of hot deformed al and almg alloys. *Material Science and Engineering A*, A207:195–201, 1996.
- [17] L. Briottet, H. Klocker, and F. Montheillet. Damage in a viscoplastic material - part ii: Overall behaviour. *Int. J. Plast.*, 14:453–471, 1998.
- [18] W. Brocks, D.Z. Sun, and A. Honig. Verification of the transferability of micromechanical parameters by cell model calculations with visco-plastic materials. *Int J Plast*, 11:971–989, 1995.
- [19] S.B. Brown, K.H. Kim, and L. Anand. An internal variable constitutive model for hot working of metals. *International Journal of Plasticity*, 5:95–130, 1989.
- [20] A. Browning, W.A. Spitzig, O. Richmond, D. Teirlink, and J.D. Embury. The influence of hydrostatic pressure on the flow stress and ductility of a spheroidized 1045 steel. *Acta Metall*, 31:1141–1150, 1983.
- [21] B. Budiansky, J.W. Hutchinson, and S. Slutsky. Void growth and collapse in viscous solids. *J Mech of Sol*, The Rodney Hill 60th Anniversary Volume:13–45, 1982.

- [22] T. Christman, A. Needleman, S. Nutt, and S. Suresh. On microstructural evolution and micromechanical modeling of deformation of a whisker-reinforced metal-matrix composite. *Mater Sci Engng A*, 107:49–61, 1989.
- [23] C.C. Chu and A. Needleman. Void nucleation effects in biaxially stretched sheets. *J Engng Mater Tech*, 102:249–256, 1980.
- [24] L.J. Colley, M.A. Wells, and D.M. Maijer. Tensile properties of as-cast aluminium alloy aa5182 close to the solidus temperature. *Materials Science and Engineering A*, 386(1-2):140–148, 2004.
- [25] A. Deschamps, S. Peron, Y. Brechet, J.-C. Ehrstrom, and L. Poizat. High temperature cleavage fracture in 5383 aluminum alloy. *Materials Science and Engineering A*, 319-321:583–586, 2001.
- [26] I. Doghri and A. Ouaar. Homogenization of two-phase elasto-plastic composite materials and structures - study of tangent operators, cyclic plasticity and numerical algorithms. *Int J Solids Struct*, 40:1681–1712, 2003.
- [27] A.L. Dons. The alstruc homogenization model for industrial aluminum alloys. *Journal of Light Metals*, 1:133–149, 2001.
- [28] I. Dulplancic and J. Prgin. The effect of extrusion conditions on the surface properties of almg63 hollow sections. In *Proceedings EE conference 2002*, pages 261–271, 2002.
- [29] J.D. Eshelby. The determination of the elastic field of an ellipsoidal inclusion and related problems. *Proc Roy Soc London, Ser. A*, 241:376–396, 1957.
- [30] M.J. Worswick et al. Damage characterization and damage percolation modeling in aluminum alloy sheet. *Acta Mater*, 49:2791–2803, 2001.
- [31] D. Fabregue and T. Pardoen. A model for the nucleation, growth and coalescence of primary and secondary voids in elasto-viscoplastic solids. *submitted*, 2005.
- [32] J. Faleskog and C.F. Shih. Micromechanics of coalescence - i. synergistic effects of elasticity, plastic yielding and multi-size-scale voids. *J Mech Phys Solids*, 45:21–45, 1997.
- [33] J. Gammage, D. Wilkinson, Y. Brechet, and D. Embury. A model for damage coalescence in heterogeneous multi-phase materials. *Acta Materialia*, 52:5255–5263, 2004.
- [34] X. Gao, J. Faleskog, and C.F. Shih. Cell model for nonlinear fracture analysis - ii. fracture-process calibration and verification. *Int J Fract*, 89:374–386, 1998.

- [35] M. Gologanu, J.B. Leblond, and G. Perrin. Theoretical models for void coalescence in porous ductile solids. i. coalescence in layers. *Int J Solids Struct*, 38:5581–94, 2001.
- [36] M. Gologanu, J.B. Leblond, G. Perrin, and J. Devaux. *Continuum Micromechanics*. P. Suquet, editor, 1995.
- [37] A. Gullerub, X. Gao, R. Haj-Ali, and R.H. Dodds. Simulation of ductile crack growth using computational cells: Numerical aspects. *Engineering Fracture Mechanics*, 66:65–92, 2000.
- [38] A.L. Gurson. Continuum theory of ductile rupture by void nucleation and growth: Part i-yield criteria and flow rules for porous ductile media. *J Engng Mater Tech*, 99:2–15, 1977.
- [39] Hibbit, Karlsson, and Sorensen. *ABAQUS/Standard version 6.5. User's Manual*. Inc. Providence, R.I., U.S., 2004.
- [40] C.L. Hom and R.M. McMeeking. Three-dimensional void growth before a blunting crack tip. *J Mech Phys Solids*, 37:395–415, 1989.
- [41] C.L. Hom and R.M. McMeeking. Void growth in elastic-plastic materials. *J Appl Mech*, 56:309–317, 1989.
- [42] Y. Huang. Accurate dilatation rates for spherical voids in triaxial stress fields. *J Appl Mech*, 58:1084–85, 1991.
- [43] G. Huber, Y. Brechet, and T. Pardoen. Void growth and void nucleation controlled ductility in quasi eutectic cast aluminium alloys. *Acta Mater*, 53:2739–2749, 2005.
- [44] J.W. Hutchinson and K.W. Neale. Influence of strain-rate sensitivity on necking under uniaxial tension. *Acta Metallurgica*, 25:839–846, 1977.
- [45] P. Joly, Y. Meyzaud, and A. Pineau. Micromechanisms of fracture of an aged duplex stainless steel containing a brittle and a ductile phase: development of a local criterion of fracture. in advances in local fracture/damage models for the analysis of engineering problems,. *The American Society of Mechanical Engineers*, 137:151–180, 1992.
- [46] J. Kim and X. Gao. A generalized approach to formulate the consistent tangent stiffness in plasticity with application to the gld porous material model. *International Journal of Solids and Structures*, 42:103–122, 2005.
- [47] H. Klocker and V. Tvergaard. Growth and coalescence of non-spherical voids in metals deformed at elevated temperature. *Int J Mech Sc*, 25:1283–1308, 2003.

- [48] D.-C. Ko, B.M. Kim, and J.C. Choi. Prediction of surface-fracture initiation in the axisymmetric extrusion and simple upsetting of an aluminum alloy. *Journal of Materials Processing Technology*, 62:166–174, 1996.
- [49] T. Kobayashi. Strength and fracture of aluminium alloys. *Materials Science Forum*, 426-432:67–74, 2003.
- [50] J. Koplik and A. Needleman. Void growth and coalescence in porous plastic solids. *Int J Solids Struct*, 24:835–853, 1988.
- [51] M. Kroon and J. Faleskog. Micromechanics of cleavage fracture initiation in ferritic steels by carbide cracking. *J Mech Phys Solids*, 53:171–196, 2005.
- [52] N.C.W. Kuijpers, J. Tirel, D.N. Hanlon, and S. Van der Zwaag. Quantification of the evolution of the 3d intermetallic structure in a 6005a aluminium alloy during a homogenisation treatment. *Materials Characterization*, 48(5):379–392, 2002.
- [53] N.K.W. Kuijpers. *PhD Thesis: Kinetics of the β -AlFeSi to α -Al(Fe,Mn)Si transformation in AlMgSi alloys*. 2004.
- [54] M. Kuna and D.Z. Sun. Three-dimensional cell model analyses of void growth in ductile materials. *Int J Fract*, 81:235–258, 1996.
- [55] D. Lassance, L. Ryelandt, F. Delannay, and T. Pardoen. Linking microstructure and high temperature ductility in aluminium enaw 6060 alloys. In *The 11th International Conference of Fracture, Turin, Italy*, 2005.
- [56] D. Lassance, L. Ryelandt, J. Dille, J.L. Delplancke, M. Rijckeboer, T. Pardoen, and F. Delannay. Effet of the homogenisation conditions on the extrudability and high temperature resistance of an aa6063 aluminium alloy. *Materials Science Forum*, 426-432:447–452, 2003.
- [57] D. Lassance, F. Scheyvaerts, and T. Pardoen. Growth and coalescence of penny-shaped voids in metallic alloys. 2006.
- [58] J.C. Lautridou and A. Pineau. Crack initiation and stable crack growth resistance in a508 steels in relation to inclusion distribution. *Engng Fract Mech*, 15:55–71, 1981.
- [59] J.B. Leblond, G. Perrin, and J. Devaux. An improved gurson-type model for hardenable ductile metals. *Eur J Mech A/Solids*, 14:499–527, 1995.
- [60] J.B. Leblond, G. Perrin, and P. Suquet. Exact results and approximate models for porous viscoplastic solids. *Int J Plast*, 10:213–235, 1994.
- [61] B.J. Lee and M.E. Mear. Stress concentration induced by an elastic spheroidal particle in a plastically deforming solid. *J Mech Phys Solids*, 47:1301–36, 1999.

- [62] F.A. McClintock. A criterion for ductile fracture by the growth of holes. *J of Appl Mech*, 35:353–371, 1968.
- [63] F.A. McClintock. Local criteria for ductile fracture. *Int J Fract*, 4:103–130, 1968.
- [64] H. Nagaumi, Takateru, and Umeda. Study of the crack sensitivity of 6xxx and 7xxx aluminum alloys. *Materials Science Forum*, 426-432:465–470, 2003.
- [65] A. Needleman. Void growth in an elastic-plastic medium. *J Appl Mech*, 39:964–970, 1972.
- [66] A. Needleman and V. Tvergaard. An analysis of ductile rupture in notched bars. *J Mech Phys Solids*, 32:461–490, 1984.
- [67] K.E. Nilsen and P.T.G. Koenis. Quantitative analysis of the homogenizing heat treatment by means of alferi particles analysis and the effect on productivity. In *Proceedings EE conference 2002*, pages 69–75, 2002.
- [68] D.M. Norris, B. Moran, J.K. Scudder, and D.F. Quinones. A computer simulation of the tension test. *Journal of Mechanics and Physics of Solids*, 26:1–19, 1978.
- [69] P. Onck, F. Scheyvaerts, and T. Pardoen. In preparation. ..., 2005.
- [70] T. Pardoen and F. Delannay. Assessment of void growth models from porosity measurements in cold-drawn copper bars. *Metallurgical and Materials Transactions A*, 29A:1895–1909, 1998.
- [71] T. Pardoen, D. Dumont, A. Deschamps, and Y. Brechet. Grain boundary versus transgranular ductile failure. *J. Mech. Phys. Solids*, 51:637–665, 2003.
- [72] T. Pardoen and J.W. Hutchinson. An extended model for void growth and coalescence. *J Mech Phys Solids*, 48:2467–2512, 2000.
- [73] T. Pardoen and J.W. Hutchinson. Micromechanics-based model for trends in toughness of ductile metals. *Acta Mater*, 51:133–148, 2003.
- [74] A. Pineau. Global and local approaches of fracture - transferability of laboratory test results to components. *A.S. Argon, editor, Topics in Fracture and Fatigue Springer-Verlag*, pages 197–234, 1992.
- [75] A.R. Ragab. Application of an extended void growth model with strain hardening and void shape evolution to ductile fracture under axisymmetric tension. *Engng Fract Mech*, 71:1515–1534, 2004.

- [76] O. Reiso, J.E. Hafsas and O. Sjöthun, and U. Tundal. The effect on cooling rate after homogenization and billet preheating practice on extrudability and section properties. part1: Extrudability and mechanical properties. *Metallurgical and Materials Transactions A*, pages 1–10, 1995.
- [77] O. Reiso, U. Tundal, and J. Andersen. The effect on cooling rate after homogenization and billet preheating practice on extrudability and section properties. part2: Microstructural investigation. *Metallurgical and Materials Transactions A*, pages 141–147, 1995.
- [78] J.R. Rice and M.A. Johnson. *The role of large crack tip geometry changes in plane strain fracture*. M.F. Kanninen, W.G. Adler, A.R. Rosenfield, and R.I. Jaffee (Eds.) *Inelastic Behavior of Solids*, McGraw-Hill, 1970.
- [79] J.R. Rice and D.M. Tracey. On the ductile enlargement of voids in triaxial stress fields. *J Mech Phys Solids*, 17:201–217, 1969.
- [80] M.N. Shabrov and A. Needleman. An analysis of inclusion morphology effects on void nucleation. *Modelling Simul Mater Sci Eng*, 10:163–183, 2002.
- [81] M.N. Shabrov, E. Sylven, S. Kim, D.H. Sherman, L. Chuzhoy, C.L. Briant, and A. Needleman. Void nucleation by inclusion cracking. *Metallurgical and Materials Transactions A*, 35A:1745–1755, 2004.
- [82] T. Sheppard. *Extrusion of aluminium alloys*. Kluwer Academic, 1999.
- [83] K. Siruguet and J.B. Leblond. Effect of void locking by inclusions upon the plastic behavior of porous ductile solids - i: theoretical modeling and numerical study of void growth. *Int J Plast*, 20:225–54, 2004.
- [84] S. Spigarelli, E. Evangelista, and H.J. McQueen. Study of hot workability of a heat treated aa6082 aluminum alloy. *Scripta Materialia*, 49:179–193, 2003.
- [85] D. Steglich and W. Brocks. Micromechanical modeling of the behaviour of ductile materials including particles. *Computational Materials Science*, 9:7–17, 1997.
- [86] D. Steglich, T. Siegmund, and W. Brocks. Micromechanical modeling of damage due to particle cracking in reinforced metals. *Computational Materials Science*, 16:404–413, 1999.
- [87] P.F. Thomason. *Ductile Fracture of Metals*. Oxford: Pergamon Press, 1990.
- [88] C.I.A. Thomson, M.J. Worswick, A.K. Pilkey, and D.J. Lloyd. Void coalescence within periodic clusters of particles. *J Mech Phys Solids*, 51:127–146, 2003.

- [89] H. Toda and T. Kobayashi. Damage behaviours of various coarse al-fe-si particles in model wrought alloys. *Materials Science Forum*, 426-432:393–398, 2003.
- [90] V. Tvergaard. Influence of voids on shear band instabilities under plane strain conditions. *Int J Fract*, 17:389–407, 1981.
- [91] V. Tvergaard. On localization in ductile materials containing voids. *Int J Fract*, 18:237–251, 1982.
- [92] F. Vermolen, K. Vuik, and S. Van der Zwaag. The dissolution of a stoichiometric second phase in ternary alloys: a numerical analysis. *Materials Science and Engineering A*, 246:93–103, 1998.
- [93] F. Vermolen, K. Vuik, and S. Van der Zwaag. A mathematical model for the dissolution kinetics of mg-2si phases in al-mg-si alloys during homogenisation under industrial conditions. *Materials Science and Engineering A*, 254:13–32, 1998.
- [94] Q.G. Wang. Microstructural effects on the tensile and fracture behaviour of aluminium casting alloys a356/357. *Metallurgical and Materials Transactions A*, 34A:2887–2899, 2003.
- [95] Q.G. Wang, C.H. Caceres, and J.R. Griffiths. Damage by eutectic cracking in aluminium casting alloys a356/357. *Metallurgical and Materials Transactions A*, 34A:2901–2912, 2003.
- [96] M.J. Worswick and R.J. Pick. Void growth and constitutive softening in a periodically voided solid. *J Mech Phys Solids*, 38:601–625, 1990.
- [97] S. Zajac, B. Hutchinson, and L.-O. Gullman. Microstructure control and extrudability of al-mg-si alloys microalloyed with manganese. *Materials Science and Technology*, 10:323–333, 1994.
- [98] Z. Zhang. A practical micro-mechanical model-based local approach methodology for the analysis of ductile fracture of welded t-joints. *PhD Thesis, Lappeeranta, Finland*, 1994.



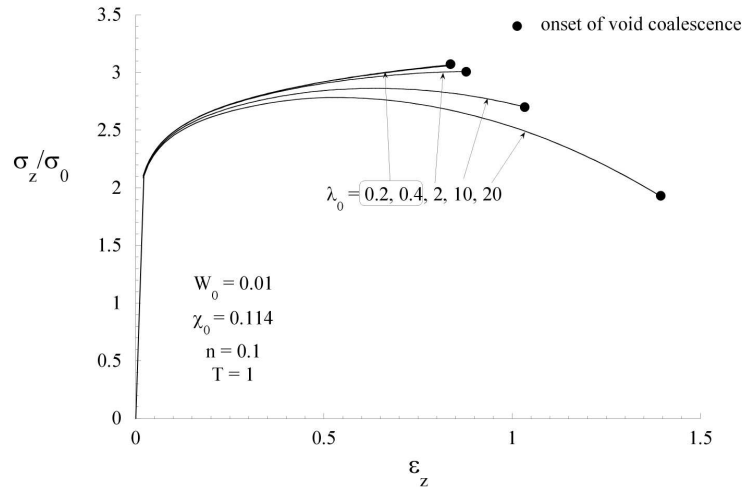
Effect of the anisotropy distribution parameter λ_0

Appendix A

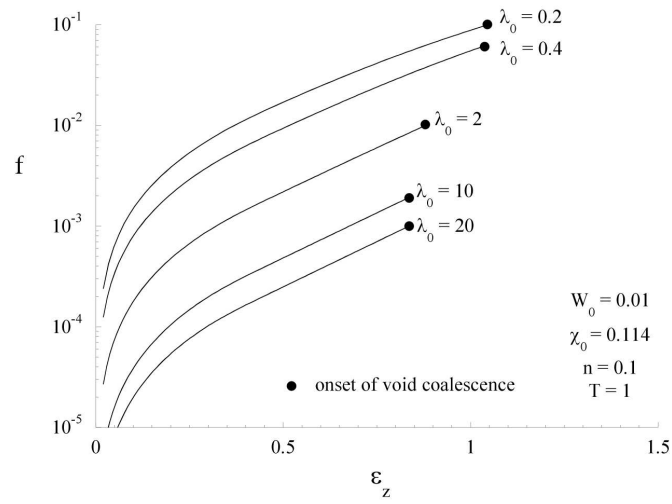
Effect of the anisotropy distribution parameter λ_0

Figure A.1 shows the effect of the anisotropy distribution parameter λ_0 on the variation of (a) the axial stress; (b) the porosity; (c) the relative void spacing; (d) the void aspect ratio as a function of the axial strain. The relative void spacing χ_0 is constant, equal to 0.114, the voids are initially-penny shaped ($W_0 = 0.01$), the stress triaxiality T is equal to 1 and the strain hardening exponent n is equal to 0.1. Figure A.1 demonstrates that the ductility is indeed affected by the value of λ_0 (which is equivalent to state that, under constant χ_0 , the ductility is affected by the initial porosity f_0) when λ_0 is sufficiently small. Figure A.1c and d show that the evolutions of both the relative void spacing and void aspect ratio are only weakly modified when changing λ_0 (or the initial porosity f_0). Hence, the differences in ductility mainly result from the change of softening on the stress associated with the change of porosity, affecting thus only the left hand side of the coalescence condition (4.17). In other words, under constant χ_0 , an effect of λ_0 , or of f_0 , is expected if the porosity becomes large enough during the process of void growth to affect the overall stress level. Typically, stress softening starts to be significant when the porosity gets larger than 1%.

Finally, in agreement with the analysis already made in [72] for initially rounded voids, Figure A.1a shows that for large λ_0 , the onset of coalescence coincides with the peak stress which, consequently, is determined by the onset of the void coalescence localization process and not due to the competition between the hardening of the matrix and the softening due to void growth.



(a)



(b)

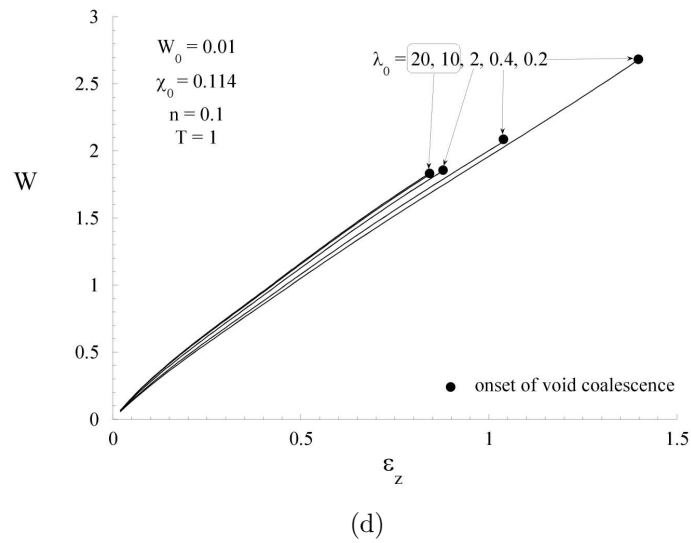
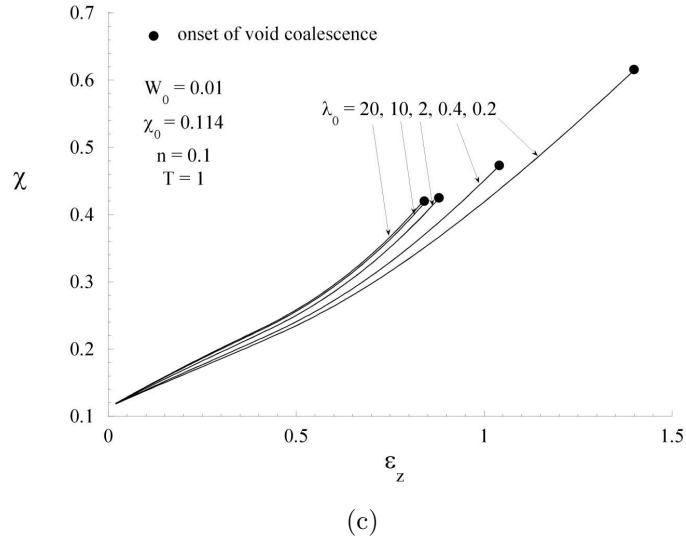


Figure A.1 – Effect of the anisotropy distribution parameter λ_0 on the variation as a function of the overall axial strain of (a) the overall axial stress; (b) the porosity; (c) the relative void spacing; (d) the void aspect ratio; for a constant relative void spacing $\chi_0 = 0.114$, penny-shaped voids ($W_0 = 0.01$), $T = 1$, and $n = 0.1$.

B

Important geometrical relationships

Appendix B

Important geometrical relationships

The non-dimensional quantities f (void volume fraction), W (void aspect ratio), λ (void anisotropy distribution parameter), χ (relative void spacing) for spheroidal voids are defined as

$$f = \gamma \frac{R_x^2 R_z}{L_x^2 L_y} \quad (\text{B.1})$$

$$W = \frac{R_z}{R_x} \quad (\text{B.2})$$

$$\lambda = \frac{L_z}{L_x} \quad (\text{B.3})$$

$$\chi = \frac{R_x}{L_x} \quad (\text{B.4})$$

where the lengths R_x , R_z , L_x and L_z have been defined on Chapter 1, section 1.6 and γ is a geometric factor which depends on the arrangement of voids: $\gamma = \pi/6 = 0.523$ for a periodic simple cubic array, $\gamma = 0.605$ for a periodic hexagonal distribution and $\gamma = 2/3 = 0.666$ for a void surrounded by a cylindrical matrix. The four non-dimensional quantities are related through

$$\chi = \left(\frac{f \lambda}{\gamma W} \right)^{1/3} \quad (\text{B.5})$$

A serie of useful relationships for the evolution rates are provided:

$$\dot{\epsilon}_x = \frac{\dot{L}_x}{L_x} \text{ and } \dot{\epsilon}_z = \frac{\dot{L}_z}{L_z} \quad (\text{B.6})$$

$$\frac{\dot{\lambda}}{\lambda} = \dot{\epsilon}_z - \dot{\epsilon}_x \quad (\text{B.7})$$

$$\frac{\dot{f}}{f} = \frac{\dot{R}_z}{R_z} + 2\frac{\dot{R}_x}{R_x} - \frac{\dot{L}_z}{L_z} - 2\frac{\dot{L}_x}{L_x} \quad (\text{B.8})$$

$$\frac{\dot{W}}{W} = \frac{\dot{R}_z}{R_z} - \frac{\dot{R}_x}{R_x} \quad (\text{B.9})$$

$$\frac{\dot{\chi}}{\chi} = \frac{1}{3} \left(\dot{\epsilon}_z - \dot{\epsilon}_x + \frac{\dot{f}}{f} - \frac{\dot{W}}{W} \right) \quad (\text{B.10})$$

$$\frac{\dot{R}_x}{R_x} = \frac{1}{3} \left(\dot{\epsilon}_z + 2\dot{\epsilon}_x + \frac{\dot{f}}{f} - \frac{\dot{W}}{W} \right) \quad (\text{B.11})$$

$$\frac{\dot{R}_z}{R_z} = \frac{1}{3} \left(\dot{\epsilon}_z + 2\dot{\epsilon}_x + \frac{\dot{f}}{f} + 2\frac{\dot{W}}{W} \right) \quad (\text{B.12})$$

C

Expressions for the parameters of the void growth model

Appendix C

Expressions for the parameters of the void growth model

For mathematical convenience, the model is not expressed in terms of f and W , but mainly in terms of the inner and outer eccentricity, e_1 and e_2 , which are uniquely related to f and W by the following equations,

$$e_1 = \sqrt{1 - \frac{1}{W^2}} \quad (\text{C.1})$$

$$\frac{(1 - e_2^2)}{e_2^3} = \frac{1}{f} \frac{(1 - e_1^2)}{e_1^3}, \text{ "prolateshape" : } W \geq 1 \text{ "} \quad (\text{C.2})$$

$$\frac{\sqrt{(1 - e_2^2)}}{e_2^3} = \frac{1}{f} \frac{\sqrt{(1 - e_1^2)}}{e_1^3}, \text{ "oblateshape" : } W < 1 \text{ "} \quad (\text{C.3})$$

The expressions of the parameters appearing in eqns 5.10 and 5.15 are given here after with a o or a p to indicate whether it belongs to the oblate shape or to the prolate shape, respectively.

$$g = 0, \text{ "p"} \quad (\text{C.4})$$

$$g = \frac{e_2^3}{\sqrt{1 - e_2^2}}, \text{ "o"} \quad (\text{C.5})$$

$$\alpha_2 = \frac{(1 + e_2^2)}{(3 + e_2^4)}, \text{ "p"} \quad (\text{C.6})$$

$$\alpha_2 = \frac{(1 - e_2^2)(1 - 2e_2^2)}{(3 - 6e_2^2 + 4e_2^4)}, \text{ "o"} \quad (\text{C.7})$$

$$\kappa^{-1} = \frac{1}{\sqrt{3}} + \frac{1}{\ln f \left((\sqrt{3}-2) \ln \frac{e_1}{e_2} \right)} + \frac{1}{\ln f} \left(\frac{1}{\sqrt{3}} \ln \left(\frac{3+e_2^2+2\sqrt{3+e_2^4}}{3+e_1^2+2\sqrt{3+e_1^4}} \right) \right) + \ln \left(\frac{\sqrt{3} + \sqrt{3+e_1^4}}{\sqrt{3} + \sqrt{3+e_2^4}} \right), \text{ "p"}$$
 (C.8)

$$\kappa^{-1} = \frac{2}{3} + \frac{\frac{2}{3}(g_f - g_1) + \frac{2}{5}(g_f^{5/2} - g_1^{5/2}) \left(\frac{4}{3} - g_f^{5/2} - g_1^{5/2} \right)}{\ln \left(\frac{g_f}{g_1} \right)}, \text{ "o"}$$
 (C.9)

with

$$g_f = \frac{g}{g+f} \text{ and } g_1 = \frac{g}{g+1}, \text{ "o"}$$
 (C.10)

$$\eta = - \frac{\kappa q (1-f)(g+1)(g+f)sh}{(g+1)^2 + q^2(g+f)^2 + 2q(g+1)(g+f)[\kappa(\alpha_1 - \alpha_2)sh - ch]}$$
 (C.11)

with

$$sh = \sinh(2\kappa(\alpha_1 - \alpha_2)) \text{ and } ch = \cosh(2\kappa(\alpha_1 - \alpha_2))$$
 (C.12)

$$\alpha_1 = \frac{[e_1 - (1 - e_1^2)\tanh^{-1}(e_1)]}{2e_1^3}, \text{ "p"}$$
 (C.13)

$$\alpha_1 = \frac{[-e_1(1 - e_1^2) + \sqrt{1 - e_1^2}\sin^{-1}(e_1)]}{2e_1^3}, \text{ "o"}$$
 (C.14)

$$C = - \frac{\kappa q (g+1)(g+f)sh}{\eta[1 - f + 2\eta(\alpha_1 - \alpha_2)]}$$
 (C.15)

$$h_s = \frac{9}{2} \frac{\alpha_1 - \alpha_1^G}{1 - 3\alpha_1}$$
 (C.16)

$$\alpha_1^G = \frac{1}{(3 - e_1^2)}, \text{ "p"}$$
 (C.17)

$$\alpha_1^G = \frac{(1 - e_1^2)}{(3 - 2e_1^2)}, \text{ "o"}$$
 (C.18)

$$h_f = (1 - \sqrt{f})^2$$
 (C.19)

$$h_{sf} = \left(\frac{1 - 3\alpha_1}{f} + 3\alpha_2 - 1 \right)$$
 (C.20)

Finally, h_T has been adjusted to give the best predictions for the void shape rates at the two strain hardening levels (only valid for $T \geq 4$):

$$h_T = 1 - 0.555T^2 - 0.045T^4 + 0.002T^6, \quad n = 0.1 \quad (\text{C.21})$$

$$h_T = 1 - 0.54T^2 + 0.034T^4 - 0.00124T^6, \quad n = 0.1 \quad (\text{C.22})$$

Interpolation can be used in the case of intermediate or varying n .



Klocker formulation for void aspect parameter k

Appendix D

Klocker formulation for void aspect parameter k

The correction term k_m proposed by Klocker and Tvergaard [47] writes :

$$\frac{k_m}{k_0} = \frac{\left(0.73 + \frac{0.25}{W_0}\right) + \left(-4.74 - \frac{2.58}{W_0}\right) \frac{1}{T} + \left(6.79 - \frac{13.74}{W_0}\right) \frac{1}{T^2}}{\left(0.09 + \frac{1.23}{W_0}\right) + \left(-1.19 - \frac{2.85}{W_0}\right) \frac{1}{T} + \left(1.75 - \frac{3.07}{W_0}\right) \frac{1}{T^2}} \quad (\text{D.1})$$

This fit is valid for m in the range 0.01 and 0.25, for a stress triaxiality T in the range 0.9 to infinity and for W_0 in the range 1/8 and 10. In case of a parameter lying outside the range of the fit, we simply use the value corresponding to the extreme value of the fit. The correction provided by relationship D.1 varies a lot for small changes of W_0 and T when both the stress triaxiality is large ($T \geq 2$) and the voids are elongated ($W_0 \geq 2$). The reason for this behavior stems from that k_0 is then very small in that domain of T and W_0 . Considering that above $T = 1.5 - 2$, effects related to void shape changes affect only weakly the coalescence, no correction is made in that case.

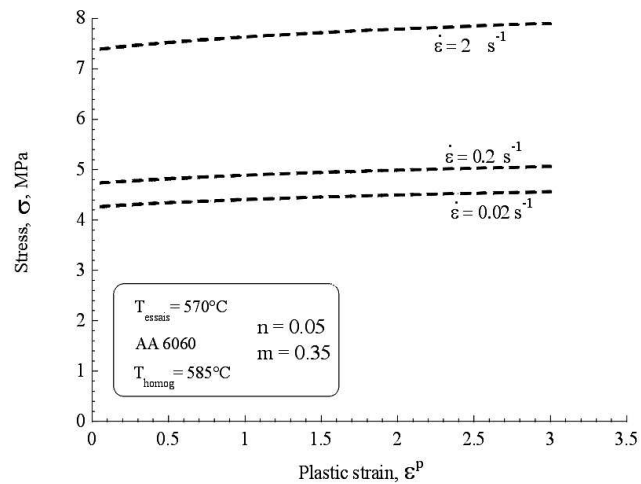
E

Flow curves identification

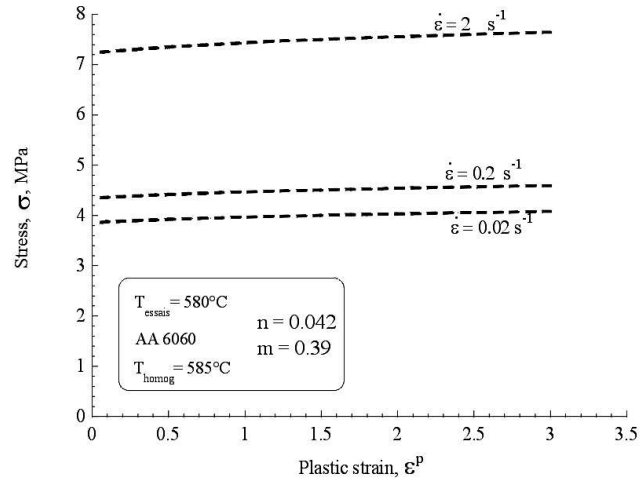
Appendix E

Flow curves identification

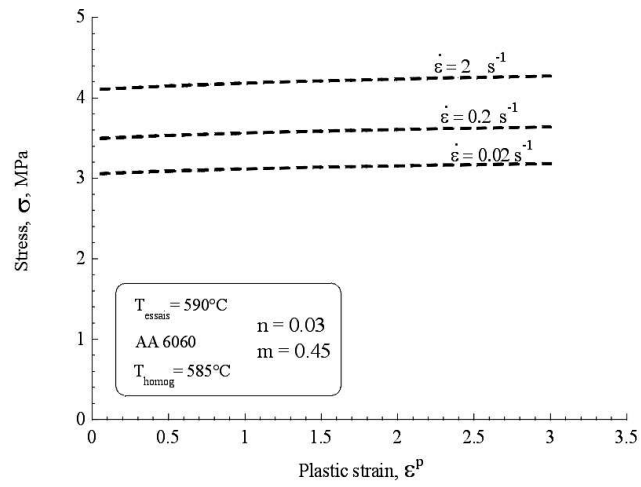
True stress - true plastic strain flow curves for different strain rates equal to 0.02, 0.2 and 2 s⁻¹ at (a,d) 570°C, (b,e) 580°C and (c,f) 550°C for the alloys (a,b) AA 6060 and (c,d) AA 6005A. Both alloys were homogenized at 585°C.



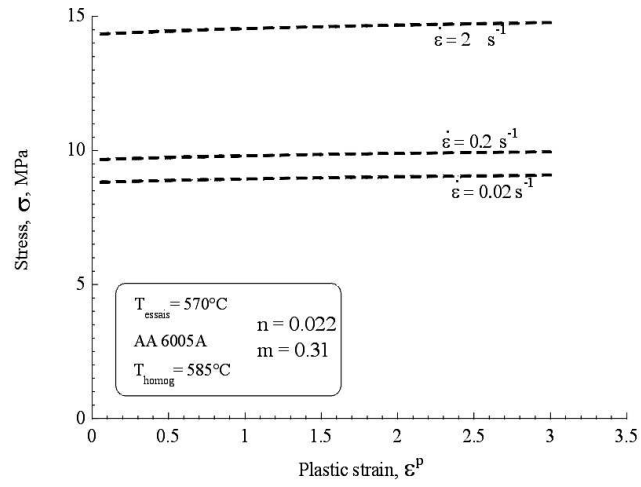
(a)



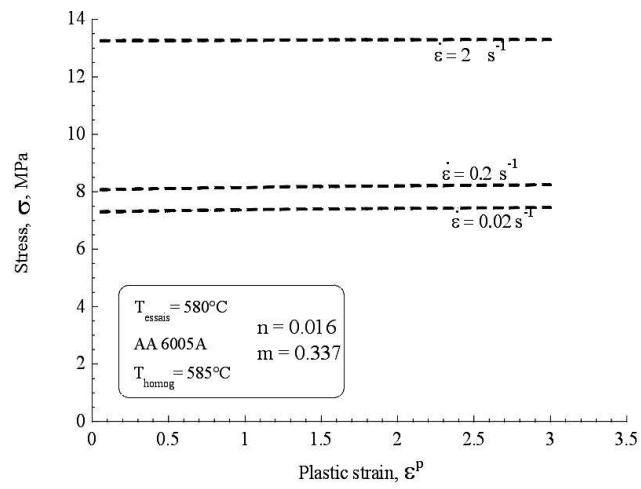
(b)



(c)



(d)



(e)

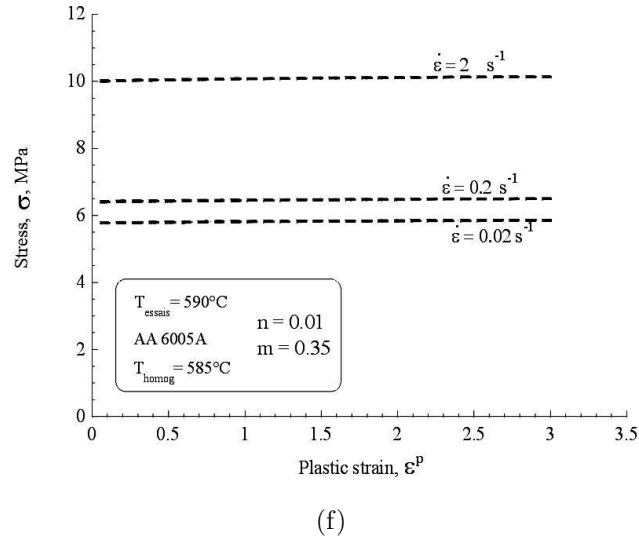


Figure E.1 – True stress – true plastic strain flow curves for different strain rates equal to 0.02, 0.2 and 2 s^{-1} at (a,d) 570°C , (b,e) 580°C and (c,f) 550°C for the alloys (a,b) AA 6060 and (c,d) AA 6005A. Both alloys were homogenized at 585°C .